NEW DEVELOPMENTS in MECHANICS and MECHANICAL ENGINEERING

Proceedings of the International Conference on Mechanical Engineering (ME 2015)

Proceedings of the International Conference on Theoretical Mechanics and Applied Mechanics (TMAM 2015)

Vienna, Austria
March 15-17, 2015

NEW DEVELOPMENTS in MECHANICS and MECHANICAL ENGINEERING

Proceedings of the International Conference on Mechanical Engineering (ME 2015)

Proceedings of the International Conference on Theoretical Mechanics and Applied Mechanics (TMAM 2015)

Vienna, Austria
March 15-17, 2015

All papers of the present volume were peer reviewed by no less than two independent reviewers. Acceptance was granted when both reviewers' recommendations were positive.

Series: Recent Advances in Mechanical Engineering Series | 13

ISSN: 2227-4596
ISBN: 978-1-61804-288-0

NEW DEVELOPMENTS in MECHANICS and MECHANICAL ENGINEERING

Proceedings of the International Conference on Mechanical Engineering (ME 2015)

Proceedings of the International Conference on Theoretical Mechanics and Applied Mechanics (TMAM 2015)

Vienna, Austria
March 15-17, 2015

Organizing Committee

Additional Reviewers

Jose Flores	The University of South Dakota, SD, USA
Abelha Antonio	Universidade do Minho, Portugal
Lesley Farmer	California State University Long Beach, CA, USA
Takuya Yamano	Kanagawa University, Japan
Miguel Carriegos	Universidad de Leon, Spain
Francesco Zirilli	Sapienza Universita di Roma, Italy
George Barreto	Pontificia Universidad Javeriana, Colombia
Eleazar Jimenez Serrano	Kyushu University, Japan
Tetsuya Yoshida	Hokkaido University, Japan
Philippe Dondon	Institut polytechnique de Bordeaux, France
Genqi Xu	Tianjin University, China
M. Javed Khan	Tuskegee University, AL, USA
Xiang Bai	Huazhong University of Science and Technology, China
Dmitrijs Serdjuks	Riga Technical University, Latvia
Hessam Ghasemnejad	Kingston University London, UK
José Carlos Metrôlho	Instituto Politecnico de Castelo Branco, Portugal
João Bastos	Instituto Superior de Engenharia do Porto, Portugal
Tetsuya Shimamura	Saitama University, Japan
Imre Rudas	Obuda University, Budapest, Hungary
Konstantin Volkov	Kingston University London, UK
Frederic Kuznik	National Institute of Applied Sciences, Lyon, France
James Vance	The University of Virginia's College at Wise, VA, USA
Angel F. Tenorio	Universidad Pablo de Olavide, Spain
Sorinel Oprisan	College of Charleston, CA, USA
Santoso Wibowo	CQ University, Australia
Jon Burley	Michigan State University, MI, USA
Kazuhiko Natori	Toho University, Japan
Shinji Osada	Gifu University School of Medicine, Japan
Francesco Rotondo	Polytechnic of Bari University, Italy
Deolinda Rasteiro	Coimbra Institute of Engineering, Portugal
Alejandro Fuentes-Penna	Universidad Autónoma del Estado de Hidalgo, Mexico
Moran Wang	Tsinghua University, China
Bazil Taha Ahmed	Universidad Autonoma de Madrid, Spain
Andrey Dmitriev	Russian Academy of Sciences, Russia
Masaji Tanaka	Okayama University of Science, Japan
Matthias Buyle	Artesis Hogeschool Antwerpen, Belgium
Kei Eguchi	Fukuoka Institute of Technology, Japan
Zhong-Jie Han	Tianjin University, China
Valeri Mladenov	Technical University of Sofia, Bulgaria
Ole Christian Boe	Norwegian Military Academy, Norway
Yamagishi Hiromitsu	Ehime University, Japan
Stavros Ponis	National Technical University of Athens, Greece
Minhui Yan	Shanghai Maritime University, China

Table of Contents

ISBN: 978-1-61804-288-0

Design and Experiment of Miniaturized and Low-Cost Robotic Fish with Customerized Electromagnetic Actuation

Zhiqing Qian, Hongzhou Liu, and Zhuming Bi

Abstract**—**Motivated by the lack of the study in developing miniaturized and low-cost biomimetic robots, we proposed a novel robotic fish with customized electromagnetic actuations. It has four degrees of freedom (DoF), which is capable of reaching any position in a 3-D space. The system design is introduced in the paper. The design covers its mechanical structure, motion control, and its communication for human-robot-interaction. The exterior shape of the robotic fish was optimized to minimize the power consumption in the operation. In prototyping, the exterior body of the robot was modeled in SolidWorks and materialized using rapid prototyping (RP) technology, and the electromagnetic drivers were customized as swing actuators for the propulsion of the robotic fish. For robotic control, AVR microcontrollers by Atmel were adopted, and the human-robot interaction was through the Bluetooth communication to minimize the needs of using a large number of sensors. In the experiments, the intents of an operator were captured by gesture sensors from hand signals, and the programs were developed to translate the human operator's inputs into the motion commends of the robotic fish. The tests on the prototyped robot have shown the feasibility of (1) customizing electromagnetic actuators for a robotic fish and (2) involving human operator in the control system to reduce the needs of sensors and increase the capability of robot to deal with uncertainties. The robotic fish has been miniaturized greatly. The proposed design concepts have their significance to be extended in developing other biomimetic robots, including medical robots.

Keywords**—**Robotic fish; biomimetic robots; human-computer interaction; electromagnetic drives.

I. Introduction

Robots are known to people with their efficiency, productivity, and autonomy. Robots are developed to replace human workers in performing dangerous, dirt, or boring tasks in various applications [24-27]. Robots have been widely applied in manufacturing and industry environments since the 1965s [1]. The advancement of robotic technologies depends greatly on that of artificial intelligence. With a rapid development of information technologies (IT), recently developed robots are diversified, miniaturized, and multi-functional; in some cases, the collaborations among robots or with human users are required to synergize the team efforts [14,15]. Various robots have been designed for different applications [1] [2]. One of the emerging research fields is the development of biomimetic underwater robots [1-5]; existing biomimetic technologies are facing challenges in making robots competitive to underwater creatures. It is generally agreed that the main challenges are caused by the fundamental difference of a marine animal and an artificial machine; for example, the skin of a marine animal is soft, wet and flexible, while the exterior of a robot is usually dry and rigid. With the evolution of over thousands of years, a biological system adapts its living environment perfectly; it is desirable to have an artificial machine, which is capable of responding its application environment like a creature [18,21-22]. However, a biological system is so complex, and it is impossible to completely mimic its behaviors and functions with a man-made robot. Taking into consideration of the cost factor and the limitations of available materials, the functional requirements of a biomimetic robot should be more focused and realistic [6].

This paper is focused on the development of a robotic fish. Existing robotic fishes can be classified in different ways. For example, different components in a robot can be actuated for swimming. The actuated components can be body segments, caudal fins, median fins, or a combination of these components, such as body and caudal fin (BCF) or median and paired fins (MPF). The swimming pattern affects the performance of a robotic fish. The swimming pattern with BCF can achieve a greater thrust and acceleration; while the swimming pattern with MPF can obtain a better mobility and higher efficiency of propulsion. It is appropriate in a low-speed movement [7]. The first robotic fish, which was also known as 'RoboTune', was developed by Massachusetts Institute of Technology (MIT) in 1994 [8]. This robot was driven by BCF and it imitated the swimming mode of tuna. Shao et al. [9] introduced a robotic fish with multiple joints

Zhiqin Qian is with Complex and Intelligent System Research Laboratory (CISRL), East China University of Science and Technology, School of Mechanical and Power Engineering, Shanghai, 200237, China (e-mail: qianzhiqin@ecust.edu.cn).

Hongzhou Lie is with Complex and Intelligent System Research Laboratory (CISRL), East China University of Science and Technology, School of Mechanical and Power Engineering, Shanghai, 200237, China (e-mail: andy_mech@126.com).

Zhuming Bi is with Complex and Intelligent System Research Laboratory (CISRL), East China University of Science and Technology, School of Mechanical and Power Engineering, Shanghai, 200237, China. He is also affiliated with Department of Engineering, Purdue University of Fort Wayne, 2101 E. Coliseum Blvd, Fort Wayne, IN 46805, U.S.A. (e-mail: biz@ipfw.edu).

inside the body. The joints were driven by DC servomotors, and the robot was proposed to be applied in the collaborative transportation. That robot was equipped with a powered tailfin to refine the robot motion. In the robot built by Zhang et al. [11], the power source was placed on the thruster of a long dorsal. This design was inspired by a "gymnarchus niloticus", whose long dorsal fin provides the main propulsion when it hunts or swims in a low speed. It can be classified as MPF.

It is worth to note that the types of actuators are one of the critical factors in the design of a robot. Actuators of conventional robots are mostly servomotors with rotational motions. In recent years, some actuators with new driving materials, such as piezoelectric ceramics and shape memory alloys (SMA), have been applied to drive robotic fishes. For example, Nguyen et al. [4] used a type of lightweight composite piezoelectric ceramic actuators (LIPCAs) to drive a robotic fish. Both of theoretical analysis and experiment showed that the maximized thrust occurred when the fin wiggled at the frequency of 3.7 Hz, and the maximized speed could reach 7.70 cm/s. SMA-actuators have shown their advantages on compact structure, noiseless operation, and low driving voltage. Wang et al. [12] used shape memory alloy wires to drive a micro-robotic fish. SMA wires were embedded in the fish body for propulsion. They argued that SMA-based actuators were very advantageous as the drivers in biomimetic fins; since the mechanisms to store or convert potential energy could be integrated into biomimetic fins to improve the swimming efficiency.

Besides the robotic structures and driving actuators, the dimensional optimization is also important. Analytical models were developed to build the relational models of design parameters and system performances. Vo et al. [3] developed a theoretical model to maximize its forward speed for a robotic fish under the given design restraints. The robotic fish was a carangiform-like fish with three joints, and the design parameters under the consideration were the amplitudes, frequencies and phase differences of actuators. The genetic algorithm (GA) was combined with the hill-climbing algorithm (HCA) to optimize all those design parameters, and the design results were validated through the experiments. Chang et al. [13] developed a hydrodynamic model to analyze the swimming behaviors of a robotic fish; they applied this model to evaluate three shapes of caudal fins including popular crescent-shaped fins, semicircle-shaped fins and fan-shaped fins. Their results showed that a caudal fin with a crescent-shape produced a lower thrust in comparison with the fin with a semi-circle or a fan-shape; however, the corresponding efficiency was the highest among three shapes.

Despite numerous researches on robotic fishes, further developments are demanding to design miniaturized and low-cost robots [23]. Therefore, we are motivated to explore the possibility of using low-cost electromagnetic drivers and involving human operators in the control loop to reduce the robot cost and increase its manipulability in the operation. A new biomimetic fish is designed; it is driven by customized electromagnetic actuators and it can be controlled remotely by users via wireless communication. To our knowledge, it is the first time where electromagnetic actuators are customized as swing actuators in robotic fishes. The rest of paper is organized as follows. In Section 2, the working principle of electromagnetic actuation is introduced; in Section 3, the designs of main components of the robotic fish are discussed, and the controlling and communication system are prototyped. In Section 4, the experiments are provided to illustrate the feasibility of using electromagnetic drivers and wireless control via human and robot interaction. Finally, in Section 5, our works are summarized and the future research in this field is introduced briefly.

II. Working Principle of Electromagnetic Actuation

Actuators in a robotic fish perform the similar functions of muscles in an animal. Three types actuators discussed in Section 1 were fully rotational serve motors, piezoelectric actuators, and SMA-based actuators. The costs for these actuators are relative high. In this section, the feasibility of customizing electromagnetic actuators for swing actuation is investigated to reduce the cost of a robotic fish.

A. Structure of Actuator

The main component in an electromagnetic actuator is the magnetic object. A driving force occurs to the magnetic object when it is exposed to a magnetic field; such a driving force can be used to move the parts, which have the connection with the magnetic object. Fig. 1 has shown the structure of a specific electromagnetic actuator; it has been applied in the proposed robotic fish. The actuator includes three main components, i.e., coils, magnets, and the swing rod. When the power supply is on, it generates the current passing through coils; in turn, the coils for the magnetic field around the magnet object. Therefore, the magnet object is subjected to a driving force within the magnetic field, and the magnitude of the driving force can be controlled by the level of current. In the illustrated configuration, the swing rod is forced to move under the magnetic field by magnet object is aligned with that of coils.

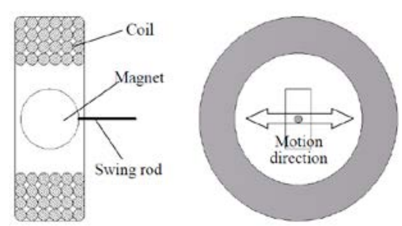

Fig.1. Principle of a specific electromagnetic actuator

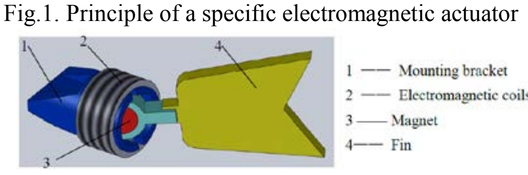

Fig.2. The setup of an actuator on robotic fish

All of joints in the proposed robotic fish are driven by such type of electromagnetic acturator. However, the size and capacity of an actuator can be varied based of the driving requirement. Fig. 2 has shown the setup when the actuator is installed on the robotic fish. The set up for the actuator includes the following parts:

Mounting bracket:	it is used to mount actuator over the body of robotic fish;
Electromagnetic coils:	it generates a magnetic field when there is a current passing through coils;
Magnet objects:	it activates the movement when the driving force becomes available;
Fin:	it serves an interface to convert internal driving force into the pushing force from the residential environment.

B. *Control of Actuator*

It can be seen that changing the current in coils causes the oscillating motion of the swing fin, the direction of motion depends on the direction of current, and the magnitude of driving force is proportional to that of the current. Therefore, controlling such an actuator is all about to control the current in the coils. A direct current is also proportional to the voltage U applied in the circuit. To simplify the actuator, the voltage U is given as a waveform in Fig. 3, and the width of the waveform pulse is controlled by the Pulse-width modulation (PWM).

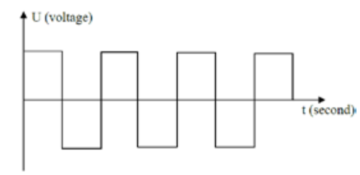

Fig.3. The voltage of electromagnetic actuator

The swing direction of the fin depends eventually on the sign of voltage applied on the coils. As shown in Fig. 4, when the voltage over the coils is positive, the fine swings towards to left; otherwise, it moves to the right when the voltage becomes positive.

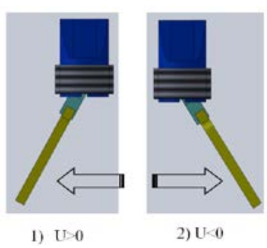

Fig.4. Swing direction depending on the positive or negative voltage

The operation of the proposed actuator is simple; however, its behaviors are very close to those of real fish. The fins on fish only have simple swings, yet, the simple swings are efficient so that fish has elegant and agile movement in water.

III. Integrated Design of Robotic Fish

In this section, the integrated design of the robotic fish is introduced, and four major tasks are the design of exterior body, the setups of actuators, motion control, and wireless communication for human robot interaction.

A. *Design of exterior body*

The body of the robotic fish serves as the house for all of the electronic components; the manifolds of the exterior body also have a great impact on the power efficiency. The robotic fish should have an internal space enough to accommodate power supply modules, microcontroller, drive modules and the electronic accessories for communication. In addition, the interface should be available on the body to install the electromagnetic actuators outside the body shell. Meanwhile, the size and shape of the body determines the amount of the resistant force when the robotic fish moves in water; therefore, under the given volume of internal space, the body shape of the robotic shape was optimized to achieve an optimized hydrodynamic performance with the minimized resistant force. More specifically, the design criteria of the robotic fish are,

The streamlined manifolds should be adopted to reduce resistant force and achieve better hydrodynamic performance.

The volume of the body should be determined by the sum of those for power supply modules, microcontroller, drive modules, and other accessories. In addition, the body should be sealed easily to the encapsulated space waterproof.

The interface should be designed to connect inside components with the actuators at outside. The interface should also include the brackets to mount driving fins.

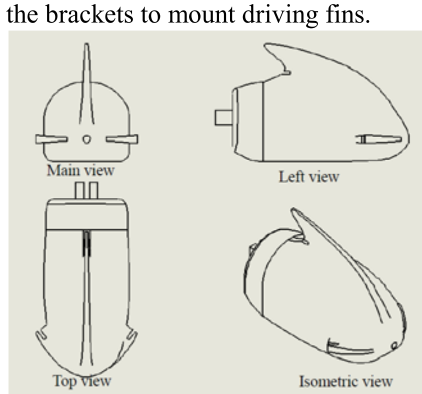

Fig.5. Drawings of the finalized body of the robotic fish

An iterative trial and error procedure was applied to optimize the size and shape of the robotic fish. At each step, all design criteria were considered to create a conceptual model of the robotic body in SolidWorks, and the model was then converted into a stereo lithography (STL) file for rapid prototyping. The prototyped body was verified to see if all of design criteria were satisfied optimally. The drawings of the finalized body were shown in Fig. 5. The exterior shape was streamlined, which was very easily made by three-dimensional printing.

As shown in Fig. 6, the body has the cavity internally to accommodate electronic components. To assembly components together appropriately, the body was cut into two parts, i.e., the front part and the back part. After all of the components were placed in the cavity, two parts were then put back together. Note that the seals must be applied on the interface of two parts to prevent water leak.

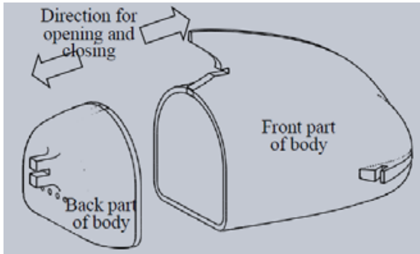

Fig.6. Two parts of the shell

To install swing fins, the body also included some features in local regions for the actuators; Fig. 7 has shown four slots to mount left, right, tail, back swing fins, respectively.

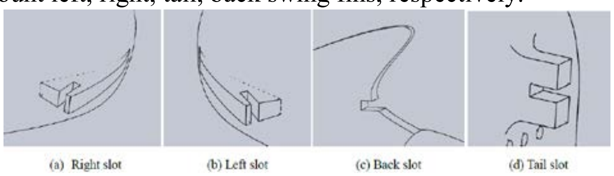

Fig.7. Design details of slots to mount swing fins

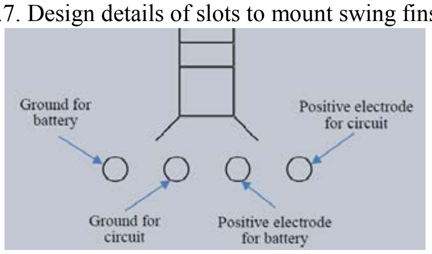

Fig. 8. Interfaces for switches and power supplies

Note that underneath the mounting bracket of the tail fin in Fig. 7(d), the interface for the connections of internal and external components was designed. An interface allows charging batteries when they are used up; it also makes the switches of the circuit accessible from the outside the body. Fig. 8 has shown the locations of pins for the ground of battery, the ground of the circuit board, the positive electrodes of battery and circuit, respectively.

The main properties of the finalized robotic body are included in Table 1. The total mass of the body is 6 (grams), and the total rounded-up volume is less than 5.9×104 (mm3), which has been greatly miniaturized.

Table 1. Properties of finalized robotic body

Item	Value	Unit
Length	57	mm
Width	30	mm
Height	34.5	mm
Mass	6	gram

B. Actuation

The actuators are specially designed so that their behaviors are swing oscillations similar to the moving patterns of fins on fish. The driven fins on the robotic fish swing left and right to get the propulsion from water for the movement. The amount of thrust force depends on the size, shape, and swing frequency of the fin. Cheng et al. [13] compared three different shapes of fins including crescent-shape, semi-circle shape, and fan-shape. Their results showed that the fin with a crescent shape produced less a thrust force than the fins with other shapes. However, the fin with the crescent shape was the most efficient during cruising due to the less loss of the lateral power. Therefore, the selection of the fin shape depends on whether a higher thrust force or higher power efficiency is preferred.

In the proposed robotic fish, four actuators are applied and mounted on tail, dorsal, and two pelvic positions, respectively. These actuators serve for different purposes as follows,

Actuator on caudal fin:	provide main thrust and assistive lateral force when it turns;
Actuators on pelvic fins:	provide main lateral force when it turns;
Actuator on dorsal fin:	provide the diving or floating force when it changes its depth.

The setup of the actuators is shown in Fig. 9. All of them are placed in the corresponding slots on the shell of the robot body. The driving power for these actuators was from the internal circuit.

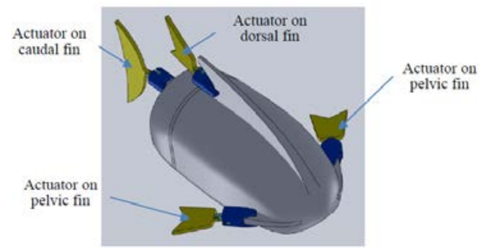

Fig.9. The setup of actuators on the robotic fish

C. Control and Communication

The control system transfers control commends into actual motions of the robotic fish. The control commends are transmitted by the wires which connect external actuators to internal micro-controller and power supplies. The wired connections are essential to the communication, where control signals are transmitted to the actuators from the micro-controller or human operator. Meanwhile, the feedbacks from the actuators or the environment are collected and transferred to the controller for the closed-loop control or decision-making at a high level.

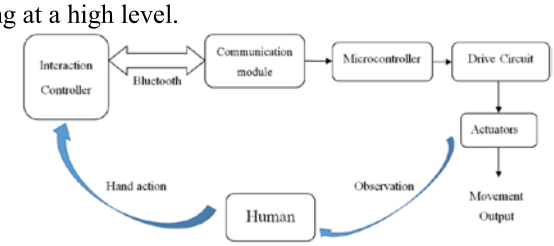

Fig.10. Human operator in the closed-loop control system

For some simple tasks, an open-loop control for an individual robot with the minimized number of sensors can fulfill tasks adequately. However, when the task becomes complicated, it needs the collaborative effort from a group of robots or with the interactive human intervention (Bi et al). Moreover, the human operator might serve as a superior sensor to observe changes in the environment and refine the motion of robot accordingly. In other words, it is advantageous to include the human operator in the closed-loop control system. Fig. 10 has illustrated an interactive control platform where a human operator can control the robotic fish directly by remote-control panel. The main components in the control system are interactive controller, communication module, microcontroller,

ISBN: 978-1-61804-288-0

drivers, actuators, and human operator. Human operator is responsible to monitor the movement of robotic fish, issue the interactive motion commends to the robot. The interactive controller is the receiver and executor of motion commends. The communication module is also responsible to transmit the acquired gesture signals and deliver control signals to actuators through Bluetooth.

The AVR microcontroller Atmega8L by Atmel were selected as the microcontroller for the robotic fish. Its specifications meet the control requirements of the robotic fish satisfactorily. Due to the advanced technologies for the high-density non-volatile memory, an Atmega8L chip has small size and low power consumption. In addition, the programs in its flash memory are rewriteable, and the reprogramming can be executed via an serial program interfaces (SPIs) including SCK, MOSI (input) and MISO (output). Table 2 gives the mapping of pins in SPIs.

Table 2. Mappings of pins in serial program interfaces

Signal	Pin	Description
MOSI	PB3	Data Input
MISO	PB4	Data Output
SCK	PB5	Timer

The input and output (I/O) interfaces in the Atmega8L microcontroller are further illustrated in Fig. 11. Eight outputs are PWM_Turn_0, PWM_Turn_1, PWM_Tail_0, PWM_ Tail _1, PWM_Left_0, PWM_ Left _1, PWM_Right_0, and PWM_ Right _1; they are H-Bridge drive circuits. The interfaces set for downloading are MISO, MOSI, SCK, and ISP_RESET. RXD and TXD for a serial I/O communication. ADC0 ~ ADC5 are the interfaces to connect AD Converters.

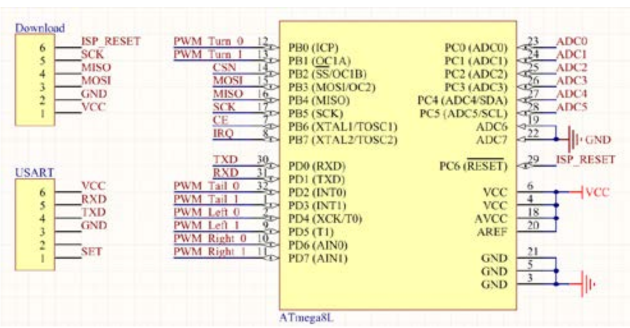

Fig.11. I/O configurations in the microcontroller

The application of a robotic fish can be restrained by the communication mode. A variety of wireless communications are available; each communication mode has its advantages and disadvantages [16,19]. In our prototyping, the bluetooth communication was selected mainly because it involves a low cost and it has been widely used in many industrial applications. For examples, the majority of personal digital assistants (PDA), such as smart phones and ipad, support the bluetooth communication. Therefore, it becomes feasible for a human operator to interact with the robotic fish via a smart phone or ipad. Fig. 12 has shown the communication system of the robotic fish.

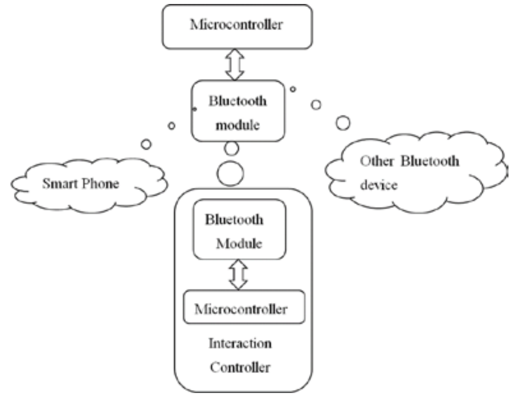

Fig.12. The communication system of the robotic fish

In the prototyping system, the selected buletooth module was BLK-MD-BC04-B, which was developed based BlueCore4-Ext by the CSR Company in U.K. The module is compatible to universal asynchronous receiver/transmitter (UART) and SPI interfaces. Furthermore, it has the advantages of a low cost, low consumption, small size, and high sensitivity of transmission. This module was adopted to communicate the micro-controller with a few of external devices.

D. Human robot interaction

A robot is a typical mechatronic device with an integration of mechanical system, electronic and electrical system, sensing system, computing and control system [17, 20]. In particular, the level of intelligence of a robot relies greatly on the information visibility in the environment. To acquire information from the environment, various sensors, such as encoders, cameras, sonars, and range finders, can be applied to obtain different types of information. The feedbacks from sensors are essential to implement closed-loop controls.

With the objective of the low cost, it is impractical to include a large number of sensors for the robotic fish. However, involving the human operator in the control system alleviates this problem greatly. Human operator can monitor the movement of the robotic fish and the environment directly. Through the remote controller, the commends to the robotic fish can be refined readily to adapt the changes of environment directly. Therefore, the interactive remote controller by the human operator serves for two purposes: (1) collect gesture signals from the attitude sensors from the operator, and (2) send and receive data as a signal transceiver. Accordingly, the human operator is responsible to (1) Observe the robotic fish and its application environment, and (2) make the decisions for the motion of robot, and issue control signals to the microcontroller via the control panel.

The most important components of the control system is the Atmega8L chip, and it is connected to other components in the system including power modules, the communication module and the module for ADXL335 sensors. Fig. 13 shows the configuration of the interactive controller. The microcontroller is required to capture gesture signals from ADXL335 sensors, and it also sends control signals to actuators via the bluetooth communication.

ISBN: 978-1-61804-288-0

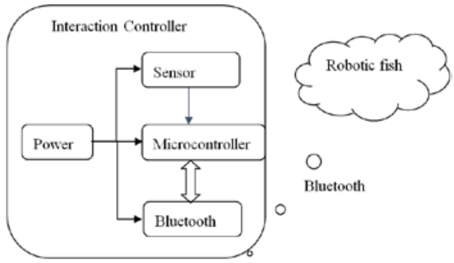

Fig.13. Configuration of interactive controller

ADXL335 is a three-axis accelerometer, which is capable of measuring the accelerations along three directions. One can calculate the posture of the robot based on the accelerations. If an acceleration is high, the inclination angle of the posture is large. The output of ADXL335 is the voltage signal so it can be transferred easily by an AD Converter. The specifications of ADXL335 are shown in Table 3.

Table 3. The specifications of ADXL335

Item	Parameter
Voltage	3~5 V
Current	400 uA
Output	Voltage
Temp.	-40 ~ 85°

IV. Prototyping and Experiments

The aforementioned components were assembled as a robotic fish. The overall volume and weight were measured. As shown in Table 4, it was found that the overall dimensions of the robotic fish are 77.84 mm in length, 48.80 mm in width, and 35.84 mm in height with a tolerance of ±0.02 mm, respectively; its total weight is 25.61 g with a tolerance of ±0.01 g. The robotic fish was greatly miniaturized in comparison with other existing robotic fishes reported in the literature.

Table 4. Physical properties of the robotic fish

Parameters	Values
Length	77.84 ±0.02 mm
Width	48.70 ±0.02 mm
Height	35.84 ±0.02 mm
Mass	25.61 ±0.01 g

The moving speed is an important measure for the robotic fish. Therefore, the robot was tested for two types of motion, i.e. the maximized forward speed and the maximized turning speed.

When the robotic fish swings its caudal fin, the thrust force is generated, and it moves forward. If the robotic fish swings one of its pelvic fins, it turns left or right depending on which pelvic fin takes action. For example, if the robotic fish swings its right pelvic fin and keep the caudal fin on the left, it turns left eventually. Otherwise, if it swings its left pelvic fin keep the caudal fin on the right, it turns right instead. The recorded sequence of the forward motion is shown in Fig. 14. The measured forward speed was 25.95 mm/s.

Fig.14. The recorded sequence of the forward motion

The recorded sequence of the turning motion is shown in Fig. 15. The measured maximized turning speed was 40 °/s.

Fig.15. The recorded sequence of the turning motion

V. Summary and Future Works

Distributed intelligence seems the most effective strategies to deal with the complexity of emerging engineering problems [16,19-22]. Instead of developing an integrated system with a higher level of complexity for advanced functionalities, a distributed system consists of a large number of modular systems; each module is autonomous, but they can collaborate with each other to achieve high-level goals at the system level. Due to the number of modules, the cost effectiveness of the distributed intelligence depends on how well to miniaturize sizes and weights, and to reduce the costs of modules. It is our understanding that little work has been done on the structural optimization of robotic fishes for the reduction of size, weight, and eventually the cost. We are motivated to design a compact robotic fish by (1) simplifying the configurations of the propulsion systems, (2) customizing low-cost electronic-magenitic actuators, (3) minimizing the body of robotic fish with the consideration of hydrodynamic performance, and (4) involving human operator in the control system to reduce the needs of sensors and increase the flexibility and robustness of the robotic fish. The design concept has been implemented and the prototyped robotic fish was tested. It was found feasible to use the customized electronic magnetic actuators to drive a robotic fish. In addition, the integrated interface allows a human operator interact with the robotic fish directly. The prototyped fish was miniaturized into a volume within 78×49×36 mm3 and the total weight of 25.6 grams. The maximized forward and turning speeds from the measurements were 25.95 mm/s and 40 °/s, respectively. It should note that the ideas of using customized electromagnetic actuators and involving human operator in control system are applicable to other robotic designs when the size, weight, and cost are critical factors to the applications.

The main purpose of the presented work was to explore the feasibility of using customized electromagnetic actuators in biometric robots and involving human operator in the control system to miniaturize robots. The prototyped robotic fish is preliminary, and we have identified the following areas to extend our research in the field: (1) to optimize the configurations of driving systems for higher speed and agility; for example, include multiple actuators on a fin; (2) to develop

ISBN: 978-1-61804-288-0

comprehensive kinematic and dynamic model for advanced control of the robotic fish; (3) to investigate the scalability of the system, so that the developed methods can be applied to any scale of robot in terms of sizes, weight, and working capacity; (4) to study the coordination and collaboration of robotic team for distributed intelligence; (5) extend the developed methods for other types of biomimetic.

REFERENCES

[1] Sitorus P E, Nazaruddin Y Y, Leksono E, Budiyono A. Design and Implementation of Paired Pectoral Fins Locomotion of Labriform Fish Applied to a Fish Robot. Journal of Bionic Engineering,2009,6:37-45

[2] Bergmann M, Iollo A. Modeling and simulation of fish-like swimming. Journal of Computational Physics,2011,230:329-348

[3] Vo T Q, Kim H S, Lee B R. Propulsive Velocity Optimization of 3-Joint Fish Robot Using Genetic-Hill Climbing Algorithm. Journal of Bionic Engineering,2009,6: 415-429

[4] Nguyen Q S, Park H C, Byun D. Thrust Analysis of a Fish Robot Actuated by Piezoceramic Composite Actuators. Journal of Bionic Engineering,2011,8:158-164

[5] Wang Z L, Hang G R, Li J, Wang Y W, Xiao K. A micro-robot fish with embedded SMA wire actuated flexible biomimetic fin. Sensors and Actuators A: Physical, 2008,144:354-360

[6] Liu Y X, Chen W S, Liu J K. Research on the Swing of the Body of Two-Joint Robot Fish [J]. Journal of Bionic Engineering, 2008, 5:159-165

[7] Rahman M M, Toda Y, Miki H. Computational Study on a Squid-Like Underwater Robot with Two Undulating Side Fins. Journal of Bionic Engineering, 2011, 8:25-32

[8] M.S.Triantafyllou, G.S.Triantafyllou.An efficient swimming machine,Scientific.1995, 272(3): 64-70

[9] Shao J, Wang L, Yu J.Development of an artificial fish-like robot and its application in cooperative transportation. Control Engineering Practice,2008,16:569-584

[10] Zhang D B, Hu D W, Shen L C, Xie H B.Design of an artificial bionic neural network to control fish-robot's locomotion. Neurocomputing, 2008,71:648-654

[11] Suleman A Crawford C.Design and testing of a biomimetic tuna using shape memory alloy induced propulsion. Computers and Structures,2008,86:491-499

[12] Wang Z L, Hang G R, Li J, Wang Y W, Xiao K.A micro-robot fish with embedded SMA wire actuated flexible biomimetic fin. Sensors and Actuators A: Physical, 2008,144: 354-360

[13] Chang X H, Zhang L P, He X. Numerical study of the thunniform mode of fish swimming with different Reynolds number and caudal fin shape. Computers & Fluids, 2012, 68:54-70

[14] Wang C, Bi Z M, Xu L D, IoT and cloud computing in automation of assembly modeling systems, IEEE Transactions on Industrial Informatics, 10(2): 1426 - 1434, 2014.

[15] Bi Z M, Xu L D, Wang C, Internet of things for enterprise systems of modern manufacturing, IEEE Transactions on Industrial Informatics, 10(2): 1537 - 1546, 2014.

[16] Wang L, Xu L D, Bi Z M, Xu Y, Data cleaning for RFID and WSN integration, IEEE Transactions on Industrial Informatics, 10(1): 408-418, 2014.

[17] Yin Y H, Xu L D, Bi Z M, Chen H, Zhou C, Novel human-machine collaborative interface for aero-engine pipe routing, IEEE Transactions on Industrial Informatics, 9(4): 2187-2199, 2013.

[18] Bi Z M, Kang B, Sensing and responding to the changes of geometric surfaces in flexible manufacturing and assembly, Enterprise Information Systems, 8(2): 225-245, 2014.

[19] Niu N, Xu L, Bi Z M, Enterprise information system architecture — analysis and evaluation, IEEE Transactions on Industrial Informatics, 9(4): 2147-2154, 2013.

[20] Bi Z M, Wang L H, Wu C, Yang G, Zhang D, multidisciplinary design optimization for engineering, Mathematic Problems in Engineering, paper ID 351097, 2013.

[21] Bi Z M, Lang S Y T, Verner M, Orban P, Development of reconfigurable machines, International Journal of Advanced Manufacturing Technology, 39(11-12): 1227-1251, 2008.

[22] Bi Z M, Lang S Y T, and Shen W M, Reconfigurable manufacturing systems: the state of the art, International Journal of Production Research, 46(4): 967-992, 2008.

[23] Bi Z M, Design of a spherical parallel kinematic machine for ankle rehabilitation, Advanced Robotics, 27(2): 121-132, 2013.

[24] Bi Z M, and Kang B, Motion purity of robotic mechanisms with desired and undesired motions, Advanced Robotics, 25(11-12): 1539-1556, 2011.

[25] B, Z M, and Jin Y, kinematic modeling of parallel kinematic machine Exechon, Robotics and Computer Integrated Manufacturing, 27(1):186-193, 2011.

[26] Bi Z M, Lin Y, and Zhang W J, The general architecture of adaptive robotic systems for manufacturing applications, Robotics and Computer Integrated Manufacturing, 26(5): 461-470, 2010.

[27] Bi Z M, Zhang W J, Chen I-Ming, and Lang S Y T, Automated generation of the D-H parameters for configuration design of modular manipulators, Robotics and Computer Integrated Manufacturing, 23(5): 553-562, 2007.

ISBN: 978-1-61804-288-0

Product Generation Development – Importance and Challenges from a Design Research Perspective

Albert Albers, Nikola Bursac, Eike Wintergerst

Abstract – This article presents a new model explaining product development from the perspective of product generation development. It is understood to be the development of a new generation of technical products by both specific carryover as well as significant new development of partial systems. New development shares may be based on shape variation as well as on a variation of the solution principle (principle variation). New product generations are always based on a reference product giving the basic structure. The reference product is understood to be a precursory or competing product, on the basis of which a new product generation is to be developed. This article presents examples of development practice and additional results of surveys that empirically support the explanation model. It is aimed at defining a systematic approach to supporting the characterization of development projects for new product generations.

Keywords – Product generation development, reference product, new development share

I. Introduction and Motivation

A few days ago, Google stopped the test phase of "Google Glass" and its further development. According to reports of the media, acceptance problems and technical deficiencies caused the project to fail. The development of Google Glass doubtlessly was a project that differed from many other development projects. But what type of project was it? Was it a new construction, a modular innovation project, or how can the project be classified? According to Schumpeter [1], an innovation would have required success on the market. And it was no new construction, because reference products, such as "glasses" or the "android software" in smartphones did already exist. The solution principles and major subsystems of the reference products were directly transferred to the new project. However, these highly creative development activities do not represent a classical adaptation construction. In the opinion of the authors, classical development methodology is still lacking appropriate explanation models to correctly describe the above-mentioned challenges associated with the development of technical products.

The following chapters will first highlight major research relating to classical development methodology and innovation management. The explanation model of product generation development given below represents a further development of these classical approaches. The synthesis project will be characterized by the basic activities of principle and shape variations. These variation activities are mostly combined to develop partial systems of a product. An empirical study reveals the importance of product generation development in practice. The need for future in-depth studies of this process by new construction methodology research approaches will be outlined.

II. Established Perspectives of Design Methodology and Innovation Management

A. Types of product development from the classical design methodology point of view

The classic design methodology distinguishes between a generating and a corrective approach. For corrective approach carrying over of parts or only minor changes to existing solution principles are typical. In order to minimize efforts due to changes with a generating approach new solutions are initiated by means of "abstraction and subsequent concretization process. [2]

In addition to this characterization Pahl and Beitz [3] differentiate product development projects in three categories: new construction, adjustment and variant construction. For their differentiation the degree of novelty, uncertainty with regard to prevailing conditions and possibility of using familiar and dominating solution principles are used [3]:

- A **new construction** results from the use of new solution principles or new combinations of known principles under changed framework conditions, with the development team having a large freedom of selection of means to implement the development objectives.
- An **adjustment construction** requires the existence and use of already known and implemented solution principles under new framework conditions. The development objective is reached by using known means to solve new problems. In case of complex construction problems, a partial new construction or an integration of individual partial systems may be included.
- A **variant construction** is based on the reuse of known and implemented solution principles under comparable framework conditions and their adaptation to the defined development objective. A variant construction in mechanics is characterized by a variation of individual parameters, such as dimensions or arrangements of components and assemblies. The objective is to meet quantitatively modified

requirements with minimum construction expenditure.

Based on this perspective, the DIN standard 6789-3 distinguishes between a technical product modification and a new construction as soon as a component or partial system of the product is exchanged to meet specific requirements.

In contrast to these classical categories of development projects, recent literature increasingly pointed out that hardly any products are completely newly developed today. For economic and risk analysis reasons, it is aimed at reaching the desired functions and properties of a new product by minimum modifications of established solutions [4], [5]. Eckert points out that the improvement of existing products is the most frequent type of product development. Most products result from modifications. Reliably working components and partial systems of complex products are carried over to the largest possible extent in order to reduce the degree of technical novelty, potential risks, and required investments e.g. in production facilities.

The degree of novelty of a product, hence, is defined not only by the number of newly developed partial systems, but also by an improvement of functions and properties of existing components and assemblies or an extension of their scope of application.

B. Product Development from the Innovation Management Point of View

Innovations are of decisive importance to companies for being permanently successful in competition. According to Schumpeter [1], an innovation is the successful establishment of an invention on the market.

Henderson and Clark [6] distinguish four types of product innovation:

- **Incremental innovations** from constructive modifications of components and their relationships to each other. Due to the limited scope of modification, the technical and economic risks are rather low. However, the economic potential also is rather limited. Incremental innovations can be planned and controlled well.
- **Architectural innovations** are based on a new configuration of already known and established functional units. They often force companies to restructure their knowledge. Another way of fulfilling the function, however, is also associated with economic potentials at moderate technical risks.
- **Modular innovations** are characterized by an exchange of individual functional units, while the basic system structure is maintained. They are associated with increased potentials of economic competitiveness, but also with accordingly increased risks.
- **Radical innovations** are not only characterized by an exchange of individual functional units, but also by a new configuration of the system structure. The development processes and market potentials are subject to high uncertainties. A considerable amount of new knowledge has to be newly generated or acquired.

The problematic of such classification of innovations lies in the fact that it can only be retrospectively assessed whether a product was successful on a market and represents an innovation. Hence, the numerous failures in product development are not considered. Failure is not an exception, but the rule.

Companies have to consider customer needs and requirements in many (partially conflicting) dimensions already in the development and validation phases of product development due to innovation pressure on a market. Examples of dimensions are functionality and cost-benefit aspects. According to the Kano Model [7] basic as well as performance and fascination requirements of the above named dimensions should be posed. These are modified in the course of product development cycle [8] and adapted to each product generation depending on current requirements and constraints of the market. The Kano model (Figure 1) and the model of the product life cycles (Figure 2) are demonstrated below. Based on Kano model new products need new fascination attributes because with time they degrade to basic and performance attributes (for ex. across multiple product generations) [9].

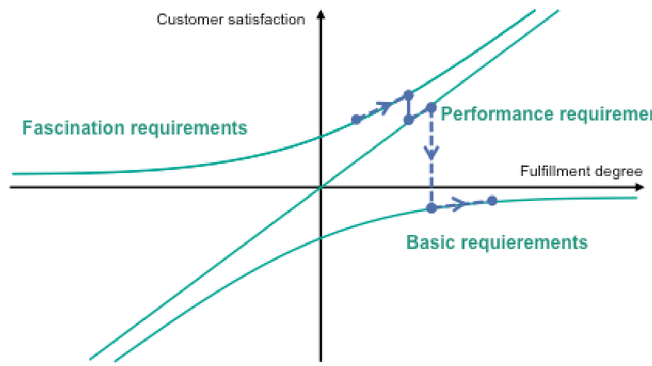

Fig. 1 Kano model [9];

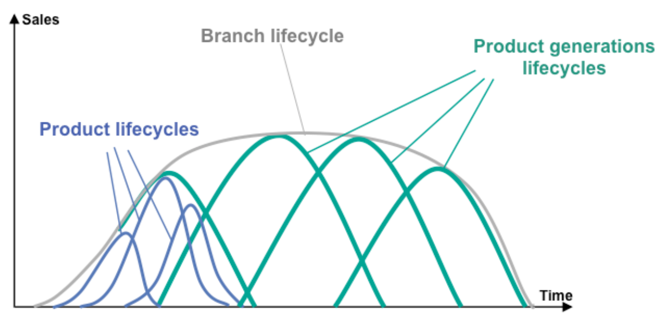

Fig. 2 Product lifecycle of product generations [8]

The defined objective is to establish a largely innovative product on the market and, at the same time, to newly develop certain partial systems only. As a) non-compliance with basic requirements results in the dissatisfaction of the customer and b) the risk associated with the variation of a solution principle often is much higher, it is recommended to meet basic requirements with minimum shape variations and, hence, minimum risk and to change the product structure slightly only, if possible. At the same time, the available resources are to be concentrated on the development of performance and

ISBN: 978-1-61804-288-0

attractiveness features (for differentiation) in order to enhance the innovation potential of a product and to extend the lifetime of innovations on the market. This can be achieved by a specific focus on selected partial systems in the planning phase of the product generation development already.

III. Product Generation Development as a new Perspective for Design Research

A. Definitions and distinction to the existing state of the art

Pahl and Beitz [3] as important representatives of classical design research acknowledge that product development projects usually cannot be classified as new design, variant- or adjusted constructions.

The authors of this article are convinced that the most development projects can be described as **product generation development** projects in practice. Hence, they propose to use this term. An explanation model will be developed and explained below. The present article is not intended to present an entirely new observation, but to combine the (so far fragmented) elements of current research in a new explanation model that reflects the “natural” conditions of development practice and enables research to develop useful methods and processes to master the challenges of product development. On the other hand, the explanation model is to serve as a basis of qualitative and quantitative planning, classification, description, and management of a project development task. The focus lies on the development practice of companies.

Product generation development is understood to be the development of a new generation of technical products by both a specific carryover (CO) and new development of partial systems. The shapes of new technical developments of individual functional units result from the activity of shape variation (SV) and the variation of solution principles, hereinafter referred to as the activity of principle variation (PV). New product generations are always based on a reference product that defines large parts of the basic structure. A reference product is understood to be a precursory or competing product, on the basis of which a new product generation is to be developed. The new development shares of a new product generation are to result in features for distinction of the new product from the reference product.

From the above perspective, a distinction of new, adjustment, and variant constructions is hardly reasonable. Instead, the shares of the different types of constructions have to be evaluated. While certain functional units are developed by means of a new solution principle (principle variation), other partial systems can be redesigned using existing solution principles (shape variation). Shape variation is based on using an existing solution principle of a reference product, while function-determining properties are varied. This existing solution principle may be the result of a technology or pre-development project or it may be derived from products, in which similar partial functions were implemented efficiently.

In a product generation development process the share of a new development of solution principles often is far smaller than that of new developments by shape variation, which may also lead to innovative solutions, i.e. solutions that are successful on the market. Hence, several new development shares of partial systems of a product can be distinguished in a new product generation:

- New development of a partial system of a product generation by principle variation (PV), e.g. by adaptation from products having similar functions and properties in other contexts or by the systematic search for alternative solution principles using e.g. construction catalogs or creativity techniques.
- New development of a partial system by shape variation (SV), with a known (and established) solution principle being carried over from a reference product or the general state of the art and the function-determining properties being varied to enhance the competitiveness, performance, and/or quality of fulfilling the function. Shape variation represents the most frequent activity of product development and a highly creative and complex process. An example is the enormous increase in the power density of gear drives by an optimization of flank geometry, material, state of the material, production process, and lubrication.
- Carryover of partial systems, i.e. existing solutions of reference products or component suppliers are transferred to new product generations. This activity shall hereinafter be referred to as carryover (CO) and also has to be planned and controlled. Constructive adaptations are to be minimized, if possible.

In the explanation presented above, the term "new development" plays a central role - not least because it is also often used in the development practice. In contrast to a "new construction" [3] in a new development, the matter is in the project, whose result (a technical construct, often a technical system consisting of several subsystems) in most cases includes a variety of constructive adjustments and variants of already known solution principles- and only few (or no) real new constructions with new solution principles in the sense of its classical definition.

In the following sections the most important relationships of product generation development will be represented by mathematical models. Modeling is intended to facilitate planning and execution of development projects by estimating and planning a) the shares of carryover from reference products, b) the shares of new developments by shape variation, and c) the shares of new developments by a significant principle variation. Depending on the situation (on the market or at the company), an individual product development process can be planned and executed by selecting the respective types of modifications after assessing their risks and importance.

A new product generation (G_{n+1}) consists of a set of partial systems (PS) that are carried over (CO), a set of newly developed partial systems by shape variation (SV), and a set of newly developed partial systems by principle variation (PV):

$$\mathrm{CS}_{\downarrow}(\mathrm{n}+1)\ \{\mathrm{PS} \mid \mathrm{CO}_{\downarrow}((\mathrm{PS}))\ \} \tag{1}$$

$$[SS]_{\downarrow}(n+1)\ \{\mathrm{PS} \mid \mathrm{SV}_{\downarrow}((\mathrm{PS}))\ \} \tag{2}$$

ISBN: 978-1-61804-288-0

$$【PS】 \downarrow (n+1) \; \{\mathrm{PS} \mid \mathrm{PV}_1((\mathrm{PS}))\} \tag{3}$$

This way a new Generation can be described as:

$$G_{n+1} = CS_{n+1} \bigcup SS_{n+1} \bigcup PS_{n+1} \tag{4}$$

The share of carry over parts ($\delta_{CO\ n+1}$) of a product generation is defined as:

$$\delta_{CO\ n+1} = \frac{|CS_{n+1}|}{|G_{n+1}|} = \frac{|CS_{n+1}|}{|CS_{n+1} \cup SS_{n+1} \cup PS_{n+1}|} \; [\%] \tag{5}$$

Analogiously, the parts of newly developed subsystems through shape variation ($\delta_{GV\ n+1}$) and newly developed subsystems through principle variation ($\delta_{PV\ n+1}$) can be calculated as follows:

$$\delta_{SV\ n+1} = \frac{|SS_{n+1}|}{|CS_{n+1} \cup SS_{n+1} \cup PS_{n+1}|} \; [\%] \tag{6}$$

$$\delta_{PV\ n+1} = \frac{|PS_{n+1}|}{|CS_{n+1} \cup SS_{n+1} \cup PS_{n+1}|} \; [\%] \tag{7}$$

The entire new development share ($\delta_{N\ n+1}$) is, thus, calculated as sum of the individual new development parts from shape variation ($\delta_{GV\ n+1}$) and prociple variation ($\delta_{PV\ n+1}$).

The values δ selected in the projecting phase already are important parameters for planning a product development process. The actually realized values for δ, which may differ from the planned values, are important parameters for risk analysis and the validation of a product generation. The authors intend to develop methods to determine and plan the shares in the future.

B. Challenges in the development of new product generations

The solution space for improving a new product generation compared to reference products is often limited to a variation of the relevant shape and process parameters. Hence, it is a special challenge to creatively generate features in which new products differ from products already available on the market. On the (often prevailing) buyers' market, a new product has to meet the customers' requirements and to be easy to produce for being competitive. Again, the best solution is the simplest solution that works. System engineers are forced to creatively explore the solution space given by technical and economic objectives and framework conditions. The creativity of system engineers does not only consist in the development of new solution principles, but especially in the specific variation of the shape of a reference product or a partial system to ensure the best possible use of the potentials of the carried-over solution principles. For instance, the principle of the Otto engine has been known for a long time. Nevertheless, it is quite often succeeded in significantly improving its performance characteristics (e. g. torque, fuel consumption) by shape variation. As a result, product innovations are generated.

The objective of the development of a new product generation is to obtain a sufficient number of features to distinguish new products (from the existing product generation and from competing or expected products on the market) and to profitably commercialize the new product generation for a period envisaged. These features should be perceivable by the customers (on the same market) and allow for a clear distinction from reference products. Moreover, these features should also be justified from the point of view of the company, e.g. cheaper production due to the newly developed partial systems. Improved functions for the customer and a simultaneous decrease in the cost of production are no conflict in principle, but a development challenge [10 & 11].

Very early in the product generation development process, important decisions have to be made, which will largely determine the innovation potential of the product on the market. The paradox of construction holds: At an early stage, much can be done, but the consequences are hardly known. Later on, it is easy to assess, but changes can hardly be made [12]. A strictly methodological and model-based product generation development process may help to overcome this paradox or at least to reduce its risk. The methods, processes, and tools required for this purpose should be in the focus of future research into development methodology.

IV. Reflection of the Clarification Model in Development Practice

For a detailed analysis of product generation development, a systemic approach is chosen with a vehicle being used as an example. Such a technical product may be understood to be the sum of its elements or partial systems and their interactions [13]. Now, the results of an empirical study shall be presented. They reflect the relevance of the explanation model outlined in Chapter 3.

A. Examples of typical product generation developments

Product generation development shall now be illustrated with the development of the iPhone, of printing machines by Heidelberger Druckmaschinen AG or of the Porsche 911 being used as examples (cf. Figure 3).

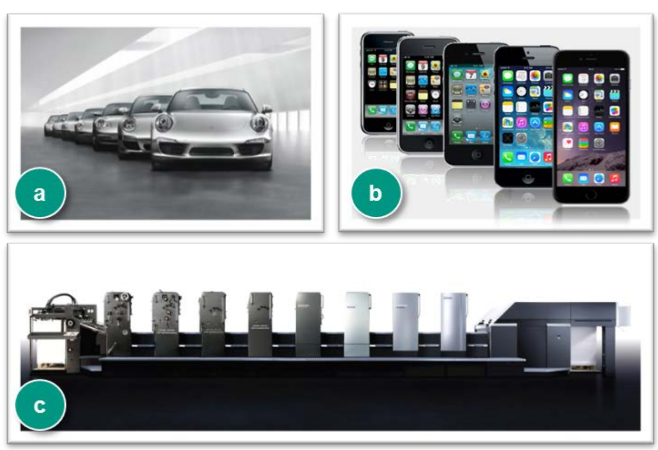

Fig. 3 Product generation developments of G_1 (left) to G_N (right)

using the example of products from Porsche (a), Apple (b) and Heidelberger-Druck (c)

For 50 years now, the Porsche 911 follows a similar basic concept (rear engine, 2+2 seats, etc.). In every generation, however, it is extended specifically by differentiation features. Examples are the adaptive front spoiler of the current generation (type 991), variable turbine geometry of the precursor generation (type 997), and the ceramic brake of its precursor (type 996). To reduce the expenditure, risk, and costs, it is often reasonable to maintain the basic structure of a reference product and to newly develop individual partial systems. Visible partial systems of the vehicle, such as the exterior (look-and-feel – SV), functions experienced by the customer, such as the ACC InnoDrive (fascination attribute – PV), and the engine (for reducing fuel consumption (performance attribute – SV) or meeting new legal requirements (basic attribute – PV or SV)) are newly developed. Other partial systems, such as wheel suspension, are carried over and integrated into the new generation. Such a mixed development process requires new methods and tools that have to be made subjects of research.

As pointed out in Chapter 2, it is reasonable to meet basic requirements by slight modifications of reference systems, if possible, and, at the same time, to support the development of differentiation features. Attractiveness attributes degrade to performance and basic attributes with time. Hence, attractiveness and performance attributes have to be renewed or even replaced constantly in new product generations. A new product generation mostly consists of unchanged (carried-over) subsystems, subsystems, whose shape was varied, and subsystems, whose principle was varied (cf. Figure 4). In line with the fractal character of a development process, these subsystems may be understood to be product generation development processes [14].

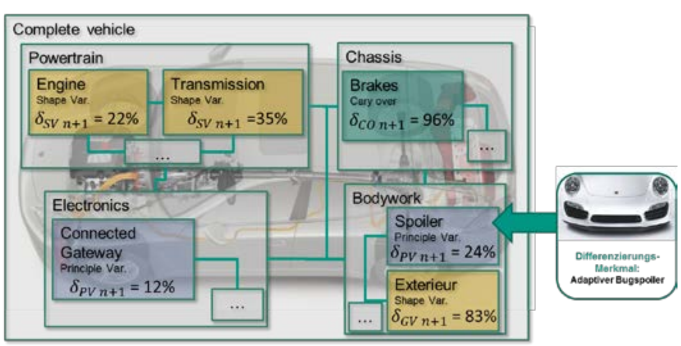

Fig. 4 System theory analysis of a vehicle in a product generation development process with the degree of renewal of the individual partial systems

B. Empirical study about the relevance of the product generation development

The mathematical model presented in Chapter 3 allows a continuous classification of product development. The state of a pure adaptation construction ($\delta_{N\ n+1}$ = 0%) or of a completely new construction according to the classical definition ($\delta_{N\ n+1}$ = 100%) is reached at the extreme values only. In an online survey, development engineers of various companies and branches were asked to assess the development focus of their companies. Using a scroll bar, the respondents were to indicate whether the focus of their development activities lay on classical adaptation development (1), completely new development (100) or on mixed forms. The results of the survey are shown in Figure 5. In total, 247 development engineers participated in the online survey. Of these, 131 answered all 33 questions.

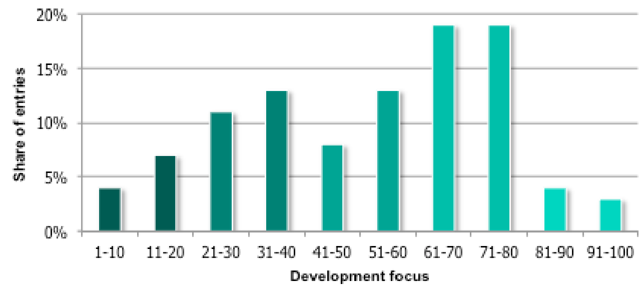

Fig. 5 Company focus: adjustment development of the existing products (1) till new developments (100)

Although the results reflect the individual opinions of the respondents, they also confirm the need for a definition of product generation development as a basic development concept, as only 11% focus clearly on adaptation development (1-20) and 7% on new development (81-100).
The survey started by asking for company characteristics providing information about the area of business. The companies are active mainly in the areas of mechanical engineering and plant construction as well as in automotive industry. Most (46%) of the respondents work at large enterprises (> 5000 employees). Small enterprises (< 250 employees) have a share of nearly 25%. In Figure 6, the branches of the companies are represented.

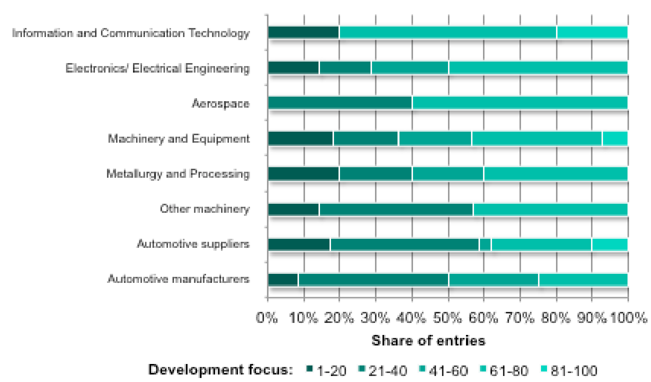

Fig 6. Companies' focus across different sectors

Over the different branches, no significant deviations from the average values can be found. Only branches, such as information and communication technologies or electronics and electrical engineering, tend to include companies with a higher new development share than e.g. companies of automotive industry. But in all branches not more than 20% of the answers can be assigned to the extreme cases of adaptation development and new development. These findings are also true for the company sizes and ages. The corresponding distributions are shown in Figure 7.

Fig 7. Companies' focus across different company sizes (left) and – age groups (right)

Relatively small and relatively young companies only are characterized by a high new development share. This can be explained by their special situation and certainly is in agreement with general perception.

V. Discussion and Outlook

It is evident from the results of Chapter 4 and work of other authors (see Chapter 2) that the practice of product development is largely characterized by the combination of various new development shares. The share of using a new partial solution in principle is rather small. Consequently, research of Albers et al. (Karlsruher Schule) concentrates on methods and processes supporting system and validation engineers in the development of new product generations by a specific shape variation requiring a sound understanding of the system or by the associative variation of solution principles. Research concentrates on a need-oriented support of methods and processes for the complete product development from the idea to the tested solution, the objective being to efficiently, safely, and innovatively develop complex and complicated products in the future.

A promising approach is test-based development (TbD) using the X-in-the-Loop (XiL) methodology [15]. This approach efficiently couples virtual and physical models of the product, the surroundings, and the user in the development process. The product can be experienced and tested in its application environment also under real-time conditions. In case of a consistent product generation development, these models will be available already in the future and can be carried over or modified slightly. This allows for an early integration of customers to verify and validate new properties of a future product generation. The later customers can test a future product during its development phase in a type of "beta version" similar to software tests. The customers' feedback can be incorporated directly in the further development of the product. Product generation developments can be supported by iPeM, the integrated product development model [16].

Based on research into product generation development, it is possible to study new methods, processes, and tools for product development. Companies are enabled to successfully commercialize products with very large new development shares by principle variation (e.g. Google Glass) as well as products with large new development shares by shape variation (e.g. Porsche 911).

The explanation model of product generation developments may be applied as a framework: In this context Google Glass may be understood to be the development of a first generation of data glasses by using the principles of their reference products "glasses" and "android software" and a large share of new developments by principle variation.

References

[1] J. Schumpeter, *„Theorie der Wirtschaftlichen Entwicklung."* Leipzig: Duncker & Humblot, 1939.

[2] K. Ehrlenspiel, *„Integrierte Produktentwicklung."* München: Hanser, 2009.

[3] G.Pahl, W.Beitz, J.Feldhusen, K.-H.,Grote, *„Pahl/Beitz Konstruktionslehre."* Berlin: Springer-Verlag, 2013.

[4] F. Deubzer, U. Lindemann, *"Networked Modelling - Use and interaction of product models and methods during analysis and synthesis."* In: Proceedings of the International Conference on Engineering Design, Stanford, 2009.

[5] C.M. Eckert, T. Alink, A. Albers, *"Issue driven analysis of an existing product at different levels of abstraction."* In: Proceedings of the International DESIGN Conference, Dubrovnik, 2010.

[6] R. Henderson, K. Clark, *"Architectural innovation: the reconfiguration of existing product technologies and the failure of established firms."* In: Administrative science quarterly, 1990 pp 9–30.

[7] N. Kano, N. Seraku, F. Takahashi, S. Tsuji, *"Attractive Quality and Must Be Quality."* In: Quality - Journal of the JSQC 14, 1984 pp 165-186.

[8] E. Wesner, *„Die Planung von Marketing-Strategien auf der Grundlage des Modells des Produktlebenszyklus."* Berlin, 1977.

[9] F. Bailom, H. H. Hinterhuber, K. Matzler, E. Sauerwein, *„Das Kano-Modell der Kundenzufriedenheit."* In: Marketing: Zeitschrift für Forschung und Praxis (1996) pp. 117-126.

[10] A. Albers, *„Das Zweimassenschwungrad der dritten Generation – Optimierung der Komforteigenschaften von PKW-Antriebssträngen."* In: Antriebstechnisches Kolloquium. Köln: Verlag TÜV Rheinland, 1991.

[11] A. Albers, *„Fortschritte beim ZMS - Geräuschkomfort für moderne Kraftfahrzeuge."* In: 5. LuK Kolloquium, 1994.

[12] H. Grabowski, K. Geiger, *„Neue Wege zur Produktentwicklung."* Raabe, Stuttgart, 1997.

[13] G. Ropohl, *„Allgemeine Technologie: Eine Systemtheorie der Technik"*, Karlsruhe: KIT Scientific Publishing, 2009.

[14] A. Albers, A. Braun, S. Muschik, *"Uniqueness and the Multiple Fractal Character of Product Engineering Processes."* In: Modelling and Management of Engineering Processes, Cambridge, 2010.

[15] A. Albers, M. Behrendt, J. Schroeter, S. Klingler, *"X-in-the-Loop: A Framework for supporting central engineering activities and contracting complexity in product engineering processes."* In: Proceedings of the International Conference on Engineering Design, Seoul, 2013.

[16] A. Albers, A. Braun, *"A generalised framework to compass and to support complex product engineering processes,"* In: IJPD 15 2011 pp 6–25.

ISBN: 978-1-61804-288-0

Propagative interactions of guided waves in structured plates

Olivier Bareille, Christophe Droz, Jean-Pierre Lainé, and Mohamed N. Ichchou

Abstract—**High-order waves' propagation with low spatial attenuation in broadband frequency range is here investigated as an alternative to some structural health monitoring techniques based on first-order wave propagation. It may encompass some of the drawbacks encountered when dealing with boundary conditions in 2D-waveguides or provide accurate wave-based inspection techniques for heterogeneous or composite beams. The wave propagation and scattering in a structured composite component is studied using time-response analysis and compared to the Wave Finite Element Methods' predictions. These waves are generated by pulse excitations of the medium. The results are based on the propagation of high-order waves in a sandwich plate made of transverse isotropic honeycomb core surrounded by fiber-reinforced skins.**

I. Introduction

FOR the last decades, numerical and experimental methods were extensively investigated to provide efficient and accurate Structural Health Monitoring (SHM) and Non Destructive Evaluation (NDE) techniques for automotive and aerospace industry [1]. Conventional NDT techniques using waves propagation are based on local ultrasonic phenomena. At high frequencies, a dispersive medium can induce a fast spatial decay of the waves amplitude. As a consequence, it becomes difficult to use the amplitude from reflected or transmitted signals for detection purpose and let alone for any monitoring use. However, for given structural configurations like in thin plate-like structures, waves like Lamb waves are prone to travel relatively long distances within the plates thickness. Such a waveguide architecture is often present in structures (ribbed plates, pipes, beam-like elongated components...).

Lamb's waves have been intensively studied and applications have been proposed for structural health monitoring, based on guided waves interactions [2]–[4]. Wilcox & al. [5] have used various experimental instruments in order to generate and measure such waves. Electromechanical devices as weel as piezoelectric sensor-actuator elements have been designed and field-tested [6]. Depending on the application, some types of waves are preferred to others [7]. As a consequence, even if the A0 Lamb's wave exhibit a large out-of-plane surface displacement, modes with a much smaller amplitude like the S0 or even the in-plane motion of the SH0 mode can be preferably used and therefore the ability of the transducer pairs to generate and to measure them must be assessed [5].

This work was supported in part by the IAPP Marie Curie project "'SMART NEST "' (FP7-PEOPLE-2011-IAPP : "'Smart Technologies for Transport Safety - Innovation Cluster Nesting (Smart-Nest)"')

Mohamed N. Ichchou is professor at École Centrale de Lyon (University of Lyon) in the Laboratory of Tribology and Dynamics of System - LTDS.

Christophe Droz is a PhD fellow supported by Airbus Helicopters

Olivier Bareille and Jean-Pierre Lainé are associate professors at Ecole Centrale de Lyon (University of Lyon) in the Laboratory of Tribology and Dynamics of System - LTDS.

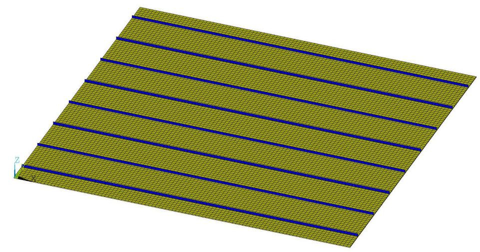

Fig. 1. The finite element model and geometry of the ribbed panel

When interacting with singularities, scattering and wave-mode conversions offer as many clues to the presence of these latter. However, based on numerical simulations, sensitivity analysis are still needed and reliable model for interpretation still need to be established to estimation both precise location and level of severity.

For such a purpose, the Wave Finite Element Method (WFEM) is particularly adapted. It uses Bloch's theorem [8] to provide significant reduction of the modelling effort, since it combines the Periodic Structures Theory (PST) with commercial finite element packages [9], [10]. Therefore, wave dispersion characteristics of a waveguide whose cross-section is modelled with FEM can be derived by solving a small quadratic eigenvalue problem [11].

A. Stiffened panel case study

Guided waves occurrence is not limited to structures whose shape exhibits a significant elongation in one direction. Indeed, guided waves can be generated in other structures with specific inner-structure settings. This can be illustrated by the following results obtained for a stiffened panel under harmonic point excitation.

The structure of the panel is depicted in figure 1. The flexural displacement field is a combination of vibrational patterns among which, for a given frequency, arise some singular behaviors. For instance, in the present case, at 2kHz, far below the range of application for Rayleigh or Lamb waves, some mechanical energy is distributed on wave-like components as shown on figure 2. The magnitude pattern of such guided-wave might be significantly affected by any unexpected singularities which would be present along its traveling path.

ISBN: 978-1-61804-288-0

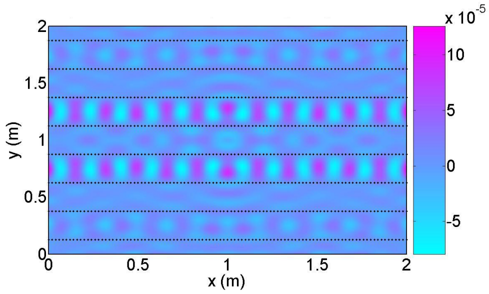

Fig. 2. Guided-wave component of the displacement field for the ribbed panel at 2kHz. The unit in z-axis is in meter.

As a concluding remark here and a preamble to what is going to be developed in the following sections, the use of structural waves can be motivated by there range of frequency and by the properties of their spatial distribution. Even for frequencies far below the Rayleigh-Lamb wave applications' ones (¡ 100 kHz), in the mid-frequency range, longer-wavelength long-distance control procedures can be foreseen. As a consequence, in the next sections, the propagative waves will be the physical phenomenon that will be considered to support the structural health analysis. However, their sensitivity to local singularities still need to be tested, before they can prove to help identifying local mechanical settings and properties.

B. Higher-order waves

Although wave-based methods are extensively employed in the offshore and aerospace industries for inspecting defects and cracks in 1D and 2D waveguides, these approaches are often involving first-order waves, such as the flexural, or Lamb waves for beams, plates, laminated or sandwich panels, and torsional waves in pipelines inspection [12]. However, when composite or large-scaled 1D waveguides are considered, first-order waves can be prone to coupling effects, or unaffected by localized defects. In this case higher-order, or localized waves may be used instead. In this paper, the propagation of high-order plane waves in a sandwich plate made of transverse isotropic honeycomb core surrounded by fiber-reinforced skins is investigated. These waves are created under pulse sinusoidal excitation. The wave scattering effects are studied using time-response analysis in the composite plate and compared to the WFEM predictions. Furthermore, these high-order waves have low spatial attenuation in broadband frequency range and can be used as an alternative to several SHM techniques based on first-order wave propagation. Some of the drawbacks could hence be circumvented, encountered when dealing with boundary conditions in 2D-waveguides or provide accurate wave-based inspection techniques for heterogeneous or composite beams.

II. WAVE FINITE ELEMENT METHOD (WFEM)

A waveguide is considered as a straight elastic structure made of N of identical substructures of same length d, connected along the direction x. The state vector is described in figure 3. Nodal displacements and forces are denoted **q** and **f**, where the subscripts 'L' and 'R' describe the cell's left and right faces. Both edges have the same number n of degrees of freedom. Mesh compatibility is assumed between the cells. The governing equation in a cell at frequency ω is written :

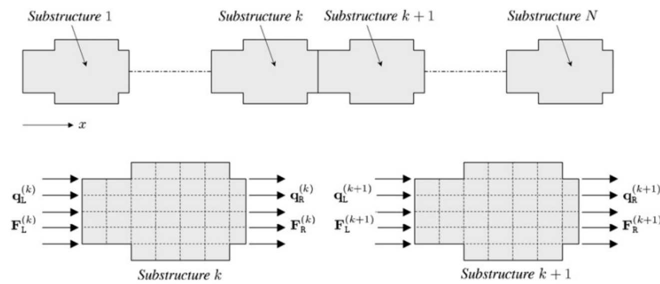

Fig. 3. Illustration of a waveguide and the state vector of a unit cell.

$$(-\omega^2\mathbf{M}+\mathbf{K})\mathbf{q}=\mathbf{f} \tag{1}$$

where $\mathbf{M}$,$\mathbf{K}$ are the mass and complex stiffness matrices, respectively. A dynamic condensation of the inner DOFs can be required if the structure is periodic. The governing equation can be written by reordering the DOFs :

$$\begin{bmatrix} \mathbf{K}_{LL} & \mathbf{K}_{LR} \\ \mathbf{K}_{RL} & \mathbf{K}_{RR} \end{bmatrix} - \omega^2 \begin{bmatrix} \mathbf{M}_{LL} & \mathbf{M}_{LR} \\ \mathbf{M}_{RL} & \mathbf{M}_{RR} \end{bmatrix} \begin{Bmatrix} \mathbf{q}_L \\ \mathbf{q}_R \end{Bmatrix} = \begin{Bmatrix} \mathbf{f}_L \\ \mathbf{f}_R \end{Bmatrix} \tag{2}$$

where $\mathbf{M}_{ii}$ and $\mathbf{K}_{ii}$ are symmetric, $\mathbf{M}_{LR}^t=\mathbf{M}_{RL}$ and $\mathbf{K}_{LR}^t=\mathbf{K}_{RL}$. $\lambda=e^{-jkd}$ is the propagation constant, describing wave propagation over the cell length d and k is the associated wavenumber, considering force equilibrium

$$\lambda\mathbf{f}_L+\mathbf{f}_R=0 \tag{3}$$

in a cell and Bloch's theorem:

$$\mathbf{q}_R=\lambda\mathbf{q}_L \tag{4}$$

into Eq. (2), it yields the following spectral eigenproblem :

$$\mathbf{S}(\lambda,\omega)=(\lambda\mathbf{D}_{LR}+(\mathbf{D}_{LL}+\mathbf{D}_{RR})+\frac{1}{\lambda}\mathbf{D}_{RL}+)\mathbf{\Phi}=\mathbf{0} \tag{5}$$

where the solutions $\mathbf{\Phi}$ stand for the wave shape associated with the displacements $\mathbf{q}_L$ of the waveguide's cell. In damped waveguides, complex wavenumbers are associated to decaying waves. Defining the state vector : $\mathbf{\Phi}=[(\mathbf{\Phi}_q)^t,(\mathbf{\Phi}_f)^t]^t$, the spectral problem can be written using the symplectic transfer matrix $\mathbf{T}$.

$$\mathbf{T\Phi}=\lambda\begin{Bmatrix} \mathbf{\Phi}_q \\ \mathbf{\Phi}_f \end{Bmatrix} \tag{6}$$

with

$$\mathbf{T}=\begin{bmatrix} \mathbf{D}_{LR}^{-1}\mathbf{D}_{LL} & \mathbf{D}_{LR}^{-1} \\ \mathbf{D}_{RL}-\mathbf{D}_{RR}\mathbf{D}_{LR}^{-1}\mathbf{D}_{LL} & -\mathbf{D}_{RR}\mathbf{D}_{LR}^{-1} \end{bmatrix} \tag{7}$$

Here, the waves associated with positive wavenumber are travelling in the positive x-direction and the negative wavenumbers describe propagation in the negative x-direction. The dynamical behaviour of the global system can be expressed by expanding amplitudes of incident and reflected waves on a basis of eigenvectors. If the structure is undamped,

ISBN: 978-1-61804-288-0

solutions are divided into propagative waves, whose wavenumbers are real, and evanescent waves for which wavenumbers are imaginary. In dissipative case, complex wavenumbers are associated to decaying waves.

III. Dispersion characteristics of a sandwich plate

A. *Description of the composite waveguide*

The rectangular sandwich waveguide is composed of a 8 mm thick homogenised honeycomb core surrounded by 1 mm thick fiber-reinforced skins. The 400 mm width cross-section is modelled using 360 linear block elements having 8-nodes and 3 degrees of freedom (DOF) per node. The waveguide is described in figure 4, a structural loss factor $\eta = 0.01$ is assumed and a detailed description of the materials is given in tables I and II.

Material	Density (kg.m^{-1})	Young Modulus (Pa)	Shear Modulus (Pa)
Nomex	24	$E_x = 5 \times 10^6$ $E_y = 5 \times 10^6$ $E_z = 46.6 \times 10^6$	$G_{xy} = 1 \times 10^6$ $G_{xz} = 10.13 \times 10^6$ $G_{yz} = 10.13 \times 10^6$

TABLE I
Material properties of honeycomb core

Material	Density (kg.m^{-1})	Young Modulus (Pa)	Shear Modulus (Pa)
TC skin	1451	$E_x = 81 \times 10^9$ $E_y = 81 \times 10^9$ $E_z = 3.35 \times 10^9$	$G_{xy} = 2.5 \times 10^9$ $G_{xz} = 2.8 \times 10^9$ $G_{yz} = 2.8 \times 10^9$

TABLE II
Material properties of fiber-reinforced skins

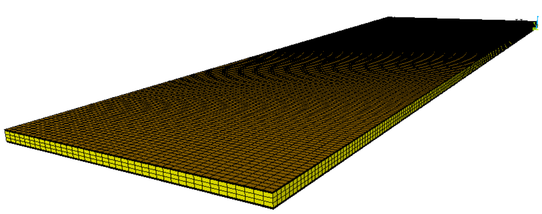

Fig. 4. Finite element model of sandwich plate involving finite width.

B. *Propagating waves and shapes*

The wavenumbers associated with the propagating waves in the sandwich waveguide are shown in figure 5. The continuous lines (—) describe first-order waves while dashed lines (- - -) represent high-order propagating waves, associated with deformed cross-sections. It can be noticed that numerous high-order waves are propagating in this structure, in addition to the four first-order waves (transverse and in-plane flexural, torsional and longitudinal waves). The cross-sectional deformed shapes associated with these first-order waves are shown in figure 6. In the considered structure, high-order waves are associated with sinusoidal deformation of the waveguide's cross-section. Their shapes are described in figure 7. The spatial attenuations of the propagating waves in the frequency range $[0, 4000]$ Hz are shown in figure 8. The wave amplitudes are given after a one meter propagation in the main direction. Although high-order waves share the same asymptotic group velocity of the first-order flexural and torsional waves, their spatial attenuations exhibit different behaviour close to each of their cut-on frequencies.

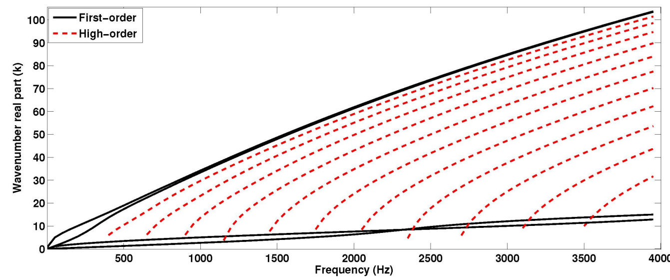

Fig. 5. Real part of the wavenumbers associated with propagating, positive-going waves.

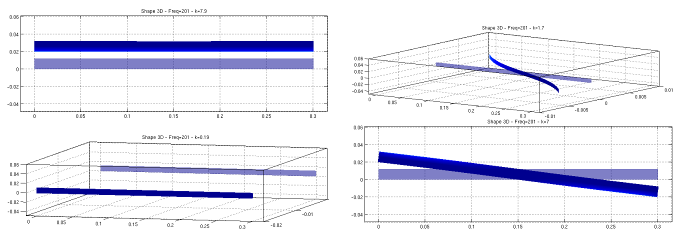

Fig. 6. Deformed shapes associated with the first-order propagating waves.

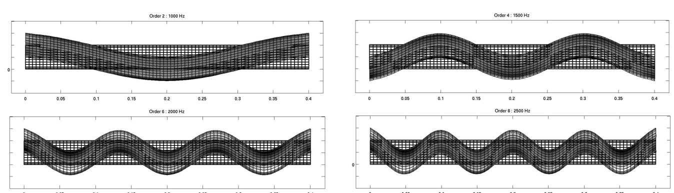

Fig. 7. Deformed shapes associated with high-order propagating waves.

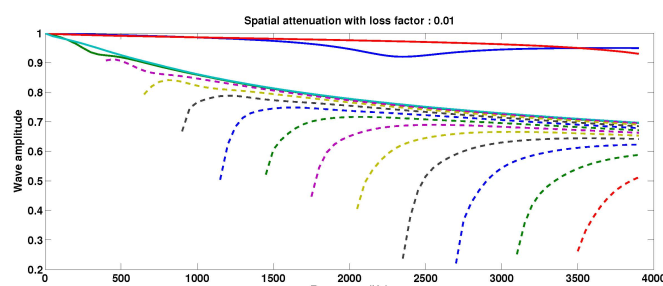

Fig. 8. Amplitudes of the propagating waves in the sandwich waveguide after 1 meter propagation.

IV. Time analysis using wave appropriation

This work is concerned with the propagation of the aforementioned high-order waves in a sandwich plate of finite dimensions. Therefore, the actuation of the waves described in figure 7 is proposed using localized vertical displacements. The shape appropriation is shown in figure 9 for the 4^{th} order flexural wave.

ISBN: 978-1-61804-288-0

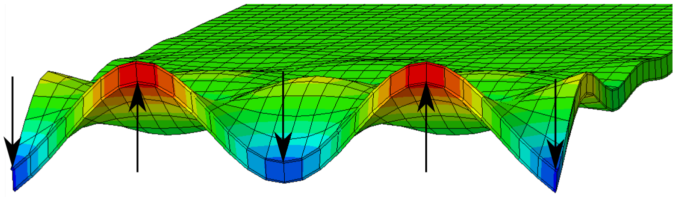

Fig. 9. Shape appropriation of the 4^{th}-order flexural wave.

The transient response under pulse train excitation (see figure 10) is determined using time-explicit simulation. The frequency spectrum of the pulse is described in figure 11. A reduced dispersion of the pulse train can be obtained by narrowing the frequency spectrum bandwidth. It can be done by increasing the number of periods in the pulse train. In

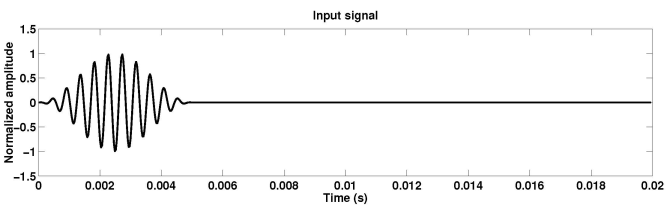

Fig. 10. Time signal of the pulse.

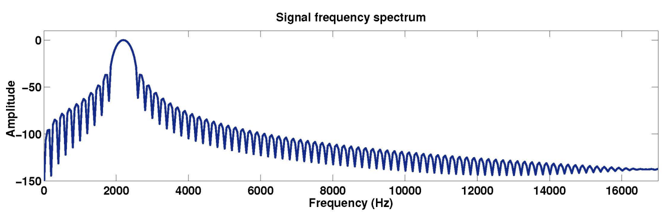

Fig. 11. Frequency spectrum of the pulse.

figure 12, the time response of the waveguide is described under a 2^{nd}-order wave at 1k Hz . Noteworthy, the wave pulse propagates without coupling effects and a slight dispersion. It can be explained since the frequency spectrum involves different group velocities for a given wave. Therefore, is seems advantageous to generates waves at higher frequencies. Similarly, the propagation of the 4^{th}-order wave is shown for a 2k Hz pulse involving 8 periods is shown in figure 13.

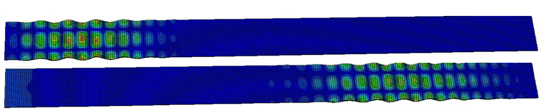

Fig. 12. Propagation and dispersion of a 2^{nd}-order wave generated at 1k Hz.

V. DISCUSSIONS

This paper is concerned with the time response of a sandwich waveguide to high-order waves, generated by appropriation of their propagating wave shapes. First, the wave dispersion characteristics are determined using the WFEM.

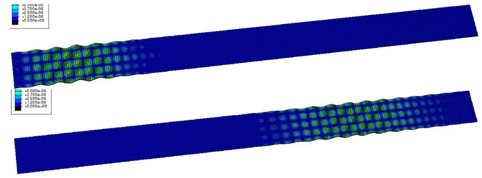

Fig. 13. Propagation and dispersion of a 4^{nd}-order wave generated at 2k Hz.

Then, the wave amplitudes are compared for first- and high-order waves after 1 meter of propagation in the considered waveguide, assuming a constant structural loss factor $\eta = 0.01$. Noteworthy, the wave attenuation is higher close to the cut-on frequencies, meaning that higher frequencies should be considered for actuating high-order propagating waves. The waves shapes being associated with sinusoidal mode shapes of the cross section, a reduced number of punctual displacements is required for producing the wave appropriation. The time response is determined for two different wave types at 1k Hz and 2k Hz. A good generation of the wave pulse is produced with a weak dispersion and no wave conversion. Therefore, it is shown that a high-order wave involving deformed cross-section can be easily actuated and propagates with dispersion characteristics predicted by the WFEM. Furthermore, these waves are expected to provide further information on defects or structural perturbations in composite, heterogeneous or large-scaled waveguides involving localized or high-order waves.

The next step would then be to develop the calculation with waveguide's singularities. The waves' interactions will certainly be emphasized or at least changed. But all this would be useless if no experimental assessment can confirm the possibility of triggering these targeted wave patterns. This shall be the goal of future works.

ACKNOWLEDGEMENTS

The authors gratefully acknowledge the IAPP Marie Curie project "‘SMART NEST "‘ (FP7-PEOPLE-2011-IAPP : "‘Smart Technologies for Transport Safety - Innovation Cluster Nesting (Smart-Nest)"’).
The authors would also like to acknowledge Airbus Helicopters for their financial support.

REFERENCES

[1] V. Giurgiutiu, *Structural health monitoring: with piezoelectric wafer active sensors*. Academic Press, 2007.

[2] M. Park, I. Kim, and Y. Yoon, "Ultrasonic inspection of long steel pipes using lamb waves," *NDT & E International*, vol. 29, no. 1, pp. 13 – 20, 1996.

[3] D. Alleyne, M. Lowe, and P. Cawley, "The reflection of guided waves from circumferential notches in pipes," *Journal of Applied Mechanics*, vol. 65, no. 3, pp. 635 – 641, 1998.

[4] J. Rose, "Ultrasonic guided waves in structural health monitoring," *Key Engineering Materials*, vol. 270, pp. 14 – 21, 2004.

[5] P. Wilcox, M. J. S. Lowe, and P. Cawley, "The excitation and detection of lamb waves with planar coil electromagnetic acoustic transducers," *Ultrasonics, Ferroelectrics and Frequency Control, IEEE Transactions on*, vol. 52, no. 12, pp. 2370–2383, 2005.

[6] I. S. S. von Ende and R. Lammering, "Lamb wave excitation with piezoelectric wafers - an analytical approach," *Acta Mechanica*, vol. 193, pp. 141 – 150, 2007.

ISBN: 978-1-61804-288-0

[7] V. Giurgiutiu, "Tuned lamb wave excitation and detection with piezoelectric wafer active sensors for structural health monitoring," *Journal of Intelligent Material Systems and Structures*, vol. 16, pp. 291 – 305, 2005.
[8] F. Bloch, "Über die quantenmechanik der elektronen in kristallgittern," *Zeitschrift für physik*, vol. 52, no. 7-8, pp. 555–600, 1929.
[9] D. Duhamel, B. R. Mace, and M. J. Brennan, "Finite element analysis of the vibration of waveguides and periodic structures," *J. Sound Vib.*, vol. 294, pp. 205–220, 2006.
[10] J. M. Mencik and M. N. Ichchou, "Multi-mode propagation and diffusion in structures through finite elements," *Eur. J. Mech. A–Solid*, vol. 24, no. 5, pp. 877–898, 2005.
[11] C. Droz, J.-P. Lainé, M. Ichchou, and G. Inquiété, "A reduced formulation for the free-wave propagation analysis in composite structures," *Compos. Struct.*, vol. 113, pp. 134–144, 2014.
[12] O. Bareille, M. Kharrat, W. Zhou, and M. Ichchou, "Distributed piezoelectric guided-t-wave generator, design and analysis," *Mechatronics*, vol. 22, no. 5, pp. 544–551, 2012.

Advanced Approaches for Mechanical Characterization On Innovative Materials

C. Barile, C. Casavola, G. Pappalettera, and C. Pappalettere

***Abstract*—**The displacement field of structures generally loaded and constrained is univocally defined if material properties are known. This represents the basic pillar of an inverse solution of the elastic problem, commonly used to characterize traditional materials. This paper describes a new approach for solving an inverse engineering problem to be applied on innovative materials, whose mechanical properties are unknown. It works iteratively and aims to minimize the difference between the displacement field measured experimentally in three-point-bending tests and their counterpart computed by FEM analysis, applying the same loads and boundary conditions. This hybrid procedure is based on a combination of an optical interferometric technique having nanometric sensitivity (Electronic Speckle Pattern Interferometry) with a numerical procedure which uses an optimization algorithm. The purpose is to predict accurately the mechanical properties of new materials, object of interest for aerospace, biomechanical and technological industries, deeply reducing costs and time.

***Keywords*—**Electronic Speckle Pattern Interferometry, FEM analysis, Inverse Problems, Mechanical characterization

I. Introduction

ONE of the most important phase in mechanical design of components consists in choosing the proper material for a specific application. A good choice should guarantee safety, high mechanical performances and low costs. Designing becomes complex when a new material is chosen. In that case it is necessary to fully characterize the material from a mechanical, physical and chemical point of view. Furthermore it usually happens that standards cannot be applied on these materials and traditional equipment is not suitable. Purpose of this study is to identify a new methodology, based on a combination of numerical and experimental techniques, able to fully characterize all types of materials: metals, sintered, composites and woods.

Identifying material properties from the indirectly related data sets is referred to as the material reconstruction inverse problem which has many other applications. For example, in structural engineering, it is used for structural damage identification [1] and for the characterization of composite materials [2], it has also been used in robotics design [3], wafer engineering [4], material mechanics [5] and fracture mechanics [6] as well as in biomedical and life science [7].

The traditional approach to mechanically characterize materials is to perform destructive tests. When material properties are known, the displacement field of a specimen generally loaded and constrained is univocally defined. This paper suggests an innovative methodology in order to determine mechanical characteristics (E, ν) of new materials by an inverse solution of the elastic problem. A hybrid approach based on the combination of Phase-Shifting Electronic Speckle Pattern Interferometry (PS-ESPI) and finite element analysis (FEM) is utilized.

Non-contact optical techniques such as (ESPI) [8,9] fit very well in the identification process in view of their capability to accurately measure displacements in real time and to gather full field information without altering specimen conditions. ESPI can measure displacement components u(x,y,z), v(x,y,z) and w(x,y,z) for each point (x,y,z) of the specimen surface. A system of fringes will appear on the specimen surface and each fringe represents the locus of an iso-displacement region. The frequency distribution of fringes can be used for recovering strain fields.

An innovative algorithm, implemented in a numerical model, automatically executes several optimization loops varying E and ν in order to minimize the objective function based on the difference between displacements evaluated by means of ESPI and the same predicted by FEM analysis.

Three-point-bending experimental tests are carried out on specimens of different materials. The experimental protocol was chosen in order to avoid rigid body motion and prevent speckle pattern decorrelation. The methodology is firstly applied on well-known material, as titanium, in order to define the set-up and to test its reliability by evaluating measurements' efficiency. Then it is applied on different materials: sintered by means of Selective Laser Melting (SLM) technique and orthotropic wood's laminate.

II. Materials and Methods

The choice of SLM and wood depends both on the great interest that they have in engineering field and also on the fact that they are difficult to be accurately characterized by traditional approaches.

In Selective Laser Melting (SLM) parts were built by adding layers of metal powder. A focused laser beam is used to fuse the powder material by scanning cross-sections generated from a 3D CAD model of the part on the surface of

C. Barile, is with Politecnico di Bari, Dipartimento di Meccanica, Matematica e Management, Bari, 70126 ITALY (corresponding author to provide phone: +39 0805962812; fax: +39 0805962777; e-mail: claudia.barile@poliba.it).

C. Casavola, G. Pappalettera, C. Pappalettere, are with Politecnico di Bari, Dipartimento di Meccanica, Matematica e Management, Bari, 70126 ITALY (e-mail: katia.casavola@poliba.it, giovanni.pappalettera@poliba.it, carmine.pappalettere@poliba.it).

ISBN: 978-1-61804-288-0

the powder bed. After each cross-section is scanned, the powder bed is lowered by one layer thickness, a new layer of material is applied on top, and the process is repeated until the part is completed. In order to obtain high density parts the powder mixture and SLM process parameters must be optimized, but this manufacturing process modifies the initial mechanical characteristics of metal powders, which strongly depend on process parameters (i.e. laser energy, scanning strategy, etc.) and were hardly predictable. Since controlling all parameters involved in the manufacturing process may be very complicated, accurate mechanical characterization of SLM components was mandatory to properly asses mechanical response. Building SLM parts was rather expensive, so traditional mechanical tensile tests are generally executed on a limited number of specimens. The hybrid procedure proposed in this work should simplify the mechanical characterization of SLM parts.

On the other hand wood is a hard, fibrous tissue. It has been used for hundreds of thousands of years for both fuel and as a construction material. It is an organic material, a natural composite of cellulose fibers (which are strong in tension) embedded in a matrix of lignin which resists compression. Wood may also refer to other plant materials with comparable properties, and to material engineered from wood, or wood chips or fiber.

There is a strong relationship between the properties of wood and the properties of the particular tree that yielded it. The density of wood varies with species. The density of a wood correlates with its strength (mechanical properties).

Engineered wood products, glued building products "engineered" for application-specific performance requirements, are often used in construction and industrial applications. Glued engineered wood products are manufactured by bonding together wood strands, veneers, lumber or other forms of wood fiber with glue to form a larger, more efficient composite structural unit. Engineered wood products prove to be more environmentally friendly and, if used appropriately, are often less expensive than building materials such as steel or concrete. These products are extremely resource-efficient because they require less resources and produce minimal waste. For our purpose we use a plywood. It is a heterogeneous, hygroscopic, cellular and anisotropic material. It is composed of cells, and the cell walls are composed of micro-fibrils of cellulose and hemicellulose impregnated with lignin. Since wood has different behavior in relation with the percentage of fibers, fibers' direction and presence of imperfection (e.g. knot), it results expensive and difficult to characterize this material by using traditional tests.

III. EXPERIMENTAL TESTS

An optical technique was used to evaluate the displacement field of the specimen, in order to determine the mechanical characteristics and to avoid the errors associated with the strain gauges application. A three-point bending test was carried out on specimens, having plate geometry. Specimens were placed on two supports placed at a distance of 90 mm.

The loading apparatus is shown in Fig. 1 together with a detail of the ESPI setup. A 2 kg loading cell DS514QD was connected to the wedge in order to measure the applied load. The load was transferred by a micrometric translation stage which pushes the loading wedge against the specimen.

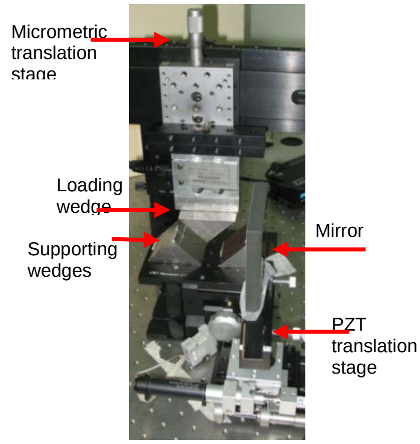

Fig. 1 Loading apparatus and detail of the optical setup. (b) Schematic of the double illumination ESPI setup

Samples were preloaded in order to minimize rigid body motions which may cause speckle decorrelation. The preload was centered on the upper surface sample. Depending on the type of material, a thin coating layer was sprayed onto the specimen surface to improve contrast of speckle fringes. The scheme of the optical set-up used for measuring u-displacements is shown in Fig. 2.

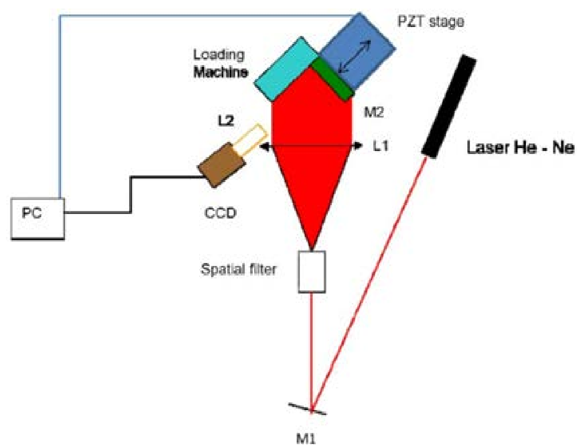

Fig. 2 Schematic of the double illumination ESPI setup

It essentially consists of a double illumination Lendeertz interferometer [9]. The light emitted by a 17 mW He-Ne laser source (λ= 632.8 nm) is expanded by a 20x microscope objective lens and spatially filtered by a 10 µm aperture pin-hole. The beam emerging from the pin-hole is successively collimated by the L1 plano-convex lens (ø=2 inch, f=40 cm). One half of the beam is then sent towards the specimen under testing at the illumination angle θ_1 = 45°. The rest of the beam is intercepted by the planar mirror M2 that reflects the light towards the specimen thus realizing symmetric double illumination. The mirror is placed on a piezoelectric translation stage (PZT) which allows the motion along the

ISBN: 978-1-61804-288-0

horizontal direction, parallel to the direction of sensitivity. The PZT is driven by a stabilized high-voltage power supply controlled by a PC. The minimum incremental displacement that can be generated is d_m = 10 nm. Each beam generates a speckle pattern on the specimen surface.

$$I(x,y) = I_{01}(x,y) + I_{02}(x,y) + 2\sqrt{I_{01}(x,y)I_{02}(x,y)}\ \cos[\varphi(x,y) + \Delta\phi(x,y)] \quad (1)$$

The phase difference Δϕ is related to the u-displacement by (2):

$$\Delta\phi = \frac{4\pi}{\lambda}\ u\ \sin\theta \quad (2)$$

Fringes are hence iso-displacement *loci* and the difference in displacement between points lying on two adjacent fringes is:

$$u = \frac{\lambda}{2\sin\theta}\, n_x \quad (3)$$

where n_x represents the fringe order.
According to (3), the sensitivity of the adopted optical set-up is 447 nm.

Phase shifting was utilized in order to obtain the phase distribution of the speckle pattern. To that purpose, a shift in phase between the two beams was introduced by changing the optical path of one of the arms of the interferometer. Phase variations were produced by moving the PZT stage. Among the different phase shifting strategies available in literature [8-10], the five frame algorithm which consists in recording five interferograms with a relative phase shift $\delta=\frac{\pi}{2}$ was utilized. In the processing phase for each shift of phase the difference between the recorded image and the reference image was determined by digitally subtracting speckle patterns. A 7x7 pixel square median filter was then applied to the five images in order to reduce noise. Phase unwrapping operation was carried out by means of the minimum spanning tree algorithm [11]. Finally, displacement maps were recovered by using the scaling (3).

IV. Numerical Model

A finite element model, with real sizes of the specimens tested, was developed in order to simulate the three-point-bending test. Because of structural symmetry, only one half was modeled.

The region of interest considered along the x-direction was about 63 mm. Kinematic constraints were imposed in order to obtain a symmetric model and to correctly reproduce the mechanism of loading. FE analysis was carried out with the ANSYS® commercial software [12]. The specimen was modeled with three-dimensional solid elements including 8 nodes each of which has 3 degrees of freedom. Although the thickness of the specimens is small compared to length, the specimen under three-point-bending was modeled as a 3D specimen in order to account for asymmetries eventually occurring in the loading process or related with constraint conditions.

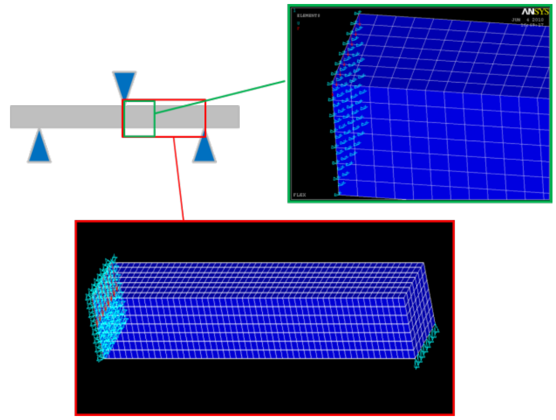

Fig. 3 Numerical model with details of analysis area

Initial values of elastic constants E and υ were assumed. They represents the design variables in the optimization algorithm that were iteratively changed in order to optimize the objective function:

$$W = \left|\frac{[U_{Node}(Trax) - U_{Node}(Comp)]_{FEM} - U_{SPER}}{U_{SPER}}\right| \quad (4)$$

It represents the difference of displacements between experimental and numerical results. Convergence analysis was carried out in order to refine the model and to obtain a mesh independent solution. The mesh usually included about 50000 elements and 60000 nodes. Fig. 3 with indications of loads and constraints is representative of all materials. Mesh size was consistent with sampling of the speckle pattern.

V. Results and Analysis

The horizontal displacement measured by ESPI was taken as target value of FE analysis. In all materials tested (titanium, SLM and wood specimens) the area monitored during experimental test was located 500 nm far from the constraint wedge and far enough from the region where the load is applied, in order to avoid the influence of local phenomena. Below results of all materials tested are presented. They show firstly titanium specimens, since it is used to define the experimental set up and to validate the approach that could be used to study also new materials. Then the efficiency is tested applying the same methodology on sintered and wood.

Titanium is an isotropic material. Samples were subjected neither to thermal treatment either to mechanical process that could modify the material properties. Young's modulus of Ti6Al4V used as target values in the numerical model was 110 GPa [13] while Poisson's ratio was fixed to 0.32. On the other hand starting values were respectively E=180 GPa and υ=0.30. The optimization minimizes the gap between displacement measured by ESPI (Δu_x Exp) and those evaluated by FEM analysis (Δu_x FEM). Table 1 summarizes results related to the optimization process: it can be observed that the error on measured displacements decreases as the loading level increases and that the residual error on displacements is less than 1%. Mechanical properties calculated for titanium alloy by means of the proposed hybrid procedure were respectively E=109 GPa and υ=0.30. The results obtained were in

ISBN: 978-1-61804-288-0

agreement with the literature ones, so it results that the proposed methodology works well [14].

Table 1 Optimization results for titanium

Load *[g]*	Δu_x Exp Fit *[nm]*	Δu_x Exp FEM *[nm]*	Error *[% 10^{-4}]*	E *[GPa]*	ν
304	313.45	313.42	6.70	109.00	0.299
467	499.05	499.05	4.62	110.23	0.299
690	729.07	729.06	3.80	109.01	0.299
870	957.95	957.95	0.17	109.90	0.299
1072	1187.97	1187.96	0.64	109.20	0.298

Fig. 4 summarizes the convergence procedure on titanium specimen for one loading step, in order to validate the algorithm function used in the optimization procedure. Difference between experimental and numerical results decreases increasing the iterations number.

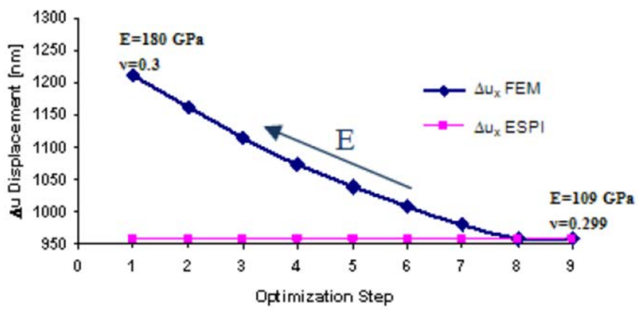

Fig. 4 Titanium optimization trend

Sintered material was assumed as isotropic and linearly elastic. This modeling choice was justified by the fact that SLM specimens were realized layer by layer and each layer may be considered as isotropic. The experimental evidence seems to confirm this assumption: in fact, the u_x displacement measured through the thickness became null at the specimen midplane. Mechanical characterization of SLM starts from Young's modulus of 166 GPa [15] related with specimens built with very similar process parameters of the SLM parts studied in this work.

The calculation procedure was lead in different steps. At the beginning only Young's modulus was optimized, then also Poisson's ratio was introduced. Moreover the loading steps were increased, in order to obtain a large number of terms of comparison between experimental tests and numerical models. As expected iso-u-displacement bands are almost parallel in the specimen near the supporting wedges. The experimental pattern (Fig. 5 (a)) is in excellent agreement with FE results (Fig. 5 (b)). The difference in displacement between points located on vertical lines at different distances from the constrained edge of the specimen was found to be insensitive to the position. The same conclusion can be drawn for all load levels considered in the experiments.

Remarkably, the experimentally measured values of u-displacement were found to be symmetric with respect to the neutral midplane of the specimen. This seems to confirm the assumption of isotropy of SLM material made in the numerical analysis.

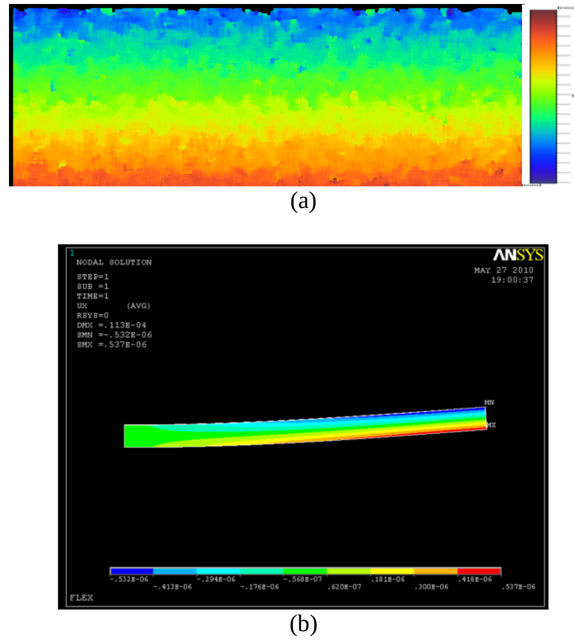

Fig. 5 (a) Horizontal displacement map near supporting wedge of the sintered material; (b) Horizontal displacement map evaluated via FEM of the sintered material

Table 2 shows the results obtained by perturbing elastic constants. Also in this case the proposed methodology seems to work: the error on measured displacements decreases as the loading level increases and that the residual error on displacements is less than 1%. Mechanical properties calculated for SLM specimen are: Young's modulus=132 GPa and Poisson's ratio= 0.30. It results important that the weight of Poisson ratio in FEM optimization is absolutely inferior than the Young's modulus, probably because the material was treated as an isotropic one [16-18].

Table 2 Optimization results for SLM

Load *[g]*	Δu_x Exp Fit *[nm]*	Δu_x FEM *[nm]*	Error *[% E-05]*	E *[GPa]*	ν
293	489.78	489.780	2.500	131.33	0.299
330	550.73	550.729	0.290	131.54	0.299
504	837.34	837.340	0.026	132.13	0.299
529	878.52	878.520	0.015	132.19	0.299
695	1151.95	1151.950	0.052	132.45	0.299
706	1170.07	1170.069	0.220	132.46	0.299
810	1341.38	1341.382	0.120	132.56	0.299

In order to verify the validity of hybrid procedure for orthotropic material another material was tested. For our purpose it was considered a plywood specimen, composed of five layers having two different thickness according to the orientation of the fibers.

It should be noted that the common practice of testing material involves the use of strain gauges. But ensuring a correct application of these transducers implies:

- the choice of a proper adhesive for porous material in order to avoid the reinforcement effect

ISBN: 978-1-61804-288-0

- the gage bonding on a proper position to ensure the reading of strains for all the laminate and not only for a single lamina
- the choice of the correct pressure grips to ensure a total tightening but not to compromise the integrity of the component (e.g. tensile test in order to obtain the elastic properties).

For these reasons an uniaxial flexural test was applied and an optical technique was used to evaluate the field displacements. The first approach of this study concerned with the macroscopic identification of the mechanical properties of the wood [19]. Five plies constituted the laminate:

- 2 plies with fibers parallel to the longitudinal axes of specimen; each ply was 2.5 mm thick
- 3 plies with fibers perpendicular to the longitudinal axes of specimen; each ply was 1.03 mm thick.

In the finite element analysis the specimen was modelled as a single isotropic block of wood. In fact it was supposed that the target value of the elastic modulus was the weighted average of the longitudinal and the transverse elastic moduli related to the thickness of each ply and the percentage of fibers'. The values of these elastic properties reported in literature were [20-21]:

- $E_L \approx 10$ GPa
- $E_T \approx 0.4$ GPa
- $\upsilon = 0.3 \div 0.4$

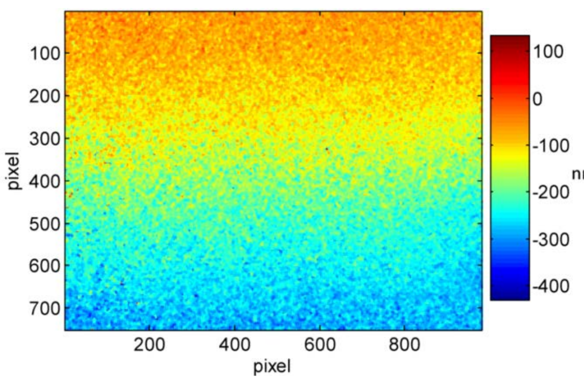

(a)

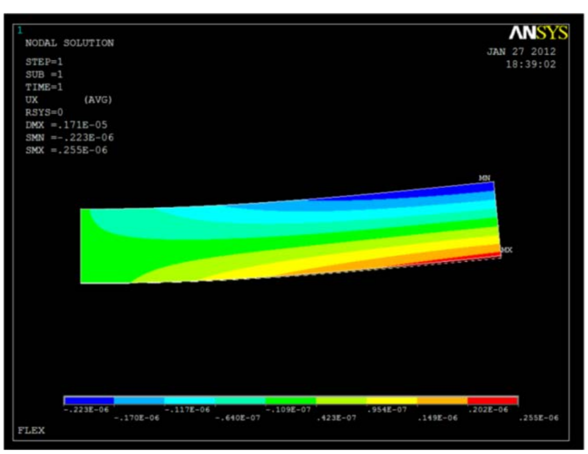

(b)

Fig. 6 (a) Experimental displacement map of a plywood specimen subjected to 200g load; (b) FEM displacement map of a plywood specimen subjected to 200g load

So the mean target value in the numerical model was calculated considering the weighted thickness referred to orientation of the fibers: E_{mean}=6.4 GPa.

As a first approach to mechanical characterize wood the design variables for the optimization analysis were respectively the mean value of elastic modulus along the specimen axis (E) and the Poisson's ratio (υ) representative for a hypothetical isotropic plate. For this reason two load steps were applied on the sample: 100 g and 200 g. Higher loads should be avoided because fringe quality could decrease due to decorrelation. The experimental displacement map relative to load 200 g provides a value of Δu_x of about 450 nm (Fig. 6 (a)).

The FE analysis applied on a model with the same sizes, load and constraints provides a value of about 445 nm (Fig. 6 (b)), in good agreement with the experimental one. The value of Poisson's ratio correspondent to this value of displacement was 0.3, the value of elastic modulus for this value of displacement is E=6.4 GPa consistent with the weighted average of literature values [22].

Also in this case iso-u-displacement bands are almost parallel in the specimen region near the supporting wedges for all loading steps.

VI. Conclusions

The hybrid procedure adopted in this paper proved itself to provide good results in determining mechanical properties on a class of different materials. The numerical results seems to be in good agreement with the experimental ones. Developments in progress are about the complete and precise characterization of all orthotropic and anisotropic materials in order to provide a fully database that can be used both in industrial and academic field as support for mechanical characterization.

References

[1] H.P. Chen, and N. Bicanic, "Inverse damage prediction in structures using nonlinear dynamic perturbation theory", *Computational Mechanics*, vol. 37, no.5, pp. 455–67, 2006.

[2] E.J. Garboczi, and A.R. Day, "Algorithm for computing the effective linear elastic properties of heterogeneous materials – 3-dimensional results for composites with equal phase Poisson ratios", *Journal of the Mechanics and Physics of Solids*, vol. 43, no. 9, pp. 1349–62, 1995.

[3] A. Joukhadar, T. Garat, C. Laugier, Constraint-based identification of a dynamic model. In: Proceedings of the intelligent robots systems (IROS'97), 1997.

[4] D.R. Franca, and A. Blouin, "All-optical measurement of in-plane and out-of-plane Young's modulus and Poisson's ratio in silicon wafers by means of vibration modes", *Measurement Science and Technology*, vol. 15, no.5, pp. 859–68, 2004.

[5] H.D. Bui, *Inverse problems in the mechanics of material*,. London: CRC Press, 1994.

[6] G. Maier, M. Bocciarelli, G. Bolzon, and R. Fedele, "Inverse analyses in fracture mechanics", *International Journal of Fracture*, vol. 138, no. 1–4, pp.47–73, 2006.

[7] L.G. Han, M. Butcher, and J.A. Noble, "Non-invasive measurement of biomechanical properties of in vivo soft tissues", *Medical Image Computing and Computer – Assisted Intervention-Miccai* 2488 (Pt 1), pp. 208–15, 2002.

[8] G.L. Cloud, *Optical Methods in Engineering Analysis*, Cambridge University Press, New York USA, 1998.

[9] C. Sciammarella, "Overview of optical techniques that measure displacements: Murray Lecture", *Experimental Mechanics*, vol. 43, no.1, pp.1-19, 2006.

[10] K. Creath, “Phase shifting speckle interferometry”, *Applied Optic*s, vol. 24, no. 18, pp. 3053–3058, 1995.
[11] N.H. Ching, D. Rosenfeld, and M. Braun, “Two-dimensional phase unwrapping using a minimum spanning tree algorithm”, *IEEE Transactions on Image Processing*, vol. 1, no. 3, pp. 355–365, 1992.
[12] *The ANSYS Users’ Manual*, Swanson Analysis System Inc., 2013.
[13] C. Casavola, C. Pappalettere, and F. Tattoli, “Experimental and numerical study of static and fatigue properties of titanium alloy welded joints”, *Mechanics of Materials*, vol. 41, no. 3, pp. 231-243, 2008.
[14] C. Barile, C. Casavola, G. Pappalettera, and C. Pappalettere, “Mechanical characterization of orthotropic materials with speckle interferometry and numerical optimization”, *Proceedings Youth Symposium on Experimental Solid Mechanics*, Trieste, Italy, (2010).
[15] C. Casavola, S.L. Campanelli, and C. Pappalettere, “Preliminary investigation on the residual strain distribution due to the Selective Laser Melting Process”, Jornal of Strain Analysis, vol. 44, no. 1, pp. 93-104, 2009.
[16] C. Barile, C. Casavola, G. Pappalettera, and C. Pappalettere, “Mechanical characterization of SLM specimens with speckle interferometry and numerical optimization”, *Conference Proceedings of the Society for Experimental Mechanics Serie* , vol. 6, pp. 837-843, 2011.
[17] C. Barile, C. Casavola, G. Pappalettera, and C. Pappalettere, “Mechanical characterization of SLM specimens with speckle interferometry and numerical optimization”, (2010) *Society for Experimental Mechanics - SEM Annual Conference and Exposition on Experimental and Applied Mechanics 2010*, vol. 3, pp. 2523-2529, 2010.
[18] C. Barile, C. Casavola, G. Pappalettera, and C. Pappalettere, “Experimental and numerical characterization of sinterized materials with speckle interferometry and optimization methods”, *10th IMEKO TC15 Youth Symposium on Experimental Solid Mechanics 2011,* pp. 35-36,Chemnitz 2011.
[19] *The Engineering Toolbox*, The engineering toolbox, 2012.
[20] *MatWeb*, Matweb material property data, 2012.
[21] D.W. Green, J.E. Winandy, and D.E. Kretschmann, *Wood handbook - Wood as an engineering material*, Forest Products Laboratory (1999).
[22] C. Barile, C. Casavola, G. Pappalettera, and C. Pappalettere, “Hybrid characterization of laminated wood with ESPI and optimization methods”, *Conference Proceedings of the Society for Experimental Mechanics Series*, vol. 3, pp. 75-83, 2013.

Corrosion Damage Monitoring of Stainless Steel by Acoustic Emission

Kaige Wu [A], Seung-mi Lee [B], Won-Sik Lee [C], Dong-Pyo Hong [D] and Jai-Won Byeon [A]

***Abstract*—**In this work, the acoustic emission signals of gas bubbling reaction during pitting corrosion of stainless steel 304 was investigated by acoustic emission(AE) technique and potentiodynamic method. The electrochemical and acoustical tests were carried out simultaneously at room temperature in a 3% NaCl solution acidified to pH 2 via a bubble-detected three-electrode system. The results showed that a short time delay was observed before AE signal detected after pit potential. This time delay was supposed to be closely correlated with a threshold of gas pressure for H_2 bubble to break-up, which again be associated with a minimum amount of corrosion. Considering the delay time, the AE signals of accumulative counts, rise time, duration in time domain shown three different stages with different signal features. The signals were compared by frequency analysis and the evolution of pit was studied by reproducible tests with different durations. The change of pits in size and quantity during corrosion process was supposed to account for different process of gas bubbling, which could again account for the different features of different stages. A good correlation between AE signals and pit quantity was observed. The results demonstrate the feasibility of employing AE signal of gas bubbling as an on-line monitoring tool for estimating non-intrusively the overall of the pitting corrosion process in stainless steel.

***Keywords*—** Acoustic Emission, Stainless Steel, Pitting Corrosion, Gas Bubbling, Cumulative Counts

I. Introduction

Stainless steels have been finding extensive applications not only in industrial field but also in people's daily life due to its unsurpassed property of excellent resistance to corrosion. This very commonly used materials, however, can undergo localized pitting corrosion, which rapidly leads to final failure.

This work was supported by the Technology Innovation Program (No. 10049237, Development of rapid mold manufacturing technology for mass customized medical devices with SLS hybrid 3D printing technology) funded By the Ministry of Trade, industry & Energy(MI, Korea)"

Kaige Wu is with the Department of Materials Science and Engineering, Seoul National University of Science and Technology, SOUTH KOREA, 139-743, SOUTH KOREA, (e-mail: kaigewu@seoultech.ac.kr)

Seung-Mi Lee is with the Department of Graduate School of NID Fusion Technology, Seoul national university of science & technology, SOUTH KOREA, 139-743, Korea, (e-mail: smlee@seoultech.ac.kr).

Won-Sik Lee is with the Advanced Process and Materials R&D Group Korea Institute of Industrial Technology, 7-47 Songdo-dong, Yeonsu-gu, Incheon, 406-840, SOUTH KOREA, (e-mail: wonslee@kitech.re.kr).

Dong-Pyo Hong is with the Department of Mechanical Systems Engineering, Chonbuk National University, Chonju, 561-756, SOUTH KOREA, (e-mail : hongdp@jbnu.ac.kr).

Jai-Won Byeon is with the Department of Materials Science and Engineering, Seoul National University of Science and Technology, Seoul, 139-743, SOUTH KOREA, (Corresponding author to provide phone: 02-970-6634; fax: 02-973-6657; e-mail: byeonjw@seoultech.ac.kr).

During all the electrochemical corrosion in laboratory research by AE technique, pitting corrosion of stainless steels has been of major concern for many years. Taking the AE signal analysis into consideration, Fregonese et al. [1-2] classified the signal into short signal and resonant signal, and the resonant signal was supposed to be associated with the evolution of H_2 bubbles within the occluded pits. Similar features were also shown by Jian Xu et al. [6], but their main disputation is when classifying the AE signals, the record length of signal was largely shorter than the duration time, which thus possibly make the classify method to be distrusted. Jirarungsatian and Prateepasen [5] used the duration to discriminate the "breakdown of passive films" and "pit growth" during pitting corrosion, but the AE waveform analysis was not studied though they proposed the 65us of duration to differentiate the two process. Taking the AE source analysis into consideration, hydrogen bubble evolution has been regarded as the most emissive source during electrochemical corrosion processes by many authors [1-7], and they suggested that hydrogen bubbles were generated inside the occluded pits as the AE source. Fregonese et al. [1] established that the hydrolysis of the resulting corrosion products leads to acidification within the pits and then to hydrogen evolution based on theoretical analysis. In this study, Acoustic emission (AE) technique was proposed to In-situ evaluate the pitting corrosion of 304 stainless steel.

II. Experimental Method

A. Material and Specimen Preparation

Table 2.1 Compositions of 304 SS investigated in the present study, wt%.

C	Si	Mn	Cr	Ni	P	S
0.07	0.55	2.00	18.01	9.00	0.02	0.03

Commercial 304 stainless steel, which composition is given in Table 2.1, was used for this work. The specimens were cut from a 2 mm thick 304 stainless steel plate into a shape size of 75mm*15mm. They were wet ground up to No. 1500 sand paper, followed by polishing from 6μm to 1μm by diamond gel. Subsequently the specimens received a passivation treatment of 30min in 20% HNO_3 at 60℃, after which they were rinsed with de-ionized water then acetone and dried in a stream of cool air.

ISBN: 978-1-61804-288-0

The exposed surface equal to 1*1 cm^2 controlled by mounting with fast curing epoxy (Araldite Rapid, Huntsman Advanced Materials (Switzerland) GmbH.) as shown in Fig. 2.1.

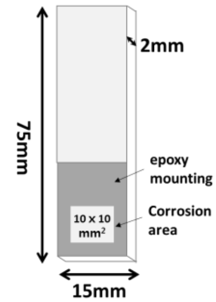

Fig. 2.1 A schematically view of specimen geometry.

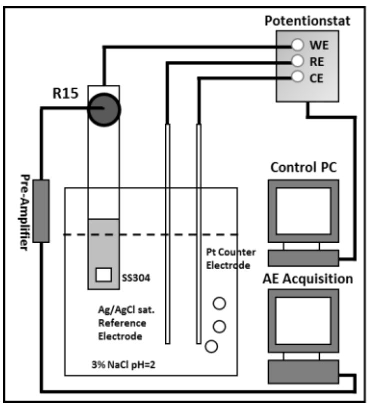

Fig. 2. 2 A schematically view of experimental apparatus: Hydrogen bubble detected three-electrode system.

B. *Electrochemical Setup for Pitting Corrosion Control*

The pitting corrosion process was controlled with apply of anodic polarization by potentiodynamic method which was carried out in a typical three-electrode electrochemical cell: A Platinum wire counter electrode (CH115, CH Instruments Inc. USA) and a reference electrode of saturated Ag/AgCl/NaCl (3M) electrode (SSE) (RE-5B, Bioanalytical Systems Inc. USA) were employed, and the specimen as the working electrode. The corrosion test was implemented in 3% sodium chloride solution acidified to an initial pH of 2 controlled by HCl, which was prepared from de-ionized water, extra pure grade NaCl (Duksan Pure Chemicals, Korea) and extra pure grade HCl (Duksan Pure Chemicals, Korea). The specimens were anodically polarized at room temperature from open circuit potential (OCP) with a scan rate of 0.4mV/s after immersion in the test solution for 20 minutes.

C. *Acoustic Emission Measurement*

As shown in Fig. 2.2, in attempting to study the AE behavior of hydrogen bubbling in corrosion process, experimental setup was designed as gas-detected system with R15 sensor (PAC, USA) employed. The R15 type sensor was mounted by ultrasonic couplant to the specimen. The other end of R15 sensor was connected to AE system via a preamplifier (PAC. USA). The AE signals were collected in one acquisition device (PCI 2 from PAC. USA). The threshold was set at 22dB and pre-amplifier was set at 40dB, respectively.

III. Results and Discussions

A. *Polarization curve*

Fig. 2.3 shows the anodic potentiodynamic polarization curve of stainless steel in 3% NaCl solution which was acidified to pH 2 by addition of HCl. In the polarization curve, when the applied potential is relatively lower than pit potential, the current density changes hardly and keeps at a relatively low level, which exhibited a range of passivity. Whereas as applied potential surpassed critical pitting potential, current density appeared to increase sharply with potential increasing. It is from this point, that metal passive film was ruptured and pits began to form on the surface of specimen.

B. *Morphology of specimen*

Fig. 2.4 shows the integrated morphologies of the specimen before and after anodic polarization process of 304 stainless steel in experimental solution, respectively. It clearly indicates that the occurrence of severe pitting corrosion on the surface of specimen after the applied polarization testing.

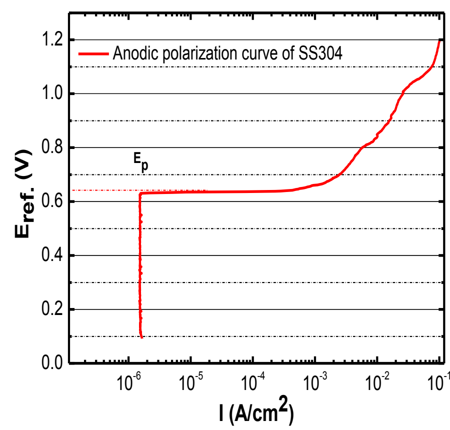

Fig. 2.3 Anodic potentiodynamic polarization curve of 304 stainless steel in 3% NaCl solution, pH=2 controlled by addition of HCl.

C. *AE activity*

Fig. 2.4 shows the integrated morphologies of the specimen

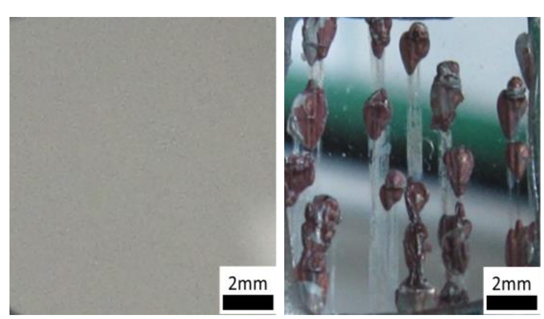

Fig. 2.4 The morphology of the specimen before (a) and after (b) pitting corrosion of 304 stainless steel in 3% NaCl solution, pH=2.

ISBN: 978-1-61804-288-0

before and after anodic polarization process of 304 stainless steel in experimental solution, respectively. It clearly indicates that the occurrence of severe pitting corrosion on the surface of specimen after the applied polarization testing.

Fig. 2.5 shows the AE signals of cumulative counts detected during pitting corrosion of stainless steel 304 in gas bubbling detected system during anodic polarization process. AE signals were not detected immediately after applied potential surpassed the pit potential. When applied potential and current density reached a certain value which is higher than pitting potential, the AE signals started to be active. This short time lagging was reported as the phenomenon of “time delay” by many researchers [4-6, 9].]. However, it should be noted that they found the phenomenon of time delay in gas-undetected system, in which the gas bubbling was supposed to be noise and was eliminated always via a salt bridge.

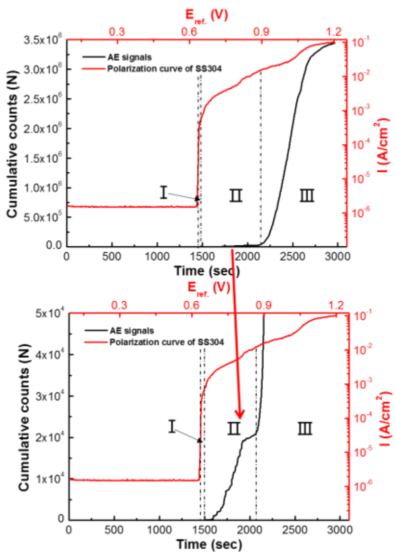

Fig. 2.5 AE signals of cumulative counts detected during pitting corrosion of stainless steel 304 in gas bubbling detected system during anodic polarization process in solution of 3% NaCl, pH=2.

In the gas-detected system, the occurrence of time delay is observed for the first time. The important critical value like potential and time corresponding to the evolution of pit and related AE signals are given in Table 2.2.

Table 2.2 Summary of important critical values corresponding to the evolution of pitting and related AE signals in Fig. 2.3 and Fig. 2.4.

E_{ocp} (V)	E_p(V)	I_p ($\mu A/cm^2$)	t_p(s)	E_{AE}(V)	I_{AE} ($\mu A/cm^2$)	t_{AE} (s)	Delay time (t_{AE}-t_p) (s)
0.091	0.636	76	1460	0.641	342	1470	10

It is worth noting that the AE signal in time domain could be divided into three stages with taking the delay time into consideration. In stage I, which is the period of delay time, the signal is zero. In stage II, the AE signal was detected after the delay time. The AE signal of cumulative counts number exhibited as rather low increasing rate, as well as the current density. Subsequently in stage III, the AE signal increased sharply with a higher increasing rate comparing to stage II. The current density in this period also increased more sharply than previous stage.

D. AE parameters

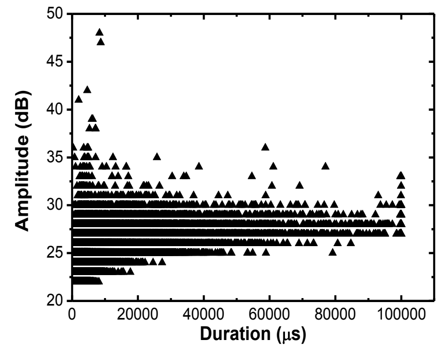

Fig. 2.6 The cross-plot of amplitude and duration of the AE signals detected during anodic polarization process of 304 stainless steel in solution of 3% NaCl, pH=2.

Fig. 2.6 shows the cross-plot of amplitude and duration of the AE signals detected during the testing. It clearly indicates a distribution feature of amplitude versus duration cluster in one region of between 22dB and 48dB.

E. AE waveforms and Hydrogen bubble evolution on the electrode.

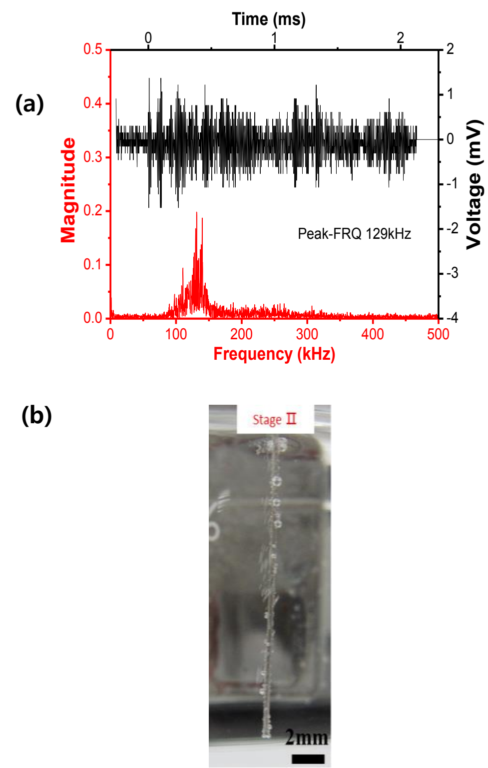

Fig. 2.7 (a) AE waveforms and corresponding FFT results (b) Morphology of bubble evolution on the surface of counter electrode.

Fig. 2.7 (a) shows the typical waveforms and their corresponding Fast Fourier Transform (FFT) analysis results of AE signals in stage II. It clearly indicates that AE signals are characterized by a frequency content between about 90kHz and 200kHz and peak frequency around 125kHz. In other hands, the duration of AE signals in this stage is less than 3000μs. Fig. 2.7 (b) shows bubble evolution on the surface of counter electrode. Note the size of breaking bubble in this stage was around 0.8mm.

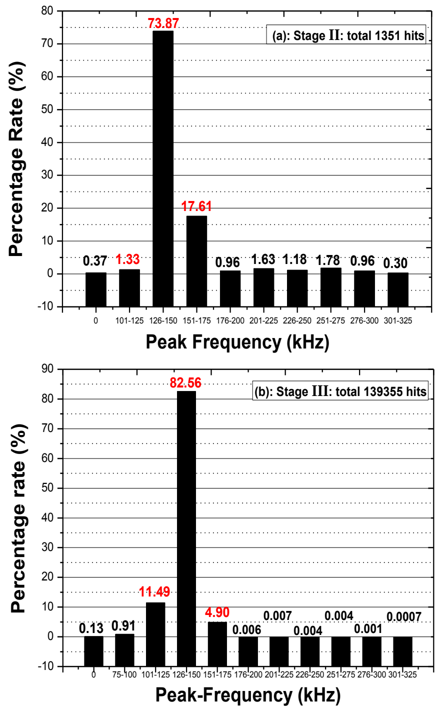

Fig. 2.8 Spectral analysis of AE activity (a) in stage II and (b) in stage III.

Fig. 2.8 (a) and (b) shows the spectral analysis of AE activity of stage II and stage III, respectively. The results of the analysis suggested that the frequency contents of stage II and stage III both cluster mainly in the range of 101 kHz and 175 kHz, reaching a ratio of 92.81% in stage II and 98.95% in stage III, respectively. Especially the range of 126 kHz and 150 kHz dominates distinctly as 73.87% in stage II and 83.56% in stage III, respectively.

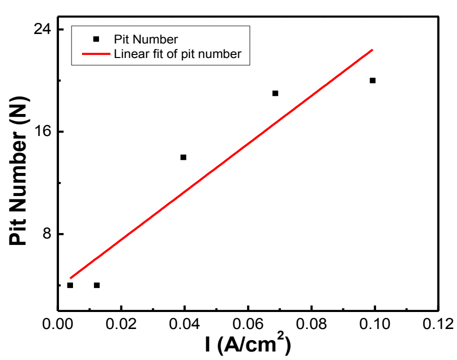

Fig. 2.9 Correlation between total pits number generated and applied anodic current density during pitting corrosion of stainless steel 304 in 3% NaCl solution, pH=2.

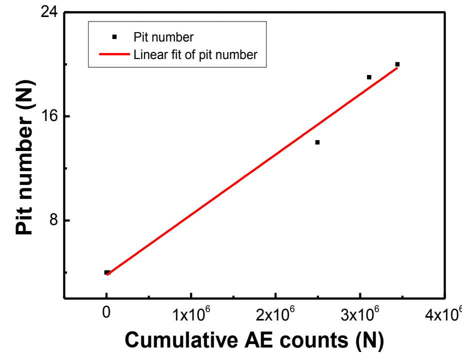

Fig. 2.10 Correlation between total pits number generated and AE signal of cumulative counts during pitting corrosion of stainless steel 304 in 3% NaCl solution, pH=2.

Fig. 2.9 shows a correlation between total pits number generated and anodic current density during the experiment process. Fig. 2.10 shows a similar correlation between total pits number generated and the AE signal of cumulative counts. The good agreement between the two curves indicates that increasing both in size and quantity of pits can be corresponding to increase of corrosion amount, thus leading to the increasing trend of AE signals.

This phenomenon is surprisingly observed for the first time in our gas-detected system, though a similar occurrence of time delay has been reported previously in gas-undetected system by many researchers [1-2, 6]. Fregonese et al. [1, 2] reported the ime delay above 1000 seconds up to 3500 seconds around. J. Xu et al. [6] also shown the time delay about a few hundred seconds. Apparently, the length of time delay in our study is far shorter than previous report results, proving our AE signal in early stage is the result of gas bubbling other than other physical sources. After considerable time corresponding to the time delay in gas-undetected system, the AE signal in our gas-detected system has presented to be huge comparing to that of pitting corrosion itself in gas-undetected system. Their effect on trend of AE signal of gas bubbling could be ignored. This proves again that AE signals in present gas-detected experiment setup could be supposed to be the result of hydrogen gas bubbling generated on counter electrode. The distribution feature of amplitude versus duration almost in one clustering (Fig. 2.8) could speak for this point to some extent.

Taking the period of time delay phenomenon into consideration, the AE signal of gas bubbling could be divided into three stages based on different features, as shown in Table 2.2. In order to interpret the evolution of AE signal and hydrogen gas bubbling, the relationship of AE and bubbles needs to discuss firstly. The acoustic energy of bubble oscillation and bubble break-up was firstly studied by Minneart [7], and then investigated and demonstrated by Strasberg [8], Leighton [9, 10] and Lec.et al. [11].

In stage I, of which gas bubbling is shown in Fig. 2.7b, after

ISBN: 978-1-61804-288-0

pit potential the bubble initiation, expansion occurred on the surface of counter electrode. When bubble breaks up, AE signals begin to be obtained. It is the period of bubble initiation and expansion that is the time delay. This time delay was supposed to be closely correlated with a threshold of gas pressure for H_2 bubble to break-up, which again be associated with a minimum amount of corrosion.

In stage II, the bubbles generate on the surface of counter electrode and break one by one as single bubble as shown in Fig. 2.7b. This computed result is in consistent with the spectral analysis result (shown in Fig. 2.8), according to which nearly 73.87% of waveform cluster in frequency range of 126 kHz and 150 kHz.

It is should be considered that these estimation could only be regarded as qualitative because the assumptions upon which the estimations were based may not be completely valid. In general, however, different evolution of bubble of different stages, gives rise to different feature of AE signals.

The AE signal of cumulative counts is found to be very good correlation with the quantity of pits as shown in Fig. 2.10. The AE signal can be quantitatively correlated with the pit number based on the linking of H_2 gas bubble revolution between them, suggesting that AE signal of gas bubbling could be a method of on-line monitoring and estimate non-intrusively the overall of the pitting corrosion process.

Conclusion

In this work, an attempt was made to study the signals of gas bubbling generated during pitting corrosion of stainless steel. Based on the present experimental study, the following conclusions can be drawn:

(1). Acoustic emission signals was detected after a short delay time after surpassing the pit potential. The “delay time” phenomenon in gas-detected system was firstly confirmed. This time delay was supposed to be closely correlated with a threshold of gas pressure for H_2 bubble to break-up, which again be associated with a minimum amount of corrosion.

(2). Considering the “delay time”, AE signals of cumulative counts, rise time and duration time with three different features were to classify corrosive pitting process into three stages.

(3). It is believed that different bubbling evolution in different stages is the main cause of different features of AE signals.

(4). Pit was very small in size and low in quantity in initial stage, then increased both in size and quantity, which corresponding to increase of corrosion amount, protons formed on counter electrode, and thus more releasing hydrogen bubbles, thus leading to the changing trend of AE signal.

(5). Serial reproducible tests clearly shows a good correlation between AE signals and pit quantity. Accordingly, based on AE signal generated from H_2 gas bubbling the extent and process of pitting corrosion could be non-intrusively studied.

References

[1] M. Fregonese, H. Idrissi, H. Mazille, Monitoring pitting corrosion of AISI 316L austenitic stainless steel by acoustic emission technique: choice of representative acoustic parameters, J. Mater. Sci., 36 (2001), pp. 557–563.

[2] M. Fregonese, H. Idrissi, H. Mazille, L. Renaud, Y. Cetre, Initiation and propagation steps in pitting corrosion of austenitic stainless steels: monitoring by acoustic emission, Corros. Sci., 43 (2001), pp. 627–641.

[3] K. Darowicki, A. Mirakowski, S. Krakowiak, Investigation of pitting corrosion of stainless steel by means of acoustic emission and potentiodynamic methods, Corros. Sci., 45 (2003), pp. 1747–1756.

[4] C. Jirarungsatian, A. Prateepasen, Pitting and uniform corrosion source recognition using acoustic emission parameters, Corros. Sci., 52 (2010), pp. 187–197.

[5] J. Xu, X.Q. Wu, E.H. Han, Acoustic emission during pitting corrosion of 304 stainless steel, Corros. Sci., 53 (2011), pp. 1537-1546.

[6] H. Mazille, R. Rothea, C. Tronel, An acoustic emission technique for monitoring pitting corrosion of austenitic stainless steels, Corros. Sci., 37 (1995), pp. 1365–1375

[7] M. Minnaert. “On Musical Air-Bubbles and the Sounds of Running Water,” Philosophical Mag. 16, 1933, p. p 235-248.

[8] Strasberg, M., Gas bubbles as sources of sound in liquids, Journal of the Acoustical Society of America, 28 (1), 1956, 20-26.

[9] T. G. Leighton, K.J. Fagan and J.E. Field. “Acoustic and Photographic Studies of Injected Bubbles.” Eur. J. Phys. 12, 1991, pp. 77-85.

[10] T.G. Leighton, The acoustic bubble, San Diego, 2002, pp. 75-79.

[11] R.M. Lec, P.A. Lewin, M. Musavi, S.W. Bang, S. Goel, S. Kwoun, E. Radulescu, Acoustic emission sensor for identification of chemical reactions, in: The 1999 joint Meeting of The European Frequency and Time Forum and The IEEE International Frequency Control Symposium, 1999, pp. 978-982.

Modelling plasticity of materials with a micro and nanostructure

Natalia.R. Kudinova, Anatoli.M. Polyanskiy, Vladimir.A. Polyanskiy, Yuriy A. Yakovlev

Abstract— Materials with the nano and micro structural elements have many useful properties. The yield point and strength of nanomaterials are in the several times larger than that of conventional materials. It is necessary to simulate correctly its properties in the strength calculations for the use of nanomaterial in machines and in constructions. Some uncertainties reduces the opportunities for using of the dislocation model for the strength calculation and predictive modeling of the nanomaterials.

An important component of the self-energy is the energy of the surface tension of the grain of structural elements. Surface tension energy is a significant part of the elastic deformation energy for the nano scale. The article gives the calculation of the volume energy density of surface tension. The dependence of the melting point and yield point on the particle size of material may be interpreted as altering the surface tension. The results of calculations and their comparison with the experimental curves are presented. The proposed approach contains a minimum number of physical parameters. This approach makes it possible to predict the mechanical properties of materials.

Keywords— micro structures, nano structures, yield stress, forming, plastic deformation, surface tension.

I. Introduction

MATEREALS with micro and nano structures have extreme mechanical characteristics. This puts a very difficult problem before a designer: to choose a proper material in design and strength analysis of machines and constructions. The structure can be changed in the course of manufacturing. For example, in pressing it is possible to assign different structures in different parts of the manufactured detail. This requires prediction of the material mechanical characteristics on the stage of the machine projecting. Such prediction is even more important in projecting new materials.

N. R. Kudinova is the Phd student in the Institute of Problem of Mechanical Engineering, RAS, V.O., Bolshoj pr., 61, St.- Petersburg, 199178 Russia (e-mail: natalii@simail.com).

V. A. Polyanskiy, is the head of laboratory in the Institute of Problem of Mechanical Engineering, RAS, V.O., Bolshoj pr., 61, St.- Petersburg, 199178 Russia and professor in the St.-Petersburg State Polytechnic University, Polytekhnicheskaya, 29, St.-Petersburg, 195259 Russia (corresponding author phone: 7-921-748-0637; fax: 7-812-297-9431; e-mail: vapol@mail.ru).

A. M. Polyanskiy is director of the RDC Electron and Beam Technologies, Ltd., st. Bronevaya, 6, St.-Petersburg, 198188 Russia (e-mail: ampol@electronbeamtech.com).

Yu. A. Yakovlev is researcher in the Institute of Problem of Mechanical Engineering, RAS, V.O., Bolshoj pr., 61, St.- Petersburg, 199178 Russia (e-mail: yura.yakovlev@gmail.com).

The needed forecast requires developing of a model for dependence of the studied material characteristics on the size and shape of the structure elements. The most important mechanical parameter of the construction material is the yield stress. On the one hand, the linear dependence of tensions on deformations in absence of yield allows one to perform the calculations of strength very accurately. On the other hand, the plastic deformation of the material makes it possible to smooth the singularities of the tension field. Thanks to the phenomenon of strengthening arising in the zones of plastic deformation, an additional reserve of strengthening is created. In forming, the plastic yielding is the main kind of deformation. In that case, the knowledge of mechanical characteristics of the material, e.g. the yield stress, becomes necessary.

The process of plastic deformation is accompanied by inelastic energy losses. The value of the yield point determines the elastic energy necessary for the onset of the material plastic deformation. In spite of the fact that the plastic deformation regime looks very much like deformation of material in the liquid phase, the specific energies needed for heating the material up to the melting temperature and total melting are by an order of magnitude higher than the specific energy of plastic deformation and maximum possible plastic deformation up to the material destruction. This is why it is accepted that the mechanism of plastic deformation is associated with sliding of the material grains [1,2] and with emission of the dislocations leading to growth of the micro-cracks [3,4,5,6].

Petch [7] explained the experimental dependence of the yield point on the size of the material grains by growth of cracks. This dependence (Hall-Petch law) is destroyed only for the grain sizes less than 1μm, and it can serve as a test for various theories of plasticity taking into account the grain size [1,2,3]. Meanwhile the formation of micro-cracks in approaching the yield point does not always occur, especially in the case of materials with nano structures. The dislocation theory of plasticity [8] predicts strong dependence of the mechanical characteristics on the density of dislocations on the grain surface. This value cannot be measured, so that the value predicted by the dislocation approach is not very large.

It is necessary to determine the main mechanism of deformation.

Apart from changing the yield point, grinding of structure elements and the grinding of structure affects the melting temperature. For example, aggregated and powdered nano-materials can have different melting temperatures, meanwhile

ISBN: 978-1-61804-288-0

in the case of metallic nano powders of pure metals in atmosphere of an inert gas we can speak that takes place the decreasing the melting temperature depending on decreasing the size of nano-powders from 20 nm to 1-2 nm [9].
The variation of melting temperature is evidently connected with the energy of surface tension since the probability for stripping of individual atoms and molecules from a crystalline as a result of thermal motion increases in decreasing the surface energy. The effect of the surface tension of crystallites on the yield point has not been studied yet. However the experimental procedure of measuring the surface tension forces per se based on the mechanism of "zero creeping" evidences existence of such effect [10]. Besides that, there exists an experimental dependence of the melting temperature on the surface tension energy for different materials, and this dependence is linear [11].

II. Estimation of Surface Density Energy

Exact Gibbs–Tolman–Koenig–Buff [12,13] equation for a spherical particle is:

$$\frac{\partial \ln \sigma}{\partial \ln R} = \frac{\frac{2\delta}{R}\left(1+\frac{\delta}{R}+\frac{1}{3}\frac{\delta^2}{R^2}\right)}{1+\frac{2\delta}{R}\left(1+\frac{\delta}{R}+\frac{1}{3}\frac{\delta^2}{R^2}\right)}. \tag{1}$$

Where σ and R are the surface tension and radius of particle, respectively, δ is the Tolmen constant.

In general case, the equation (1) cannot be solved explicitly. In theory, the condition R≫δ, is usually introduced, that allows simplifying expressions in brackets in (1). In that case elementary integration gives the well-known expression [14]:

$$\sigma = \frac{\sigma^{(\infty)}}{1+\frac{2\delta}{R}}. \tag{2}$$

Where $\sigma^{(\infty)}$ is the surface tension for a plane surface. When using the condition R≫δ,one obtains another analytical expression for the surface tension [14]:

$$\sigma(R) = \sigma^{(\infty)} exp\left(-\frac{2\delta}{R}\right). \tag{3}$$

However it is possible to show that the general solution of (1), in the case that δ does not depend on R, can be expressed in an analytical form:

$$\sigma = \frac{\sigma^{(\infty)} R}{\delta} e^{\left(-\sum_{k=1}^{3}\frac{x_k^2 \ln(\frac{R}{\delta}-x_k)}{3x_k^2+4x_k+2}\right)}. \tag{4}$$

Where x_k={-0.558;-0.721+i0.822;-0.721-i0.822} - are the roots of the cubic equation $3x^3+6x^2+6x+2=0$

Further, Fig.1 shows the surface tension functions for the exact solution (4) and the approximations usually used in literature.

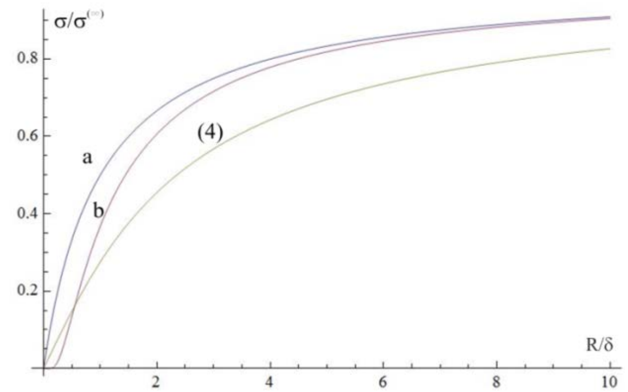

Fig.1. Scaled functions of surface tension for the exact solution (4) and the approximations $\sigma(r) = \sigma^{(\infty)}\left(1-\frac{2\delta}{r}\right)$- (a), $\sigma(R) = \sigma^{(\infty)} exp\left(-\frac{2\delta_\infty}{R}\right)$- (b).

The use of well-known linear dependence of the melting temperature on the surface tension energy allows one to construct a model dependence of the melting temperature on the particle size. Fig.2 shows such dependence for gold (experimental points) and calculated functions.

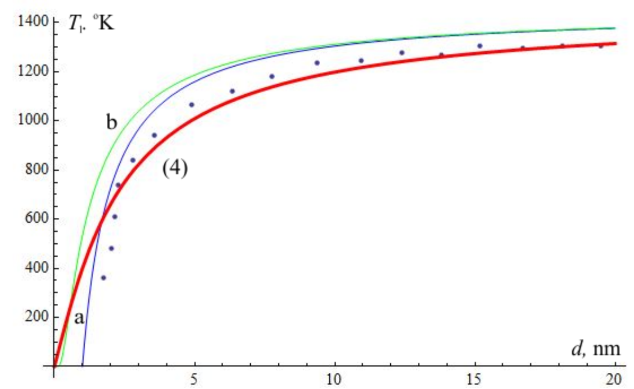

Fig.2. Dependence of the melting temperature for gold on the particle diameter d. Experimental values (points) and calculation results obtained using the approximate formulas $T_l = T_0\left(1-\frac{d}{r}\right)$- (a), $T_l = T_0 e^{-\frac{2\delta(\infty)}{d}}$, - (b) and exact solution of Gibbs–Tolman–Koenig–Buff equation $T_l = \frac{T_0 R}{\delta} e^{\left(-\sum_{k=1}^{3}\frac{x_k^2 \ln(\frac{R}{\delta}-x_k)}{3x_k^2+4x_k+2}\right)}$ - (4).

Comparison of the plots shows that the exact solution describes well the experimental data in the range of the particle sizes from 3 to 20 nm. At the same time, the approximate functions suffer from very large (up to 100%) uncertainty. Thus the exact solution (4) provides an adequate description for variation of the melting temperature. This justifies the use of it in the further calculations..

III. Connection between fluidity limit and surface tension

As follows from Fig.1, the specific energy of surface tension decreases in decreasing the size of material particles down to the values less than 10 nm. Its values for most of metals with larger structural elements are of the order of σ = 1-2 J/m2. Elastic energy stored in metal in single-axis stretching till the yield point for steels is about 90 MJ/m3. Let us compare this energy with the volume density of surface tension energy ρσ. Suppose for the sake of simplicity the spherical shape of particles. Then this value equals $\rho_\sigma = 3\sigma/R$. Even at the characteristic size of crystallite of 2R = 200 nm the value of ρ_σ becomes equal to the maximum energy of elastic deformation. Consequently, construction of models for plastic deformation of micro-disperse materials requires taking into account the surface energy. One can expect that this energy is responsible for mechanisms of plastic deformation in this case.

To check this hypothesis, let us use the Hall-Petch law [15,7] which was uncovered as an empirical dependence. To explain this dependence, Petch suggested to consider origin and development of a micro-cracks in a grain of the size 2R. Now, both time and the function itself and deviation from it at nanometer sizes of crystallites are explained solely by the dislocation mechanism of plastic deformation.

According to the Hall-Petch law the fluidity limit τ and the grain size d for polycrystalline material are connected by the relation:

$$\tau = \tau_0 + K(2R)^{\frac{-1}{2}}. \qquad (5)$$

Where τ0 is a certain frictional tension which is necessary for sliding of dislocation, K is a material constant often called “H-P coefficient”. These values are estimated from experimental data.

Let us consider the origin of plastic deformation. For most of metals this process is characterized by the fact that the deformations grow practically without increasing the tensions. In the simplest case, single-axis stretch, the tensions can be considered constant. Consequently, the energy of plastic deformation should be proportional to the yield point. Suppose that the plastic deformations give rise to growth of inner surface of a crystallite without essential change of its volume. Then in the beginning of plastic yielding the mechanical tensions should compensate for both elastic deformations of crystallites and surface tension forces. As a result, the yield point should be linearly dependent of the surface energy. This makes it possible to approximate the dependence of H-P in terms of the dependence of the surface energy on the size of particles. Using the exact solution (4) of the equation of Gibbs–Tolman–Koenig–Buff we can obtain dependence of the volume density of surface tension energy for the material containing spherical particles. This dependence is shown in Fig.3

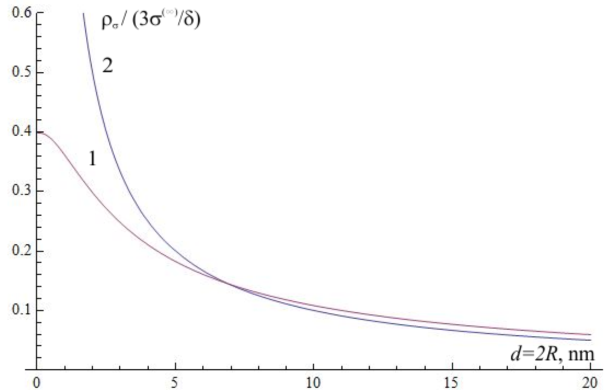

Fig.3. Dependence of surface tension per the unit of volume $\rho_\sigma = 3\sigma/R$ for gold. 1) - using the formula (4); 2) - using approximation by the H-P law.

The following two regions can be discerned in Fig.3. At the grain size larger than 5 nm, the obtained dependence can be approximated using the H-P law, while at the sizes less than 5 nm we observe a finite value for the volume density of the surface energy. We can interpret plasticity as variation of the surface energy: if the material “begins to flow” this means that the allowed value of the surface energy (shown in Fig.3 for gold) was exceeded.

IV. Conclusion

Thus the energy of surface tension can play an important role in plastic deformation of micro and nano disperse materials. This mechanism opens the possibility for constructing new models for plastic deformation without using dislocation theory.

Exact solution of the equation Gibbs–Tolman–Koenig–Buff allows more adequate describing dependence of the melting temperature on the particle size in the range from 3 to 20 nm, that supports the hypothesis of the crucial role of surface tension forces in plastic yielding of micro an nano disperse materials.

Acknowledgment

The financial support of the Russian Foundation for Basic Research, grants 12-08-00386-a, 14-08-00646-a is gratefully acknowledged.

References

[1] U.F Kocks, The relation between polycrystal deformation and single crystal deformation, Metal. Trans., 1970, Vol.1, N5, pp. 1121-1143.

[2] Kim H.S. A composite model for mechanical properties of nanocrystalline materails, Scr. Mater.,1998, Vol.39, N 8, pp. 1057-1061.

[3] M.Yu. Gutkin and I.A. Ovid'ko, Physical Mechanics of Deformed Nanostructures. Volume 1: Nanocrystalline Materials, Yanus, St.Petersburg, 2003.

[4] H.K. Birnbaum, P. Sofronis, Hydrogen-enhanced localized plasticity—a mechanism for hydrogen-related fracture, Materials Science and Engineering: A, Volume 176, Issues 1–2, 31 March 1994, pp. 191-202.

[5] P. Sofronis, Y. Liang, N. Aravas, Hydrogen induced shear localization of the plastic flow in metals and alloys, European Journal of Mechanics

- A/Solids, Volume 20, Issue 6, November–December 2001, pp. 857-872.
[6] D. Delafosse, T Magnin, Interfaces in Stress Corrosion Cracking: A Case Study in Duplex Stainless Steels Solid State Phenomena, 1998, p. 221
[7] N.J. Petch, The cleavage strength of polycrystals. J. Iron and Steel Inst., 1953, v. 174, pp. 25−28.
[8] I.A. Ovid'ko, N.V. Skiba, Enhanced dislocation emission from grain bounda-ries in nanocrystalline materials, Scripta Materialia, Vol. 67, N1, 2012, pp.13-16.
[9] Ph. Buffat, J.-P. Borel, Size effect on the melting temperature of gold particles, Physal Revise, v.13, 1976, pp. 2287-2298.
[10] H. Udin, A. J. Shaler and J. Wulff Metall. Trans. AIME, 1949, Feb., p. 186
[11] S. Sh. Rehviashvili, E.V. Kishtikova: submitted to Journal Letters to ZTF (2006), pp.50–55.
[12] P Frank, Buff, Spherical Interface. II. Molecular Theory, J. Chem. Phys. 23, 419 (1955); doi: 10.1063/1.174200
[13] Frederick O. Koenig, On the Thermodynamic Relation between Surface Tension and Curvature, The Journal of Chemical Physics 18, 449 (1950); doi: 10.1063/1.1747660
[14] V.M. Yurov, V.S. Portnov, N.H. Ibraev, S.A. Gurchenko, The surface tension of solid bodies, small particles and thin membrans, Phys.-math. №11, 2011
[15] E.O.Hall, Deformation and ageing of mild steel, Proc. Phys. Soc. London, ser. B, v. 64, №1, 1951, pp. 747−753.

GDI spray impact characterization by optical techniques for the assessment of 3D numerical models

Luigi Allocca, Michela Costa, Alessandro Montanaro, Ugo Sorge

Abstract— Design and optimization of injection systems for internal combustion engines must be realized possibly by relying on detailed analyses, as those achievable through multidimensional engine modeling or by experimental investigations performed on optically accessible engines or under engine like conditions in confined vessels. As regards spark ignition engines, in particular, direct injection technology is being considered as an effective mean to achieve the optimal air-to-fuel ratio distribution at each engine operating condition, either through charge stratification around the spark plug, or by creating a stoichiometric mixture under the highest power demands. The impact of a spray on the piston or cylinder walls causes the formation of a liquid film (wallfilm) and the so-called secondary atomization of droplets. The wallfilm may have no negligible size, especially in cases where the mixture formation is realized under a wall guided mode.

The present study is focused on the characterization of both a multi-hole spray and a single hole spray in their impact over a cold or hot plate. A 3D CFD model, whose assessment relies on the collected experimental data, is also developed with the future scope of its application within numerical simulations of entire engine working cycles. A free spray sub-model of high portability allows correctly predicting the spray dynamics at different injection conditions, while the spray-wall impingement sub-model makes evident the gasoline splashing and deposition phenomena.

Keywords—Computational fluid dynamics, GDI injection, secondary evaporation, spray impact.

I. Introduction

MIXTURE formation is fundamental for the development of the combustion process in internal combustion engines, for the highest release of energy and the formation of the lowest amount of undesired pollutants. Direct injection (DI) in the combustion chamber is today regarded as the most valuable solution for an effective engine control over the whole working map of both compression ignition and spark ignition engines. Today engines, indeed, strongly differ from yesterday engines, so that traditional tools and techniques used for their design are becoming insufficient for the required challenges of energy and environmental performance, also due to the fact that the fuels landscape is continuously evolving and becoming more complex. In this change from a test-first culture to an analysis-led design process, numerical simulation tools, as CFD (computational fluid dynamics) models, are becoming increasingly important to accelerate the time to market of high-efficiency clean power sources for transportation [1]. Assessing predictive numerical models is therefore strongly demanded by the scientific community and the manufacturers acting in the automotive field, especially to correctly predict important phenomena as mixture formation in DI engines.

Fuel delivery in the combustion chamber of an internal combustion engine is realized through properly mounted injectors delivering highly pressurized sprays in the intake air. A fuel spray can be regarded as a train of droplets of different size, suffering various concurring effects as they travel within the surrounding atmosphere. Roughly speaking, aerodynamic forces at the liquid air interface tends to amplify initial perturbations to the liquid surface and to lead to instability and detachment of small droplets, whereas surface tension tends to preserve the initial shape of liquid surfaces. The net effect is what is indicated as spray break-up or atomization into droplets that are smaller and smaller as the distance from the nozzle exit section increases. Initial droplets size at the injector exit section may be regarded either as constant or as variable according to some distribution, whose value or expected value, respectively, is inversely proportional to the square of the injection velocity [2]. This is proportional to the square root of injection pressure, hence droplet diameter at the exit section is practically inversely proportional to injection pressure. This last is an important parameter strongly affecting the mixture formation process, so much so that the development of internal combustion engines in the last thirty years has proceeded in strict conjunction with that of injection systems.

This work was in part supported by the Italian Government funding *PON 01_1517: Innovative methodologies for the development of automotive propulsion systems* and *PON 01_2211: Multiair evolution, an innovative spark ignition propulsion system with ultra-low CO2 emissions*.

L. Allocca is with the National Research Council of Italy (CNR), Istituto Motori, Viale Marconi, 4 – 80125, Naples, ITALY (e-mail: l.allocca@im.cnr.it).

M. Costa is with the National Research Council of Italy (CNR), Istituto Motori, Viale Marconi, 4 – 80125, Naples, ITALY (e-mail: m.costa@im.cnr.it).

A. Montanaro is with the National Research Council of Italy (CNR), Istituto Motori, Viale Marconi, 4 – 80125, Naples, ITALY (corresponding author phone: +390817177223; fax: +390812396097; e-mail: a.montanaro@im.cnr.it).

U. Sorge is with the National Research Council of Italy (CNR), Istituto Motori, Viale Marconi, 4 – 80125, Naples, ITALY (e-mail: u.sorge@im.cnr.it).

In spray dynamics, an aspect that deserves particular attention is its possible impact over cylinder or piston walls. In particular, in GDI (gasoline direct injection) engines, a quantity of injected fuel may be intentionally directed towards the piston head, which exhibits a pit and an adjacent nose redirecting droplets towards the spark plug (wall-guided mixture formation) [3]. Spray droplets hitting on the surface may be rebounded, stick to form a film, or undergo heating and secondary evaporation. The deposited fuel on the wall evaporates more slowly than free droplets, and may not permit achieving the desired spatial distribution of the air-to-fuel ratio prior to ignition. This may determine non effective combustion development and formation of pollutants. The same deposition of a gasoline film on the chamber walls is a relevant source of unburned hydrocarbons and particulate matter [4]. Therefore, controlling the amount of impacting droplets, their trajectory and the evaporated gasoline mass after impact is a challenging task, whose analysis needs a synergic use of advanced experimental and numerical techniques [5].

Form the experimental point of view, the access to engine combustion chambers is feasible only on laboratory engines. Hence, studies concerning sprays is often effected through experiments conducted within confined environments under either non-evaporating or evaporating conditions that reproduce engine like conditions. From the modelling perspective, the dynamics of a free spray issuing in a gaseous atmosphere must account for break-up, coalescence, turbulent dispersion and evaporation. Available sub-models are often empirical, due to the complexity of the involved phenomena, and need a boring phase of tuning that strongly depends on the expertise of the user. Modelling the outcome of an impinging spray, on the other hand, could be carried out by focusing attention on the impact of individual droplets on a surface, but it is obvious that a droplet clouds behaves very differently from a single one [6]. A critical review on the matter is proposed by Moreira *et al.* [7]. From this work, it clearly appears that experiments on single droplets have surely contributed to identify various fluid-dynamic regimes of droplet-wall interaction and to quantify size, velocity and angle of ejection of secondary droplets, as well as of deposited mass over surfaces. In dense sprays, on the other hand, the impact between droplets has to be taken into account, as the possible interaction with already deposited liquid films.

As regards heat transfer, the basics of transient boiling of droplet streams and sprays consider four regimes [8]. At relatively high surface temperatures, the liquid-solid contact is very brief because the liquid is separated from the surface due to an insulating vapor layer (film boiling regime). The lower limit of temperature for this regime is the Leidenfrost point, below which droplets partially enter into contact with the wall and the heat transfer rate becomes inversely proportional to the surface temperature (transition boiling regime). This occurs until the critical heat flux (CHF) point is reached. As the surface temperature further decreases, droplets make efficient contact with the surface, and heat transfer reaches the highest rates (nucleate boiling regime), till the so-called bubble incipient point. Below this limit, boiling is a consequence of single phase convection.

The just discussed reasoning clearly highlights the need for studies devoted to characterize the spray impact over walls, especially in cases where these are at high temperature, as in the present work. The scope is the quantification of the effect of temperature on the spray outcome after impact needed for the assessment of 3D models suitable of being applied to the simulation of the working cycle of a GDI engine for the prediction of the termo-fluidynamic phenomena underlying the energy conversion process and the optimization of the control strategies.

Two kind of analyses are here performed. The first concerns the impact on a wall of a spray generated by a multi-hole GDI injector, that is experimentally characterized through image acquisition by a CCD camera. The second consists in a more basic study effected through the schileren technique of the impact of a single hole spray. In both the cases different wall temperatures are assumed. Commercial gasoline is used (ρ=740 kg/m^3) within all the tests, as delivered by a hydro-pneumatic injection system without rotating organs. The experimental work serves to the assessment of a predictive 3D numerical model able to reproduce the whole phenomenon, and, in particular, the secondary atomization occurring after impact.

II. Experimental Characterization of a Multi-Hole Spray Impact

The considered GDI injector is a mini-sac 7-hole Bosch HDEV 5.1 with solenoid actuation. It is characterized by a hole diameter of 0.179 mm and a static flow rate of 13.7 g/s at the injection pressure of 10 MPa. Figure 1 represents the position of the 7 holes on the injector tip and the footprint of the spray on a plane placed at a distance of 30 mm.

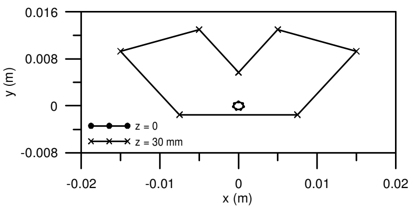

Figure 1. Injector hole distribution and spray footprint on a plane placed at 30 mm from the injector tip.

A preliminary campaign is conducted to support the validation of the developed 3D CFD numerical model, consisting of three different kind of characterizations: measurements of the delivered instantaneous mass flow rate through a Bosch tube, images acquisition of the spray issuing in an optically accessible vessel containing nitrogen under controlled conditions of temperature and pressure (298 K and 0.1 MPa, respectively), images acquisition of the spray impingement over a flat plate placed orthogonally to the injector axis under cold and hot plate conditions. The injection

ISBN: 978-1-61804-288-0

system and the synchronized image acquisition set-up are managed by a programmable electronic control unit (PECU). This is an open system able to reproduce the injector energizing currents for the desired strategy in terms of number of injection pulses, durations, rise and dwell times. The PECU reproduces as an output a TTL signal, related to the injection event, for synchronizing the consecutive images management and acquisitions.

The gasoline mass flow rate is measured by means of an AVL Fuel Injection Gauge Rate System working on the Bosch tube principle [9, 10]. Figure 2 shows the link between the solenoid energizing current profile and the corresponding fuel injection rate measured by the AVL Meter at the injection pressure of 15 MPa and for an energizing time of 1.46 ms. The delay of 0.35 ms is observed between the activation of the electronic signal and the first appearance of gasoline droplets into the vessel. This is assumed in the following as the start of injection (SOI). For the considered strategy the total amount of injected fuel is equal to 26.21 mg/str.

Images of the spray, enlightened by powerful flashes, are collected at different instants from SOI by means of a synchronized CCD camera, 1376x1040 pixels, 12 bit resolution, 0.5 μs shutter time. An overview of the experimental scheme for the image acquisition is reported in ref. [11]. The captured images are processed off-line by means of a proper software, able to extract the parameters characterizing the spray dynamics, namely penetration length and cone angle of one of the seven jets compounding the spray. A set of 5 images is collected for each injection condition for a statistical analysis of the cycle-to-cycle dispersion. The image processing analysis is carried out in different steps: image acquisition and background subtraction, filtering, fuel spray edges determination and tip penetration measurements. Background subtraction and median filter procedures allows removing the impulse noise and stray light, so to maintain sharp the spray edge. This is determined by selecting an intensity threshold level for separating the fuel region from the background ambient gas.

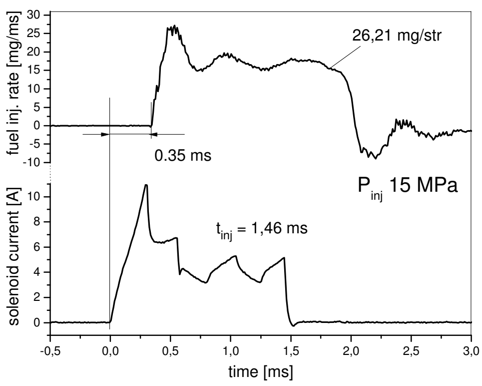

Figure 2. Solenoid energizing current and fuel injection rate.

Characterization of the spray impingement on a wall is made by introducing a stainless steel flat plate into the vessel. The plate is located at 20 mm from the nozzle tip. The average roughness of the wall is 1.077 μm, measured by the Stylus Profilometer, Model Surtronic 3 by Rank Taylor Hobson. Two cases are discussed, the first with the plate being at room temperature, the second with a plate temperature of 200°C. All the experiments are performed at ambient pressure and temperature. Images of the spray impact are reported in paragraph III, together with the relevant numerical results.

III. Numerical simulation of a multi-hole spray impact over a wall

A. *Free spray*

The 3D sub-model able to simulate the dynamics of the gasoline spray issuing from the considered injector is developed in the context of the software AVL Fire™ [12], in such a way to simulate the experiments performed by mounting the injector and delivering sprays in an optically accessible vessel. The followed approach is the classical coupling between the Eulerian description of the gaseous phase and the Lagrangian description of the liquid phase. The governing equations are here not reported for the sake of brevity; the interested reader may refer to the book by Ramos [13]. The train of droplets entering the computational domain in correspondence of the injector holes exit section suffers various concurring effects as it travels. Details of the model are given in the paper by Costa *et al.* [11]. Here it is only worth pointing out that the droplets break-up phenomenon is simulated according to the sub-model of Huh-Gosman [14] whose constant C_1 (regulating the break-up time) is adjusted by means of a tuning procedure. The effects of the turbulent dispersion on the droplets dynamics is simulated through the sub-model by O'Rourke [15], coalescence through the sub-model by Nordin [16], evaporation through the sub-model by Dukowicz [17]. Initial size of droplets at the nozzle exit section, is considered as variable according to a probabilistic log-normal distribution, whose expected value is given by the following theoretical diameter, where τ_f is the gasoline surface tension, ρ_g the surrounding gas density, u_{rel} the relative velocity between the fuel and the gas, C_d a constant of the order of the unity (indeed taken equal to the unity), and λ^* a parameter deriving from the hydrodynamic stability analysis and indicating the dimensionless wavelength of the more unstable perturbation to the liquid-gas interface at the injector exit section:

$$D_{th} = C_d \left(\frac{2\pi\tau_f}{\rho_g u_{rel}^2} \right) \lambda^* . \tag{1}$$

The variance of the distribution, σ, is another sub-model parameter to be properly tuned.

Tuning is effected through an automatic procedure developed by authors, that solves a single objective optimization problem. In other words, instead of resorting to a search of the values of the constants by trial and error, i.e. for successive approximations, an optimization problem is set-up, where the Simplex algorithm is used to reduce the error

ISBN: 978-1-61804-288-0

between the results of the numerical computations and the experimental measurements relevant to the penetration length. The automatic procedure allows obtaining a model of high "portability", i.e. such to be applied as it is to different operating conditions, or even to sprays generated by different injectors. Figure 3, as an example, represents the comparison between the experimentally measured penetration length (of one of the seven jets compounding the spray) and the numerically computed one (as averaged over the seven jets) for two different injection pressures, considered in the explored range 5 to 23 MPa.

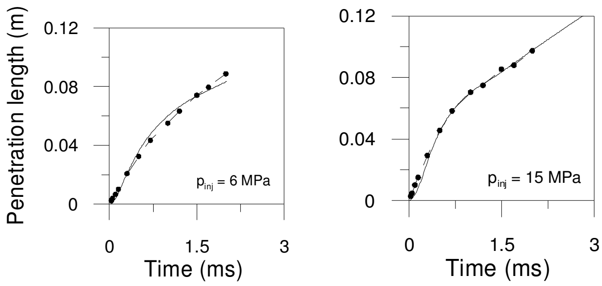

Figure 3. Numerical (continuous line) and experimental (dashed line with dots) penetration lengths of the GDI spray in a confined vessel at the injection pressures of 6 and 15 MPa. From ref. [11].

B. Spray-wall impact

The experimental characterization of the spray impingement on a wall located at 20 mm from the nozzle tip is presented. The average roughness of the wall is 1.077 μm, measured by the Stylus Profilometer, Model Surtronic 3 by Rank Taylor Hobson. The plate is at room temperature or heated at 200°C. All the experiments are performed at ambient pressure and temperature.

From the numerical side, two different spray impingement models are considered, the one proposed by Mundo and Sommerfeld [18] and the one proposed by Kunkhe [19]. This last accounts for the dependence of the phenomenon upon the wall temperature, namely it considers not only the momentum, but also the energy balance equation before and after the impact.

In the model proposed in ref. [18], authors distinguish between two regimes, deposition and splash. In the deposition regime all of the liquid remains on the wall, while in the splash regime a part of the droplet is deposited and another part reflected away from the wall. According to authors, transition from one regime to the other can be described by the so-called splashing parameter K, function of the Reynolds and the Ohnesorge numbers:

$$K = Re^{1.25}\,Oh\,. \qquad (2)$$

The dimesionless numbers Re and Oh are defined as follows:

$$Re = \frac{\rho_d d_d u_{d,\perp}}{\sigma_d} \qquad Oh = \frac{\mu_d}{\sqrt{\rho_d \sigma_d d_d}}$$

being ρ_d the droplet density, d_d the diameter, $u_{d,\perp}$ the normal component of velocity, σ_d the surface tension, μ_d the dynamic viscosity. For K <57.7 droplets are deposited completely at the wall without bouncing or breaking-up. The kinetic energy of the droplet is dissipated, independently on wall roughness. In the splashing regime (K>57.7), the impingement process is more complex. Increasing the momentum of the droplets undergoing impact, a larger mass fraction is atomized and reflected. During splashing, droplets are partially shattered to produce a different droplet size spectrum for the reflected droplets. Increasing K (higher momentum, less surface tension), the reflected droplets tend to be smaller and have a narrower bandwidth of the size distribution.

Empirical correlations, here not reported for the sake of brevity, are used to derive the droplets reflection angle (as a function of the incident angle), the reflected mass fraction, the reflected droplet size and the tangential velocity component. To avoid exceptionally small droplets, which could result in an increased evaporation rate and in destabilization of the spray model, the diameter reduction ratio is limited. Details about the afore mentioned issues can be found in [18].

The model proposed by Kuhnke [19] distinguishes, instead, between four regimes, defined as a function of the parameter K:

$$K = \frac{(\rho_d d_d)^{3/4} u_{d,\perp}^{5/4}}{\sigma_d^{1/2} \mu_d^{1/4}}\,. \qquad (3)$$

Figure 4 represents the limit of each regime, in the K,T* plane, where $T^*=T_w/T_s$ being T_w the wall temperature and T_s the surface temperature of droplet. In the deposition regime impacting droplets completely stick on the wall and create a wallfilm. In the splashing regime particles are atomized and smaller secondary droplets form after their impact on the wall. Under rebound conditions, a vapour layer between the droplet and the wall is formed, that prevents a direct contact and leads to a reflection of the impacting droplets, without formation of wallfilm. In the thermal regime, droplets also disintegrate into secondary ones, again without wallfilm formation.

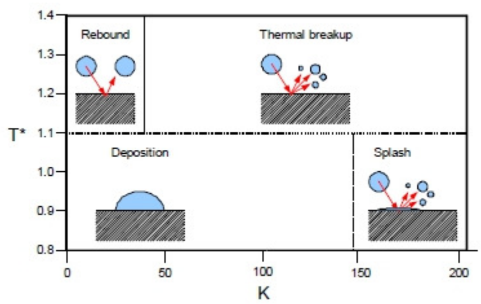

Figure 4. Impact regimes of the Kuhnke's model.

Within the present work, computations are performed to reproduce the experimental campaign devoted to investigate the phenomenon of impingement with the aim of establishing which of the afore described models is to be preferred. The simulation of the experiments is made from one hand to validate the spray-wall interaction models, from the other to actually evaluate the importance of keeping into account the effects of the wall temperature on the reflected droplets dynamics. The computation of the spray wall impingement is started by preliminary simulating the heat transfer by natural convection between the hot surface and the surrounding air, before the spray injection, for a period of time reasonably comparable with the heating time of the aluminum plate by the thermal resistances. This allows considering the actual value of the temperature of the air surrounding the plate at the time of impingement.

Figure 5 shows the comparison between the experimentally collected and the numerically elaborated images of the spray impingement on a wall being at a temperature of 293 K at the instants of time of 700 and 1100 µs after SOI. Injection pressure is equal to 5.5 MPa. The Kuhnke's model better reproduces the droplets behaviour. Increasing the plate temperature to 473 K, as in Figure 6, one may note again a better performance of the Kuhnke's model, due to the effects deriving from the heat transfer occurring at the wall, which becomes more important. The heat transferred to the droplets from the wall gives a contribution to the latent heat of vaporization thus determining droplets secondary evaporation.

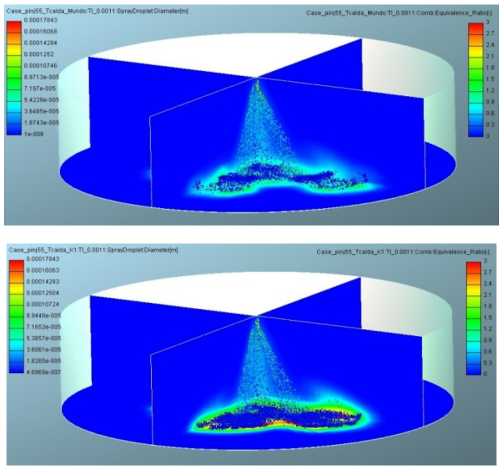

Figure 7. Spray and equivalence ratio distribution on three orthogonal planes as computed through the models by Mundo-Sommerfeld (top) and Kuhnke (bottom). T_w= 473 K.

Just to give an example of the weight of the transient heating, one may look at Figure 7, that represents both the

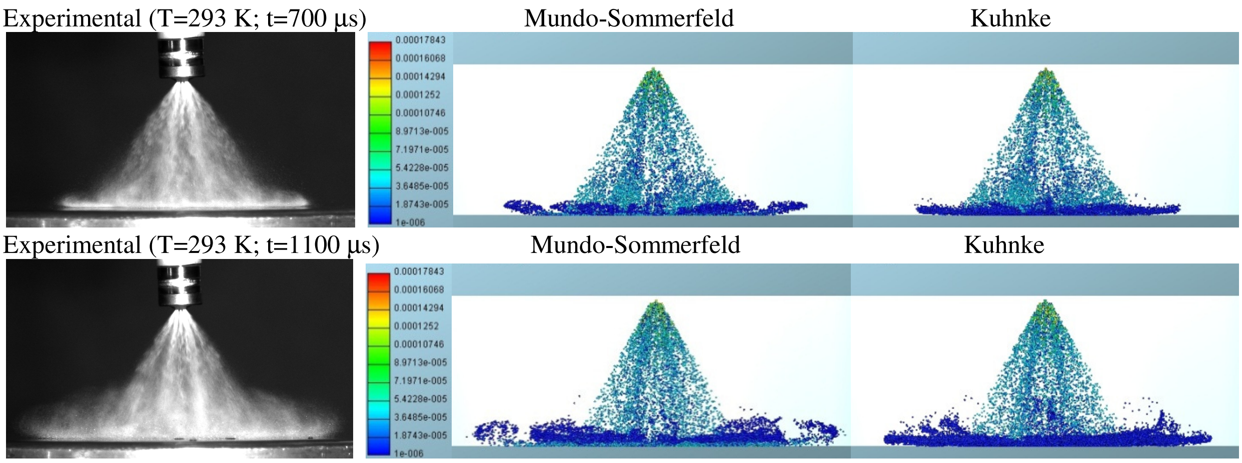

Figure 5. Experimental images of the spray (left) impinging on a plate being at T_w=293 K, at the instants of 700 µs (top) and 1100 µs (bottom) and as computed by the models by Mundo-Sommerfeld and Kuhnke.

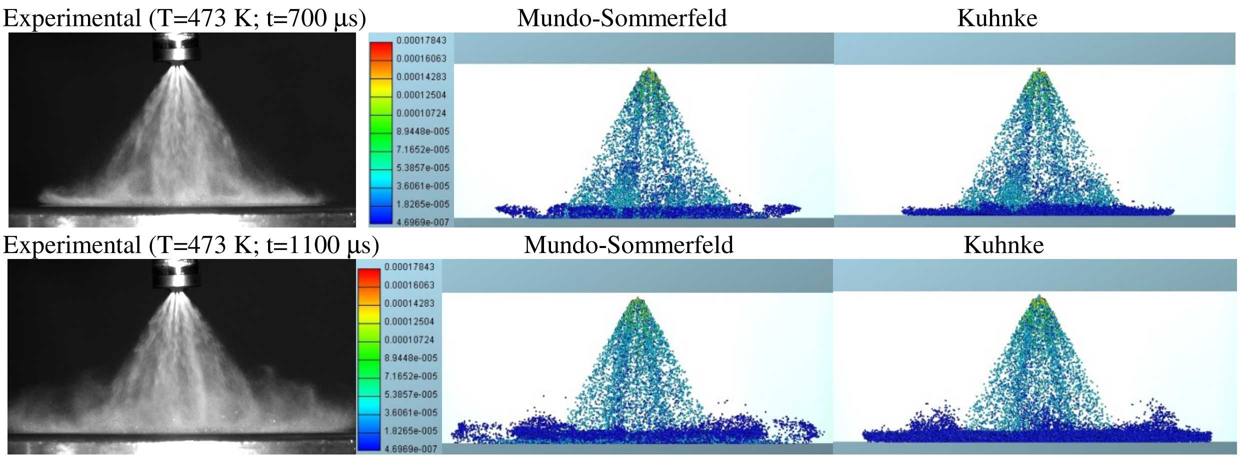

Figure 6. Experimental images of the spray (left) impinging on a plate being at T_w=473 K, at the instants of 700 µs (top) and 1100 µs (bottom) and as computed by the models by Mundo-Sommerfeld and Kuhnke.

ISBN: 978-1-61804-288-0

spray and the equivalence ratio distribution of the air-gasoline mixture on three orthogonal planes, one of which being the hot plate, at the instant of time equal to 1100 µs after SOI, as computed by the two models. The wall temperature is equal to 473K. A higher amount of gasoline in the vapour phase derives from considering the heating effect of the wall, according to the model proposed by Kuhnke. A measure of this can be assumed as the relative difference in the global equivalence ratio of the mixture, that reaches the 36% at the considered instant of time of 1100 µs after SOI.

The reliable prediction of both the dynamics of a free spray and the qualitative agreement of the simulation of the impact on both a cold and a hot wall prove the suitability of the two-phase flow sub-models of being included within a CFD model of the whole engine working cycle.

IV. EXPERIMENTAL CHARACTERIZATION OF A SINGLE-HOLE SPRAY IMPACT THROUGH SCHIELEREN TECHNIQUE

The second considered example is the impact of a single hole spray, whose analysis is effected through the schieleren technique.

A Magneti Marelli IHP-279 electro-injector is used, single-hole axially-disposed, 0.200 mm in diameter, nozzle length to diameter L/d=1 having a static flow of 2.45 g/s at 10.0 MPa and driven by the home-made ECU. An 80 mm diameter aluminum flat plate is positioned 22.5 mm downstream of the injector tip, orthogonally to the spray axis. The plate is heated in the range 298 – 573 K by electric resistances and controlled in temperature by a J-type thermocouple located in its center, 1.0 mm below the wall surface. A Watlow series 985 thermostatic system fixes and controls the temperature in a range of +/- 1 K.

The optical investigations are performed through an in-line schlieren set-up, whose schematic view is reported in Figure 8. The light, from a 1 mm blue LED (52 lumen), is firstly collimated using a 2 inches 200 mm focal length lens (L_1) and passes through the measurement volume, delimited by two quartz windows, 80 mm wide and 30 mm thick. A second lens (L_2), 500 mm focal length, focuses the light beam on the high-speed camera. A horizontal knife-edge is placed in the focus plane for the schlieren fulfillment. The diameter of the lenses realizes a 50 mm diameter parallel beam through the sample volume that is not tight fitting both the optical accesses and impingement plate diameters. The choice of the authors is to investigate half of the spray impact domain.

Images are captured by C-Mos high-speed camera (Photron FASTCAM SA4), 90 mm macro-focal lens, operating in external mode and synchronized with the injection event. The images are acquired on a 640x464 pixels window size with a time resolution of 80 ms. The resulting spatial resolution is 25.5 pixel/mm. Five consecutive events are acquired by the C-Mos camera for each injection condition for an evaluation of the jets spread.

Cycle-resolved images of the gasoline impact on the heated plate are stored on a remote computer for digital processing treatments to extract both the liquid and vapor contours. The explored conditions are 5.0, 10.0, 15.0 and 20.0 MPa as injection pressure, 473 and 573 K as wall temperatures, at 1.0 ms of nominal injection duration. Tests are conducted at ambient temperature and atmospheric backpressure of the gas in the vessel.

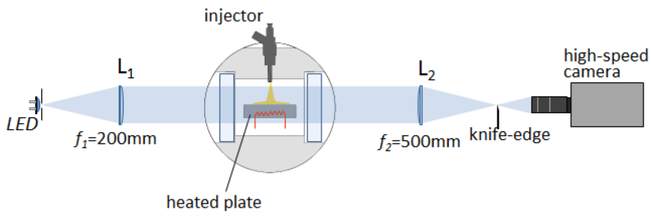

Figure 8. Schematic in-line schlieren set-up.

V. NUMERICAL SIMULATION OF A SINGLE-HOLE SPRAY IMPACT OVER A WALL

The results of the application of the free spray sub-model described in paragraph III to the here considered single-hole injector prove being less precise than in the previously considered cases of sprays generated by the multi-hole injector. Nevertheless, the numerically predicted spray penetration of 22.5 mm from the injector tip is reached at a time that is in good agreement with the experimentally measured one, as shown in Figure 9 for two different injection pressures. This allows having a certain confidence in the model prediction capability as the spray impacts on the wall.

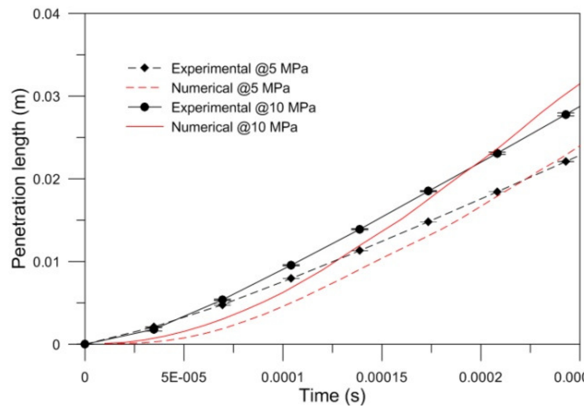

Figure 9. Comparison between the experimentally measured and numerically computed penetration length of the free spray for two injection pressures.

The evaporation sub-model is substituted with the multicomponent model described in ref. [20].

An example of the results suitable of being obtained through the numerical model in the simulation of the impact of the single hole spray is given Figure 10, which shows the comparison between the experimentally collected and the numerically computed images of the impingement on a wall being at temperature of 473 K at the instants of time of 240 (a), 500 (b) and 800 µs (c) after SOI.

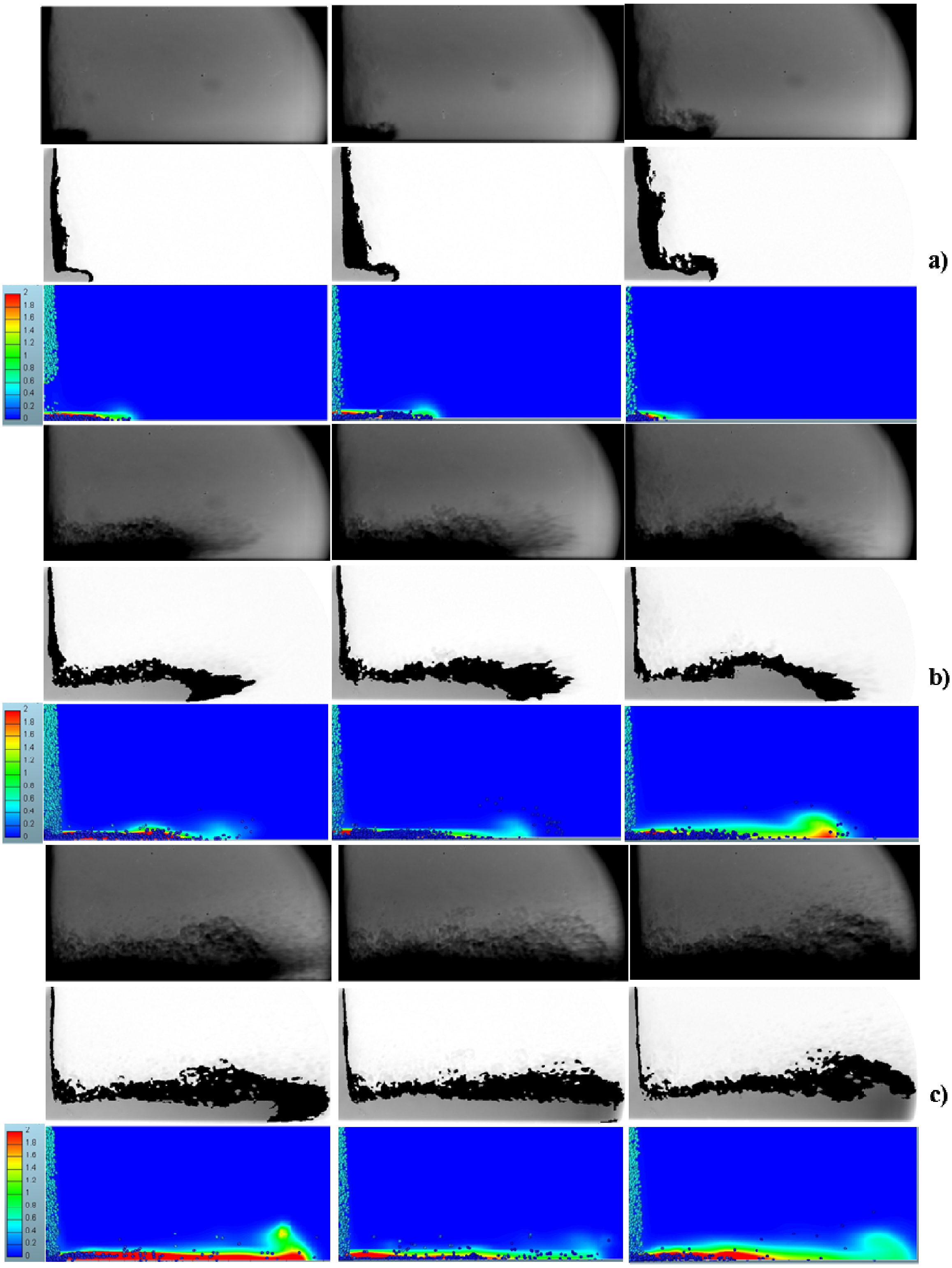

Figure 10. Comparison between experimentally collected (top), processed (middle) and numerically computed (bottom) images of spray impact. Numerical results are represented as the liquid droplet cloud and as distribution of the mixture equivalence ratio on a plane passing through the spray axis at T_w=473 K for 240 (a), 500 (b), and 800 ms (c) after SOI and for p_{inj}=10 (left), 15 (center) and 20 MPa (right).

More precisely, the experimental images (top) are represented, as they are collected and after the filtering procedure (middle), whereas the numerical images (bottom) represent the liquid droplets and the vapor phase distribution on a plane passing through the spray axis. Evaporation is the result of both the multi-component primary evaporation of gasoline and the secondary evaporation consequent the impact event. Injection pressure, along the columns, is equal to 10

ISBN: 978-1-61804-288-0

(left), 15 (center), and 20 MPa (right). The effects of the injection pressure on the experimental images are marked in moving from left (10 MPa) to right (20 MPa). At the same interval of time after SOI, the higher the injection pressure, the longer is the width penetration because of the increased velocity (and the component parallel to the plate surface) of the impacting droplets. The highest velocity of the spray produces a better atomization of the fuel bulk just at the nozzle exit section. In fact, the vapor phase diffusion at 240 ms is wider with increasing pressure, as it is in the free evolving phase (center and right of the figure). Furthermore, despite of a largest amount of injected fuel at 20 MPa the vapor phase increases prominently, with respect to the lowest pressure, due to a finest atomization consequent the highest impact velocity and to an easier vaporization. This reflects into a greatest amount of vapor and in a more complex fluid dynamic behavior with curls and bouncing. The history repeats at 500 and 800 µs with more intricate fluid dynamic behaviors due to a greatest multitude of impacting droplets. The numerical results correctly predict the experiments at 500 and 800 ms from the SOI and at the highest pressures while they tend to overestimate the penetrations at early stage of injection.

The Kuhnke's model is here properly adjusted. In particular, the heat penetration coefficient at the interface between the wall and the liquid, b, that is accounted for in the Wruck's assumption about the transient heat transfer, is calculated with reference to the aluminum properties. The following equation is employed:

$$b = \sqrt{k\rho c}\ , \tag{4}$$

where k is the thermal conductivity, r is the density and c is specific heat [21]. The Wruck's schematization considers both the wall and the droplets as semi-infinite media with respect to the instantaneous contact point. The heat transferred to the droplets from the wall contributes to the latent heat of vaporization and determines the secondary evaporation. The external contour of the computed vapor phase distribution is quite in a reasonable agreement with the one experimentally evaluated through the schieleren technique. The need of a proper use of the model proposed by Kuhnke is evident since the gasoline mass in the vapor phase, hence the vapor phase diffusion, may be underestimated in the case the model is applied in its default state. This clearly shows the importance of having at disposal reliable measurements of the vapor diffusion consequent the impact of a spray on a wall, that, indeed, are hardly realizable, especially under real engine operating conditions. At the injection pressure of 10 MPa, left side of Figure 10, the width of the vapor phase seems initially overestimated. At greater times, this quantity is instead underestimated because of the great influence of the deposition regime. This effect also influences the vapor layer height, which is lower in the numerical analysis. The model proposed by Kuhnke, indeed, is not yet optimized to account for the evaporation from the wall-film, thus indicating the need of its revision with respect to this aspect. Figure 10 also shows that increasing the injection pressure increases the vapor layer width, in agreement with the experimental findings and the expected behavior of an impinging spray.

A quantitative comparison between the experimentally measured and the numerically computed vapor width is reported in Figure 11 for the injection pressures of 10, 15, and 20 MPa and the wall temperatures of 473 (left) and 573 K (right). For p_{inj} = 10 and 15 MPa, an overestimation of the width at the early instants is depicted. Afterwards, there is a reversal behavior due to the high deposition regime, which slows down the vapor layer diffusion around 450 ms at T_w=473 K and 350 ms at T_w=573 K. Moreover, the curves show a more marked underestimation of the numerical results at the temperature of 573 K. Finally, at the highest injection pressure there is a better agreement between experimental and numerical results even starting from the early stages of the injection process.

Finally, the effects of the model assumptions, applied to the impingement at p_{inj} = 20 MPa, are reported in Figure 12 at 240 (a), 500 (b), and 700 µs (c) after SOI. The images depict a comparison between the experimental and numerical behavior of the impacting spray. Numerical images represent the liquid phase as the droplets cloud, and the vapor phase as equivalence ratio distribution on a plane passing through the spray axis. A good agreement appears up to 500 µs for the widths along the plate, while, at later times, an underestimation of the numerical results arises. The numerical tendency is to saturate the slip propagation and increasing the thickness, particularly in the final curl.

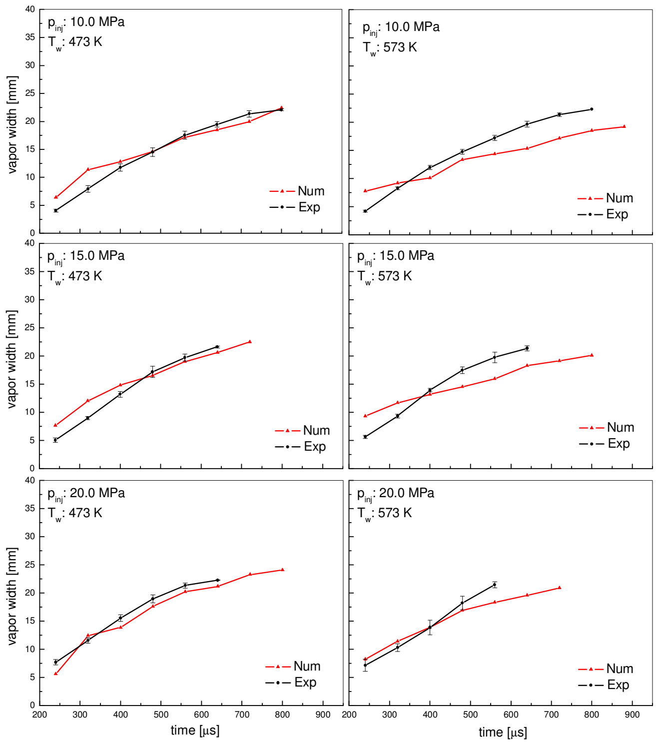

Figure 11. Comparison between experimental and numerical vapor width for 10, 15, and 20 MPa injection pressure and T_w = 473 K (left) and 573 K (right).

ISBN: 978-1-61804-288-0

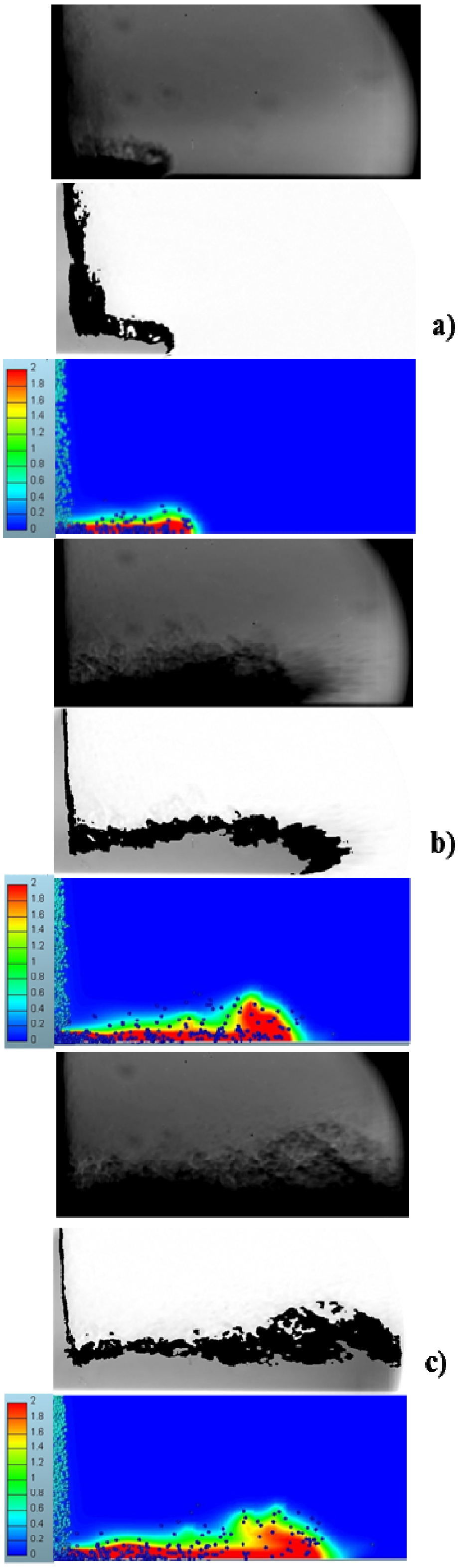

Figure 12. Comparison between experimentally collected (top), processed (middle) and numerically computed (bottom) images of spray impact at 240 (a), 500 (b), and 700 µs (c) after SOI for p_{inj}=20 MPa and T_w = 573 K. Numerical images show droplets and equivalence ratio on a plane passing through the spray axis.

Increasing the wall temperature from 473 to 573 K enhances the secondary evaporation, as shown in Figure 13, where the comparison between experimental data and numerical results relevant to the same injection pressure, 15 MPa, and time ASOI, 500 µs, at T_w=473 (left) and 573 K (right) is reported. Increasing the wall temperature has an effect on both the liquid phase, with much dispersed droplets, and on the vapor phase whose diffusion appears increased in both the directions orthogonal and parallel to the wall. The effect in the direction orthogonal to the wall is more evident.

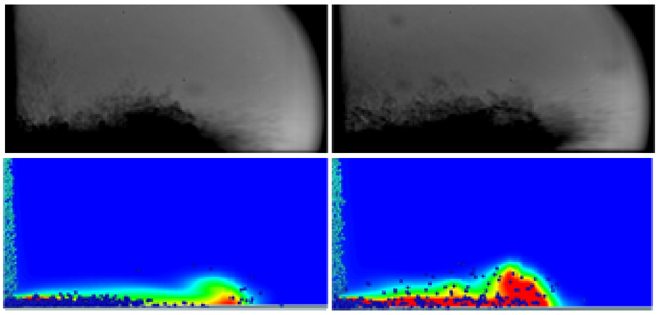

Figure 13. Comparison between experimentally collected (top) and numerically computed (bottom) images of the spray impact at 500 µs ASOI for p_{inj} = 15 MPa and T_w = 473 K (left) and T_w = 573 K (right).

VI. Conclusion

Multiple droplet impacts, liquid deposition over piston or cylinder walls, secondary atomization, heat transfer on spray impaction in GDI engines depend upon injection timing, that is the most essential engine operating parameter for mixture formation and combustion development. By simply varying time of injection, one may either realize homogeneous charges (stoichiometric or rich) either stratified charges, characterized by a rich zone around the spark plug and leaner zones towards the walls for an overall lean operation and lower heat losses at the liner. Injector requirements are however more stringent for stratified combustion to ensure that a combustible charge is properly prepared for ignition by the spark plug. A factor playing a relevant role in the mixture preparation is the spray impact on piston or cylinder walls, which may be intentional, as in wall guided systems, or unintentional and anyway such to create non optimal mixing of gasoline with air and to be an undesired source of pollutants. Present work considers the impact of both a GDI multi-hole spray and a single hole spray over a cold or hot wall. The collected data serve to evaluate the droplet behavior after impact, with the main aim of assessing a predictive numerical 3D CFD model suitable of being included within simulations of entire engine working cycles. Although a commercial software environment is used, the choice of the more suitable sub-models needs a careful comparison with experimental data relevant to engine like conditions.

Between available models the one proposed by Kuhnke reveals quite appropriate to reproduce the liquid rebounding

ISBN: 978-1-61804-288-0

and splashing and the secondary evaporation consequent the droplet transient heating. An underestimation of the vapor diffusion is however noticed in still air conditions, that, however, is believed to have a lower weight when actual engine operation is treated, due to the intense charge motion and the high level of turbulence intensity characterizing the operation of real engines.

REFERENCES

[1] R. W. Carling, “Predictive Simulation of Combustion Engine Performance in an Evolving Fuel Environment”, Sandia National Laboratories Report, 2010.

[2] J. B. Heywood, *Internal Combustion engine fundamentals*. New York: McGraw-Hill, 1998.

[3] C.Wang, H. Xu, J. M. Herreros, J. Wang, R. Crancknell, “Impact of Fuel and Injection System on Particle Emissions from a GDI Engine”, *Applied Energy*, vol. 132, pp. 178–191, 2014.

[4] Y. S. Shim, G. M. Choi, D. J. Kim, “Numerical and Experimental Study on Effect of Wall Geometry on Wall Impingement Process of Hollow Cone Fuel Spray under Various Ambient Conditions”, *International Journal of Multiphase Flow*, vol. 35, pp. 885-895, 2009.

[5] M. C. Drake, D. C. Haworth, “Advanced Gasoline Engine Development Using Optical Diagnostic and Numerical Modeling”, *Proceedings of the Combustion Institute*, vol. 31, pp. 99-124, 2007.

[6] N. Ashgriz Ed., *Handbook of Atomization and Sprays - Theory and Applications*, Springer, New York, 2011.

[7] A. L. N. Moreira, A. S. Moita, M. R. Panao, “Advances and Challenges in Explaining Fuel Spray Impingement: How Much of Single Droplet Impact Research is Useful?”, *Progress in Energy and Combustion Science*, vol. 36, pp. 554-580, 2010.

[8] J. D. Bernardin, I. Mudawar, “Transition Boiling Heat Transfer of Droplets Streams and Sprays”, *Journal of Heat Transfer*, vol. 129, pp. 1605-1610, 2007.

[9] W. Bosch, SAE Technical Paper 6607496, 1966.

[10] I. Wallace,., “Injection Rate Gauge: Pass Off Information and User Instructions”, Graz, 2002.

[11] M.Costa, U. Sorge, L., Allocca, “CFD optimization for GDI spray model tuning and enhancement of engine performance”, *Advances in Engineering Software*, 49, pp. 43-53, 2012.

[12] https://www.avl.com/web/ast/fire

[13] J. I. Ramos, *Internal Combustion Engine Modelling*, CRC Press, 1989.

[14] K. Y. Huh, A. D. Gosman, “A Phenomenological Model of Diesel Spray Atomization”, International Conference on Multiphase Flows, Tsukuba, Japan, 1991.

[15] P. J. O’Rourke, F. V. Bracco, “Modeling of Drop Interactions in Thick Sprays and a Comparison with Experiments”, IMECHE, London, 1980.

[16] N. Nordin, “Complex Chemical Modeling of Diesel Spray Combustion”, PhD Thesis, Chalmers University of Technology, 2001.

[17] J. K. Dukowicz, “Quasi-Steady Droplet Change in the Presence of Convection”, informal report Los Alamos Scientific Laboratory, Los Alamos Report LA7997-MS, 1979.

[18] C. Mundo , M. Sommerfeld, C. Tropea, “Droplet-Wall Collisions: Experimental Studies of the Deformation and Breakup Process”, *International Journal of Multiphase Flows*, vol. 21(2), pp. 151-173, 1995.

[19] D. Kuhnke, “Spray Wall Interaction Modeling by Dimensionless Data Analysis”, PhD Thesis, Technische Universität Darmstadt, 2004.

[20] G. Brenn, L. J. Deviprasath, F.Durst, “Computations and Experiments on the Evaporation of Multi-Component Droplets”, Proceedings 9th International Conference Liquid Atomization Spray Systems (ICLASS), Sorrento, 2003.

[21] N.Wruck, U. Renz, “Transient Phase-Change of Droplets Impacting on a Hot Wall”, Transient Phenomena in Multiphase and Multicomponent Systems: Research Report, pp. 210–226, 2007.

Permeability of Winding on the Bobbin Core

K. Adamek

Abstract— The paper deals with numerical flow simulation in permeable yarn winding of the defined shapes of bobbins. Permeability parameters are evaluated from permeability measuring on the real bobbins of various stiffness. The sensibility of the designed measuring device is sufficient for the given range of winding stiffness. The procedure can be automatized with storage of measured data for following evaluation of the whole winding process. The flow inside of the wound volume is explained by numerical flow simulation.

Keywords— **Numerical flow simulation, permeability, winding stiffness (winding density)**

I. Introduction

One of the standard methods for colouring of textile yarns consists in plunging a wound bobbin in dyeing bath and repeated reciprocal pushing-through of the bath from the bobbin axis direction through the perforated bobbin core, further through the wounded layer of yarns to the bobbin outer surface and vice versa. Of course, the flow resistance of such permeable layer of wound yarns depends on the layer density (stiffness) and on the layer thickness, too, which is different in the middle and at the faces of the bobbin shape. The result of such uneven flow could be an uneven intensity of coloration and further an uneven colouring of final product, for instance woven fabric, knitwork, etc.

A. Used Methods

Known methods of winding stiffness evaluation use the measuring of resistance force, for instance against the needle penetration into the wound yarn layer or against the rotation of flat needle, pushed in the wound yarn layer. Another method measures the resilience characteristics of falling testing body by the wound surface. The general disadvantage of results from such methods is the punctual measuring, only, containing the objective error of used measuring device (for instance mechanism friction, clearances) and subjective error of operator, too. For the determination of the average values of measured results it is necessary to make more measuring for each bobbin, together with statistical evaluation. It is known that such method needs many time and the variability of such results is considerable.

This work was supported by the Czech Grant No. NPU-L012.

K. Adamek is with VUTS Liberec, 46001, Czech Rep.; e-mail: karel.adamek@vuts.cz).

B. New Method

The principle of the proposed method exactly corresponds to the real procedure of said dyeing – the pushing the dyeing bath through the volume of wound yarn layer. The fluid flow through the permeable yarn volume is measured – in the stiffer wound layer the flow resistance is higher and the flow passage is lower. Using the same shape and dimensions of the wound bobbins, it remains the only one parameter – its permeability, depending on the winding stiffness. In the case when the outer dimensions of the winding (diameter, length) are not standard, the winding permeability is changing, too.
From practical reason the air is used instead water solution. The aim of the method is the relative comparison of permeability / stiffness of individual wound bobbins, not any absolute value. It is clear that the permeability of water is absolutely other than that for air.

II. Permeability

A. Permeability Measuring

A simple measuring device [1] was used for measuring the permeability of yarn layer wound at various stiffness, see Fig. 1. The air inlet is set at suitable pressure value measured by pressure gauge (1); the air flow is measured by flow meter (2). The perforated core (3) is closed by two plugs so that the air is flowing out through the yarn layer (4) wound on the core. The measured air volume is proportional to the real stiffness of the winding.

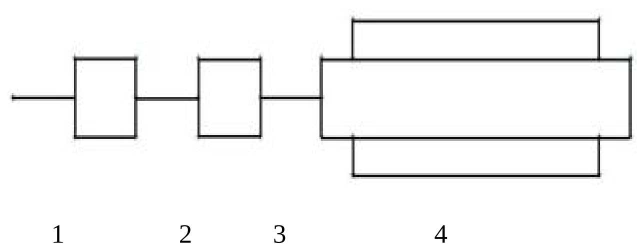

Fig. 1 Scheme of measuring device

For the defined range of stiffness, the presented method is sufficiently sensitive. The measured characteristics

$$V(m^3/h) = f\,(\Delta p(kPa)) \qquad (1)$$

for various possible stiffness of winding, see Fig. 2. For the soft bobbin (No. 1), there it is characteristic its higher flow, comparing with the hard one (No. 13).

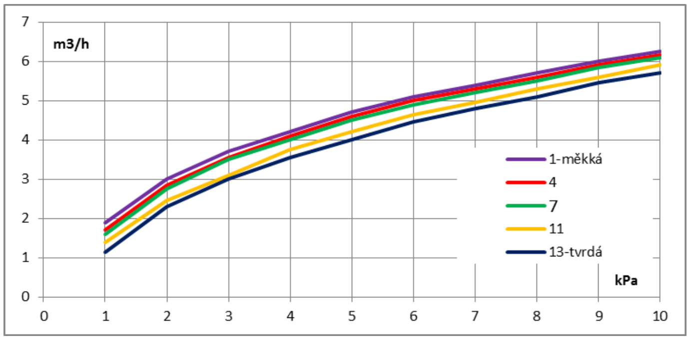

Fig. 2 Permeability of measured bobbin samples (1 = soft, 13 = hard)

B. Permeability Evaluation

The permeability of the observed layer is given by its flow resistance. After [2], [3] etc., this resistance consists from linear term, typical for instance for soaking at small velocities (so-called Darcy's law) and from quadratic term, typical for flows around bodies or through channels (Weissbach's or Moody's law)

$$\Delta p = C_2 \,.\, \rho/2 \,.\, tl \,.\, w^2 \; + \mu / \alpha \,.\, tl \,.\, w \qquad (2)$$

where

w = V/S (m/s)	flow velocity
V (m^3/s)	volume flow
S (m^2)	flow cross section
tl (m)	layer thickness
ρ (kg/m^3)	medium density
μ (m^2/s)	viscosity (for air 1,375e-5)
α, C_2	permeability parameters [3].

Two unknown permeability parameters α, C_2, depending on the layer structure, are necessary to determine. In a real permeable structure, there usually exists some combination of both such limiting cases (linear term, only or quadratic term, only).

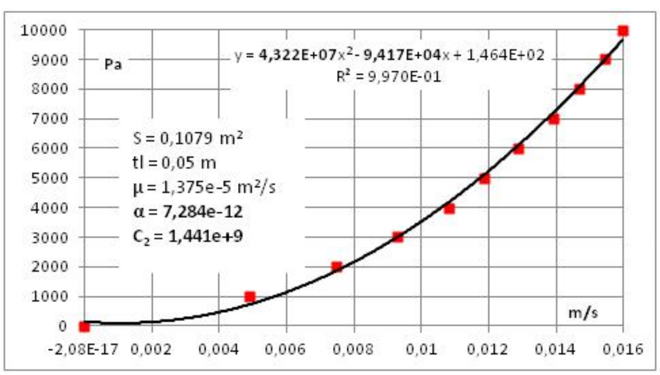

Fig. 3 Evaluated permeability (as an example)

From the measured characteristics V = f (Δp) in Fig. 2 it is necessary to create an inverse characteristic Δp = f (V) to get the equation formally corresponding with the above mentioned formula Δp = f (w, w^2) (2).

In Fig. 3, there is presented the resulting function (as an example), together with simple substitution by quadratic function [5]. The achieved correlation coefficient is very high (R^2 = 0.997).

Comparing the coefficients of linear and quadratic terms from Fig. 3 with the above mentioned formula (2) for pressure resistance it is possible to determine two unknown permeability parameters α and C_2 of the measured winding. The mentioned absolute term (here 146.6) represents the absolute error of measuring and of the used substitution. But for the used working pressure difference of 10 kPa it is negligible.

C. Model Description – one bobbin

For understanding of processes into the wound permeable volume during the flowing through it should be to use any suitable flow simulation.

For rotational geometry of the bobbin with central cavity it is appropriate to use an axis-symmetrical model and to use the transverse plane of symmetry as well. The two determined permeability parameters above should be used as a local "pressure jump" [3], while the flow resistance of the wound bobbin is uniformly distributed along and across the thick layer of the winding. So it is necessary to divide the volume of the permeable layer of wound yarns into more elementary layers in both radial and axial directions. In such a way, the volume is divided into many elementary volumes of elementary permeability.

The model geometry is designed after the real shape of the bobbin. In order to be able to use the suitable axis-symmetrical model, the core body should be designed with narrow radial gaps of equal cross-section, instead of rows of individual holes.

Meshing of such simple geometry is without problems, with smaller elements in narrow radial gaps. Defined boundary conditions are logical from previous description – pressure inlet/outlet at axial inlet/outer outlines or reverse, pressure jumps and axis. The solution is running without problems with good convergence.

Remark: In the real operation, there is used a dyeing liquid, but for this modelling it is used air. The principle of both solutions remains the same.

D. Results of the Simulation

The following serial of Figures shows the typical parameters of the flow field – velocity, pressure and streamlines. Using the planes of symmetry, there is displayed the upper half of the modelled area, only, the rotation axis is situated at the bottom of each Figure. Absolute values of observed flow parameters are not important here, in general the maximum value is red, the minimum is blue – the same as in the light spectrum.

The rotational axis is situated always horizontally down, due to save extent of the article, the only one (upper) symmetrical half of the model is outlined here. And more, one typical result is presented here, only, other solved cases give similar results.

The first set (Fig. 4 to Fig. 6) presents the result for the flow direction from the perforated core axis to the periphery; the

ISBN: 978-1-61804-288-0

second set (Fig. 7 to Fig. 9) is for the reverse flow direction, from the periphery to the axis. While the pressure field is really reversed, the field of the absolute value of the velocity and the streamlines field, too, seem to be the same.

In general, on both velocity and streamlines fields, it is visible the “short-circuit” flow between the axial inlet through the core axis and axial outlet through the side front of the winding, in both flow directions (from the axis to the periphery and on the contrary, too). In the middle part of the winding the flow is radial, unaffected by boundary conditions. At both faces of the wound body it is visible an expressive flow bend into the reverse direction. This result is very important for correction of designed measuring method after the Par. II-A. Firstly, the streamlines images (Fig. 6 and Fig. 9) show an important influence of faces boundary condition – in the middle part the flow is exactly radial, but at faces the flow is deformed. So the global measuring of the bobbin permeability should be replaced by measuring in the middle part, only.

Remark: The velocity scale is suppressed here, to get a more detailed velocity field in the volume of the winding. The flow in the core is not interesting here; the empty area means the higher velocity value in the axial tube (out of the used scale).
It is clear that a model with higher number of smaller volumes of elementary permeability gives better results, but the time of solution is increasing.

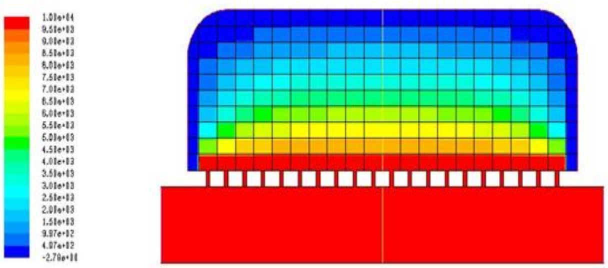

Fig. 4 Pressure field - flow from the axis (max.) to the periphery (min.)

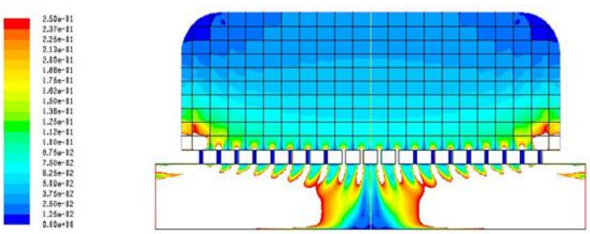

Fig. 5 Velocity field (suppressed scale) – flow from the axis to the periphery

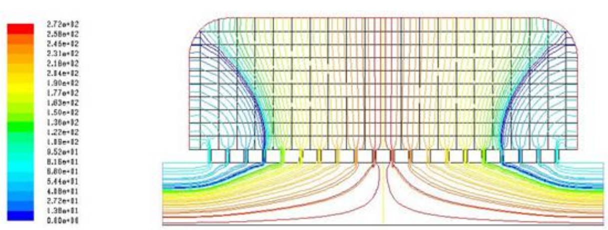

Fig. 6 Streamlines - flow from the axis to the periphery, „short-circuit“ flow at faces

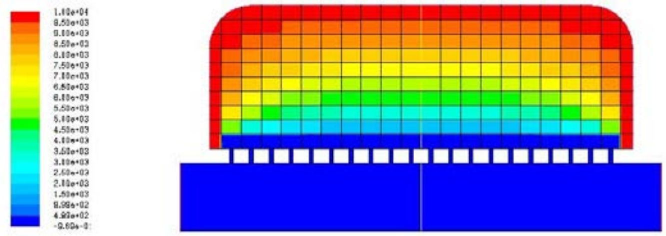

Fig. 7 Pressure field - flow from the periphery (max.) to the axis (min.)

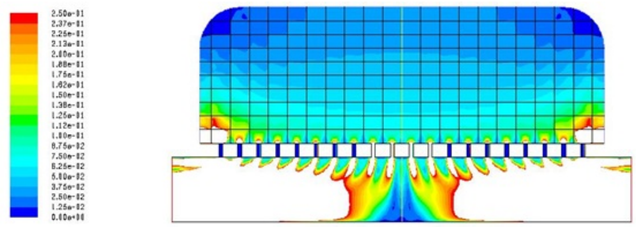

Fig. 8 Velocity field - flow from the periphery to the axis (suppressed scale)

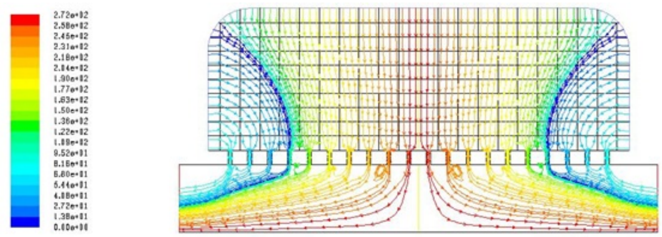

Fig. 9 Streamlines - flow from the periphery to the axis, „short-circuit“ flow at faces

The relative simple meshing together with standard procedure of standard commercial code make no problems as to the stability of convergence.

E. Suppression of short-circuits

The next set, Fig. 10 to Fig. 12, presents the simulation of the real situation in the dyeing tank, i.e. the flow in the relatively narrow gap between two adjoining bobbins, situated side by side as in real equipment. The rotation axis remains the same at the bottom of each Figure, left and right edge of each Figure is situated in the middle plane of symmetry. Without next investigation it is possible to say that such configuration could suppress partially the flow through front (side) faces of adjacent bobbins. Only one case is presented here – axial inlets are defined at the ends of cores, i.e. in the central part of the Figures, see the streamlines.

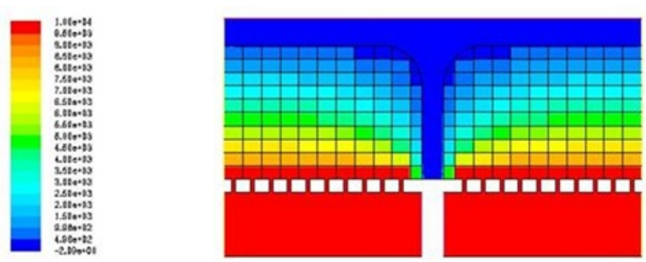

Figure 10. Pressure field in the gap between two adjacent bobbins

ISBN: 978-1-61804-288-0

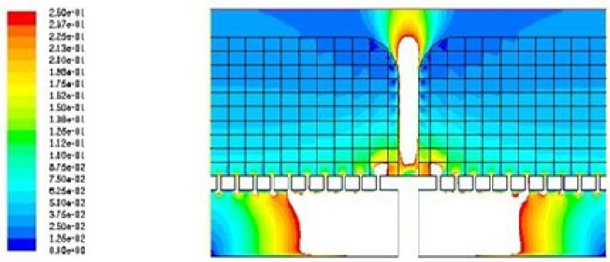

Figure 11. Velocity field between two adjacent bobbins (suppressed scale) – maximum outflow in the free gap (from side faces of both bobbins), not in the wound volume

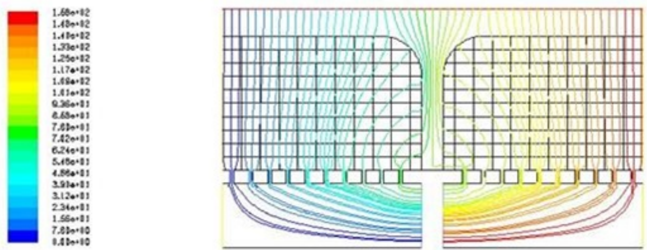

Fig. 12 Streamlines between two adjacent bobbins (flow from axis to the periphery, as in Fig. 6)

Comparing Fig. 12 (view on the gap between two halves of adjoining bobbins) with Fig. 6 (view on the one whole bobbin) we can state that the effect of the "short-circuit" flow is here suppressed a little.

Similar suppression could be made by any rigid radial partition between both bobbins, see for instance Fig. 13. In both cases the most streamlines remain radial, the axial deformations due to the short-circuit through frontal faces are suppressed, so we can state that conditions for uniform dying are kept in the major part of the winding volume.

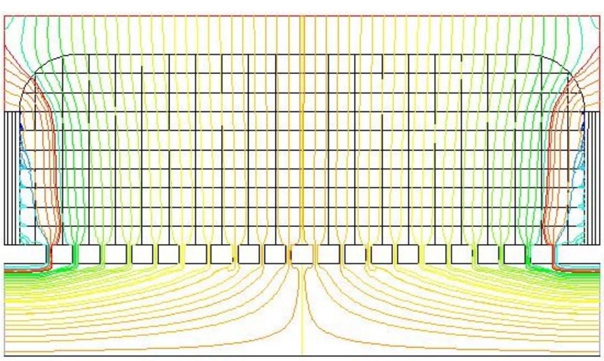

Fig. 13 Frontal partition suppressing the short-circuit flow

Another suppression could be made by blinding of several end orifices in the core body – see Fig. 14, where 0-1-2 orifices are shut and the flow velocity (m/s) along the radius (m) of the front face is more uniform, the effect of the short-circuit is suppressed.

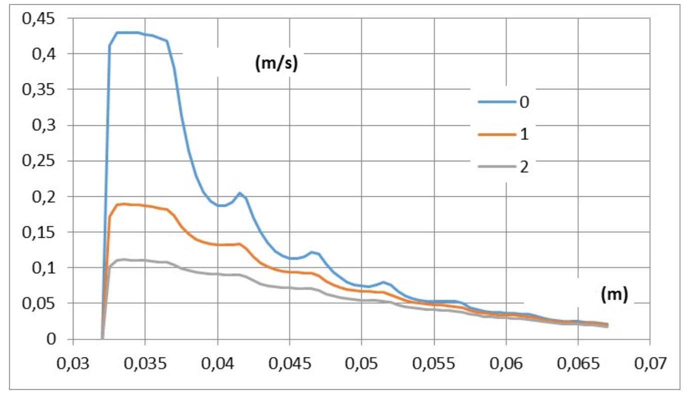

Fig. 14 Velocity suppressing at the frontal side of the bobbin by blinding of 0-1-2 rows of orifices in the perforated core

F. Situation in a real dyeing machine

The last model presents the situation in a real dyeing tank, where sets of four bobbins are situated in sequence. So we can state that such configuration makes some suppression of short-circuit flows, as mentioned on the Fig. 10 to Fig. 12 above. This set of Fig. 15 to Fig. 17 presents fields of velocity, pressure and streamlines of such configuration – the flow direction from axis to the contour, only, as on the Fig. 4 to Fig. 6.

At first we can state that the cross-section of the common inlet is sufficient, it allows the uniform flow distribution in all four bobbins.

At seconds, small gaps, only, between front faces of adjacent bobbins achieve some suppression of short-circuit of the flow through front faces. It is important for more uniform flow through the winding volume.

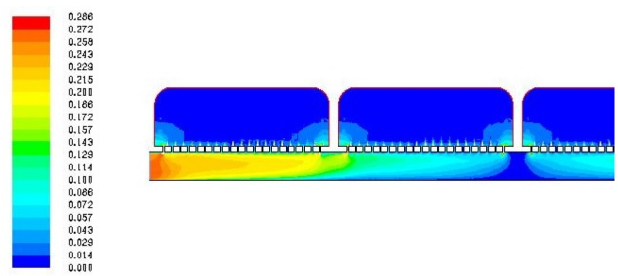

Fig. 15 Velocity field in configuration of four bobbins

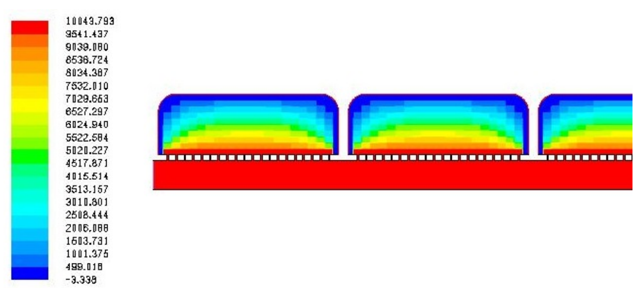

Fig. 16 Pressure field in configuration of four bobbins

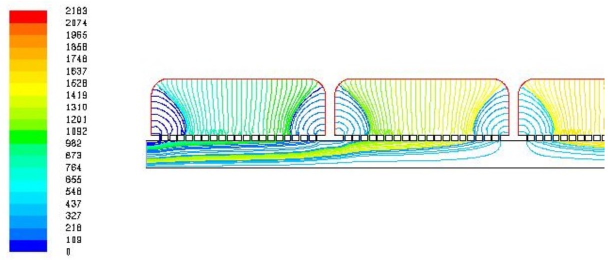

Fig. 17 Streamlines in configuration of four bobbins

Evaluating the received results of numerical flow simulation we can state that the common inlet is well dimensioned, in each of four bobbins just one quarter of the whole flow is flowing, small deviations are due to numerical error of the simulation.

But the flow distribution in each bobbin volume is very non-uniform – the volume flow through the front faces is very high, 230% approx. of the average flow and the flow through the radial periphery is 43%, only of the average flow. So the dyeing time must be longer, corresponding to this lower flow, to get uniform coloration of the whole bobbin volume. Some "overdyeing" is not possible, the textile material can be saturated, only, by coloring agents, not “oversaturated”.

G. *Uneven stiffness of wound layer*

On the really wound yarn layer the uneven stiffness (permeability) can be observed. Even if the yarn brake effect remains the same, the inner layer on the small radius receives higher density (stiffness) comparing with the outer layer on the bobbin contour. The effect of such phenomenon is simulated, too, results are as follows:

Fig. 18 presents different flow resistances for hard – medium – soft bobbin.

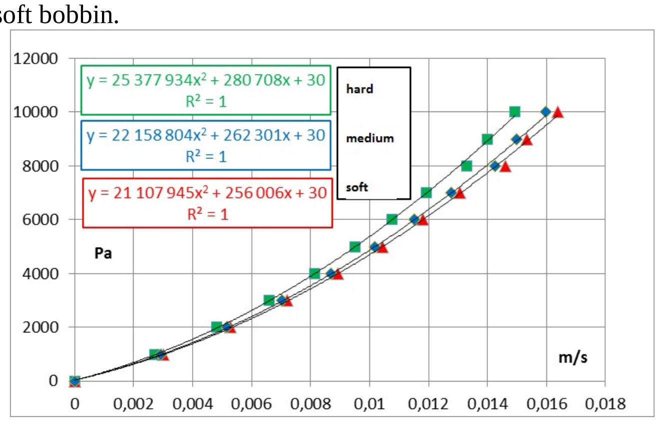

Fig. 18 Different flow resistance for hard – soft bobbin

Using such different parameters on three radial layers we can state that differences of the flow are not important, see the Tab. 1.

Tab. 1 Relative flows at various winding stiffness

	inlet	outlet		
winding	core	front	arc	periphery
	%			
const soft	100,0	47,0	7,2	45,7
const med	97,6	45,9	7,1	44,6
const hard	91,2	42,9	6,5	41,7
stepped	98,9	47,2	7,1	44,5

As an illustration, only, the Fig. 19 presents the velocity field for comparison with previous results - here at different scale, but very similar character. Other flow field parameters are very similar to previous, too, so they are not presented here.

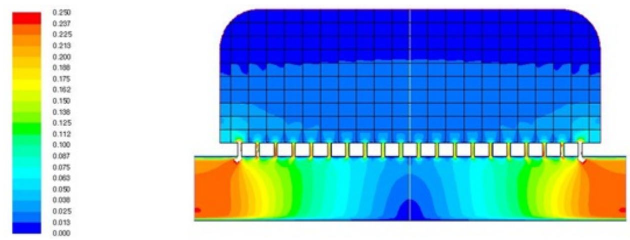

Fig. 19 Velocity field in the winding of three layers of different permeability in radial direction

III. Conclusion

The proposed method [1] of air permeability measuring for the testing the stiffness of the yarn layer wound on the perforated core is simple and reliable, suitable for serial operation with automated manipulation and data storage. And more, using any simple marking of individual bobbins it is possible to determine retroactively the reason of found defective stiffness of wound bobbin (working unit, yarn brake etc.).

The presented method of the numerical flow simulation, for instance [4], gives a good overview about the flow through the yarn layer wound on the perforated core and about the uniform dyeing of yarn material, too. Finally, for the real operation, in such a way, there could be tested the optimal results of such simulations, only. In this way, the costs of development are reduced and the results can be directly used in a real plant.

In general, the numerical flow simulation can predict the influence of any inserted obstacle /partition at the bobbin front face on the more uniform flow through the winding, without necessary experiments. It remains to judge the positive effect of the uniform flow and the uniform dyeing of wound yarn layer, too, contrary to the higher manipulation requirements when preparing a system of bobbins for dyeing.

The density (permeability) of the wound layer can be non-uniform in radial direction, so the flow penetration can be affected. This influence can be simply simulated, but real values of permeability must be defined by measuring. Flow ratio for soft/hard bobbin is 1.1 approx. and is well detected by designed method of permeability measuring.

ISBN: 978-1-61804-288-0

ACKNOWLEDGMENT

Our acknowledgment is given to VUTS Liberec – Centre for Development of Machinery Research, for the support of this development in the framework of the grant NPU-L02.

REFERENCES

[1] K. Adámek, "Device for classification of winding stiffness", Czech patent. No. 304933, Dec. 17, 2014
[2] O. Maštovský, *Fluid Mechanics*, SNTL Praha, 1963 (in Czech)
[3] Software Fluent, v. 6.3.26.
[4] K. Adámek, "Permeability of Textile Layers", XVIth Int. Conf. Applic. of Exp. and Numer. Meth. in Fluid Mech. ŽU Žilina, 6 p., 2008 (in Czech)

Methodology framework for surface shape evaluation

Cupar A., Kaljun J., Pogacar V., and Stjepanovic Z.

Abstract— This paper treats interdisciplinary topics for alternative surface analysis and its evaluation. Analysis methodology and its results can be used in design and styling to tell us what kind of surface shapes are present. Advanced graphical algorithm tool Grasshopper® (GH) is used to build analysis procedure. Several new introduced approaches are used and briefly presented. A framework of simplified classification is also presented, where similarity with color valuation can be seen. GH's procedure builds quite complex bundle of components and connections therefore just major steps in this algorithm are explained.

Keywords— analysis, design, methodology of surface evaluation

I. Introduction

A SURFACE of designed object is the communication language that interacts with users. This framework of methodology that analyses existing products is a great tool for numerical shape evaluation. Furthermore the analysis can be used to achieve products with well styled and designed surface. The procedure and its practical use is presented in following chapters.

Different practical exams are shown in this chapter. First the fundamental surfaces are analyzed. Analysis of two real objects follows. The results and discussions related to the analysis using the developed shape evaluation procedure are included into this chapter.

II. Theoretical part

A. Review of related works

Shape usually starts with simple curve and furthermore with 2D drawing as described in [1] and [2]. This 2D drawing impacts 3D shape of an object. In the FIORES project [3]-[8] mayor researchers proposed several terms for styling properties and features in CAID. By means of questions and observation of communication between stylists and engineers, a list of terms that describe the styling properties was composed. These are:

- Radius/Blending
- Convex/Concave
- Tension
- Straight/Flat
- Hollow
- Lead in
- Soft/Sharp
- S-Shaped
- Crown
- Hard/Crude
- Acceleration [3]-[8]

Some of these terms for specific properties are very similar or unclear and need to be refined. Therefore we tried to simplify them into a new classification.

Interesting classification of relative distances (RD) and directional fragmentation (DF) of 2D boundary shapes was presented in [9]. Method uses property that different shapes have different combinations of RD and DF. Shape presentations of different rooms, cities and states were used in experimental part. Several other classification methods were presented in [9] but mostly for 2D shapes.

Methods for analysing aesthetic impression of curves have already been developed. Considering Harada [10] are those curves parts of logarithmic graphs. Graph curvature in dependence of path – K(s) and K-vector in logarithmic curvature histogram (LCH) were observed. Aesthetic curve was defined as a curve whose LCH is a straight line. Authors in [11] used this method to determine objects' impression. They provided CAD system which can *feel* the same impression on curved surfaces like human designers can. On the base of LCH they proposed three types of surfaces by human impression: convergent, divergent and neutral. They observe some Japanese objects and conclude that they have convergent impression and European objects divergent impression. According LCHs five general classes for aesthetic curves were proposed: minus, zero, plus, plus-minus and minus-plus [10]. Other authors in [12] have also observed and analysed spatial aesthetic curve segments. They created graphs K(s) and LCHs of those curves. Author Yoshida evaluated aesthetic curves, which can be considered as a generalization of the Clothoid, the logarithmic spiral, the circle involute, and the circle in [13].

B. Methodology

Methodology of surface evaluation is developed to establish the meta-language in design communication which was perceived as necessary part of styling in [3]-[8]. The first step is analysis of existing geometry and the second is synthesis of newly created geometry considering desired property.

Early stage of classification of surfaces has already been proposed in [14]. Furthermore the classification was changed to be simpler and more logical and is still under development.

Five classes are now shrunken into three properties that are characterising surfaces similar as colours in color space [15],

ISBN: 978-1-61804-288-0

where each colour is presented as a mix of values L*, a* and b*. Our geometrical space consist of these three axes:

- Curvature – **C**
- Symmetry – **S** and
- Substantialness –**B**

Therefore a surface is indicated as (C, S, B), where curvature goes from – to + sign. Zero determinates neutral curvature and means plane. Negative values mean concave surface and positive values are for convex surfaces. They are evaluated with sign and values of entities in nxn matrix. Value is calculated as arithmetic average of normalized nxn distances including preposition sign.

Symmetry takes just positive values. Zero means perfect symmetry of a surface observed over middle column of nxn matrix. Symmetry can be detected as differences between entities pairs compared over middle column. The first and last column are compared and second and the last but one. The middle one stays untouched in this case. Symmetry is calculated as arithmetical average of all entity pairs.

Substantialness is third property to indicate size or width of the surface. We have had discussions about this property name because terms are limited and it is not easy to take the proper one. Terms "solid" and "slim" were also in discussion but we take substantialness because it describes property better. It is calculated as ratio between length and width of the observed surface projected on triangular plane.

1) Grasshopper's procedure

Grasshopper® (GH) is a graphical algorithm tightly integrated with 3D modelling tool Rhinoceros (RH). Grasshopper is an add-on and runs within the RH application. Procedures are created by dragging components onto a canvas as presented in figure 1. Outputs of these components are then connected to the inputs of subsequent components. Grasshopper is mainly used to build generative algorithms and it acts like a programming tool. Many of Grasshopper's components create 3D geometry. Procedures may also process other types of algorithms including numeric, textual, audio-visual or haptic applications.

GH is used because of complex algorithms that can be used out of the box and can be easily connected and combined.

First we have to explain prefix "nxn". Nxn comes from GH procedure where 5x5 point grid is used to define number of intersections. N has to be odd number and can be changed from

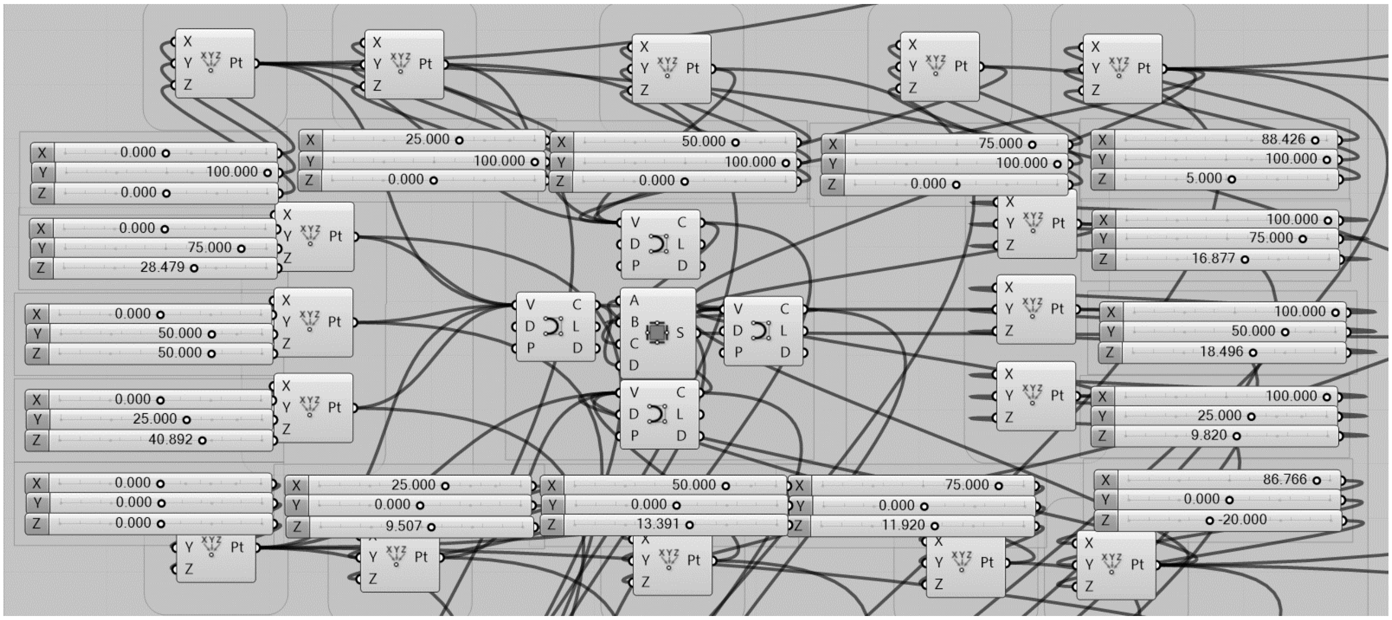

Fig. 1 Small fragment of GH canvas and nxn procedure.

3x3 up. But to show fundamental functionality the grid 5x5 shows enough details therefore whole nxn procedure basis on 5 by 5 points.

GH nxn procedure is a new approach in surface evaluation. It became quite complex bundle of components and connections. Therefore is hard to show whole procedure in one view. One fragment of GH procedure is shown in figure 1. This part defines four bounding curves which build Coons patch surface hereinafter. This "synthetic" surface is then evaluated in nxn analysis core.

Furthermore curvature graph K(s) and LCH on selected curve on surface can be calculated and presented. Practical use of those graphs is shown in experimental part hereinafter. K(s) and LCH charts are already known [10]-[13] and are here used for fair curve evaluation. Some more analyses are shown in [16]. Curvature is analyzed and shown on several practical examples.

GH nxn procedure requires input geometry as synthetic surface, mesh or imported NUBS surface. From type of input geometry depends how GH procedure starts. Analysis core stays the same. Short preview of steps for surface shape evaluation in GH nxn procedure is shown in table 1. Several logical steps are present where every following step has an input of one or more previous components. Hereinafter are shown graphical results of GH nxn procedure.

Table 1 Short preview of steps for shape evaluation in nxn procedure.

Step 1:	Input geometry	Synthetic surface or	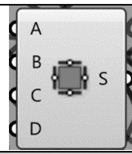
		Imported 3D mesh or	
		Imported NURBS surface.	
Step 2:	Triangle plane through point A, B and C.		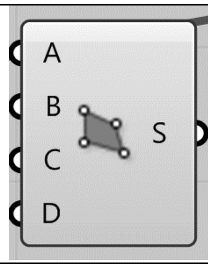
Step 3:	Projection of input surface on triangular plane.		
Step 4:	Offset of projection on both sides.		
Step 5:	5x5 points segmentation on offsets.		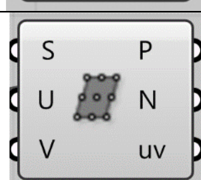
Step 6:	Lines through segmentation points.		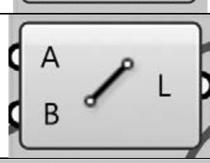
Step 7:	Creating points on intersections of lines with input surface and lines with planar surface.		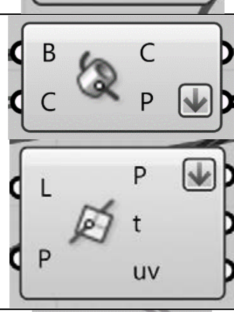
Step 8:	Nxn vectors starting at intersection points on triangular plane and ending at intersection points on input surface.		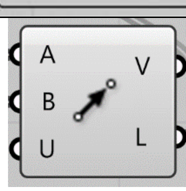
Step 9:	Nxn matrix of lengths and directions of nxn vectors.		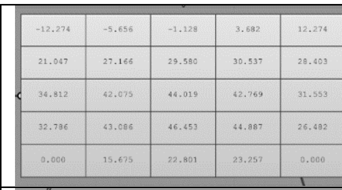 -12.274 · -5.656 · -1.128 · 3.682 · 12.274 21.047 · 27.166 · 29.580 · 30.537 · 28.403 34.812 · 42.075 · 44.019 · 42.769 · 31.553 32.786 · 43.086 · 46.453 · 44.887 · 26.482 0.000 · 15.675 · 22.801 · 23.257 · 0.000
Step 10:	Normalized lengths and directions of nxn matrix.		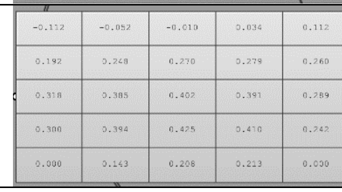 -0.112 · -0.052 · -0.010 · 0.034 · 0.112 0.192 · 0.248 · 0.270 · 0.279 · 0.260 0.318 · 0.385 · 0.402 · 0.391 · 0.289 0.300 · 0.394 · 0.425 · 0.410 · 0.242 0.000 · 0.143 · 0.208 · 0.213 · 0.000

a) Step 1

Three types of input geometries are acceptable.

First is synthetic surface, generated with part of our GH procedure. This part of procedure is shown in figure 1. Surface is defined with four bounding curves. Every curve is defined with five points. Each point has three coordinates that can be manipulated. It is important to make proper smooth surface which is not overlapped or wrinkled.

Second input is mesh that can be obtained, inter alia, with 3D scanner. The so called nxn frame has to be defined first. The nxn frame determines observation area of the mesh and has to be defined manually in this analysis.

Further steps present analysis core of GH procedure hereinafter that is same for any type of input geometry.

b) Step 2

Through points A, B and C is defined triangular plane presented in figure 2. This triangle also defines direction of the surface. Considering Podehl [5] are natural directions from bottom to top and from left to right. In this framework the direction is determined manually and should present orientation of the surface in space according products use.

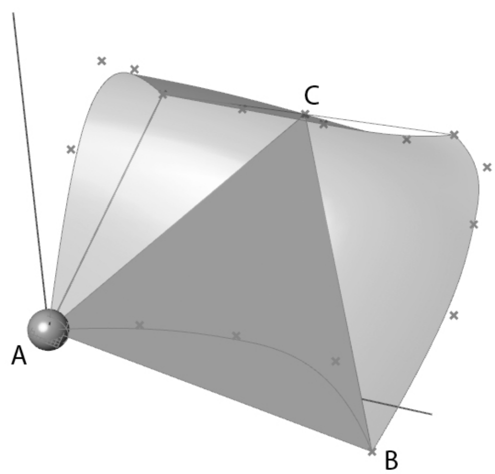

Fig 2 Triangular nxn plane defined with point A, B and C which shows natural direction of analyzed surface "UP".

Distance from point A to point C is also defined as nxn length used for distances normalization hereinafter. Point A and B are placed at the corners of the bottom edge of the surface. Point C is in the middle of the line that connects upper

ISBN: 978-1-61804-288-0

corners of the surface as explained in figure 2.

c) Step 3

Surface is projected on the same plane as triangular nxn plane lies. The planar nxn surface projection is created as shown in figure 3 marked with darker color.

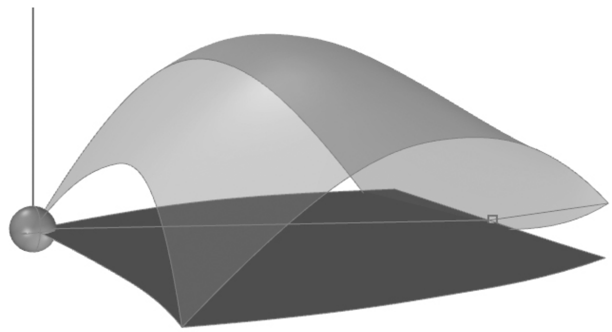

Fig 3 Surface is projected on the same infinite plane as triangular nxn plane lies.

d) Step 4

There are created two offsets on each side of the planar surface projection as figure 4 shows. Distance of both offsets can be changed and should be far enough not to intersect the analyzed surface.

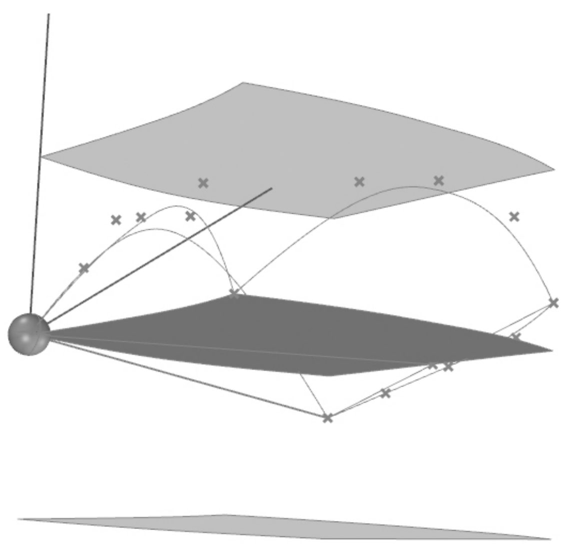

Fig 4 Two offset on each side of projected surface are created.

e) Step 5

This step provides surface segmentation with point grid 5 by 5 points on both offsets shown in figure 5.

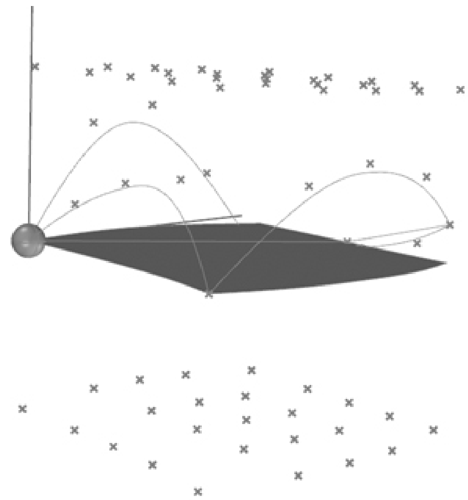

Fig 5 Both offset surfaces are segmented with 5x5 points.

f) Step 6

Point on both offsets are paired and connected with parallel lines with starting points on one offset and ending on other.

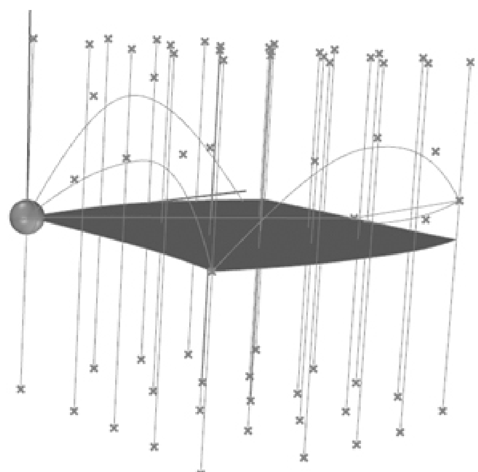

Fig 6 Segmentation points are connected with lines.

g) Step 7

Intersection points between lines and analyzed surface are marked in step 7. Similar are marked intersection points on planar projected surface.

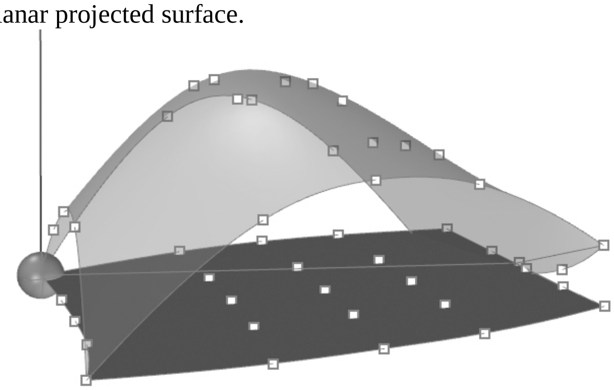

Fig 7 Intersection points between lines and analyzed surface are created and intersection points between lines and projected planar surface are created.

ISBN: 978-1-61804-288-0

h) Step 8

In step 8 a vector field is created. Vectors have starting points at projected planar surface and ending points at intersection points on analyzed surface. Vectors are used because they have direction that is important to correctly determine curvature of surface. This direction is considered furthermore as positive or negative sign of value in nxn matrix.

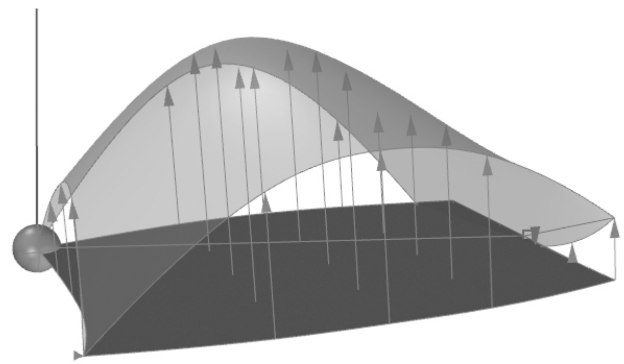

Fig 8 Vectors are connecting intersection points.

i) Step 9

The results of nxn analysis as actual distance with preposition sign are shown in table 2. Negative sign of the value means that the vector shows down. Or with other words; the surface lies under the nxn triangular plane. Table 2 presents analysis for the surface shown in figure 3, 7 and 8.

Table 2 The results of nxn analysis as actual distances with preposition sign.

-12.274	-5.656	-1.128	3.682	12.274
21.047	27.166	29.580	30.537	28.403
34.812	42.075	44.019	42.769	31.553
32.786	43.086	46.453	44.887	26.482
0.000	15.675	22.801	23.257	0.000

The nxn matrix also follows natural directions and is not the same as in mathematical writing. It has swapped rows over middle row. So the matrix starts with entry (0,0) at bottom left corner as shown in form (1).

$$\begin{bmatrix} a_{n-1,0} & \cdots & a_{n-1,n-1} \\ \vdots & . & \vdots \\ a_{0,0} & \cdots & a_{0,n-1} \end{bmatrix} \qquad \text{Form (1)}$$

Starting point marked with (0,0) is at the bottom left side on analyzed surface, same as in nxn matrix. This enables to locate position of same point in 3D space and in nxn matrix.

j) Step 10

Table 3 The results of nxn analysis as normalized distances with preposition sign.

-0.112	-0.052	-0.010	0.034	0.112
0.192	0.248	0.270	0.279	0.260
0.318	0.385	0.402	0.391	0.289
0.300	0.394	0.425	0.410	0.242
0	0.143	0.208	0.213	0

Nxn matrix collects normalized values of distances, combined with directions. Normalized means that every nxn distance is divided by value of nxn length. Nxn length is shown in figure 2 as distance A-B. With normalization the size of an object is irrelevant. Entities (0,0) and (0,4) have always value 0. All other values can be positive or negative depending of the analyzed surface.

III. EXPERIMENTAL PART

Different examples are shown in this chapter. First the fundamental surfaces are analyzed. This synthetic surfaces are created with procedure, shown in figure 1. At the end are two applicative cases. First is analysis of headlight of a car.

A. Fundamental surfaces

Some fundamental synthetic surfaces are shown in this chapter. Appropriate vectors were created with nxn procedure as shown in figures 11 to 14. Numerical result are shown in tables 4 to 6. Negative sign means the direction of vector downwards (-Z). Values for C,S and B numerical results are marked with bold text.

1) Plane

Analysis of not curved synthetic surface gives an nxn matrix with zeroes while there are no vectors to create. Boundary points have all Z coordinate zero. All points are equally arranged in X and Y direction in steps: 0, 25, 50, 75 and 100 units and have appropriate coordinates.

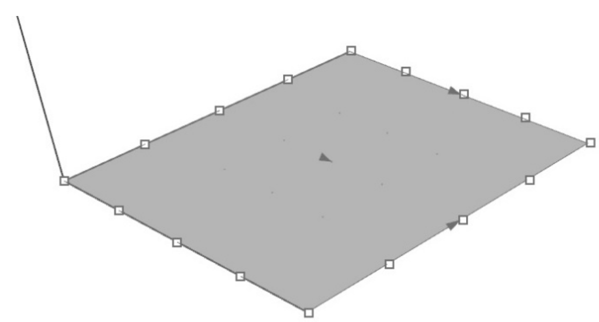

Fig 10 Synthetic plane.

Table 4 The results of nxn analysis as actual distances with preposition sign.

0.00	0.00	0.00	0.00	0.00
0.00	0.00	0.00	0.00	0.00
0.00	0.00	0.00	0.00	0.00
0.00	0.00	0.00	0.00	0.00
0.00	0.00	0.00	0.00	0.00

C= 0
S= 0
B= 100

ISBN: 978-1-61804-288-0

2) Simple symmetrical convex surface

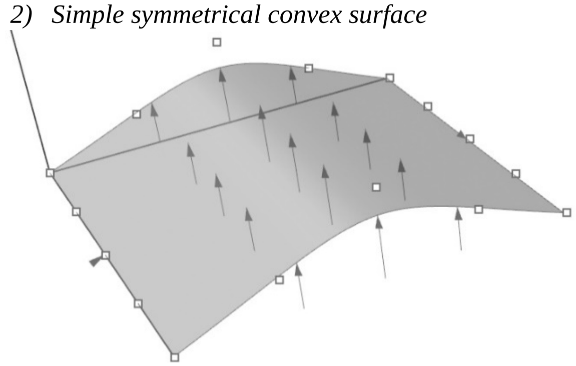

Fig 11 Simple synthetic symmetrical convex surface.

Table 5 The results of nxn analysis as actual distances with preposition sign for convex surface.

0.00	0.00	0.00	0.00	0.00
0.11	0.11	0.11	0.11	0.11
0.16	0.16	0.16	0.16	0.16
0.11	0.11	0.11	0.11	0.11
0.00	0.00	0.00	0.00	0.00

C= 7,6
S= 0
B= 100

3) Simple symmetrical concave surface

Simple symmetrical concave surface was created as shown in figure 12.

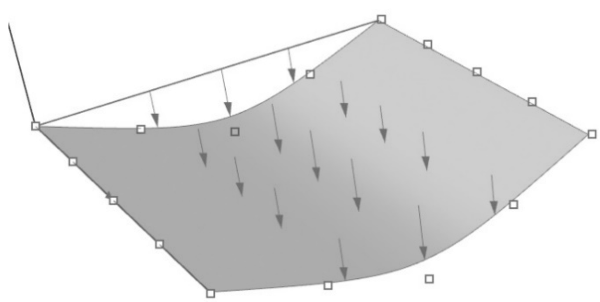

Fig 12 Simple synthetic symmetrical concave surface

Table 6 The results of nxn analysis as actual distances with preposition sign for concave surface.

0.00	0.00	0.00	0.00	0.00
-0.11	-0.11	-0.11	-0.11	-0.11
-0.16	-0.16	-0.16	-0.16	-0.16
-0.11	-0.11	-0.11	-0.11	-0.11
0.00	0.00	0.00	0.00	0.00

C= -7,6
S= 0
B= 100

4) Two directional symmetrical concave surface

Figure 13 shows concave surface bended in two directions (X and Y).

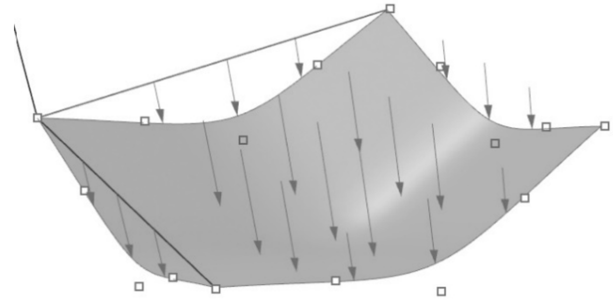

Fig 13 Synthetic two directional (X and Y) symmetrical concave surface.

Table 7 The results of nxn analysis as actual distances with preposition sign for two directional concave surface.

0.00	-0.11	-0.16	-0.11	0.00
-0.11	-0.22	-0.27	-0.22	-0.11
-0.16	-0.27	-0.31	-0.27	-0.16
-0.11	-0.22	-0.27	-0.22	-0.11
0.00	-0.11	-0.16	-0.11	0.00

C= -15,21
S= 0
B= 100

5) Inflection surface

Synthetic inflection surface has positive vectors in one direction and negative in other direction as shows figure 14.

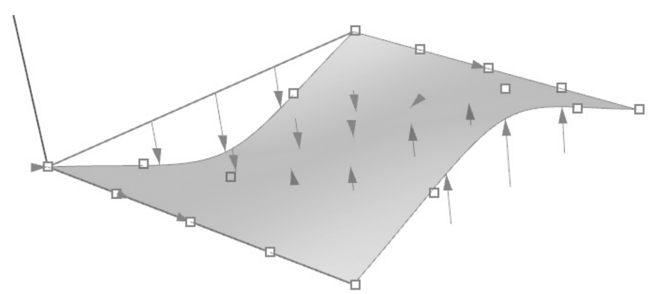

Fig 14 Synthetic inflection surface has vectors in positive and negative direction.

Table 8 The results of nxn analysis as actual distances with preposition sign for inflection surface.

0.00	0.00	0.00	0.00	0.00
-0.11	-0.06	0.00	0.06	0.11
-0.16	-0.08	0.00	0.08	0.16
-0.11	-0.06	0.00	0.06	0.11
0.00	0.00	0.00	0.00	0.00

C= 0
S= 200
B= 100

B. Real 3D scans

Two real objects were 3D scanned are analyzed with nxn procedure in this section. First is the front headlights surface and second is tail of a sports car. Nxn matrix, K(s) and LCH are shown in both cases. Sports car hood was reverse engineered with Rhinoceros add-in T-splines. This add-in

ISBN: 978-1-61804-288-0

enables A-class surfaces creation that are very important in product design to achieve good looking design.

a) Front headlights surface

Figure 15 shows scan of a real object. The classification is still under development therefore a table 9 will be explained and not token as an absolute result. The surface is more extended inwards on the right side, therefore are in the most right column negative values. The surface shows convexity in the lower middle side because there are the highest values, marked with gray in table 9.

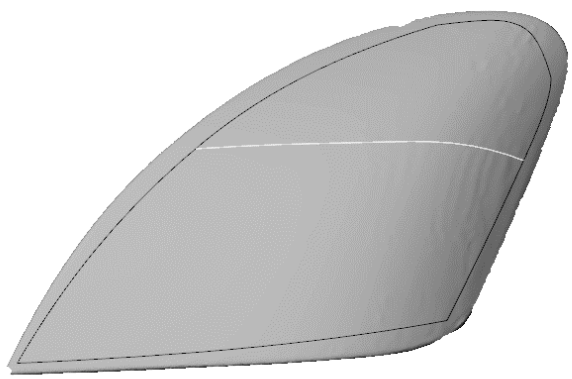

Fig 15 Front headlights surface with section curve.

Table 9 The results of nxn analysis as actual distances with preposition sign.

0,017	0,010	0,002	-0,009	-0,027
0,050	0,052	0,050	0,028	-0,030
0,070	0,081	0,085	0,058	-0,022
0,056	0,079	0,092	0,073	-0,010
0,00	0,037	0,063	0,063	0,00

C= 3,467
S= 110,2
B= 59,3

Fig 16 Graph K(s) and LCH of section curve of the headlight.

Section curve of headlight shown in figure 15 is analyzed. Figure 16 presents K(s) graph on the left side and LCH on the right side. Graph K(s) shows smooth chart except at peak. That means the section line presents smooth curve excepting this location where curvature changes drastically. LCH is unequal and does not show any specific property.

b) Sports car tail

Real sports car was scanned and reverse engineered. Good NURBS surfaces transitions were desired by a customer. Anyway existing global shape of a car must be followed. Therefore was compromised where some minimal shape changes were allowed and where not.

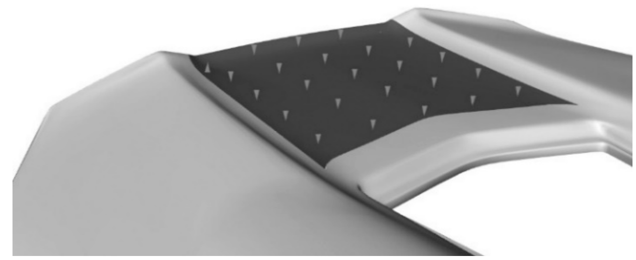

Fig 17 Darker surface of reverse engineered sports car tail was analyzed with nxn procedure.

On the tail of sports car was created transverse section curve for curvature analysis as shown in figure 18.

Table 10 The results of nxn analysis as actual distances with preposition sign.

-0.011	-0.007	0.000	-0.007	-0.011
-0.009	-0.009	-0.002	-0.009	-0.009
-0.007	-0.011	-0.004	-0.011	-0.007
-0.005	-0.012	-0.008	-0.012	-0.005
0.000	-0.012	-0.009	-0.012	0.000

C= -0,75
S= 0
B= 78

The table 10 shows the concavity of analyzed surface while most of the values are negative.

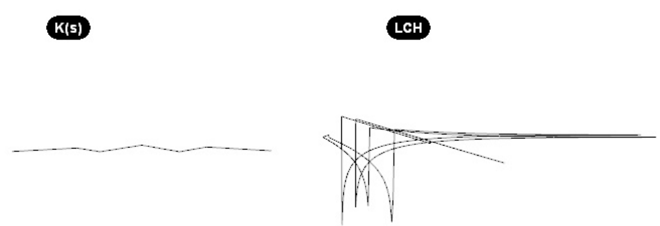

Fig 18 K(s) and LCH charts of sports car tail section.

Figure 18 shows graph K(s) on the left side where minimal symmetrical waving is detected. On this part the existing shape of a car was followed by creating this surface with T-splines.

LCH on the right side of figure 18 presents piecewise beautiful section curve while histogram has straight line curve as part of it. That proves that surfaces and consequently section curves drawn with T-splines are fair curves as shown in [10].

IV. DISCUSSION

The results of nxn procedure are presented in previous section as numerical values C, S and B. These values allow us to evaluate surfaces. On that base they will be distributed in several classes later on.

ISBN: 978-1-61804-288-0

C is for curvature and is zero if the surface is flat and presents a plane. For positive values the surface is convex and for negative it is concave.

S is for symmetry. Zero symmetry means perfect symmetrical surface. All the values are processed with absolute value therefore are just positive. Greater the value more is surface asymmetric.

B is for substantialness and can be only positive. 100 means equal width and height of the surface. All other values are between 0 and 100. At 0 there is just one curve and not surface any more therefore it will not be used.

V. Conclusions and Future Work

Methodology framework for evaluation of surfaces using nxn procedure gives us reasonable results for surface evaluation on cases described in chapter III. It cannot be discussed about classification of results at this stage while it is still under development.

As additional the fairness of section curves can be evaluated as shown in case Sports car tail. Here we get thus an analytical tool for the design features checking and errors detection.

Whole nxn procedure could be implemented using any programming language like C++ or java and operated like standalone program or add-on for different programs.

This development model makes sense so it can be used for expert system support for the design of complex products, among which is certainly in the first place car design. Proposal of intelligent advisor system was presented in [17].

In order to achieve desired refinements and fine-tuning of our shape evaluation procedure and methodology for surface shape evaluation we are continuously adding a substantial number of new examples – scans of real objects from a variety of areas of product design.

References

[1] V. Cheutet, C. E. Catalano, J. P. Pernot, B. Falcidieno, F. Giannini, and J. C. Leon, “3D sketching for aesthetic design using fully free-form deformation features,” *Comput. Graph.*, vol. 29, no. 6, 2005, pp. 916–930.

[2] V. Cheutet, “2D semantic sketcher for car aesthetic design,” *CPI2007*, 2007.

[3] F. Giannini, M. Monti, and G. Podehl, “Aesthetic-driven tools for industrial design”, Journal of Engineering Design, Vol. 17, No. 3, 2006, 193–215.

[4] F. Giannini, M. Monti, and G. Podehl, “Styling properties and features in computer aided industrial design”, Computer Aided Design & Applications, Vol. 1, No. 1–4, 2004, 321–330.

[5] G. Podehl, “Terms and Measures for Styling Properties”, 7th International Design Conference – Design 2002, 2002, 879–886,

[6] F. Giannini, “A Survey to Evaluate how non Designers Perceive Aesthetic Properties of Styling Features,” Comput. Aided. Des. Appl., vol. 10, no. 1, 2012, pp. 129–138.

[7] F. Giannini, M. Monti, and G. Podehl, “Styling properties and features in computer aided industrial design,” *Comput. Aided. Des. Appl.*, vol. 1, no. 1–4, 2004, pp. 321–330.

[8] F. Giannini, E. Montani, M. Monti, and J.-P. Pernot, “Semantic evaluation and deformation of curves based on aesthetic criteria,” *Comput. Des. Appl. Comput. Des. Appl.*, vol. 8, no. 3, 2011,pp. 449–464.

[9] E. Shpuza, “A Coupled Configurational Description of Boundary Shape Based on Distance and Directionality,” Artif. Intell. Eng. Des. Anal. Manuf., vol. 25, no. 4, 2011, pp. 357–374.

[10] Harada, T., Yoshimoto, F., & Moriyama, M. “*An Aesthetic Curve in the Field of Industrial Design*”. In Proceedings of the IEEE Symposium on Visual Languages. Washington, DC, USA: IEEE Computer Society. 1999

[11] Kanaya, I., Nakano, Y., & Sato, K. *Simulated Designer’s Eyes — Classification of Aesthetic Surfaces*. Design Discourse, Vo.l II(No. 4) 2007

[12] N. Yoshida and T. Saito, “Compound-Rhythm Log-Aesthetic Curves,” vol. 6, no. 1, 2009, pp. 1–10.

[13] N. Yoshida and T. Saito, “Interactive aesthetic curve segments,” *Vis. Comput.*, vol. 22, no. 9–11, 2006, pp. 896–905.

[14] Cupar, A, Pogacar, V, Stjepanovic, Z. “Methodology for Analysing Digitised Geometry”, Chapter 56 in DAAAM International Scientific Book 2013, 2013,pp. 903-920, B. Katalinic (Ed.), Published by DAAAM International, ISBN 978-3-901509-94-0, ISSN 1726-9687, Vienna, Austria

[15] Available from: http://dba.med.sc.edu/price/irf/Adobe_tg/models/cielab.html

[16] A. Cupar, V. Pogacar, and Z. Stjepanovic, “Methodology for Surfaces Analysis and Classification,” *Univers. J. Mech. Eng.*, vol. 2, 2014, pp. 64–70.

[17] J. Kaljun, U. Sancin, G. Harih, and B. Dolšak, “Aesthetics as parameter of intelligent design support,” 2012, pp. 1293–1300.

The One and Two Dimensional Wavelet Transform Applied in Unsteady Industrial Phenomena

A.Amoresano, C.Allouis, G.Langella, V.Niola, G.Quaremba

***Abstract* -** The analysis of transient phenomena in very short duration is today carried out through classical techniques based on the study of spectra and, more in general, by Fast Fourier Transform (FFT) and its variants. Starting from the assumption that the dynamic phenomena, in most cases are not stationary, in this paper a methodology based on the one and two dimensional DWT integrated with other theories (*i.e.*, Fuzzy Logic and Chaos Theory) to analyse unstable phenomena is presented. Two applications are described. The first, based on the one dimensional DWT, analyses accelerometric signals by recording the vibrations on the head of a cylinder of a naval Internal Combustion Engine (ICE). The second, based on a two dimensional DWT, analyses the image frames recorded by using a Fast Infrared Camera. The application of the presented methodology shows how, applying the 1D-DWT, it is possible experimentally to rebuild the in-cylinder pressure profile and recover information about the correct functioning of the diesel engine. The technique applied in the 2D-DWT dimensions permits to discover humming conditions in gas turbine burner .

Key-words Industrial Application, Unsteady Phenomena, Wavelet Transform.

I. INTRODUCTION

The analysis of transient phenomena in very short duration is today developed by classical techniques based on the study of frequency spectra and, more generally, of the FFT spectra and its modifications. The limits of these techniques, generally, depend on the application on periodic phenomena. Many phenomena leading to unstable conditions are not periodic.

In order to analyze such phenomena it is possible to assume these varying slowly in time (“quasi-stationary”) taking into account that, phenomena of very short duration, are not able to be described by use these working hypotheses. The goal of this research, of which this work is a significant frame, is the study, the development and testing of alternative techniques and methods of analysis which can be used -under the aforesaid conditions. The study of a “dynamic system”, carried out by using the theory of the Wavelet Transform integrated with suitable filters in order to enhance aperiodic events or weak signal, can be, respectively “prodromes” of a failure or “descriptors” of unstable physical phenomena.

The Wavelet Transform is divided in Continuous Wavelet Transform (CWT) and Discrete Wavelet Transform (DWT), and the latter, in redundant systems and discrete frames of orthonormal bases. It is sufficient to note that the environment in which the wavelets are "set" is the multidimensional Hilbert space, *i.e.*, a complete pre - Hilbert space. For our purposes the space R^n satisfies the properties of a Hilbert space. It has been defined, in this research, a particular “adaptive” function, which is a complete orthonormal system (basis). In this way it allows the study of the impulsive phenomena with an accuracy, resolution and reliability which, currently, it is not possible to achieve with other methods. Furthermore, the use of the Wavelet Transform, allows the identification of possible "anomalies" such as spikes, very rapid transients, instantaneous frequency variations, etc .. In this research, such technique has been integrated with other techniques and ideas belonging to the theory of chaos. And this, both because any system, "Real" , is always non-linear and for the particular attitude that those sophisticated diagnostic tests have in highlighting the dynamic evolution of dynamic systems.

In this paper two applications in two different fields, mechanical and combustion, are presented. The first case concerns the study of the dynamical evolution of an Internal Combustion Engine (ICE) and the “health” analysis of the connected mechanical components. All those can provide both important information on the operating status of the engine and actions for the cost saving. The approaches for analyzing the health of engine are various. For instance, it has been addressed by using the neuro-fuzzy systems [1]-[3]. This approach allows to follow the behavior of the engine and to increase systematically the knowledge of the operation of the engine and its characteristic details. Although this technique is widely used to predict failure or unstable conditions in mechanical device [3]-[5], often the fault of the mechanical components depends on other conditions such as bad lubrication, misfiring or overpressure in the internal combustion engine, etc. [5]-[7]. In this paper, starting from an accelerometer signal (Fig. 1), it has been processed by using the 1D – wavelet. The method presented is based on the principle that a signal, a time series, or any analytical function can be transformed into another set consisting of numerical wavelet coefficients each representative of a particular frequency corresponding to a predetermined scale [8].

The second case is an application of the 2D-Wavelet Transform. The acquired signal is a 3D matrix (Pixel, Pixel, Time) image recorded by using a IR camera (Fig.2).
The application of Infrared Thermography (IT) gives interesting results by monitoring thermo-mechanical systems. In fact, it provides a complete representation of the effective working conditions. Numerous experimental studies and numerical models were developed to understand the behavior of burners in gas turbines; in particular there are current researches aimed at understanding fuel/air interaction in the premixing duct, upstream of the combustion chamber [9]-[12]. Indeed, the characterization of the fuel mixing with air is very important for the optimization and the choice of the injection technology, which is important since it influences the homogeneity of the fuel/air mixture. Unfortunately, developments in premixed combustion are generally accompanied by increase in occurrence of oscillating combustion [13],[14]. Unstable combustion refers to self-sustained combustion oscillations at or near the acoustic frequency of the combustion chamber, which are the result of the closed-loop coupling between unsteady heat release and pressure fluctuations. The heat release fluctuations produce pressure fluctuations and it is well known and well understood; however, the mechanisms whereby pressure fluctuations result in a heat release fluctuations are not known. Rayleigh [15] postulated that, for the pressure oscillations to be amplified, the heat release and pressure fluctuations must be in phase. The exact mechanism of unstable combustion is not yet completely understood. New available technology as Fast InfraRed Imaging (FAIRI) allows instabilities investigation in the 2-dimensions [16],[17]. In this case study the methodology of 2D wavelet is applied. It is applied on recorded images by use FAIRI. The capability of this technique is based on fast infrared imaging in individuating the flame structure and the fluid dynamic fluctuations and the eventual correlations between them. This case study is carried out recording infrared images of a 3MW test rig combining FAIRI, pressure fluctuation and flame front frequency.

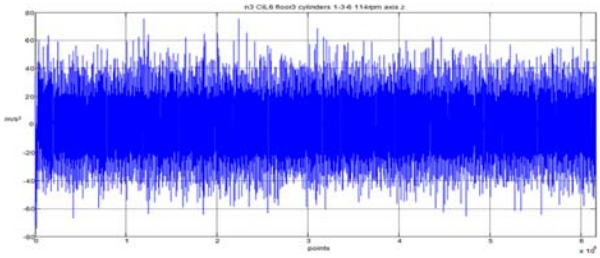

Fig. 1 Raw signal acquired by three-axial accelerometer

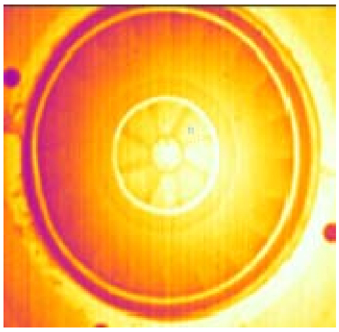

Fig. 2 Sample image acquired by infrared thermal camera

II. One and Two Dimensional Wavelet

The wavelets used in this paper are those proposed by Daubechies [18] (1992). She constructed a series of mother wavelets (indexed by N and denoted by db$N$) with each mother in the series having regularity proportional to N. Each Daubechies's wavelet is compactly supported in the time domain. Typically wavelets of class m_r are specifically constructed so that some properties are verified [20].
A mother wavelet ψ is a function of zero h-th moment

$$\int_{-\infty}^{+\infty} x^h \psi(x)dx = 0, \quad h \in \mathbf{N}. \qquad (1)$$

From this definition, it follows that, if ψ is a wavelet whose all moments are zero, also the function ψ_{ik} is a wavelet, where

$$\psi_{jk}(x) = 2^{j/2}\psi(2^j x - k).$$

And,

$$\int_{-\infty}^{+\infty} 2^{j/2} x^h \psi(2^j x - k)dx =$$
$$= 2^{j/2}\int_{-\infty}^{+\infty} \frac{1}{2^j}\left(\frac{y+k}{2^j}\right)^h \psi(y)dy =$$
$$= \frac{2^{j/2}}{2^{j(h+1)}}\int_{-\infty}^{+\infty} (y+k)^h \psi(y)dy =$$
$$= \frac{2^{j/2}}{2^{j(h+1)}}\sum_{m=0}^{h}\binom{h}{m} k^{h-m}\int_{-\infty}^{+\infty} y^m \psi(y)dy = 0. \quad (2)$$

Wavelets, like sinusoidal functions in Fourier analysis, are used for representing signals [21].

Now, let us consider a wavelet ψ and a function φ such that $\{\{\varphi_{j_0 k}\},$

$$\{\psi_{jk}\}, k \in \mathbf{Z}, j = 0, , 2, \ldots\} \qquad (3)$$

is a complete orthonormal system. By Parseval theorem, for every $s \in L^2(R)$, it follows that

$$s(t) = \sum_k a_{j_0k}\varphi_{j_0k}(t) + \sum_{j=j_0}^{j_1}\sum_k d_{jk}\psi_{jk}(t)\,. \quad (4)$$

The decomposition of a signal $s(t)$ by wavelet (*i.e.*, the CWT) is represented by the following detail function coefficients

$$d_{jk} = \int_{-\infty}^{+\infty} s(\tau)\cdot\frac{1}{\sqrt{2^j}}\psi\left(\frac{\tau-k}{2^j}\right)d\tau \qquad (5)$$

and by the approximating scaling coefficients

$$a_{j_0k} = \int_{-\infty}^{+\infty} s(\tau)\cdot\psi(\tau-k)d\tau\,. \ (6)$$

Note that d_{jk} can be regarded, for any j, as a function of k. Consequently, it is constant if the signal $s(t)$ is a smooth function, having considered that a wavelet has zero moments. To show the above mentioned property, it is sufficient to expand the signal in Taylor's series.

An example of wavelets is given by Daubechies' family {db$N$, $N = 1, 2, \ldots$} [20]. It is

$$supp\ \varphi \subseteq [0, 2N-1] \qquad supp\ \psi \subseteq [0, 2N-1]$$

and

$$\int_{-\infty}^{+\infty} x^h\psi(x)dx = 0\,, \quad h = 0, 1, \ldots, N-1.$$

Moreover, there is the following smoothness property: for any $N > 2$, the D2N wavelets verify

$$\varphi, \psi \in H^{\lambda N}, \quad 0.1936 \le \lambda \le 0.2075,$$

where $H^{\lambda N}$ is the Hölder smoothness class with parameter λ.

Now, let us consider two dimensional signals $f(x, y)$ which are square-integrable over the real plane: $f(x, y) \in L^2(R^2)$. A wavelet basis for $L^2(R)$ is to take the simple product of one-dimensional wavelet

$$\Psi_{j_1j_2k_1k_2}(x, y) = \psi_{j_1k_1}(x) \quad \psi_{j_2k_2}(y)\,. \qquad (7)$$

It is easy to show that Ψ's as defined above are indeed wavelets and that they form an orthonormal basis for $L^2(R)$.It can been show that the "detail space" W_j is itself made up of three orthogonal subspaces as follows:

$$\begin{aligned}\Psi^1(x, y) &= \varphi(x)\psi(y);\\ \Psi^2(x, y) &= \psi(x)\varphi(y); \quad (8)\\ \Psi^3(x, y) &= \psi(x)\psi(y).\end{aligned}$$

Mallat [23] notes that the three sets of wavelets correspond to specific spatial orientations: the wavelet Ψ^1 corresponds to the horizontal direction (H), the wavelet Ψ^2 with the vertical direction (V) and Ψ^3 with the diagonal (D). For more details see [18] - [24].

III. One Dimensional Wavelet - Application to Internal Combustion Engines

For a meaningful representation, from a qualitative and quantitative point of view, it is useful to use diagrams geometrically averaged over time. The extraction of the geometrical average from the accelerometric raw periodical signals allows to delete or to filter all those "dynamical fragments" that are not related to well-defined dynamical events of the mechanical system but rather to spurious or purely random or occasional events. These, in particular, form the set of points defined "noise". In such a way, the denoising of the signals is "natural", *i.e.*, without using sophisticated filters. After this preliminary treatment, the signal can be processed by a DWT [25][26]. To detect the existence of an incipient damage (*e.g.*, the spike) and to make the methodology most efficient and effective, the method has to be applied on the signals geometrically "averaged" starting from a "raw" signals obtained by the accelerometers without any application or pretreatment of an instrumental filter. The technique cited here is the "synchronous average". By definition, the following equation gives the average of a synchronous function

$$\bar{y}(t) = \frac{1}{N}\sum_{n=0}^{N-1} x(t + nT_R)\ (9)$$

where T_R is the period of synchronization and N the number of the averages performed. The progressive geometrical mean is defined as follows:

$$\bar{x}_{g_j} = \left|\prod_{i=1}^{n} x_{ij}\right|^{\frac{1}{n}}, \quad j = 1, \ldots, N^*, n = 1, 2, \ldots, M \quad (10)$$

where N^* is the number of points constituting a period and M is the number of sampled periods.

The method for the determination of the *morpho*-dynamical starts from the detection of a fixed point. In this application, this reference value is identified in the maximum vibrational pressure value inside the cylinder reached during the combustion phenomenon. When the highest in-cylinder pressure (Instantaneous Pressure) is reached (for short, IPv) as well as the Mean of the Instantaneous vibrational in-cylinder

Pressure (for short, MIPv) [19] The assessment is performed by applying the WT, which comprises, as the first stage, the etection of two types of signals: the accelerometric signal *z(t)* detected along the *z* axis (fig.1) (*i.e.*, the cylinder axis of the engine) and the tacho signal. The "peak detection" has the task of identifying those peaks of the tacho signal which allow to extract, from the accelerometric signal *z(t)*, a complete revolution of the crankshaft (Tab.1). To perform this step, two kinds of information are required as input: 1) the number of pulses provided by the tacho signal for each revolution of the crankshaft and 2) the sampling frequency of the accelerometric signal and the tacho signal. By means of such information, the macro-block "peak detection" identifies the peaks of tacho signal.

Tab.1 Morpho-dynamic algorithm for MIPv

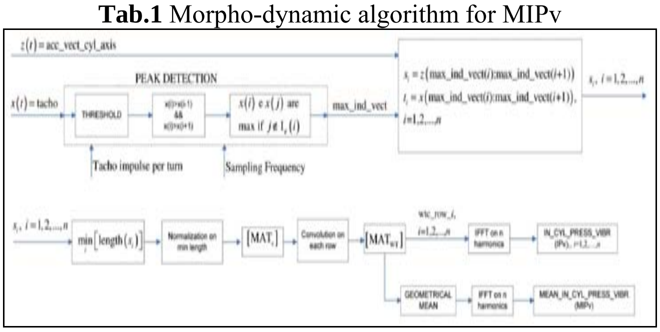

Known the indexes of such time series, and consequently the positions of each element defined as peak, a quasi-periodic accelerometric sequence, generated during a complete revolution of the crankshaft, can be extracted: $s_1, s_2, \ldots, s_N$ (Tab.1). In addition, let be, the tacho $t_1, t_2, \ldots, t_N$ series associated to the accelerometric $s_1, s_2, \ldots, s_N$ series. These sequences have not equal length, depending on the irregularity of the engine. It is possible to suppose the property of the pseudo-stationary sequence, so, normalizing them with respect to their minimum length, each accelerometric series will have the same length and it will be a row of the matrix [MAT_S] (Tab.1). The convolution between each row of [MAT_S] with an appropriate wavelet function generates the matrix [MAT_{WT}], composed of *n* rows of wavelet coefficients. The WT is based on a family of functions.

$$\psi_{a,b}(t) = \frac{1}{\sqrt{a}} \psi\left(\frac{t-b}{a}\right), a > b \in R \quad (11)$$

where ψ is a function, localized both in time and frequency, known as the "mother wavelet". The function $\psi_{a,b}(t)$ is obtained by applying the operations of shifting (*b*-translation) in the time domain and scaling in the frequency domain (*a*-dilation) to the mother wavelet. Incidentally, based on Parseval theorem, for any $s \in L^2(R)$, it follows that

$$s(t) = \sum_k a_{j_0 k} \varphi_{j_0 k}(t) + \sum_{j=j_0}^{j_1} \sum_k d_{jk} \psi_{jk}(t). \quad (12)$$

The relation (12) is the "multiresolution expansion of *s*". This means that any $s \in L^2(R)$ can be represented as a series, convergent in $s \in L^2(R)$, where a_k and d_{jk} are some coefficients, and $\{\psi_{jk}\}, k \in Z$ is a basis for the space W_j. The space W_j is the resolution level of the multiresolution analysis. As last notation, $j_0 = int\, log_2(N)$ where *N* is the length of the accelerometric signal.

In terms of signal processing, a wavelet basis generates a constant octave band filter bank structure [22],[23]. Therefore, the WT is a better solution for a time-frequency analysis of signals with high frequency components. By interpolating each row of the matrix [MAT_{WT}], by means of the Inverse Fast Fourier Transform (IFFT), with a suitable number of *n* harmonics, yields the trend of IP_V (Tab.1). In fact, any signal $s \in L^2(R)$, if satisfies certain conditions, can be written as a sum of "phasors" in discrete time

$$s(t) = \sum_{n=0}^{N-1} V_n e^{i\frac{2\pi}{N}nt} \quad .(13)$$

The Fourier coefficients V_n can be obtained from the IFFT

$$V_n(t) = \frac{1}{N} \sum_{t=0}^{N-1} f(t) e^{-i\frac{2\pi}{N}nt} \quad .(14)$$

By performing on the matrix [MAT_{WT}] a geometrical mean operation/interpolation by IFFT with *n* harmonics it reconstructs the diagram of MIP_V (Fig.3).

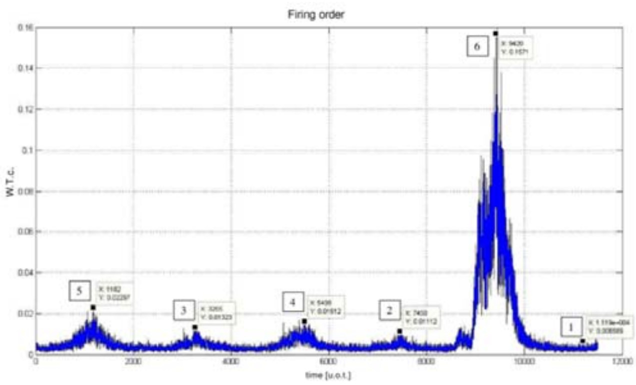

Fig. 3 MIPv reconstruction

IV. Two Dimensional Wavelet - Application to Gas Turbine Burners

In the case of two Dimensional Wavelet it is important to enhance that the space in which the wavelets are set is a multidimensional Hilbert space that is a complete pre-Hilbert space. In this application, the R^n space satisfies the properties of the Hilbert space. Such an orthonormal complete system (basis) allows the study of thermal systems with an accuracy

and resolution better than other methods. Mathematically, the first step is a convolution between the signal from the thermal camera and the chosen wavelet function. This function has the characteristic to dilate and contract. Its contracted version detects the high-frequency components in the original signal while, the dilated versions, detects the low-frequency components. With this assumption, it is possible to correlate the original signal with the wavelet functions of different sizes. In this way, wavelet coefficients of detail and approximation for the different scales are defined. The correlations, obtained for different kinds of the wavelet functions are, in general, presented in diagrams called “multi resolution decomposition”.
In this approach, the 2D-WT decodes the two-dimensional image obtained by the thermal camera (FAst InfraRed Image, for short, FAIRI). Furthermore, a suitable algorithm allows decomposing the two-dimensional signal (matrix image). In this way, it is possible to study the signal (the image matrix) along three different directions: horizontal, vertical and diagonal (Tab.2). The image is then discretised along a one-dimensional scale and, consequently, an algorithm based on the neural network [27][28]can be applied. Such a methodology is very suitable when the systems show non linear characteristics. In the mathematical field, a singularity is a point where a function is not differentiable although it is differentiable around it. The singularities, also called discontinuities, are sudden changes of a signal that occur in very short time.

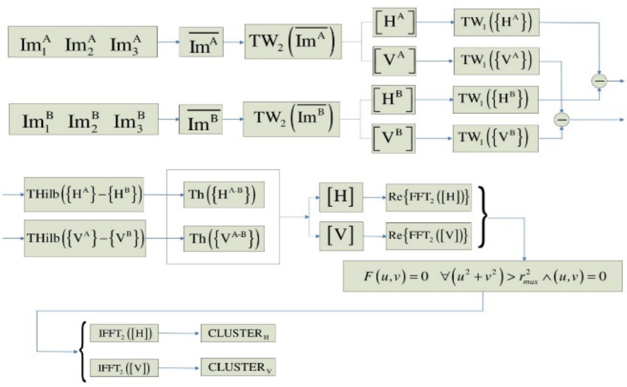

Tab. 2 Morpho-dynamic algorithm for clusters

The use of an high-cut filter permits to suppress these singularity. The identification of discontinuities, in signals and images as well as their localization do not depend only on the filtering process as it might appear at first sight. The singularities into signals represent the trend of physical quantities observed [19]. They have a high content of information and denote the occurrence of transient phenomena and rare events. In a 2D signal (*i.e.*, images) the singularities represent the contours of objects, changes in the properties of absorption or reflection of the bodies, lighting variations, temperature variations, important thermal gradients, etc. In the block diagram in Tb.2 the functional flow of the implemented methodology applied for the image processing is shown.

The application of this methodology to a Gas Turbine Burner (GTB) is able to extract the pre-humming and the humming frequencies in working conditions.
During and before the humming phase a film of the burner has done by means of the infrared-thermal camera. Fig.4 is an example of an IR recorded frame.
Through a program, developed on Matlab® platform, on each thermal frame is selected, by means of cropping, the so-called Area Of Interest (AOI), as shown in Fig 4.

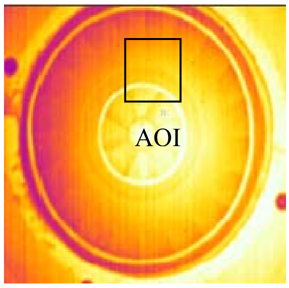

Fig. 4 AOI – Example of Area Of Interest

The AOI is important to avoid undesirable effects due to the reflection of the material and to focus the analysis only in the most significant zone. It permits, furthermore, to ease the computational process.

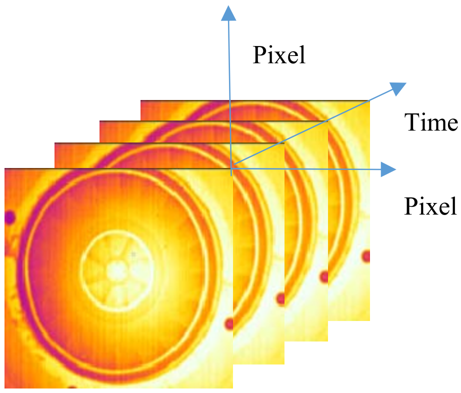

Fig. 5 3D Matrix

The signal to elaborate is a 3D matrix Fig.5 and, consequently the AOI forms a series of images, which thermally evolve along the time axis. Fixing an interval of time, submultiple of the elapsed time of the entire acquisition sequence, the entire set of images will be divided in n subintervals. Inside this interval a succession of images will be extracted in succession, *i.e.*, if the subinterval is composed by 20 images it will be extract the first five and the last five depending it by the Nyquist and Shannon theorem. This eliminates any type of accidental fluctuations, in this case thermal fluctuations, caused, for example, by superficial micro-circulations due to convective motions or to edge effects (in which are concentrated further dissipation of thermal energy).
Subsequently, the comparison of the frames geometrically averaged at different times has be done. In such a way two

ISBN: 978-1-61804-288-0

geometrically averaged images arise**:** $\overline{(Im)}^A$ and $\overline{(Im)}^B$ (Tab.2).
Subsequently, the method involves the use of a two-dimensional WT in order to filter the two averaged images $\overline{(Im)}^A$ and $\overline{(Im)}^B$. This operation generates the matrices $[H^A]$, $[V^A]$, and $[H^B]$, $[V^B]$ which allow to enhance the gradients for each of the images mainly on vertical (V) and horizontal (H) matrices [15]. The next step of the method consists on developing a single array (vectorization) starting from each of the previous matrix. .At this point, the methodology put in evidence a difference between corresponding arrays. On such differences, applying the Hilbert Transform, the thermal gradients arise. Subsequently, a finer selection is performed on the previous gradients with reference to the background noise always present in the images. After a careful selection of the highest thermal gradients, it reconverts the signal in matrix form. Thus we obtain the matrices $TW_1(\{H^A\})$; $TW_1(\{V^A\})$ and $W_1(\{H^B\})$; $TW_1(\{V^B\})$, holding information about the highest gradients for mainly horizontal and vertical analysis respectively. The method proceeds by assessing the real part of the two-dimensional Fourier Transform of the two H and W $(Re, FF[\![WT]\!]_2([H])$ and $(Re, FF[\![WT]\!]_2([H]))$ matrices. In the two-dimensional topological metric space the clusters showing mainly vertical and horizontal gradients of the starting images (H and V CLUSTERH CLUSTERV) are reconstructed, by two-dimensional inverse Fourier transform $(Re, IFF[\![WT]\!]_2([H])$ e $(Re, IFF[\![WT]\!]_2([H]))$
The selection of harmonics useful for this reconstruction is determined by selecting a threshold that allows a good filtering between the peaks of the gradient and the background noise. In fact, all the components of two-dimensional images which does not have a radius, composed of horizontal and vertical components of image, greater than a predetermined value, are deleted. Usually, this value was pre-set in correspondence with a maximum radius to which corresponds the maximum curvature of the energy function calculated onto the [H] and [V] images. Applying, a neural system SLNN is applied on images geometrically averaged, in order to obtain a denoised image to the actual feature [27]-[29] The overlapping of this image on the clusters identified by the WT, permits to visualize the region with low gradient and to follow it during the elapsing time.
The Fig.6 shows the region (red circle) with the same thermal gradient.

Fig. 6 cluster - image overlapping

V. CONCLUSION

The application of a methodology based on the WT has been presented. This methodology has been applied on two case studies the first related to an accelerometer signal and the second to an infrared image signal.

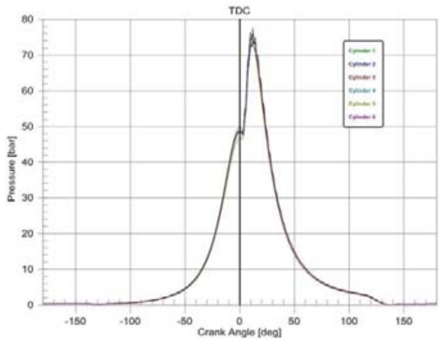

Fig. 7 Pressure diagram by the Engine

The proposed method is non-invasive, reliable and easy to implement. It could be performed with a real-time monitoring system. In the first case the results, referred to the pressure diagrams, are of "vibrational nature". From a qualitative point of view, the comparison with the actual pressure development is good. It is possible to compare the morphology of the reconstructed signal with the actual pressure diagram given by the maker Fig.7. By comparing, in this case, the shape of two profiles it is easy to verify a good similarity Fig 8. This approach allows also to have some interesting evaluations about the "health" of the engine.

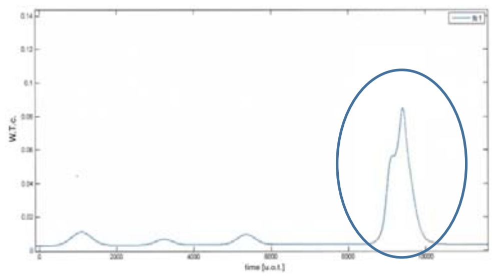

Fig. 8 Pressure diagram rebuilt by means of accelerometric signal

The results of all the techniques present a good correlation about the frequency analysis of the combustion instabilities. Moreover, the use of the IR imaging abled to map these instabilities with respect to the burner design and came out as a helpful tool for the burner design and for the development of a methodology for comparing different burners operating in different conditions from thermal-acoustic point of view. Image analysis is a special case of signal processing, one that deals with two-dimensional signals representing digital frames in which is included also the noise. This study illustrates an application of a new method for signal processing based on the decomposition of complex signal performed by wavelet.
It has been focused that, the conjunction of the wavelet with the infrared thermography technique, can concur in

determining the dynamical and morphological difference shown by thermographic patterns. In Figg 9 and 10 the precession motion in humming has been measured with the described technique and the results are agree with the experimental data.

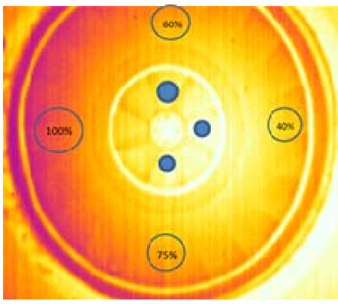

Fig. 9 Map of the "humming" phenomenon

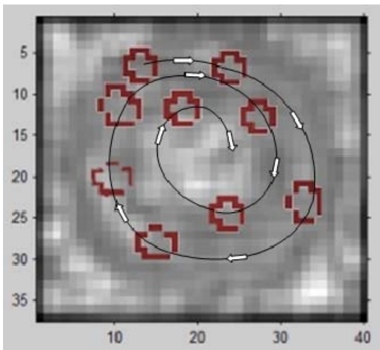

Fig. 10 – Evolution of turbulent clusters under humming conditions

REFERENCES

[1] Wilson Q. Wanga , M. Farid Golnaraghib, Fathy Ismailb *Prognosis of machine health condition usingneuro-fuzzy systems* Mechanical Systems and Signal Processing 18 (2004) pp. 813–831.

[2] J. Milewski1 , Ł. Szabaowski1 and J. Kuta1, *Internal Combustion Engine controlled by Artificial Neural Network*, Tech Science Press SL, vol.7, no.3, pp.187-202, 2012.

[3] Jian-Da Wua, Cheng-Kai Huanga, Yo-Wei Changb, Yao-Jung Shiaob, *Fault diagnosis for internal combustion engines using intake manifold pressure and artificial neural network*, Expert Systems with Applications, Volume 37, Issue 2, March 2010, Pages 949–958.

[4] Xun Wang, Neil McDowell,Uwe Kruger, Geo McCullough, George W. Irwin, *Semi-physical Neural Network Model in Detecting Engine Transient Faults using the Local Approach*, Proceedings of the 17th World Congress, The International Federation of Automatic Control, Seoul, Korea, July 6-11, 2008.

[5] Wilson Q. Wang, Fathy Ismail and M. Farid Golnaraghi, *Assesment of Gear Damage Monitoring Techniques Vibration Measurements*, Mechanical Systems and Signal Processing (2001) 15(5), 905-922

[6] Dr. hab. inż. Czech P. The Use Of Vibration *Signals And RBF Neural Networks In The Process Of Identification Of Pressure In Internal Combustion* - Engine Cylinder Machines, Technologies, Materials. ISSN 1313-0226. ISSUE 5/2013.

[7] Zhiqiang Wang *Study on Fault Diagnosis of Fuel Injection Based on Vibration Signal Analysis of High-pressure Fuel Injection Pipe*, Applied Physics Research, Vol. 1, No 2. 2009.

[8] Jian-Da Wu*, Chiu-Hong Liu *An expert system for fault diagnosis in internal combustion engines using wavelet packet transform and neural network* Expert Systems with Applications 36 (2009) 4278–4286.

[9] Cowell L. H. and Smith K. O., *"Development of a Liquid-Fueled, Lean-Premixed Gas Turbine Combustor"*, Journal of Engineering for Gas Turbines and Power, vol. 115, p 554, 1993.

[10] Gradinger T. B., Inauen A., Bombach R., Kappeli B., Hubschmid W., Boulouchos K., "*Liquid-fuel/air premixing in gas turbine combustors: experiment and numerical simulation"*, Combustion and Flame, vol. 124:3, pp 422-443, 2001.

[11] Brandt M., Rachner M., Schmitz G., "*An Experimental and Numerical Study of Kerosene Spray Evaporation in a Premix Duct for Gas Turbine Combustors at High Pressure*", Combustion Science and Technology, vol. 138, p 313, 1998.

[12] Snyder T. S., Rosfjord T.J., McVey J.B., Hu A.S., Schlein B.C., *"Emission and Performance of a Lean-Premixed Gas Fuel Injection System for Aeroderivative Gas Turbine Engines"*, Journal of Engineering for Gas Turbines and Power, vol. 118:1,pp 38-45, 1996

[13] Dowling A.P., Hubbard S., *"Instability in lean premixed combustors"*, Proc. Instn. Mech., Part A: 214, p 317, 2000.

[14] Venkataraman K.K., Preston L.H., Simons D.W., Lee B.J., Lee J.G., Santavicca D.A., *"Mechanism of Combustion Instability in a Lean Premixed Dump Combustor"*, Journal and Propulsion and Power, vol. 15:6, p 909, 1999.

[15] Rayleigh J.W.S., "The Theory of Sound", Macmillan, New York, 1945.

[16] Allouis C., Beretta F., Amoresano A., *"Experimental Study of Lean Premixed Prevaporized Combustion Fluctuations in a Gas Turbine Burner"*, Combustion Science and Technology, vol.180, pp 900-909, 2008.

[17] Allouis C., Pagliara R., Saponaro A., *"Fast infrared imaging for combustion stability analysis of industrial burners"*, Experimental Thermal and Fluid Science, vol. 43, pp. 2–8, 2012.

[18] Daubechies, I., *Ten lectures on Wavelets, SIAM*, Philadelphia, Pennsylvania, 1992.

[19] C.Allouis, A.Amoresano, F.Beretta, *Experimenta Study Of Lean Premixed Prevaporized Combustion Fluctuations In A Gas Turbine Burner*, Combustion

Science And Technology, Volume 180, Issue 5,2008, Pp 900-909

[20] Härdle, W., Kerkyacharian, G, Picard, D. and Tsybakov, A., *Wavelets Approximation and Statistical Applications*, Springer, Berlin, 1998.

[21] Antoniadis, A., Oppenheim, G., *Lecture notes in Statistics - Wavelets and Statistics*, Springer, 1995.

[22] Kaiser, G., *A Friendly Guide to Wavelets, Birkhäuser*, 1999.

[23] Mallat, S.G., *A theory for multiresolution signal decomposition: the wavelet representation*, IEEE Transactions on Pattern Analysis and Machine Intelligence, 11:674-693, 1989.

[24] Antoniadis, A., Oppenheim, G., *Lecture notes in Statistics - Wavelets and Statistics*, Springer, 1995

[25] I Daubechies, Orthonormal bases of compactly supported wavelets, Comm. in Pure and Applied Mathematics. No. 41, 909-996, 1988.

[26] MV Wickerhauser, *Adapted Wavelet Analysis from Theory to Software*, IEEE PRESS, AK Peters, Natick, Massachusetts, 1994.

[27] Niola, V., Quaremba, G., *Evaluation of image denoising using fuzziness measures*. Trans. on Systems, Vol. 5, Issue 7, July 2006, pp 1546-1554.

[28] Niola, V., Quaremba, G., Savino S., *The objects location from images binarized by means of self-learning neural network*, Trans. on Systems, Vol. 4, Issue 4, April 2005, pp 417-423.

[29] A Amoresano, G Langella, V Niola, G. Quaremba, *Advanced Image Analysis of Two-Phase Flow inside a Centrifugal Pump*, Advances in Mechanical Engineering, - Volume 2014 (2014), Article ID 958320.

Amedeo Amoresano was born in Naples on October 27, 1963. He achieved his degree in Mechanical engineering at University of Naples Federico II in 1991. In 1994 he achieved his PhD in Thermomechanical and Energetic Systems discussing a thesis on the fluidodynamic of two phase systems. He is member of the ILASS Europe (Institute of Liquid and Spray Atomization Systems), AIVELA (Associazione Italiana Velocimetria Laser Doppler). In 1997 he became researcher at the University of Naples “Federico II” at DiME (Mechanical and Energetic Department). From 2001 he is Assistant Professor of Fluid Machinery and Energy Conversion Systems. From 1997 he is advisor for the italian government on the Innovative Power Plant. In 2007 he was responsible of PRIN (National Research Program). To day he is Associated Professor at the Ateneo “Federico II” of the Naples University and responsible in SP1 of the UE EERA JP for Energy Industrial Applications. He is author of more of 100 publications in the field of Two phase flow, Solar Energy, Combustion Diagnostic.

ISBN: 978-1-61804-288-0

Modelling of biogas, solar and a ground source heat pump greenhouse heating system by using ensemble learning

H. Esen, M. Esen, and T. Yuksel

Abstract-In the present work, the biogas, solar and a ground source heat pump (BSGSHP) greenhouse heating system which will be modeled by ensemble model (neural network (NN), support vector machine (SVM) and K-nearest neighbors (K-NN)) has eight inputs and one output. Due to high heating costs and fossil fuel use, the interest in alternative or renewable energy sources for greenhouse heating is currently high. When we compare NN results with the results that are obtained with ensemble model, we can see easily the superiority of the ensemble model.

Keywords- Biogas, ensemble learning, ground, neural network.

I. Introduction

Greenhouse is a structure that growing plants. These structures are used in the industry, from small to large structure construction. Greenhouses allow for greater control over the growing environment of plants. Due to population growth, the need is met greenhouse for agricultural products. Hence, the demand for greenhouse food industry is increasing over the years [1-3].

A solar greenhouse collects and stores heat during the day, keeps the heat inside at night and on cloudy days. A solar greenhouse is oriented to maximize southern glazing exposure [4].

This work was supported in part by the Scientific Research Projects Management Council of the Fırat University for this study performed under project with grant no. 2009/1827.

H. Esen, Department of Energy Systems Engineering, Faculty of Technology, Fırat University, 23119 Elazig, TURKEY (424-237-0000-4276; fax: 424-236-7064; e-mail: esenhikmet@gmail.com).

M. Esen, Department of Energy Systems Engineering, Faculty of Technology, Fırat University, 23119 Elazig, TURKEY (424-237-0000-4375; fax: 424-236-7064; e-mail: esenm1@gmail.com).

T. Yuksel Department of Automotive Engineering, Faculty of Technology, Cumhuriyet University, 58100 Sivas, TURKEY (346-219-1010-2317; 424-236-7064; e-mail: tyuksel@cumhuriyet.edu.tr).

Greenhouse industry, a growing issue in agriculture in Turkey, chiefly because of favorable climatic conditions. However, for the healthy growth of plants, plants still need to heat during the winter night. Greenhouse heating is among the most energy-consuming activities during the winter season in our country.

In many energy systems applications, performance/ efficiency prediction is very important. It is recommended that intelligent systems (artificial neural network (ANN), adaptive neuro-fuzzy inference system (ANFIS), support vector machine (SVM) and ensemble model) can be used to estimate the performances/efficiencies of thermal systems in engineering applications. More specifically, they used ANN for quasi-steady-state modelling of the greenhouse environment [5-6], for model dynamics [7] for reminiscent model-based optimization and for constructing an expert decision system. Seginer [8] illustrated some ANN applications to greenhouse environmental temperature control. Two examples are the mimicking of a model-based optimal (feed-forward) controller and a human optimizer (expert grower), who uses some feedback information from the state of the crop. Blasco et al., [9] have focuses on development of control algorithms by incorporating energy and water consumption to maintain climatic conditions in greenhouse. Ehret et al., [10] are developed and tested the concept of using neural network models to accurately predict cuticle cracking in both pepper and tomato fruit from growing conditions in commercial greenhouses. Speetjens et al., [11] have showed the suitability of the extended Kalman filter (EKF) for automatic, on-line estimation and adaptation of parameters in a physics-based greenhouse model. Wang et al., [12] presents the support vector machines regression modeling method and online learning approach for the greenhouse environment and is structured. Ma et al., [13] examined the greenhouse temperature model based on ANFIS, using the experimental data to adjust the parameters of the model and parameters can be determined ultimately converge to some value.

The purpose of this study was to show that a BSGSHP greenhouse heating system have been planned and placed into the greenhouse. In addition to, BSGSHP system which will be modeled by ensemble model has eight inputs and one output. In all cases, the ensemble model performed successful results.

II. BSGSHP SYSTEM DEFINITION AND EXPERIMENTAL VALIDATION

This study analysed the greenhouse structure has been established in a village 25 km west of Elazığ, Turkey. In the literature, it is stated that the greenhouse temperature be kept in the 23 °C [14]. The sizes of the sera used in this study are 4 m x 6 m x 2.1 m. The greenhouse was made of polycarbonate material. The used polycarbonate sheets are 6 mm twin-wall panels, and are almost as transparent as glass.

Experiments conducted with BSGSHP system under steady-state conditions in the heating mode 2009 and 2010 years. The temperature measurement points (red color) of experimental study are given in Fig. 1.

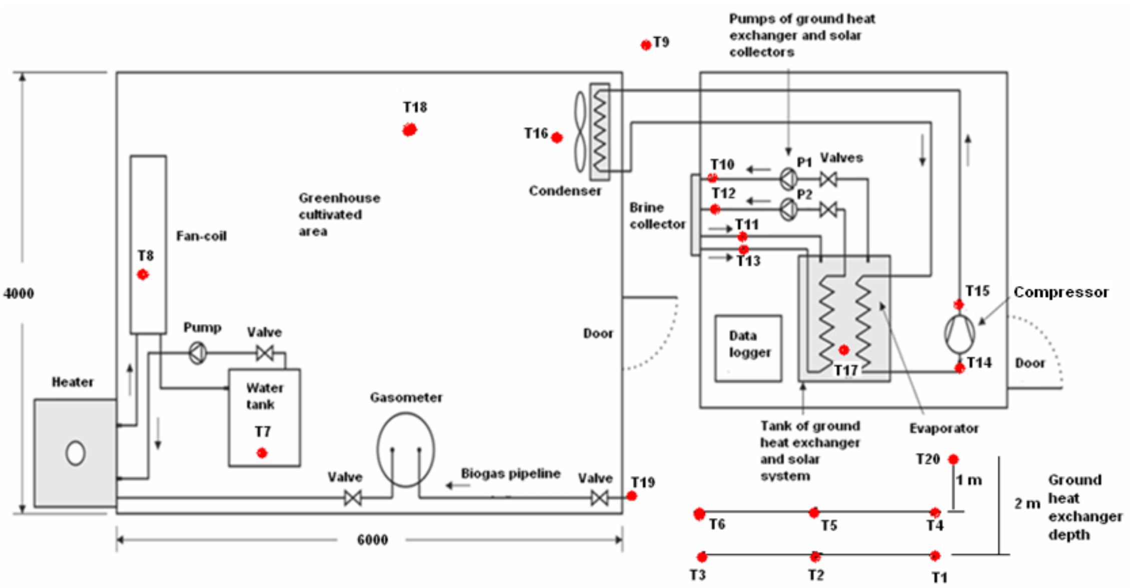

Fig. 1. The sketch of temperature measurement points of BSGSHP system

The temperatures (T1, T2, T3, T4, T5, T6: ground; T7: biogas water tank; T8: blowing up fan-coil; T9: outdoor area; T10: inlet of ground heat exchanger (GHE); T11: outlet of GHE; T12: inlet of solar collectors; T13: outlet of solar collectors; T14: inlet of compressor; T15: outlet of compressor; T16: condenser fan; T17: tank of GHE and solar system; T18: indoor greenhouse; T19: generator; T20: ground at 5 cm).

The heat rejection rate in the condenser is calculated by

$$\dot{Q}_{con} = \dot{m}_{ref}\,(h_{con,i} - h_{con,o})\,. \tag{1}$$

The heat transfer rate in the evaporator is

$$\dot{Q}_{eva} = \dot{m}_{ref}\,(h_{eva,o} - h_{eva,i})\,. \tag{2}$$

The work input rate to the compressor is

$$\dot{W}_{comp} = \frac{\dot{m}_{ref}\,(h_{comp,o} - h_{comp,i})}{\eta_{icomp}\eta_{mcomp}}\,. \tag{3}$$

Hence, the COP of the BSGSHP can be determined as

$$COP_{hp} = \frac{\dot{Q}_{con}}{\dot{W}_{comp}}\,. \tag{4}$$

The coefficient of performance of the entire system (COP_{sys}) is calculated by the following equation,

$$COP_{sys} = \frac{\dot{Q}_{con}}{\dot{W}_{comp} + \dot{W}_{pumps} + \dot{W}_{fancoil}}. \quad (5)$$

In the first part of the experiment, soil temperatures were utilized without an external heater. In the last part of the experiment, the generator was prepared. Mesophilic fermentation were kept for 45 days at a temperature between 25 °C and 38 °C. According to information obtained from the literature survey, generator temperature is kept at a constant 27 ± 3 °C. The released amount of biogas for the duration of experiments under these conditions is given in Fig. 2. During this experiment, the amount of biogas produced from the generator is about 2200 liters.

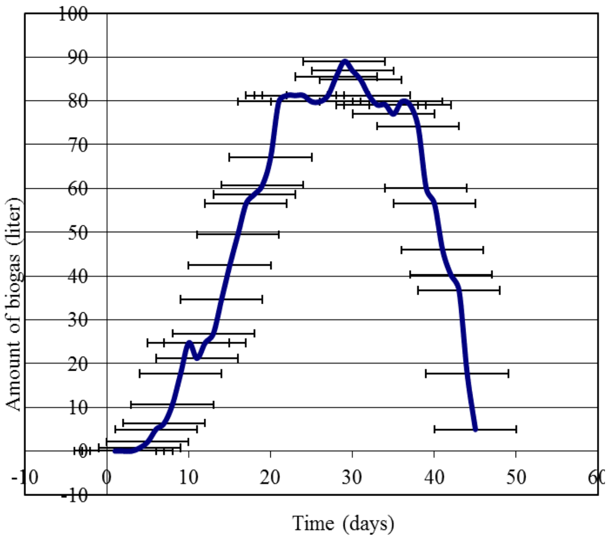

Fig. 2. The amount of produced biogas

In this period, the exchange according to the days of the amount of gas produced by the soil, reactor and outdoor air temperatures are shown in Fig. 3. A maximum amount of gas produced in the 29 day period was 89 litres.

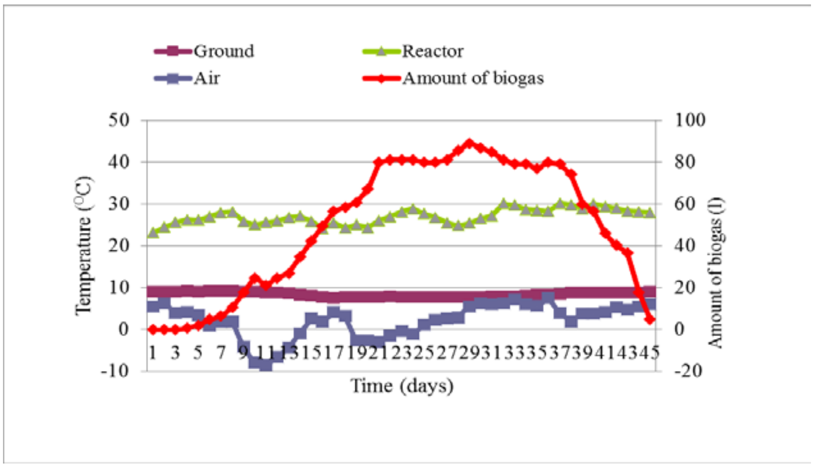

Fig. 3. The exchange according to the days of the amount of gas produced by the soil, reactor and outdoor air temperatures

Main heat loss from greenhouse occurs at night. Heat loss between 7 am and 8 pm is 5 kW. Average daily heat loss is 4.67 kW. The gas produced from generator under mesophilic conditions was measured by gasometer. The gas exiting gasometer is then reached the water heater. The gas obtained from the gasometer pressurizing prepared for combustion in the water heater. The hot water enters to the fan-coil where it carries its heat to the greenhouse, and then distributed through the water tank another time. This progression is repeated to increase the temperature of water in the tank. When the water temperature reaches approximately 45 °C, the system automatically stops for preventing fuel consumption. The greenhouse air, outside air, tank water, and fan-coil air temperatures measured for biogas system are shown in Fig. 4.

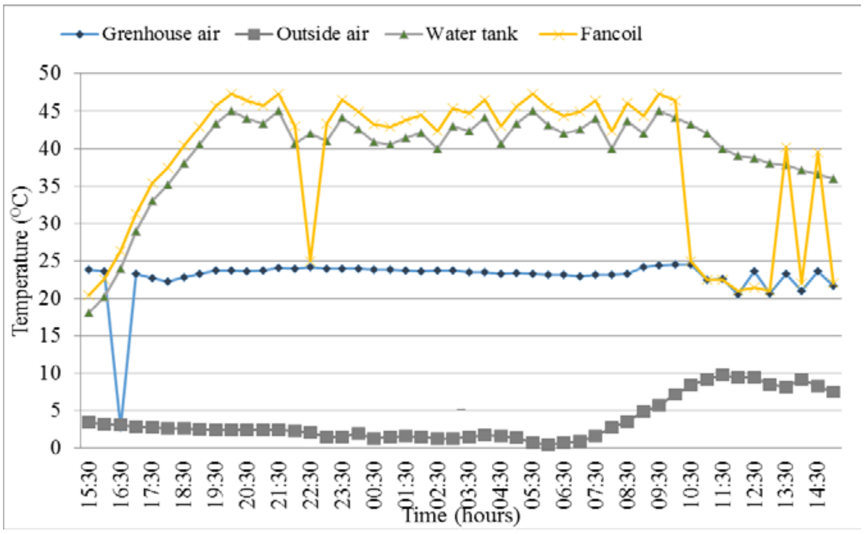

Fig. 4. Temperature change of greenhouse environment, outside air, tank water and fan temperatures

When the greenhouse internal temperature reaches 23 °C (according to ref. [14] greenhouse temperature range is set between 20 °C and 29 °C), the fan-coil unit stops. Hence, the greenhouse temperature does not increase and power consumption reduces.

Ground heat exchanger (GHE) in the established system is slinky (spiral). To prevent freezing of water during the winter, antifreeze is added to the water. The water-antifreeze solution in the slinky GHE (see Fig. 1) extracts heat from the earth and carries it into the tank of GHE and solar system. The solution transfers its heat to refrigerant (Freon 22) fluid in the evaporator of the heat pump. The refrigerant evaporates by absorbing heat from the solution and then enters the compressor. The refrigerant is compressed by the compressor and then enters the condenser, where it condenses. A fan blows across the condenser to move the warmed air of the greenhouse. The GSHP system is disabled as the biogas system when the indoor air temperature reaches 23 °C. When the temperature drops below 20 °C, the GSHP system automatically stops. At night and in cloudy conditions, the GSHP system operates successfully alone. The average system performance is calculated as 2.48. According to the literature, this value is moderate [15-17].

III. Ensemble Learning

The ensemble learning is to employ multiple modeling methods and combine their results [18]. Ensemble approach is a mixture of various models (Neural Network (NN), Support Vector Machines (SVM) and decision tree) [19].

SVMs are supervised learning models which aim to achieve data analyzing, patterns recognition and classification and regression analysis based on a linear arrangement of structures derived from the variables [20] SVM uses nonlinear kernel functions to change the input data to a high dimensional feature space in which the input data becomes more manageable compared to the original input space. Moreover, in the classification problem, SVM aims to find a mathematical characterization of a hyper plane that separates the training data into several classes.

K-NN is one of the well-known classification methods [21-22]. It learns by comparing a given test tuple with training tuples that are similar to it. When a new instance is introduced, K-NN finds the k-nearest neighbors of this new instance and determines the label of the new instance by using these k instances. An example of k-NN classification is depicted in Fig. 5 [23]. The test sample (green circle) should be classified either to the first class of blue squares or to the second class of red triangles. If k = 3 (solid line circle) it is allocated to the second class because there are 2 triangles and only 1 square inside the inner circle. If k = 5 (dashed line circle) it is allocated to the first class (3 squares vs. 2 triangles inside the outer circle).

ISBN: 978-1-61804-288-0

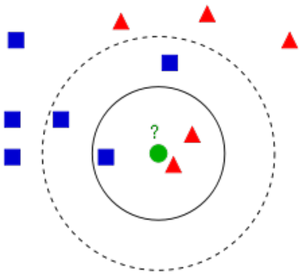

Fig. 5. An example of K-NN classification

In *k*-fold cross validation dataset is randomly split into *k* exclusive subsets of nearly equal size and the holdout method is repeated *k* times. At each time, one of the *k* subsets is used as the test set and the other *k-1* subsets are put together to form a training set. The advantage of this method is that it is not important how the data is divided. Every data point seems in a test set only once, and seems in a training set *k-1* times. Therefore, the verification of the efficiency of the suggested method against to the over-learning problem should be revealed.

To evaluate the results obtained models need to use some statistical approaches. Some statistical methods, such as the root-mean squared (RMS), the correlation coefficient (R), and the coefficient of variation (COV) may be used to compare predicted and actual values for model validation.

The error can be calculated by the RMS, defined as [24-25]:

$$RMS = \sqrt{\frac{\sum_{m=1}^{n}(y_{pre,m} - t_{pre,m})^2}{n}}, \qquad (6)$$

In addition, the correlation coefficient (R), and the coefficient of variation (COV) in percent are defined as follows:

$$R = \frac{\sum_{m=1}^{n}((y_{pre,m} - y_{mea})(t_{pre,m} - t_{mea}))}{\sqrt{\sum_{m=1}^{n}(y_{pre,m} - y_{mea})^2 \sum_{m=1}^{n}(t_{pre,m} - t_{mea})^2}} \qquad (7)$$

$$COV = \frac{RMS}{|t_{mea}|}100 \qquad (8)$$

where n is the number of data patterns in the independent data set, y_{pre} indicates the predicted, t_{pre} indicates the actual dataset. t_{mea} and y_{mea} is the mean value of measured and predicted data points respectively.

IV. SIMULATION RESULTS

In this study, BSGSHP greenhouse heating system which will be modelled by ensemble model has eight inputs and one output. Ground temperatures at 2 meters (Tg), brine solution entering temperature (Twa,i), brine solution leaving temperature (Twa,o), biogas tank temperature (Ttank), greenhouse temperature (Tgh), fan-coil temperature (Tfc), ambient temperature (Ta), the value of solar radiation (I) constitutes the input variables of the model. The COP_{sys} is the output variable of the ensemble model. The data set for the available system included 33 data patterns. Due to the 3-fold cross validation test 22 data patterns were used for training the ensemble model and the remaining 11 patterns were used as the test data set for trained ensemble model.

We used 13 neurons for hidden layers of the NN topology. We chose the linear activation function for the output layer. Moreover, the perceptron learning algorithm is used. For finding the optimum parameters for SVM, we investigated a search mechanism in the 2D gamma vs. sigma plane for obtaining the optimum gamma and sigma values [24, 26]. The Radial Basis Function (RBF) kernel is selected which yielded the best performance in the experiments. For K-NN, we set the k value as 3.

The prediction results of the ensemble modeling for BSGSHP system are presented in Table 1. The last raw of Table 1 shows the average prediction result of the 3-fold cross validation. In all cases, the ensemble model performed successful results. As the results indicate, Ensemble prediction method performed reasonably well in modeling the graduate scores.

Table 1. Ensemble prediction result for BSGSHP

Ensemble model		RMS	Correlation coefficient (R)	COV
	First fold	0.0009	0.9995	0.0402
	Second fold	0.0027	0.9903	0.1073
	Third fold	0.0012	0.9921	0.0485
	Average	0.0016	0.9940	0.0653

Average 0.0016 RMS, almost 100 % correlation coefficient (R) and 0.0653 COV values are obtained. Moreover, we compared the ensemble model with a single model. We selected the NN structure because of its wide usability property. In Table 2, the NN results are tabulated.

Table 2. NN prediction result for BSGSHP system

NN model		RMS	Correlation coefficient (R)	COV
	First fold	0.1974	0.9754	7.8331
	Second fold	0.0803	0.9868	3.2176
	Third fold	0.1189	0.9798	4.7892
	Average	0.1322	0.9807	5.2800

As we can see that NN modeling algorithm produced reasonably prediction results, where average 98.07 % correlation coefficient (R), 0.1322 RMS and 5.2800 COV values are obtained with 3-fold cross validation test. The worst results are obtained by the NN method for first fold of the database where lower correlation coefficient, and (97.54%) and higher RMS (0.1974) and COV (7.8331) values are recorded. When we compare NN results with the results that are obtained with Ensemble model, we can see easily the superiority of the Ensemble model.

Figure 6 shows the graphical illustration of the actual and predicted samples for Ensemble model and NN for second fold of the dataset. There are 11 test samples. As we can see that the Ensemble predictions are close enough to the actual samples.

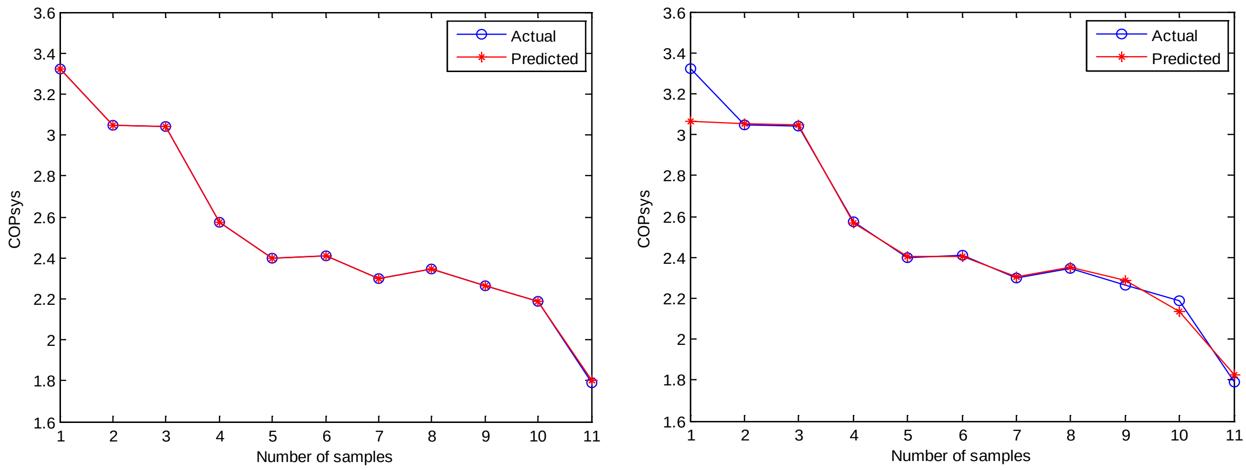

(a) (b)

Fig. 6. Prediction results for first scenario (a) Ensemble method and (b) NN

V. Results and discussions

The results and recommendations from this study are listed below:

i) Using the heating process of biogas, energy saving is provided. Chemical reaction of methane in the generator, the temperature of the generator remains constant. Thanks to the biogas system, the greenhouse temperature remains at a constant 23 °C.

ii) Slinky types of GHE is proved to be successful in the greenhouse heating. During the experimental studies, we have seen that low (1 °C) soil temperature swings.

iii) High storage temperatures with solar energy systems can be obtained. Solar energy is stored in the soil and thus can support the biogas system.

iv) Ensemble prediction method performed reasonably well in modeling the graduate scores. Average 0.0016 RMS, almost 100 % correlation coefficient (R) and 0.0653 COV values are obtained.

v) Prediction of system performance values are compared with data obtained from an experimental study. Ensemble model with simulation studies, we found to be effective in energy applications.

References

[1] S.K. Chou, K.J. Chua, J.C. Ho, and C.L. Ooi, "On the study of an energy-efficient greenhouse for heating, cooling and dehumidification applications," *Appl. Ener.* vol. 77(4), Apr. 2004, pp. 355-373.

[2] V.P. Sethi, and S.K. Sharma, "Survey of cooling technologies for worldwide agriculture greenhouse applications," *Sol. Ener.* vol. 81(12), 2007, pp. 1447-59.

[3] V.P. Sethi, and S.K. Sharma, "Survey and evaluation of heating technologies for worldwide agriculture greenhouse applications," *Sol. Ener.* vol. 82(9), 2008, pp. 832-859.

[4] R. Gupta, G.N. Tiwari, A. Kumar, and Y. Gupta, "Calculation of total solar fraction for different orientation of greenhouse using 3D-shadow analysis in Auto-CAD," *Ener. Build.* vol. 47, April 2012, pp. 27-34.

[5] I. Seginer, T. Boulard, and B.J. Bailey, "Neural network models of the greenhouse climate," *J. Agri. Eng. Res.* vol.59, 1994, pp. 203-216.

[6] R. Linker, I. Seginer, and P.O. Gutman, "Optimal CO_2 control in a greenhouse modeled with neural networks," *Comput. Electron. Agric.* vol. 19, 1998, pp. 289-310.

[7] I. Seginer, and I. Ioslovich, "Crop model reduction and simulation in reduced space," *Acta Horticulturae*, vol.406, 1996, pp.63-71.

[8] I. Seginer, "Some artificial neural network applications to greenhouse environmental control," *Comput. Electron. Agric.* vol.18, 1997, pp.167-186.

[9] X. Blasco, M. Martínez, J.M. Herrero, C. Ramos, and J. Sanchis, "Model-based predictive control of greenhouse climate for reducing energy and water consumption," *Comput. Electron. Agric*. vol.55(1), 2007, pp. 49-70.

[10] D.L. Ehret, B.D. Hill, D.A. Raworth, and B. Estergaard, "Artificial neural network modeling to predict cuticle cracking in greenhouse peppers and tomatoes," *Comput. Electron. Agric*. vol.61(2), 2008, pp.108-116.

[11] S.L. Speetjens, J.D. Stigter, and G. van Straten, "Towards an adaptive model for greenhouse control," *Comput. Electron. Agric.* vol.67(1-2), 2009, pp.1-8.

[12] D. Wang, M. Wang, and X. Qiao, "Support vector machines regression and modeling of greenhouse environment," *Comput. Electron. Agric.* vol.66(1), 2009, pp.46-52.

[13] L. Ma, J. Ji, and J. He, "The study of greenhouse temperature modeling based on fuzzy neural network," 978-1-4244-7161-4/10/$26.00 ©2010 IEEE.

[14] J. Myster, R. Moe, "Effect of diurnal temperature alternations on plant morphology in some greenhouse crops-a mini review," *Scientia Horticulturae* vol.62, 1995, pp.205-215.

[15] M. Inalli, and H. Esen, "Experimental thermal performance evaluation of a horizontal ground-source heat pump system," *Appl. Ther. Eng*. vol.24(14-15), 2004, pp.2219-2232.

[16] H. Esen, M. Inalli, and M. Esen, "Technoeconomic appraisal of ground source heat pump system for a heating season in eastern Turkey," *Ener. Conv. Manage*. vol.47(9-10), 2006, pp.1281-1297.

[17] H. Esen, M. Inalli, and M. Esen, "Numerical and experimental analysis of a horizontal ground-coupled heat pump system," *Build. Env.* vol.42(3), 2007, pp.1126-1134.

[18] A. Krogh, and J. Vedelsby, "Neural Network Ensembles, Cross Validation and Active Learning. Advances in Neural Information Processing Systems 7, MIT Press, 1995.

[19] A. Krogh, and P. Sollich, "Statistical mechanics of ensemble learning," *Physical Review*, vol.55(1), 1997, pp.811–825.

[20] J.A.K. Suykens, and J.P.L. Vandewalle, "Least squares support vector machine classifiers," *Neural Proc. Letters*, vol.9(3), 1999, pp.293–300.

[21] A. Sengur, "Prediction of protein cellular localization sites using a hybrid method based on artificial immune system and fuzzy k-NN algorithm," *Digi. Sign. Proces*. vol.19(5), 2009, pp.815-826.

[22] H. Guldemir, and A. Sengur, "Online modulation recognition of analog communication signals using neural network," *Expert Sys. Appl.* vol.33 (1), 2007, pp.206-214.

[23] Wikipedia, 2013. (http://en.wikipedia.org/wiki/k-NN)

[24] H. Esen, M. Inalli, A. Sengur, and M. Esen, "Modelling a ground-coupled heat pump system by a support vector machines," *Rene. Ener.* vol.33(8), 2008a, pp.1814-1823.

[25] H. Esen, M. Inalli, A. Sengur, and M. Esen, “Forecasting of a ground-coupled heat pump performance using neural networks with statistical data weighting pre-processing,” *Int. J. Therm. Scien.* vol.47(4), 2008b, pp.431-41.

[26] H. Esen, F. Ozgen, M. Esen, and A. Sengur, “Modelling of a new solar air heater through least-squares support vector machines,” *Expert Sys. Appl.* vol.36(7), 2009, pp.10673-10682.

H. Esen, he was born in Elazığ, Turkey in 1977. He graduated from the Mechanical Engineering Department of Firat University in 2000 and he received MSc degree from the same university in 2003. He gained Ph.D degree from Firat University in 2008. He became associated professor in 2011 at Firat University Energy Systems Engineering Department. He is interested in renewable energy sources.

Numerical Study Regarding the Behaviour of a Multilayer Slab on Shock and Impact

Marin Lupoae, Cătălin Baciu, Daniel Constantin, Dumitru Matahala, Dan-Ilie Buliga

Abstract— The use of the multilayered slabs for the protection of the military or civilian shelters has proved a rational solution, over time, in terms of construction engineering. The usual theoretical approach used to determine the response of the protected structure under shock or impact, although extremely useful, has not captured all the details regarding the behaviour of the layered slab under such loadings. The paper addresses, in terms of a numerical study, the influence of the different parameters of the layers (thickness, material, layout) and weapons of destruction (speed and angle of inclination of the projectile, depth of penetration and perforation etc.) on the maximum deformation of the base layer of the layered slab. The results show a good concordance between the theoretical and numerical results for certain values of the above mentioned parameters.

Keywords — multilayer slab, shelter, explosion, impact

I. Introduction

The world today is faced with an increasing number of risks regarding the individual and group safety. These risks can be natural disasters (earthquakes, hurricanes, tornadoes, etc.) or manmade events (terrorist attack, technological accidents or armed conflicts). Therefore, it is necessary to adopt and implement a set of adequate and consistent measures to protect the population from the potential consequences of the extreme loading effects resulted from the natural phenomena or the manmade actions. Thus, it has been and will always be needed to develop military and civilian shelters to protect the personnel and facilities.

For some fortifications and shelters for people or combat equipment, this type of composite floor, consisting of several layers, has been used since the time of the Second World War, instead of the simple slab (cast-in-place or precast concrete single layer slabs). Taking into account the good behaviour under impact and explosion of the multilayered slab, this solution has represented an ideal one in terms of construction works, being used in the post-war period for the defensive works carried out in different countries around the globe.

A projectile launched on an obstacle can act on its surface, but also inside of the element, after it penetrates up to a certain depth, beyond the protection of the structural elements. In the latter case, the projectile produces, until it explodes, a local damage (penetration and scabbing) in addition to a global one, as a result of the initial shock. After the detonation of the explosive charge of the projectile, the local damage will be extended thus leading towards a more severe global action on the structure.

In the case of an obstacle protected by a multilayer slab, the projectile can perforate the camouflage layer and reach the rigid layer on which it would produce the above listed effects. If the projectile does not have a sufficient enough kinetic energy to perforate the rigid layer, then only the distributed pressure generated by the explosion of the active charge of the projectile will act on the structure. The pressure will be transmitted to the base layer through the elastic (distribution) layer. It follows that, unlike the case of other structures where the effects of the local and global actions occur simultaneously, practically overlapping, the structures having distribution layers are affected only by the global action and its effects are obviously significantly diminished.

The dynamic actions on fortifications can have very high values in general. Having a particularly complex nature, their exact values cannot be established in all cases by analytical models. Therefore, the response of structures to this type of actions is difficult to be determined. Considering that, it is important to establish, using a numerical study, the best distribution of the layers (in terms of thickness, number and sequence) in order to obtain a minimum deflection of the base layer of the multilayer slab.

There are few papers in the literature regarding the influence of the multilayer plates on the behaviour of the underground structures subjected to blast and impact. Thus, Hongyuan and Guowei [1] proposed a double-layered floor to mitigate the in-structure shock of the underground buildings, but their proposal referred to an interior slab used to protect the inside personnel and the contained devices (against the shock or the severe vibration induced by the detonation).

Other papers studied aspects regarding the ground shock induced on the underground structures by explosions [2] - [3], with special emphasis on the influence of the propagation

Marin Lupoae is with Military Technical Academy, Bucharest, Romania, 39-49 George Cosbuc Blv., 050141, phone +40213354660; fax: +40213355763; e-mail: mlupoae@mta.ro.

Cătălin Baciu is with Military Technical Academy, Bucharest, Romania; e-mail: baciucatalin2001@yahoo.com.

Daniel Constantin is with Military Technical Academy, Bucharest, Romania; e-mail: dconstantin77@yahoo.com.

Dumitru Matahala is with Military Technical Academy, Bucharest, Romania;e-mail:matahala@rdslink.ro

Dan-Ilie Buliga is with Military Technical Academy, Bucharest, Romania; e-mail: dan.ilie.buliga@gmail.com.

ISBN: 978-1-61804-288-0

medium for the shock wave. Chen et al. [4] - [5] conducted a theoretical and experimental investigation related to the dynamic response of underground structures subjected to shock and impact.

The present paper proposes a detailed numerical analysis to determine the influence of various factors (thickness of the layers, type of material for the elastic layer, number and distribution of the layers on one hand and projectile velocity and angle of impact on the other hand) on the maximum deformation of the base layer.

II. Theoretical Aspects

In the technical literature, a unified theory for calculating the multilayer slab has not yet been developed. Some references regarding this aspect are made in [6] and [7]. The first paper suggests that the multilayer slabs can be considered, in terms of oscillations, as a particular case of the anisotropic plates and the second one presents some practical examples of calculations, based on the use of approximate methods.

A multilayer slab generally consists of: a camouflage layer, a rigid (protection) layer, an elastic (distribution) layer and a base (structural, resistance) layer. In short, the role and composition of each component can be defined as follows (from the surface to the shelter):

The camouflage layer is made of vegetable earth, having a minimum thickness, strictly necessary to allow the vegetation growth and to cover and conceal the protective structure.

The rigid layer is designed to prevent the projectile or the aerial bomb to perforate it and thereby to explode inside of it. For this reason, it is usually made of concrete or stone masonry, having a large thickness, which gives it a very high bending stiffness (in calculations it is considered as infinite stiffness). When dynamic loadings act on it, this layer moves entirely through a translational displacement due to its high rigidity, distributing the loadings over a large area and thus favouring the behaviour of the protective structure. In literature this layer is also called the explosion layer.

The elastic layer is designed to work together with the rigid layer in order to distribute the dynamic loadings on a surface as large as possible and to absorb the blast energy that propagates through the material of this layer. It is usually made by a powdered material, with or without cohesion (clay, sand, gravel, etc.). Sometimes this layer is called the distribution layer.

The base layer or *structural layer* is actually the top slab of the construction and it is made like any other ordinary slab designed for dynamic loadings.

In order to achieve proper results, we neglect the influence of the camouflage layer, taking into consideration only its weight.

For a normal multilayer slab consisting of three layers, subjected to a concentrated impulse, the maximum deflection of the base layer can be obtained using the following equation [8]:

$$w = \frac{4 \cdot H_0}{a \cdot b \cdot \omega \cdot \rho} = \frac{4 \cdot H_0 \cdot a \cdot b}{\pi^2 (a^2 + b^2) \cdot \sqrt{(\rho_1 + \rho_2 + \rho_0 h_0)(R_1 + R_2)}} \tag{1}$$

where

$$\omega = \pi^2 \left(\frac{1}{a^2} + \frac{1}{b^2} \right) \sqrt{\frac{R_1 + R_2}{\rho_1 + \rho_2 + \rho_0 h_0}} \tag{2}$$

is the main pulsation of the base layer, H_0 is the impulse of the projectile/ aerial bomb at the contact point with the rigid layer; a and b are the planar dimensions of the layers; R_1 and R_2 are the stiffnesses of the rigid and base layers respectively,

$$R = \frac{E \cdot h^3}{12(1-\mu)}. \tag{3}$$

Also, h is the thickness of a layer, μ is the Poisson`s ratio, ρ_1 and ρ_2 are the surface densities of the rigid and base layers respectively (index 1 is for rigid layer, 2 for the base layer and 0 for the distribution layer), ρ_0 is the density of the elastic layer and E is the longitudinal elastic modulus.

In order to take into account the changing of the material properties of the layers corresponding to a high speed impact and explosion strain rate, according to [9], the value of the longitudinal elastic modulus was changed. For compression, the value of elastic modulus E varies depending on the strain rate according to the following relation:

$$E_{imp} = E_{stat} \cdot \left(\dot{\varepsilon} / \dot{\varepsilon}_0 \right)^{0.026} \tag{4}$$

where E_{imp} is the elastic longitudinal modulus corresponding to the impact and E_{stat} is the elastic modulus for the static conditions, $\dot{\varepsilon}_0 = 30 \cdot 10^{-6} s^{-1}$. In terms of the strain rate, the impact of the projectile/ aerial bomb on the layered slab may be considered as a hard impact [9] and $\dot{\varepsilon}$ has values between 10^0 s^{-1} □i $5 \cdot 10^1$ s^{-1}.

III. Numerical Simulation

The phenomenon of the interaction between the aerial bomb/ projectile and the layers of a shelter and also the interaction between the shock waves resulting from the detonation of the explosive charge of the warhead and the layers of the protective structure are very complex and require a thorough study to accurately determine the behaviour of the layer material under impact and explosion loadings. The conditions under which these phenomena occur can greatly vary, depending on the speed of the projectile/ bomb, the contact angle, the remaining velocity at the point of contact, the number, type and thickness of the layers, the amount of explosive charge and its position in relation to each layer.

A. Initial data

To determine the influence of the various parameters on the behaviour of the layers under dynamic loading, an aviation bomb of 500 kg was established as a potential source of dynamic action. Its most important characteristics are: the total mass of 510 kg and the mass and type of the explosive charge - 250 kg of TNT.

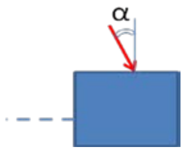

Fig. 1 The angle of the bomb at the contact point

To highlight the influence of the different parameters of the layers on the behaviour of the base layer, the following default configuration was chosen:

- all three layers have the same planar dimensions 6.00m x 5.00m and the same thickness – 30 cm;
- the base layer is simply supported on the boundary and it directly supports the above two layers;
- the rigid layer and the base layer consist of reinforced concrete, while the elastic layer is made of sand.

The action on the above mentioned configuration of the layered slab is produced by an aerial bomb of 500 kg, at a contact angle α of 25° and a remanent velocity at the contact point of 200 m/s. The angle of the bomb at the contact point is shown in fig. 1.

From this initial configuration the following scenarios were established: impact in table 1 and explosion in table 2.

B. *Material models*

The simulation of the impact between the bomb and the layered slab was carried out using the software AUTODYN/ ANSYS. Five material models were used for the impact schematization: *Steel 1006* to model the bomb shell, *TNT* material model for the explosive charge (for the impact the TNT material model was used as an inert charge without initiating the detonation), *Concrete 35MPa* material model for the rigid and base layers and *Sand* material model for the material of the distribution layer. All the above mentioned material models are defined in the AUTODYN library. Two new material models for soil [10] and LECA (Light Expanded Clay shale Aggregates) [11] were implemented in AUTODYN in order to quantify the influence of these two types of materials of the elastic layer on the maximum deflection of the base layer at shock and impact. The main characteristics of materials used for the distribution layer are presented in table 3. In addition, to model the effect of the shock wave resulting from the detonation of the warhead explosive charge, the *Air* material model from the AUTODYN library was used.

The *RHT* material model was used to describe the failure of the concrete under impulse loadings. The *RHT* concrete model is an advanced plasticity model for brittle materials developed by Riedal et al [12]. It is particularly useful for modelling the dynamic loading of the concrete.

Table 3 Material characteristics of the distribution layer

Material	**fc [MPa]**	**E [GPa]**	**G [MPa]**	**Density [kg/m^3]**
Concrete	35	36	16.7*10^3	2750
Sand			76.90	1674
Soil			37.64	1368
LECA			27.40	320

One of the most important parameters of the *RHT* model is the shear damage. The damage *D* is assumed to accumulate due to the inelastic deviatoric straining (shear induced cracking) using the following equation:

$$D = \sum \frac{\Delta \varepsilon_{pl}}{\varepsilon_p^{failure}} \tag{5}$$

where

$$\varepsilon_p^{failure} = D_1 \left(P^* - P^*_{spall} \right)^{D2} \tag{6}$$

and $\Delta \varepsilon_{pl}$ is the effective plastic strain; $\varepsilon_p^{failure}$ is the failure plastic strain; D_1, D_2 are the material constants; P^* is the pressure normalized with respect to the compression strength and P^*_{spall} is the normalized hydrodynamic tensile limit. Based on the shear damage parameter, AUTODYN exports a damage variable, which shows the level of failure for concrete.

C. *Geometric model*

To achieve the geometric model, the type of solver suitable for each material model used was taken into account. For the simulations of the impact of the bomb on the layered slab, the Lagrange solver was used. Thus, all the layers and the bomb were modelled using a Lagrangian solver. In the case of the *TNT* explosive charge, the model is considered just as a mass, without the initiation of its detonation being required. The shape of the bomb was modelled, fig. 2, as close as possible to the 500 kg bomb, taking into account that in the analytical model the shape parameter of the projectile does not appear as a separate parameter.

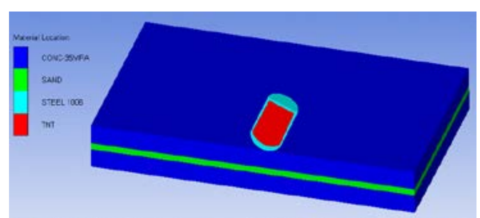

Fig. 2 Geometric model for the bomb and the rigid, distribution and base layers

To simulate the effects of the detonation of the explosive charge the Euler solver was used for modelling both the explosive charge and the air as the medium of propagation for the shock wave. Since the bomb hits the concrete plate (rigid layer) at an angle of 25° (table 1), for the 3D models a symmetry plan can be considered in order to model half of the bomb and layers (fig. 2).

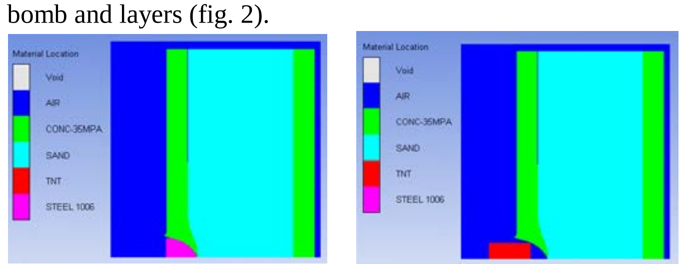

a) Penetration of the bomb   b) Placement of the explosive charge

Fig. 3 Geometric model for the impact and explosion

In case of the explosive charge detonation, a 2D modelling was chosen to decrease the total number of elements and therefore the running time. The layers and the bomb were modelled as in the case of impact, fig. 3a.

It should be noted that the 3D simulation of detonation requires an additional volume to be filled with air, going beyond the boundary of the bomb and layers, leading to at least twice the number of elements and therefore to an unacceptable runtime. For this reason a 2D modelling was chosen for impact followed by the explosion. Because symmetry provides faster simulation times and less use of the system resources, in 2D modelling a normal impact of the bomb on the layers was considered (a model with an impact angle different than zero is not a symmetrical model). After the geometric modelling and setting of the initial and boundary conditions, the problem was run to an appropriate time for the chosen scenario. When the time limit was reached, the bomb was replaced by the explosive charge, situated approximately in the same position (fig. 3b) and then it was initiated.

IV. RESULTS AND DISCUSSIONS

A. *The analytical model results*

The variation of the maximum deformation of the base layer according to equation (1), for different thicknesses of the elastic layer (made of sand) is shown in fig. 1.

Table 1 Simulation scenarios for impact

Scenario \ Parameter		Thickness of rigid layer, [cm]	Thickness of elastic layer, [cm]	Material sfor elastic layer	Thickness of base layer, [cm]	Remanent velocity at the contact point, [m/s]	Impact angle
S1 Influence of the thickness of elastic layer	S.1.1	30	10	sand	30	200	25°
	S.1.2	30	30	sand	30	200	25°
	S.1.3	30	50	sand	30	200	25°
	S.1.4	30	100	sand	30	200	25°
	S.1.5	30	150	sand	30	200	25°
S2 Influence of the material for elastic layer	S2.1	30	150	soil	30	200	25°
	S2.2	30	150	LECA	30	200	25°
S3 Influence of the impact angle		30	150	sand	30	200	0°
S4 Influence of the initial impulse, m*kg/s	S4.1 $9*10^3$	30	80	sand	30	20	25°
	S4.2 $15*10^3$	30	80	sand	30	33.2	25°
	S4.3 $30*10^3$	30	80	sand	30	88.5	25°
	S4.4 $60*10^3$	30	80	sand	30	133.5	25°
	S4.5 $90*10^3$	30	80	sand	30	200	25°
	S4.6 $100*10^3$	30	80	sand	30	230	25°
S5 Influence of the thickness of base layer	S5.1	30	80	sand	50	200	25°
	S5.2	30	80	sand	80	200	25°
	S5.3	30	80	sand	100	200	25°

Table 2 Simulation scenarios for explosion

Scenario \ Parameter	Type of explosion	Type of layer	Explosive charge	Material / thickness of layer, (cm)		
				Rigid layer	Elastic layer	Base layer
S6.1 Contact detonation with rigid layer (SR)	contact	rigid	250 kg TNT	concrete/30	sand/150	concrete/30
S6.2 Explosion in rigid layer (SR)	inside	rigid	250 kg TNT	concrete/30	sand/150	concrete/30
					soil/150	
					LECA/150	
S6.3 Explosion in elastic layer (SE)	inside	elastic	250 kg TNT	concrete/30	sand/150	concrete/30
S6.4 Contact detonation with base layer (SP)	contact	base	250 kg TNT	concrete/30	sand/150	concrete/30

ISBN: 978-1-61804-288-0

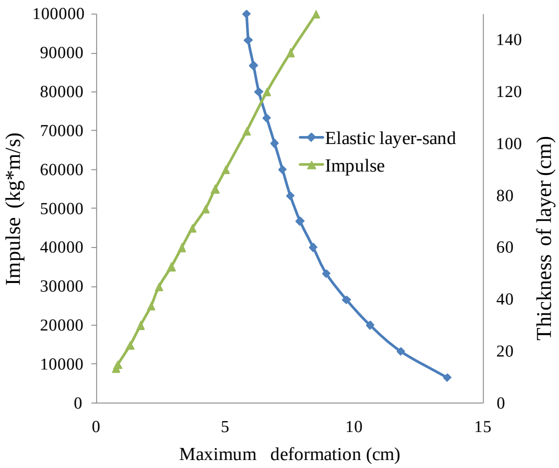

Fig. 4 The influence of the thickness of the elastic layer and the bomb velocity at the contact point on the maximum deflection of the base layer (analytical model)

The rigid and the base layers are made of reinforced concrete with a thickness of 30 cm. Also, on the same figure the variation of the maximum deflection of base layer function depending on the bomb impulse at the contact point is shown (the elastic layer has a thickness of 80 cm).

It can be observed (fig. 4) that the increasing of the elastic layer thickness will produce the decreasing of the maximum deformation of the base layer. The same observation is made when the velocity of the bomb in the contact point has lower values.

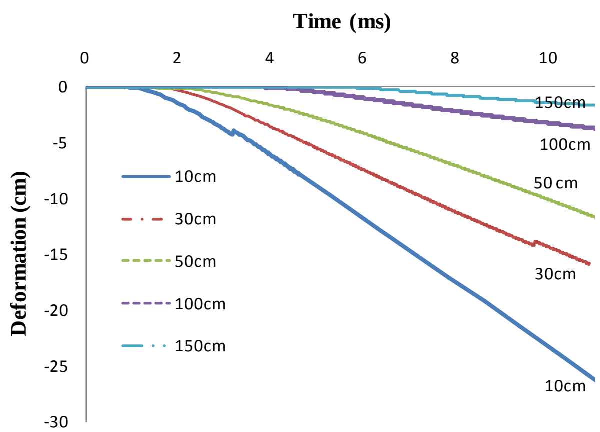

Fig. 5 The influence of the thickness of the elastic layer on the maximum deflection of the base layer

B. *The influence of the thickness of the elastic layer*

To establish the influence of the elastic layer thickness, the base layer deformation was determined using virtual gauges placed at the bottom of the base layer. The material used for the elastic layer was sand, having a thickness of 10, 30, 50, 100 and 150 cm. The maximum deformation of the base layer depends on the elastic layer thickness as shown in fig. 5.

Analyzing the graph presented in fig. 5, it results that the maximum deformation of the base layer decreases when the thickness of the sand layer increases. There is a good concordance between the theoretical model and the simulation for small values of the elastic thickness (a small difference of 11% for the 30 cm thickness of the elastic layer). For large thicknesses of the elastic layer, the theoretical model provides much higher values for the maximum deformation of the base layer than the simulations.

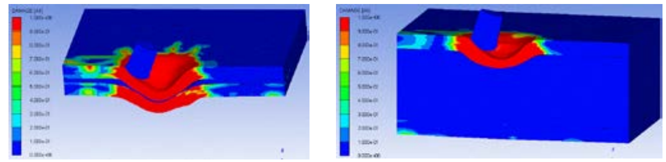

a) Damage level at t=12.00 ms for a 10cm thickness of the elastic layer

b) Damage level at t=11.27 ms for a 150cm thickness of the elastic layer

Fig. 6 Damage levels for different thicknesses of the elastic layer

The level of damage of the base layer (varies from 0 - blue, which means no plastic deformation to 1 - red, which means that the material in that area suffers a complete damage) for the imposed thickness of the elastic layer, fig. 6, shows that the base layer is not affected when the thickness of the elastic layer (made of sand) has the value of 150 cm.

C. *The influence of the elastic layer material*

Three types of material were tested for the elastic layer: sand, soil and LECA [11]. For each studied case the same thickness of 150 cm for the elastic layer was used, the other characteristics being the same as in Table 1. The variation of the maximum deformation of the base layer depending on the type of material used for the elastic layer can be seen in fig. 7.

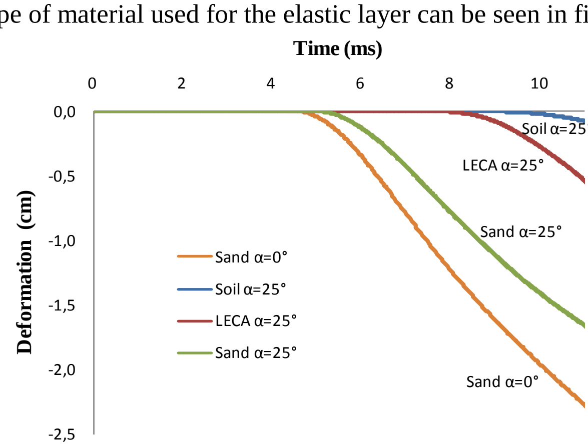

Fig. 7 The influence of the elastic layer material on the maximum deflection of the base layer

It was found that the type of soil material used for the simulation [10] can be a good solution to mitigate the shock produced as a result of the bomb impact, followed by the LECA and the sand. Also, the analysis of the level of destruction, fig. 8, shows that the angle of the bomb when it moves through the rigid layer changes depending on the compressibility of the elastic layer (fig. 8 and fig. 6b).

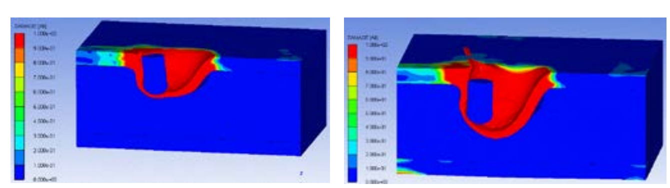

a) Level of damage at t=16.25 ms (elastic layer: material – soil, thickness - 150 mm)

b) Level of damage at t=15.40ms (elastic layer: material – LECA, thickness - 150 mm)

Fig. 8 Level of damage of the base layer function of the elastic layer material

D. The influence of the angle of the bomb impact

To study the influence of the angle of the bomb impact on the deformation of the base layer, an angle of zero degrees was chosen instead of the value of 25° used for all other cases. The elastic layer was made of sand and had a thickness of 150 cm and the other characteristics of the layers and the bomb are presented in Table 1.

By analyzing fig. 7 it can be seen that the effect of the bomb impact on the base layer is maximum when the impact angle of the bomb is zero. This conclusion can also be reached by comparing the level of damage of the base layer for an angle of impact of 25°, fig. 6b and 0°, fig 9 for the same type of material and thickness of the elastic layer.

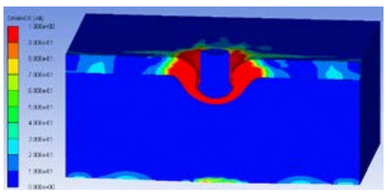

Fig. 9 Level of damage for an impact angle of 0° at t=10.42ms (elastic layer: material – sand, thickness - 150 cm)

E. The influence of the bomb impulse

To determine the influence of the bomb impulse at the contact point on the deformation of the base layer, six different bomb velocities were used, the other characteristics of the layers and bomb being presented in Table 1.

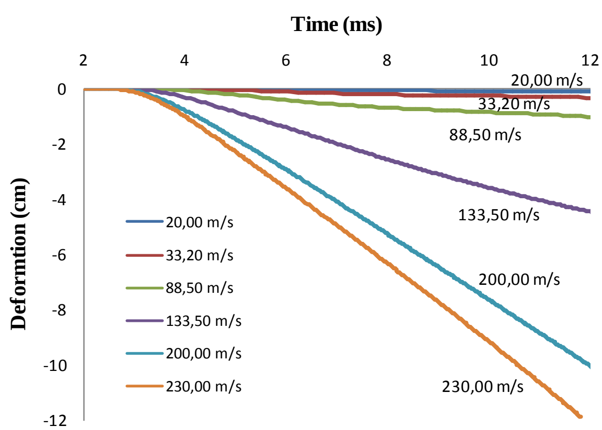

Fig. 10 The influence of the bomb impulse on the maximum deformation of the base layer

The variation of the maximum deformation of the base layer depending on the bomb impulse is shown in fig. 10.

It can be noticed that the maximum deformation of the base layer increases as the value of the velocity at the contact point increases, fig. 10. At velocities of 200 m/s and above, the maximum deformation value of the base layer exceeds 10 cm. By comparing the values of the analytical models (fig. 4) with the ones from the numerical model (fig. 10), it can be observed that the theoretical models lead to lower values of the maximum deformations. The analysis of the deformation of the base layers, fig. 11, shows that at low speeds of the bomb the ricochet of the bomb appears at the point of contact due to the resistance of the concrete, a phenomenon that cannot be surprised in theoretical models.

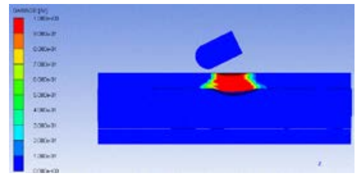

a) Level of damage at t=6.70 ms, bomb velocity = 20,00 m/s

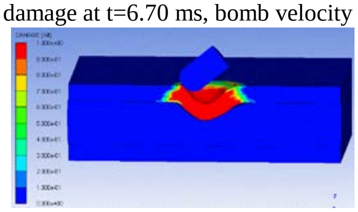

b) Level of damage at t=5.56 ms, bomb velocity = 32,20 m/s

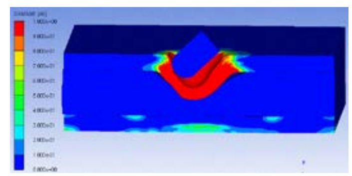

c) Level of damage at t=52.17 ms, bomb velocity = 88,50 m/s

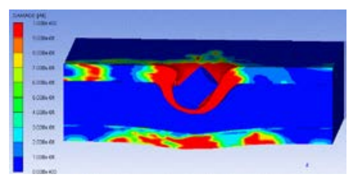

d) Level of damage at t=11.83 ms, bomb velocity = 230 m/s

Fig. 11 Level of damage of the base layer depending on the bomb impulse at the contact point

F. The influence of the thickness of the base layer

To determine the influence of the base layer thickness on the deformation of the same layer, different levels of thickness were used (30, 50, 80 and 100 cm). The thickness of the rigid layer was 30 cm and that of the elastic layer (made of sand) 80 cm. The other characteristics are those presented in table 1. The variation of the maximum deformation of the base layer depending on its thickness is shown in fig. 12.

ISBN: 978-1-61804-288-0

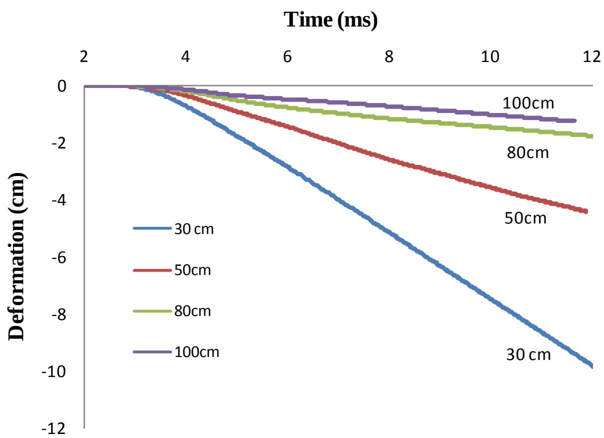

Fig. 12 The influence of the thickness of the base layer on its maximum deformation

It is obviously found that the maximum deformation of the base layer decreases with the increasing of its thickness. Also, it was interesting to make a comparison between the maximum deformation of the base layer depending on the thicknesses of the different base (SP) and elastic (SE) layers, fig. 13. It can be seen that almost the same maximum deformations are obtained for the following combinations of layers:

- 30 cm SP and 150 cm SE ~ 80 cm SP and 80 cm SE;
- 30 cm SP and 100 cm SE ~ 50 cm SP and 80 cm SE.

This comparison (fig. 13) shows that it is more economical to use a thicker elastic layer (SE of 150 cm or SE of 100 cm - sand) than a thinner base layer (SP of 80 cm or SP of 50 cm– concrete) to obtain the same relative level of protection.

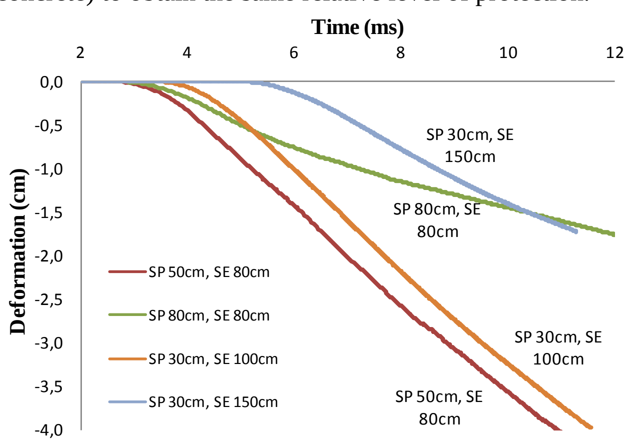

Fig. 13 The comparative analysis of the maximum deformation of the base layer depending on the thicknesses of the base (SP) and elastic (SE) layers

G. The interpretation of the results for the explosion

In order to analyze the results of different explosion scenarios, a comparison between the graphs of the maximum deformations of the base layer was used, fig. 14 (a detailed graphical representation in the time interval 4 s to 6 s is shown in fig. 14b). First, the detonation in contact with rigid layer produces a deformation of the base layer represented by *Contact Detonation SR (SE – sand)* curve, fig. 14a.

When the rigid layer is perforated and the detonation occurs inside the elastic layer (curves *Explosion in SE-sand* and *Explosion in SE-LECA)*, the deformation of the base layer is higher for sand than LECA, fig. 14b. Also, starting time for the deformation of base layer is higher for LECA than sand, that means the LECA material is more compressible than sand. Second, the maximum deformation of the base layer (SP) when the bomb perforated the rigid layer (SR), passed through the elastic layer (SE) of sand and came into contact with the base layer is presented in figure 14a (*Bomb impact (SE-sand)*). The detonation of the explosive charge in contact with the base layer (*Contact detonation SP (SE – sand)*) produces a total destruction of the base layer, which was confirmed by the destruction level of the base layer, fig. 15. The time shifting of the curves in fig. 14 is due to the different times when the impact or explosion is produced.

It is interesting to follow the slope of the graphs in fig. 14. The slope deformation produced by the advancing bomb is less pronounced compared to those produced by the explosion of the charge of the bomb. As the detonation occurs closer to the base layer, the slope of the curve increases (the slope of the *Contact detonation SR (SE-sand)* curve is smoother than the slope of the curve *Explosion in SE (SE-LECA*), which in turn is less than that for the *Contact detonation SP (SE-sand)* curve).

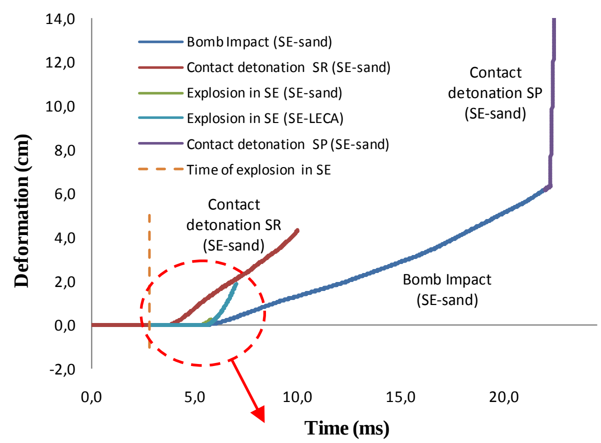

a)

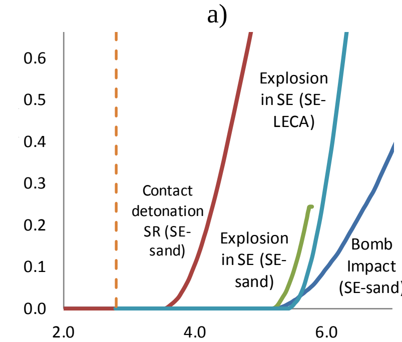

b)

Fig. 14 The comparative analysis of the maximum deformation of the base layer depending on different explosion scenarios

ISBN: 978-1-61804-288-0

Also, it appears that the starting time for the base layer deformation for the *Contact detonation SR (SE-sand)* of 4 ms is smaller than the starting time for the *Bomb impact*, of 5.9 ms. The explanation may be that the speed of propagation of the shock wave produced after the detonation of the explosive charge is higher than the shock wave resulting from the impact of the bomb.

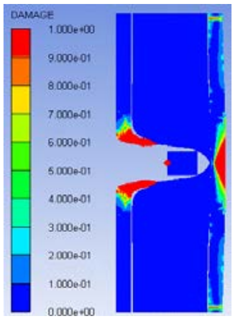

Level of damage at t=21.93 ms, (the initiation of the explosive charge)

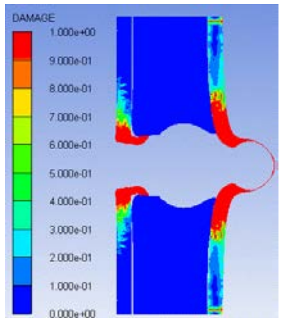

Level of damage at t=24.50ms

Fig. 15 Level of damage for the base layer when the explosive charge is detonated in contact with the base layer

V. CONCLUSIONS

The numerical simulations revealed that for the bomb characteristics taken into account (velocity at the contact point - 200 m/s and 25° impact angle) and for the configuration of the slab with three layers of protection (rigid, elastic and base layer), the thickness of the elastic layer consisting of sand must be of at least 150 cm in order for the supporting layer not to suffer any damage.

By introducing the material of the elastic layer as a parameter, it was found that the best attenuation material for the impact scenario is the soil material (soil type prairie with 7% moisture [10]), followed by sand at a small difference. For the explosion, the best mitigation is obtained using the LECA material, but the differences from the soil and sand are small and the costs of the materials have to be taken into account.

Using a larger number of layers does not always provide better results in terms of deformation of the base layer. It was found that the elastic layer thickness (whose thickness can be changed with lower costs) plays an important role in reducing the deflection of the base layer. As the elastic layer thickness increases, better results are obtained when it works alone, not distributed in several layers, even if between those layers an additional rigid layer is also added.

In the case of the detonation of the explosive charge it was found that the level of destruction of the base layer increases as the explosion occurs closer to it and the blast shock wave mitigation is more efficient for the LECA type material than for sand or soil.

ACKNOWLEDGMENT:

This paper has been financially supported within the project entitled "*Horizon 2020 – Doctoral and Postdoctoral Studies: Promoting the National Interest through Excellence, Competitiveness and Responsibility in the Field of Romanian fundamental and Applied Scientific Research*", contract number POSDRU/159/1.5./140106. This project is co-financed by the European Social Fund through the Sectorial Operational Programme for Human Resources Development 2007/2013. Investing in people!

REFERENCES

[1] Z. Hongyuan, M. Guowei - *Double-layer floor to mitigate in-structure shock of underground structures: A conceptual design*, Engineering Structures, 35 (2012), pp. 314–321.

[2] Y. Lu - *Underground blast induced ground shock and its modelling using artificial neural network*, Computers and Geotechnics, Volume 32, Issue 3, April 2005, pp. 164–178.

[3] J.C. Li, H.B. Li, G.W. M, Y.X. Zhou - *Assessment of underground tunnel stability to adjacent tunnel explosion*, Tunnelling and Underground Space Technology 35 (2013) pp. 227–234.

[4] H.L. Chen , Z.C. Xia , J.N. Zhou , H.L. Fan, F.N. Jin - *Dynamic responses of underground arch structures subjected to conventional blast loads: Curvature effects*, Archives of Civil and Mechanical Engineering, 13 (2013) pp. 322–333.

[5] H.L. Chen, J. Zhou, H. Fan, F.Jin, Y. Xu, Y. Qiu - *Dynamic responses of buried arch structure subjected to subsurface localized impulsive loading: Experimental study*, International Journal of Impact Engineering 65 (2014) pp. 89-101.

[6] P. Lardy - *Sur une methode nouvelle de resolution du probleme des dalles restangulaires encastrees*, Publications de l'Institut de Statique Appliquée de l'Ecole Polytechnique Fédérale de Zurich Vol. 13, 1953;

[7] G. Oprea, M. Josan – *Elements for multi-layered plates calculations*, Military Academy Publishing House, Bucharest, 1978 (in Romanian);

[8] D. Matahală – Study of the behavior of the layered plates under dynamic loadings used for military structures, PhD Thesis, Military Technical Academy, Bucharest, 2014

[9] Comite Euro-International du Beton – Concrete structures under impact and impulsive loading, Synthesis Report, Dubrovnik, Aout 1988

[10] D. Fiserova - *Numerical analyses of buried mine explosions with emphasis on effect of soil properties on loading*, PhD thesis, Defence College of Management and Technology, Cranfield University, England, 2006

[11] L. Laine - *Numerical Simulations Of Ground Shock Attenuation Layers For Swedish Rescu Centres And Shelters* , Proceedings of the 4th Asia-Pacific Conference on Shock and Impact Loads on Structures, CI-PremierPTE LTD, Singapore, November 2001, pp. 353-360

[12] W. Riedel, K. Thoma, S. Hiermaier, E. Schmolinske - *Penetration of Reinforced Concrete by BETA-B-500, Numerical Analysis using a New Macroscopic Concrete Model for Hydrocodes*. Proc. Internationales Symposium , Interaction of the Effects of Munitions with Structures, Berlin Strausberg, 03.-07. Mai 1999, pp 315 - 322

Forward Kinematic Analysis of an Industrial Robot

Daniel Constantin, Marin Lupoae, Cătălin Baciu, Dan-Ilie Buliga

Abstract— To be able to control a robot manipulator as required by its operation, it is important to consider the kinematic model in design of the control algorithm. In robotics, the kinematic descriptions of manipulators and their assigned tasks are utilized to set up the fundamental equations for dynamics and control.. The objective of this paper is to derive the complete forward kinematic model (analytical and numerical) of a 6 DOF robotic arm (LR Mate 200iC from Fanuc Robotics) and validate it with the data provided by robot's software.

Keywords — forward kinematic, Denavit-Hartenberg parameters, Robotic Toolbox

I. Introduction

Kinematics is the science of geometry in motion. It is restricted to a pure geometrical description of motion by means of position, orientation, and their time derivatives. In robotics, the kinematic descriptions of manipulators and their assigned tasks are utilized to set up the fundamental equations for dynamics and control [1]. These non-linear equations are used to map the joint parameters to the configuration of the robot system. The Denavit and Hartenberg notation [2],[3] gives us a standard methodology to write the kinematic equations of a manipulator. This is especially useful for serial manipulators where a matrix is used to represent the pose (position and orientation) of one body with respect to another.

There are two important aspects in kinematic analysis of robots: the *Forward Kinematics* problem and the *Inverse Kinematics* problem. Forward kinematics refers to the use of the kinematic equations of a robot to compute the position of the end-effector from specified values for the joint parameters Inverse kinematics refers to the use of the kinematics equations of a robot to determine the joint parameters that provide a desired position of the end-effector.

The purpose of this paper is to obtain the forward kinematic analysis for the Fanuc LR Mate 200iC Robot, to make model of robot using Robotic Toolbox® for MATLAB® and validate it with the data provided by robot's software. The information can be use in the future design and production of the robot to make it faster and more accurate postwar period for the defensive works executed in different countries around the globe.

Daniel Constantin is with Military Technical Academy, Bucharest, Romania; 39-49 George Cosbuc Blv., 050141, phone +40213354660; fax: +40213355763; e-mail: dconstantin77@yahoo.com.

Marin Lupoae is with Military Technical Academy, Bucharest, Romania; e-mail: mlupoae@mta.ro.

Cătălin Baciu is with Military Technical Academy, Bucharest, Romania; e-mail: baciucatalin2001@yahoo.com.

Dan-Ilie Buliga is with Military Technical Academy, Bucharest, Romania; e-mail: dan.ilie.buliga@gmail.com.

II. Theoretical aspects

The forward kinematics problem is concerned with the relationship between the individual joints of the robot manipulator and the position and orientation of the tool or end-effector.

A serial-link manipulator comprises a set of bodies, called links, in a chain and connected by joints. A link is considered a rigid body that defines the spatial relationship between two neighboring joint axes. The objective of forward kinematic analysis is to determine the cumulative effect of the entire set of joint variables.

The Denavit and Hartenberg notation for describing serial-link mechanism geometry is a fundamental tool for robot analysis. Given such a description of a manipulator it can be use for established algorithmic techniques to find kinematic solutions, Jacobians, dynamics, motion planning and simulation.

In order to perform a forward kinematic analysis of a serial-link robot, based on Denavit - Hartenberg (D-H) notation it is necessary to achieve a five steps algorithm:

1. Numbering the joints and links

A serial-link robot with n joints will have $n+1$ links. Numbering of links starts from *(0)* for the fixed grounded base link and increases sequentially up to *(n)* for the end-effector link. Numbering of joints starts from *1*, for the joint connecting the first movable link to the base link, and increases sequentially up to n. Therefore, the link *(i)* is connected to its lower link *(i - 1)* at its proximal end by joint *(i)* and is connected to its upper link *(i + 1)* at its distal end by joint *(i + 1)*.

2. *Attaching a local coordinate reference frame* for each link *(i)* and joint *(i+1)* based on the following method, known as Denavit - Hartenberg convention [2], [3].

Fundamentally is necessary to describe the pose of each link in the chain relative to the pose of the preceding link. It is expected that this to comprise six parameters, one of which is the joint variable the parameter of the joint that connects the two links. The Denavit-Hartenberg formalism [2]-[4], [6] uses only four parameters to describe the spatial relationship between successive link coordinate frames, and this is achieved by introducing two constraints to the placement of those frames the axis x_i is intersecting or perpendicular to the axis z_{i-1}. The choices of coordinates frames are also not unique, different people will derive different, but correct, coordinate frame assignments.

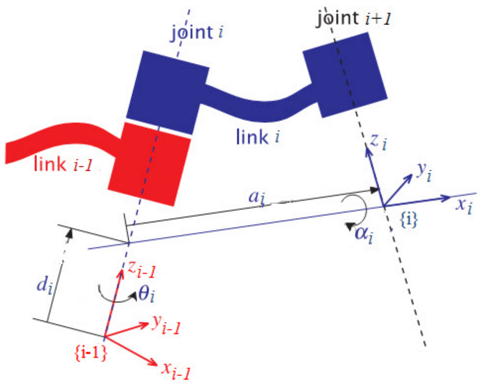

Fig. 1 D-H frames allocation and parameters (adapted from [4])

In this paper it is used the standard D-H notation [4]. It begins by assignation of z_i axes. There are two cases to consider: if joint *(i +1)* is revolute, z_i is the axis of revolution of joint *(i +1)* and if joint *(i +1)* is prismatic, z_i is the axis of translation of joint *(i +1).*

Once it was established the z_i-axes for the links, it must establish the base frame $\{0\}$. The choice of a base frame is nearly arbitrary. Once frame $\{0\}$ has been established, begins an iterative process in which it is defined frame $\{i\}$ using frame $\{i-1\}$.

In order to set up frame $\{i\}$ it is necessary to consider three cases:

(a) *Axes* z_{i-1} *and* z_i *are not coplanar* (fig.1): The line containing the common normal z_{i-1} to z_i define x_i axis and the point where this line intersects z_i is the origin of frame $\{i\}$.

(b) *Axis* z_{i-1} *is parallel to axis* z_i: The origin of frame $\{i\}$ is the point at which the normal that passes through origin of frame $\{i-1\}$ intersects the z_i axis. The axis x_i is directed from origin of frame $\{i\}$, toward z_{i-1} axis, along the common normal.

(c) *Axis* z_{i-1} *intersects axis* z_i: The origin of frame $\{i\}$ is at the point of intersection of axes z_{i-1} and z_i. The axis x_i is chosen normal to the plane formed by axes z_{i-1} and z_i. The positive direction is arbitrary.

In all cases the y_i-axis is determined by the right-hand rule: $y_i = z_i \times x_i$.

3. Establish D-H parameters for each link

The fundamentals of serial-link robot kinematics and the Denavit-Hartenberg [2], [3] notation are well covered in standard texts [6]. Each link is represented by two parameters: the *link length* (a), and *link twist* (α), which define the relative location of the two attached joint axes in space. Joints are also described by two parameters: the *link offset* (d), which is the distance from one link to the next along the axis of the joint, and the *joint angle* (θ), which is the rotation of one link with respect to the next about the joint axis. For a revolute joint θ_i is the joint variable and d_i is constant, while for a prismatic joint d_i is variable and θ_i is constant. The link length and link twist are constant.

Using the attached frames (fig.1), the four parameters that locate one frame relative to another are defines as:

- θ_i (joint angle) is the angle between the x_{i-1} and x_i axes about the z_{i-1} axis;
- d_i (link offset) is the distance from the origin of frame $\{i-1\}$ to the x_i axis along the z_{i-1} axis;
- a_i (link length) is the distance between the z_{i-1} and z_i axes along the x_i axis; for intersecting axes is parallel to $z_{i-1} \times z_i$;
- α_i (link twist) is the angle between the z_{i-1} and z_i axes about the x_i axis.

4. Calculate the matrix of homogeneous transformation for each link.

The reference frame $\{i\}$ can be located relative to reference frame $\{i-1\}$ (fig.1) by executing a rotation through an angle θ_i about z_{i-1} axis, a translation of distance d_i along z_{i-1} axis, a translation of distance a_i along x_i axis and a rotation through an angle α_i about x_i axis. Trough concatenation of these individual transformations, the equivalent homogeneous transformation is:

$$^{i-1}T_i(\theta_i, d_i, a_i, \alpha_i) = R_z(\theta_i) \cdot T_z(d_i) \cdot T_x(a_i) \cdot R_x(\alpha_i) \qquad (1)$$

where $R()$ and $T()$ are the 4×4 homogeneous transformation matrix for rotation and translation that are well covered in literature [1], [4] and [6].

Equation (1) can be expanded as:

$$ {}^{i\text{-}1}T_i = \begin{bmatrix} c\theta_i & -s\theta_i \cdot c\alpha_i & s\theta_i \cdot s\alpha_i & a_i \cdot c\theta_i \\ s\theta_i & c\theta_i \cdot c\alpha_i & -c\theta_i \cdot c\alpha_i & a_i \cdot s\theta_i \\ 0 & s\alpha_i & c\alpha_i & d_i \\ 0 & 0 & 0 & 1 \end{bmatrix} \qquad (2) $$

where: $c\theta_i$ is $\cos(\theta_i)$ and $s\theta_i$ is $\sin(\theta_i)$.

Since the homogeneous transformation matrix of the frame $\{i\}$ related to the frame $\{i\text{-}1\}$, ${}^{i\text{-}1}T_i$ is a function of a single variable, it turns out that three of the above four quantities are constant for a given link, while the fourth parameter, θ_i for a revolute joint and d_i for a prismatic joint, is the joint variable.

5. Compute the kinematics equations of the robot

The coordinate transformations along a serial robot consisting of n links form the kinematics equations of the robot is:

$$ {}^{0}T_n = \prod_{i=1}^{n} {}^{i\text{-}1}T_i \qquad (3) $$

where ${}^{i\text{-}1}T_i$ is the homogeneous transformation matrix of the frame $\{i\}$ related to the frame $\{i\text{-}1\}$.

The result will be a 4×4 matrix that gives us the information about orientation or rotation ($\boldsymbol{n}$ - normal vector, $\boldsymbol{o}$ - orientation vector, $\boldsymbol{a}$ - approach vector) matrix and position ($\boldsymbol{p}$ - vector) vector of the last frame $\{n\}$ relative to the first frame $\{0\}$:

$$ {}^{0}T_n = \begin{bmatrix} \boldsymbol{n} & \boldsymbol{s} & \boldsymbol{a} & \boldsymbol{p} \\ 0 & 0 & 0 & 1 \end{bmatrix} \qquad (4) $$

III. ANALYTICAL FORWARD KINEMATIC ANALYSIS OF 6 DOF - LR MATE 200IC ROBOT

The LR Mate 200iC is an industrial robot manufactured by FANUC Robotics and designed for a variety of manufacturing and system process. We have that type of robot in our Robotics Laboratory. The manipulator provides a payload of 5 kg capacity in a compact modular construction and reach of 704 mm with enough flexibility and higher reliability trough the harmonic drives in its six-axis. The LR Mate 200*i*C Robot is an electric servo-driven mini robot offering best-in-class performance in a light, efficient, accurate and nimble package. This robot is ideal for fast and precise applications in all environments [5].

From the fig.2 it can be seen that the LR Mate 200iC has a serial 6-DOF robotic arm with six revolute joints ($R \perp R \parallel R \perp R \perp R \perp R$).

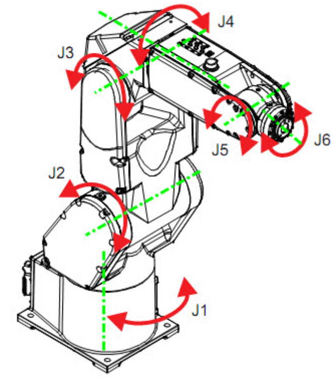

Fig. 2 Joints of LR Mate 200iC Robot from Fanuc Corporation

In order to make a forward kinematic analysis for of LR Mate 200iC Robot it is numbered links and joint and it is attached local coordinate reference frames (fig.3). The origin of frame $\{0\}$ it is choosen to be intersection of axis from joint (1) with a perpendicular plan that contains the axis of joint (2).

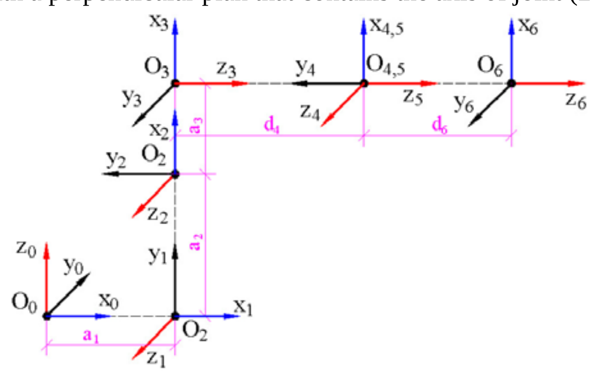

Fig. 3 Coordinate reference frames for LR Mate 200iC Robot

The Table 1 summarizes the D-H parameters for each link as follows from fig.2 in accord with step 4 from previous section:

Table 1 D-H parameters for LR Mate 200iC Robot

Link	θ_i	d_i	a_i	α_i
1	θ_1	0	a_1	$\pi/2$
2	θ_2	0	a_2	0
3	θ_3	0	a_3	$\pi/2$
4	θ_4	d_4	0	$-\pi/2$
5	θ_5	0	0	$\pi/2$
6	θ_6	d_6	0	0

According to equations (2) and (3) it is obtain matrix of homogeneous transformation for each link and we compute the kinematics equations of the robot:

$$
\begin{aligned}
{}^{0}T_6 = & \begin{bmatrix} c_1 & 0 & s_1 & a_1 \cdot c_1 \\ s_1 & 0 & -c_1 & a_1 \cdot s_1 \\ 0 & 1 & 0 & 0 \\ 0 & 0 & 0 & 1 \end{bmatrix} \cdot \begin{bmatrix} c_2 & -s_2 & 0 & a_2 \cdot c_2 \\ s_2 & c_2 & 0 & a_2 \cdot s_2 \\ 0 & 0 & 1 & 0 \\ 0 & 0 & 0 & 1 \end{bmatrix} \cdot \\
& \cdot \begin{bmatrix} c_3 & 0 & s_3 & a_3 \cdot c_3 \\ s_3 & 0 & -c_3 & a_3 \cdot s_3 \\ 0 & 1 & 0 & 0 \\ 0 & 0 & 0 & 1 \end{bmatrix} \cdot \begin{bmatrix} c_4 & 0 & -s_4 & 0 \\ s_4 & 0 & c_4 & 0 \\ 0 & -1 & 0 & d_4 \\ 0 & 0 & 0 & 1 \end{bmatrix} \cdot \qquad (5) \\
& \cdot \begin{bmatrix} c_5 & 0 & s_5 & 0 \\ s_5 & 0 & -c_5 & 0 \\ 0 & 1 & 0 & 0 \\ 0 & 0 & 0 & 1 \end{bmatrix} \cdot \begin{bmatrix} c_6 & -s_6 & 0 & 0 \\ s_6 & c_6 & 0 & 0 \\ 0 & 0 & 1 & d_6 \\ 0 & 0 & 0 & 1 \end{bmatrix} = \begin{bmatrix} n_x & o_x & a_x & p_x \\ n_y & o_y & a_y & p_y \\ n_z & o_z & a_z & p_z \\ 0 & 0 & 0 & 1 \end{bmatrix}
\end{aligned}
$$

where:

$$
\begin{aligned}
n_x &= c_1(c_{23}(c_4c_5c_6 - s_4s_6) - s_{23}s_5c_6) + s_1(s_4c_5c_6 - c_4s_6) \\
n_y &= s_1(c_{23}(c_4c_5c_6 - s_4s_6) - s_{23}s_5c_6) - c_1(s_4c_5c_6 - c_4s_6) \\
n_z &= s_{23}(c_4c_5c_6 - s_4s_6) - c_{23}s_5c_6 \\
o_x &= c_1(-c_{23}(c_4c_5s_6 + s_4c_6) + s_{23}s_5s_6) - s_1(s_4c_5s_6 - c_4c_6) \\
o_y &= s_1(-c_{23}(c_4c_5s_6 + s_4c_6) + s_{23}s_5s_6) + c_1(s_4c_5s_6 - c_4c_6) \\
o_z &= -s_{23}(c_4c_5s_6 + s_4c_6) - c_{23}s_5s_6 \qquad (6) \\
a_x &= c_1(c_{23}c_4s_5 + s_{23}c_5) + s_1s_4s_5 \\
a_y &= s_1(c_{23}c_4s_5 + s_{23}c_5) - c_1s_4s_5 \\
a_z &= s_{23}c_4s_5 - c_{23}c_5 \\
p_x &= c_1(a_1 + a_2c_2 + a_3c_{23} + d_4s_{23} + d_6(c_{23}c_4s_5 + s_{23}c_5)) + d_6s_1s_4s_5 \\
p_y &= s_1(a_1 + a_2c_2 + a_3c_{23} + d_4s_{23} + d_6(c_{23}c_4s_5 + s_{23}c_5)) - d_6c_1s_4s_5 \\
p_z &= a_2s_2 + a_3s_{23} - d_4c_{23} + d_6(s_{23}c_4s_5 - c_{23}c_5)
\end{aligned}
$$

In the equations (6) it is make the following notation: $c_i = \cos(\theta_i)$, $s_{ij} = \sin(\theta_i + \theta_j)$.

IV. NUMERICAL FORWARD KINEMATIC ANALYSIS OF 6 DOF - LR MATE 200IC ROBOT AND COMPARISONS

To carry out the numerical forward kinematic I used Robotic Toolbox ® (version 9.9) for MATLAB® developed by Peter Corke professor at Queensland University of Technology. The Toolbox has always provided many functions that are useful for the study and simulation of classical arm-type robotics, for example such things as kinematics, dynamics, and trajectory generation. The Toolbox provides functions for manipulating and converting between datatypes such as: vectors; homogeneous transformations; roll-pitch-yaw and Euler angles and unit-quaternions which are necessary to represent 3-dimensional position and orientation. These parameters are encapsulated in MATLAB objects, robot objects can be created by the user for any serial-link manipulator. It can operate with symbolic values as well as numeric. The Toolbox is based on a very general method of representing the kinematics and dynamics of serial-link manipulators [4]. The Robotic Toolbox is an open-source, available for free and its routines are generally written in a straightforward manner which allows for easy understanding [7].

Numerical values for LR Mate 200iC Robot from [5] are:

$a_1 = 0.075[m]$, $a_2 = 0.300[m]$, $a_3 = 0.075[m]$,

$d_4 = 0.320[m]$ and $d_6 = 0.080[m]$.

In order to create a model of the LR Mate 200iC Robot using Robotic Toolbox , the D-H parameters from Table 1 have been used.

```
%The LR Mate 200iC from FANUC Robotics
L(1)=Link([0  0 0.075 pi/2 0]);
L(2)=Link([0 0 0.3 0 0]);
L(3)=Link([0 0 0.075 pi/2 0]);
L(4)=Link([0 0.32 0 -pi/2 0]);
L(5)=Link([0 0 0 pi/2 0]);
L(6)=Link([0 0.08 0 0 0]);
Fanuc = SerialLink(L, 'name', 'LRMate200iC');
```

Fig. 4 Creating the model of robot in Robotic Toolbox

Firstly a vector of $Link(\theta_i, d_i, a_i, \alpha_i, \sigma_i)$ objects was created and after that it was used *SerialLink* command to create the model of robot with the name LRMATE200iC (fig.4). The parameters of *Link* object are the D-H parameters defined in section 2: joint angle (θ_i), link offset (d_i), link length (a_i), link twist (α_i) and a parameter for type of joint σ_i ($\sigma_i = 0$ for revolute joint and $\sigma_i = 1$ for prismatic joint).

The *fkine*(**q**) method (fig.5) use for calculation the same algorithm presented in section 2 [4], [7] and is the pose of the robot end-effector as an SE(3) homogeneous transformation (4×4) for the joint configuration **q** ($1 \times \mathrm{n}$), where **q** is interpreted as the generalized joint coordinates. In case of LR Mate 200iC Robot (six revolute joints robot) the generalized joint coordinates is represented by a vector (1×6):

$$\mathrm{q} = [\theta_1 \;\; \theta_2 \;\; \theta_3 \;\; \theta_4 \;\; \theta_5 \;\; \theta_6] \qquad (7)$$

```
>> T=Fanuc.fkine([0 pi/2 0 0 0 0])

T =

    0.0000   -0.0000    1.0000    0.4750
    0.0000   -1.0000   -0.0000   -0.0000
    1.0000    0.0000   -0.0000    0.3750
         0         0         0    1.0000
```

Fig. 5 Homogeneous transformation of robot in Robotic Toolbox

A pose of the robot, based on the kinematic model, can be visualized graphically using *plot(**q**)* method (Line 3 in Table 2). A stick figure polyline joins the origins of the link coordinate frames [7].

It was implemented the equation (6) in a Matlab function in order to calculate the forward kinematics based on algorithm presented in section 2.

Table 2 Results

q	$\begin{bmatrix} 0 & \frac{\pi}{2} & 0 & 0 & 0 & 0 \end{bmatrix}$	$\begin{bmatrix} 0 & \frac{\pi}{4} & \frac{5\pi}{12} & -\frac{\pi}{3} & -\frac{\pi}{2} & 0 \end{bmatrix}$	$\begin{bmatrix} \frac{\pi}{12} & \frac{\pi}{3} & -\frac{\pi}{12} & \frac{\pi}{6} & -\frac{\pi}{4} & \frac{\pi}{6} \end{bmatrix}$
FK eq. (6)	$\begin{matrix} 0.0000 & -0.0000 & 1.0000 & 0.4750 \\ 0.0000 & -1.0000 & -0.0000 & -0.0000 \\ 1.0000 & 0.0000 & -0.0000 & 0.3750 \\ 0 & 0 & 0 & 1.0000 \end{matrix}$	$\begin{matrix} 0.8660 & -0.4330 & 0.2500 & 0.5468 \\ 0.0000 & -0.5000 & -0.8660 & -0.0693 \\ 0.5000 & 0.7500 & -0.4330 & 0.4024 \\ 0 & 0 & 0 & 1.0000 \end{matrix}$	$\begin{matrix} 0.8010 & -0.5980 & -0.0268 & 0.4850 \\ -0.5506 & -0.7537 & 0.3588 & 0.1592 \\ -0.2348 & -0.2727 & -0.9330 & 0.0119 \\ 0 & 0 & 0 & 1.0000 \end{matrix}$
Robot Poses (RTB)	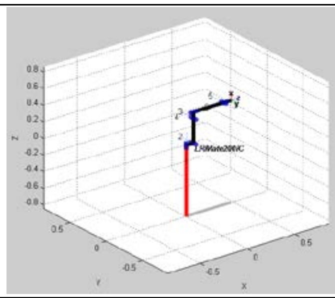	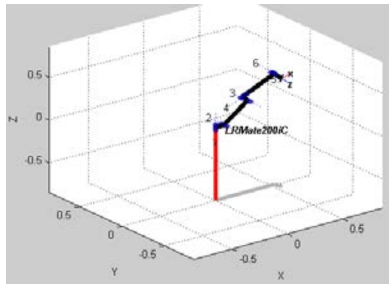	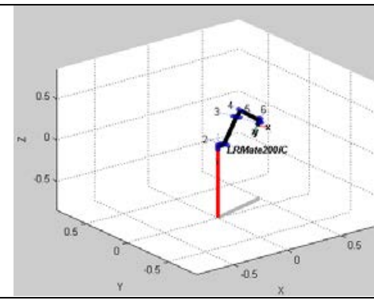
FK (RTB)	$\begin{matrix} 0.0000 & -0.0000 & 1.0000 & 0.4750 \\ 0.0000 & -1.0000 & -0.0000 & -0.0000 \\ 1.0000 & 0.0000 & -0.0000 & 0.3750 \\ 0 & 0 & 0 & 1.0000 \end{matrix}$	$\begin{matrix} 0.8660 & -0.4330 & 0.2500 & 0.5468 \\ 0.0000 & -0.5000 & -0.8660 & -0.0693 \\ 0.5000 & 0.7500 & -0.4330 & 0.4024 \\ 0 & 0 & 0 & 1.0000 \end{matrix}$	$\begin{matrix} 0.8010 & -0.5980 & -0.0268 & 0.4850 \\ -0.5506 & -0.7537 & 0.3588 & 0.1592 \\ -0.2348 & -0.2727 & -0.9330 & 0.0119 \\ 0 & 0 & 0 & 1.0000 \end{matrix}$
LR Mate 200iC Robot poses			
Angles Robot	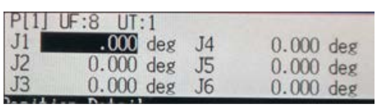	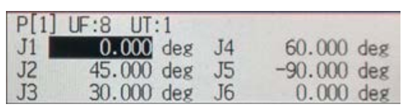	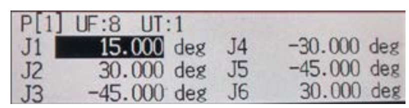
FK Robot	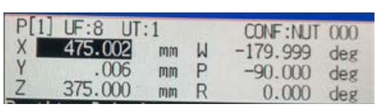	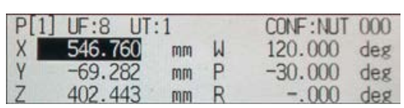	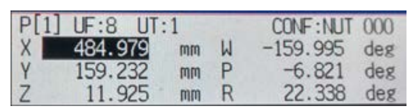

In order to validate the model of forward kinematic further tests were conducted. It was imposed three generalized coordinate vector **q** (line 1 in table 2) to be use. The first pose it is named the rest pose. The result from use of equation (6) is presented in Table 2 (line 2). In the line 3 of Table 2 is presented the representation of the three pose using the *plot(**q**)* method from Robotic Toolbox. The homogeneous transformation for the joint configuration resulted from *fkine* method is presented in line 4 (Table 2). The real pose of LR Mate 200iC Robot for each **q** is presented in line 5 from Table 2. The line 6 from Table 2 presents the capture image from robot's teaching pendant (a control box for programming the motions of a robot) display of position joints angle. The final line from Table 2 presents teach pendant display capture image for the position and orientation (equivalent for kinematic equations).

The LR Mate 200iC Robot teach pendant use the following notation: Ji for joint angle (θ_i), $[X\ Y\ Z]$ for position vector $\mathrm{p} = [p_x\ p_y\ p_z]$ and $[W\ P\ R]$ for rotation angle around axes $[x\ y\ z]$.

For compute the rotation matrix of the homogeneous transformation it was the following equation:

$$R = Rot_z(R) \cdot Rot_y(P) \cdot Rot_x(W) \qquad (8)$$

where $Rot_z(R)$ is the rotation matrix around axis z with R angle ($Rot_y(P)$ and $Rot_x(W)$ similarly) [6].

Taking into account all from above it can be deliver the final homogeneous transformation of the robot:

$$T=\begin{bmatrix} R & p \\ 0 & 1 \end{bmatrix} \tag{9}$$

The difference between angle from teach pendant display and generalized coordinate vector (line 1 and 6 from Table 2) results as robot software makes some adjustments in order to protect robot from fails: angle of joint 2 is considered in opposite direction and added with $\pi/2$; when robot is moving axis 2 with a value, the same value is subtracted from angle of joint 3 and angle of joint 4 is considered in opposite direction. Note that graphical representation of the kinematic model (line 3) and capture of the robot (line 5) are the same.

Taking in consideration remarks from previous paragraph there is almost a perfect match between the three types of results: analytically, numerically and data from robot software (small differences appear on teach pendant display resulted from the precision of the robot ± *0.02[mm])[5].*

V. CONCLUSIONS

In this paper it was studied the forward kinematics by two different techniques: analytically using a five step algorithm derived from Denavit and Hartenberg notation and numerically using Robotic Toolbox ® for MATLAB® developed by Peter Corke. We make all calculation on LR Mate 200iC Robot from Fanuc Robotics and in order to validate the model of forward kinematic we compare the results with what robot's software measurated and displayed on teach pendant.

Summing up the results, it can be concluded that is almost perfect match between the three types of results: analytically, numerically and data from robot software.

Also this paper shows that using Robotic Toolbox ® for MATLAB® is a very useful and fast tool to study the forward kinematics for industrial robot.

The information can be use in the future design of the robot to make it faster and more accurate. In our future research we intend to concentrate on Inverse Kinematics, Jacobian and Dynamics of the robot LR MATE 200iC.

ACKNOWLEDGMENT:

This paper has been financially supported within the project entitled "*Horizon 2020 – Doctoral and Postdoctoral Studies: Promoting the National Interest through Excellence, Competitiveness and Responsibility in the Field of Romanian fundamental and Applied Scientific Research*", contract number POSDRU/159/1.5./140106. This project is co-financed by European Social Fund through Sectoral Operational Programme for Human Resources Development 2007/2013. Investing in people!

REFERENCES

[1] Paul, Richard (1981),"Robot manipulators: mathematics, programming, and control: the computer control of robot manipulators". MIT Press, Cambridge, MA. ISBN 978-0-262-16082-7.

[2] Denavit, Jacques; Hartenberg, Richard Scheunemann (1955), "A kinematic notation for lower-pair mechanisms based on matrices", Trans ASME J. Appl. Mech 23: 215–221.

[3] Hartenberg, Richard Scheunemann; Denavit, Jacques (1965), Kinematics synthesis of linkage, McGraw-Hill series in mechanical engineering, New York: McGraw-Hill, p. 435.

[4] Corke, Peter (2011) *Robotics, Vision and Control: Fundamental Algorithms in MATLAB*, ISBN 978-3-642-20144-8,. Springer Tracts in Advanced Robotics, 73. Springer, Berlin.

[5] Fanuc Robotics Europe S.A. (2015, February 12) , LR MATE SERIES, Retrieved from http://www.fanucrobotics.co.uk/ ~/media/Global/Files/Downloads/Datasheets/EN/LR_Mate_EN.ashx

[6] M. Spong, S. Hutchinson, and M. Vidyasagar, Robot modeling and control. Wiley, 2006.

[7] http://www.petercorke.com/RTB/robot.pdf

The performance measurement of the parabolic trough solar collector

Jozef Matusov, Peter Durcansky, Richard Lenhard

Abstract **-** The performance of the parabolic collector depends on several factors such as the size and shape of the parabolic trough collector, shape and area of the focal heat exchanger and optical properties. Another very important parameter that depends on the position and location of the solar collector is a value of the intensity solar irradiation. The performance measurement of the collector was carried out in the northern part of Slovakia, in the city Zilina. The captured solar energy in the form of sunlight by solar trough collector was concentrated to focal heat exchanger. Subsequently this energy was changing into a thermal energy. The thermal energy was led away from the focal heat exchanger by means of a heat-transfer medium. This paper deals with performance measurement of parameters of the parabolic trough collector with absorption area 10.25 m^2 and real area of focal heat exchanger 1.66 m^2.

Keywords – flow, intensity of solar radiation, parabolic trough collector, sensors

I. Introduction

Every type of solar collector captures sunlight and converts it to a thermal energy [1]. In general the collectors are divided into two main types. There are flat and concentrating collectors. For reaching higher temperatures of heat-transfer media are used the concentrating parabolic collectors [2].

In our case we have dealt with designing of the parabolic trough solar collector (Fig. 1), which would be able to heat the heat-transfer medium - air on approximately temperature 300 °C. This temperature and amount of energy would be sufficient for starting a hot-air engine [3]. Therefore, the overall dimensions of the collector based on the parameters of the hot-air engine. In the theoretical way it was expected, that thermal performance could be achieved 3-5 kW. After calculating the intensity of solar irradiation for city Zilina, was determined the surface area of collector 10.25 m2, where width is 1,744 m and length is 5.88 m. The reflective surface of collector is covered by special solar film from company 3M and its name is 3M Solar Film 1100 with 94% reflectivity [4].

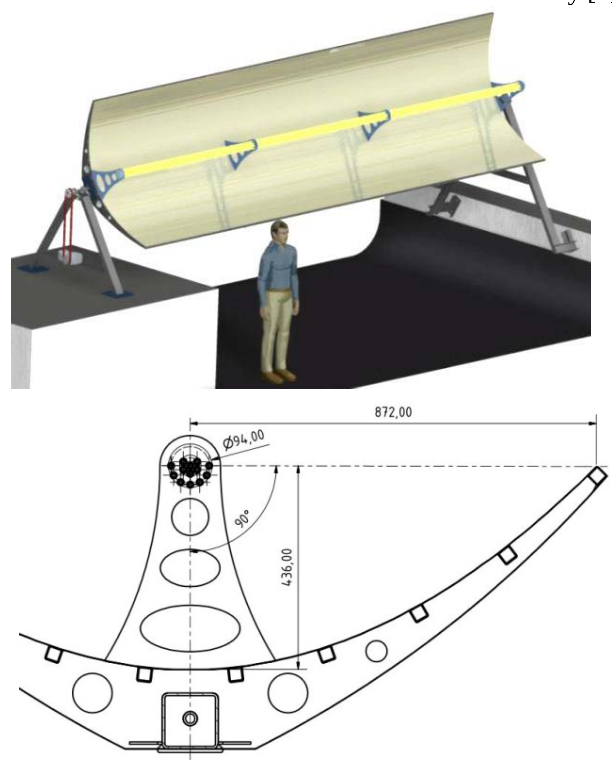

Fig. 1 The 3D model of the parabolic trough solar collector and main collector dimensions.

Another designed part of collector was the heat exchanger which was situated in the focus of parabolic trough solar collector. The estimated pressure value of the heat-transfer medium was 1 MPa in the whole system. This heat exchanger consists of thirteen pipes, and every pipe has outer diameter 12 mm, wall thickness 2 mm and length 5.869 m [11].

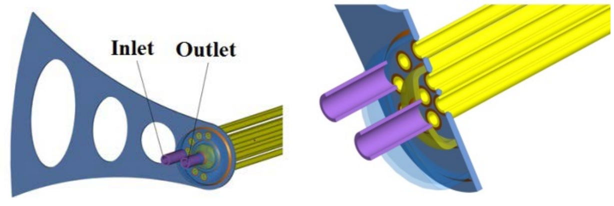

Fig. 2 Inlet and outlet working fluid - air from the heat exchanger.

This work has been supporting within the project "Research on new ways of converting heat from renewable energy sources to electricity using new advanced cycles" ITMS 26220220117 and by European regional development fund and From the State budget of Slovakia "Research Center, University of Zilina" ITMS 26220220183.

Numerical part of this work had been solved by Jozef Matusov in the Institute for Energy Systems and Thermodynamics, Vienna University of Technology, three-month internship supported by program Action Austria – Slovakia.

JOZEF MATUSOV is with the Research Centre, University of Zilina, Univerzitna 1, 010 26 Zilina, Slovakia (+421 42 5132858; e-mail: jozef.matusov@rc.uniza.sk).

PETER DURCANSKY is with the Research Centre, University of Zilina, Univerzitna 1, 010 26 Zilina, Slovakia (e-mail: peter.durcansky@rc.uniza.sk).

RICHARD LENHARD is with the Research Centre, University of Zilina, Univerzitna 1, 010 26 Zilina, Slovakia (e-mail: richard.lenhard @fstroj.uniza.sk).

The exchanger has two parts (Fig. 2). The first (9-12) - the entrance part consists of six pipes and the second (1-7) - the output part consists of the seven pipes [5]. The material of pipe is EN 1.7715 (14MoV6-3). The pipes of heat exchanger were painted with a special selective coating with an absorption coefficient of 0.9 [6].

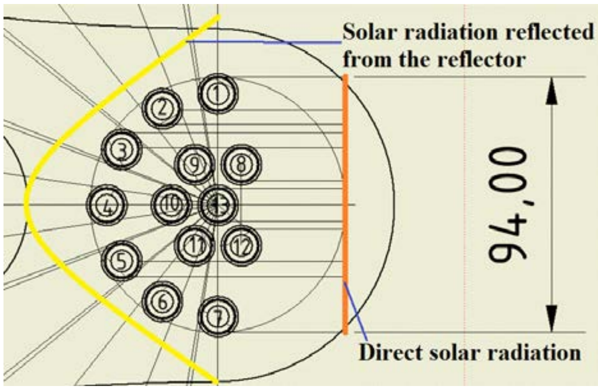

Fig. 3 Ideal impact of solar radiation to pipes of the focal heat exchanger.

The amount of incident energy for each pipe was found graphically in program Autodesk Inventor from the 3D model of the heat exchanger, which is identical to real one. In the figure (Fig. 3) is shown the solar radiation incidence on the pipes of heat exchanger and their mutual shielding. From the analysis were obtained the size of the light surfaces for every tube [7].

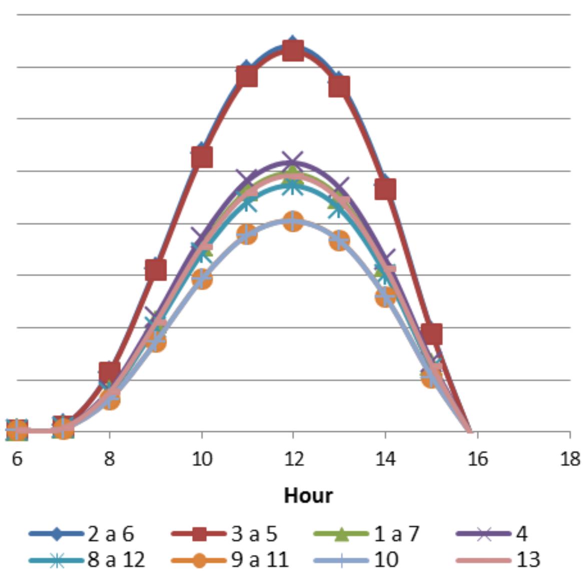

Fig. 4 Range of heat flow for every pipe of heat exchanger dependent on optical efficiency and date in year.

The graph (Fig.4) was constructed based on graphical analysis, optical efficiency calculation and amount of solar radiation during day where is see, that the greatest amount of heat flow passes through the tubes labeled 2 and 6. If the solar energy was absorbed to each pipe in same amount it would be ideal case.

II. Connecting Diagrams of Sensors and Components of the Measuring System

For determining of performance parameters of the parabolic trough collector was designed connection diagram of the main components and sensors. The type and range of sensors was chosen on the basis of the input and output values from the numerical calculation of exchanger collector. The amount of volumetric flow to heat exchanger was set to the condition that the velocity of the air in the pipes exchanger did not exceed 15 m/s. This condition was taken over from the theory of calculation exchangers to heat the working fluid air [8]. The number of sensors for measuring instantaneous values of temperature, pressure, flow rate and intensity of solar radiation is the same as is shown in the picture (Fig. 5).

For the performance measurement of focal heat exchanger was necessary to set up value of air flow rate [9]. The air passing through the focal exchanger was heated from the inlet temperature to the outlet temperature. Slide valve was installed for the setting pressure on the end of the output pipe from the exchanger. The compressed air was delivered to compressor from surrounding atmosphere and its capacity was 25 m^3 per hour with outlet pressure 900 kPa. From the compressor was delivering the air to pressure tank with capacity 1000 liters. The measurement was run on the basis of specified pressure and mass flow.

In the assembly of experimental devices were placed the following sensors of:

- pressure – Ahlborn FD 8214 12R with measuring range 0÷10 bar,
- temperature – air in the storage tank ZA9030-FS2 (Pt 100, from - 200 to 400°C), air in atmosphere FTA683-2 (Ni-Cr-Ni, from - 100 to 200°C), air in the heat exchanger ZA9030-FS (NiCr-Ni, till 870 °C),
- flow – rotary piston gas meter PREGAMAS G65 DN 50 with high-frequency pulser A1K, with number of impulses 14025 per $1m^3$,
- meteorological station – wind direction FV614, wind velocity FAV6152, intensity of solar radiation for global sunlight FLA613GS.

All sensors were connected to a measurement logger and from there subsequently to a computer. Measured values as a temperature, pressure, intensity of solar radiation and flow rate were saved to memory at 10 second intervals. These values were automatically written to a spreadsheet program Microsoft Excel.

III. Course of the Performance Measurements of the Parabolic Trough Solar Collector

The experimental measurements were possible done only during direct sunlight, because this type of collector isn't able to convert different type of solar sunlight to heat energy in the focal heat exchanger. If the amount of clouds are increasing, collector performance is decreasing rapidly.

During the measurement of performance trough solar

ISBN: 978-1-61804-288-0

collector, the permanent volume flow of the air was 3.75 dm^3/s. The excess pressure 0.5 bar was set up with a slide valve in the system. Other values were measured on the basis of the current state, which depended on the intensity of solar radiation, ambient temperature and an incidence angle of the solar radiation. For achieve the best possible performance, was necessary constantly turning an absorption area of trough solar collector directly to the Sun (Fig. 6).

Fig. 6. Turning of the trough solar collector during the measurement

The measurements of the parabolic trough collector usually lasted 140 -150 min.

In this paper are shown results of the measurement which started in time 9:05 with intensity of solar radiation 610 W/m^2. In this time was calculated optical efficiency 0.7 and heat flux 4.37 kW. The maximum value of the air temperature was 116.5 °C reached in 120th minute of measurement, when the intensity of solar radiation was 867 W/m^2.

During the measurement, we found that the contractor of collector fixed the ends of focal exchanger tubes and thus limited the effect of thermal expansion. This caused the change in the geometry pipes of the focal exchanger (Fig. 7) [12].

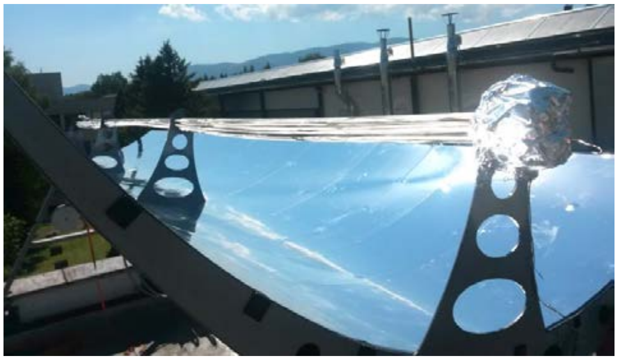

Fig. 7 Change the shape geometry of pipes in the focal heat exchanger.

IV. MEASUREMENT RESULTS

Heat performance of the focal heat exchanger was calculated according to calorimetric equation (1) from the inlet and outlet air temperature from the heat exchanger, the mass flow rate and specific heat capacity of air for a medium value of temperatures [10].

$$\dot{Q} = \dot{m}.c_p.(t_{outlet} - t_{inlet})\,[\mathrm{W}] \quad (1)$$

The focal exchanger is divided on two parts, therefore were recorded three types of temperatures which are shown in the graph (Fig. 8):

- inlet temperature to the heat exchanger (Inlet)
- temperature of the tube plate (Solar 1)
- outlet temperature from the heat exchanger (Outlet).

From these three temperatures were calculated performance of the first part and the second part of the exchanger and also the total performance of the focal heat exchanger.

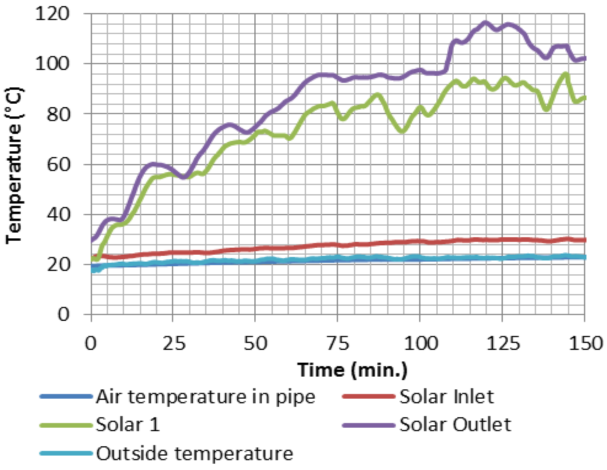

Fig. 8 Course of temperatures during performance measurement of the focal exchange

Mass flow rate of air was constant in the heat exchanger and its value was 6.7 g/s. In the graph (Fig. 10) is shown the dependence of the total performance on the intensity of incident solar radiation on 1 m^2. Significant effects on the performance of heating air in heat exchanger have: the ambient temperature, wind speed and direction, accuracy of rotation collector to the Sun. In the pictures (Fig. 9, Fig. 10) is possible see influence wind on overall performance during increasing the intensity of solar irradiation.

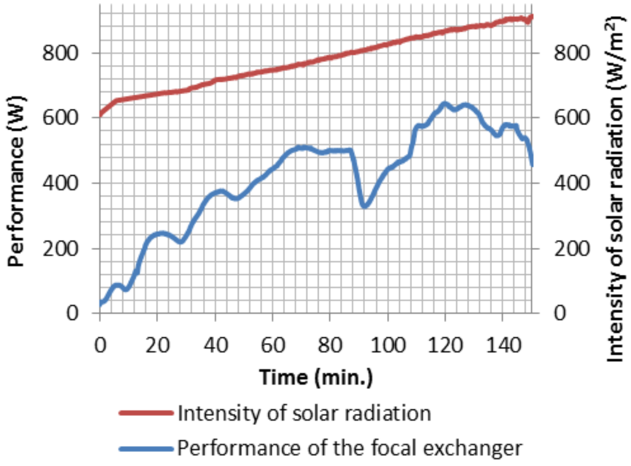

Fig. 10 Dependence of total performance of the focal heat exchanger on the intensity of solar radiation.

Numerical model was created according to theory Heat Transfer Analysis and Modeling of a Parabolic Trough Solar Receiver Implemented in Engineering Equation Solver [1]. Through calculation were obtained information about the energy gain for heating the heat transfer medium - air, depending on the amount of energy delivered by the energy source - the Sun. Considered parameters for calculation were: geometry exchanger and collector, optical characteristics, properties of heat transfer medium depending on pressure and temperature, inlet temperature, flow rate of the working fluid, the intensity of solar radiation, wind speed and ambient air temperature. From the calculation were obtained following values: the efficiency of the collector, the outlet temperature of the heat transfer medium, the quantities of heat energy, thermal, optical and pressure loss of the exchange. The equations include correlations, which is predicting the circumstances of in energy balance according to the type of the collector and the heat transfer medium, optical properties, and environmental influences.

V. Conclusion

From the measurements it was found, that the greatest impact on the performance of the focal exchanger had increase amount of clouds and the speed of wind which flows along the axis of focal exchanger. Another impact on the performances values was caused by changed shape of the pipes in the focal exchanger.

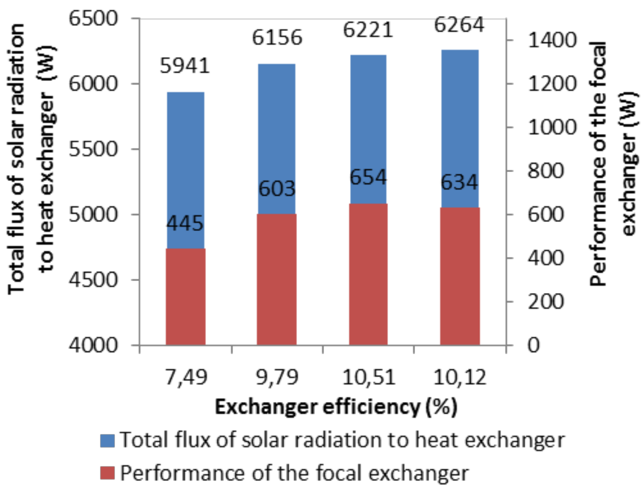

Fig. 11 Selected efficiency values

By calculation, but also by measurement were confirmed that the greatest loss of heat exchanger is caused by a free and forced convection to the surrounding area. The reducing of these losses would contribute to the increasing of overall performance. Therefore another research is dealing with the placing the focal exchanger into a glass-envelope with a vacuum process. This solution will increase the efficiency of heating the working medium.

During the measurements was achieved the highest efficiency 10.12% by heat performance 654.09 W (Fig. 11) and total flux value of solar radiation 6221 W.

Comparison of the measured values with mathematical model was done in program Excel, with the theoretical equations [1].

In this case is shown comparison, where was achieved the highest performance in the focal exchanger, under the following conditions:

- inlet air temperature at the exchanger 29.9 °C,
- air temperature at the tube plate with vaulted bottom 92.6 °C,
- outlet air temperature from the exchanger 116.5 °C,
- mass flow rate 6.7 g/s.
- absolute pressure 1.5 bar.
- heat flux of solar radiation incident on the exchanger 6220.7 W,
- wind speed 0.3 m/s and ambient air temperature 20.4 °C.

Required power obtained by calculating for heating of the air in the first part of the exchanger was 421.4 W, in the second part 162.3 W and total power required to heat the air was 583.7 W. From the entered values were calculated the losses which are shown in Table I.

Type of losses	1st part of exchanger	2nd part of exchanger	Total losses
Heat loss by free convection	1000.5 W	1572.5 W	2573 W
Heat loss by forced convection at a wind speed of 0.3 m/s	1772.8 W	1948.2 W	3721 W
Heat loss by radiation into the environment	805.1 W	978.8 W	1783.9 W

Table I. Heat loss calculations the heat exchanger.

The total required performance for heating the air from temperature 29.9 °C to 116.5 °C considering losses by wind, with velocity 0.3 m/s was 6088.6 W. In the case of windlessness the necessary performance was 4940.7 W. Wind effect acting on the pipes of exchanger caused the loss 1147.9 W.

The difference between the calculated and the measured value of required thermal performance is 132.1 W, what constitutes 2% deviation.

Acknowledgment

This work has been supporting within the project "Research on new ways of converting heat from renewable energy sources to electricity using new advanced cycles" ITMS 26220220117 and by European regional development fund and From the State budget of Slovakia "Research Center, University of Zilina" ITMS 26220220183.

Numerical part of this work had been solved by Jozef Matusov in the Institute for Energy Systems and Thermodynamics, Vienna University of Technology, three-month internship supported by program Action Austria – Slovakia

References

[1] FLORISTAL, R. 2003. *Heat transfer analysis and modeling of a parabolic trough solar receiver implemented in engineering equation*

solver, National Renewable Energy Laboratory, Colorado, NREL/TP-550-34169

[2] D. MILLS, ''Advances in solar thermal electricity technology'', Solar Energy, 76 (1–3) (2004), pp. 19–31.

[3] A. RAGURAM and K. LINGESWARAN, ''Design of Stirling Engine and Solar Collectors to Run an Automobile Alternator'', Middle-East Journal of Scientific Research 20 (7): 815-818, 2014 ISSN 1990-9233

[4] O. P. Akinjiola and U. B. Balachandran. ''Concentrated Solar Thermal (CST) System for Fuelwood Replacement and Household Water Sanitation in Developing Countries'', Journal of Sustainable Development; Vol. 5, No. 6; 2012 ISSN 1913-9063, E-ISSN 1913-9071 Published by Canadian Center of Science and Education

[5] Robert Pitz-Paal, (2007) , HIGH TEMPERATURE SOLAR CONCENTRATORS, in *Solar Energy Conversion and Photoenergy Systems* , [Ed. Julian Blanco Galvez, Sixto Malato Rodriguez], in Encyclopedia of Life Support Systems (EOLSS), Developed under the Auspices of the UNESCO, Eolss Publishers, Oxford ,UK, [http://www.eolss.net]

[6] O. García-Valladares and N. Velázquez, ''Numerical simulation of parabolic trough solar collector: Improvement using counter flow concentric circular heat exchangers'', International Journal of Heat and Mass Transfer 52 (2009) 597–609

[7] M. Mussard and O. J. Nydal, ''Influence of solar tracking inaccuracy and sun rays modeling on the efficiency of a small-scale parabolic trough'', 2013 ISES Solar World Congress

[8] Soteris A. Kalogirou, ''Solar thermal collectors and applications'', Progress in Energy and Combustion Science 30 (2004) 231–295

[9] M. J. Brooks, (February 2005) ''Performance of parabolic trough solar collector'', http://hdl.handle.net/10019.1/1821

[10] Angela M. Patnode, (2006), ''Simulation and Performance Evaluation of Parabolic Trough Solar Power Plants'', Master of science (Mechanical Engineering), University of Wisconsin – Madison

[11] J. Matusov, S. Gavlas, M. Malcho, (2013), ''Proposal of the parabolic though solar collector'', ALER 2013 [electronic source] Alternative energy sources: 9th year scientific and technical conference with international participation: Liptovsk Jyn 2.-4. October 2013. - Liptovsky Mikulas: SES, 2013. - ISBN 978-80-89456-15-4. - CD-ROM, [6] s.

[12] J. Matusov, M. Malcho, S. Gavlas, (2013), ''Optimalization of gripping the focal absorber of parabolic trough solar collector due to thermal expansion during operation'', TRANSCOM 2013: 10-th European conference of young research and scientific workers: Zilina, June 24-26, 2013, Slovak Republic. - Zilina: University of Zilina, 2013. - ISBN 978-80-554-0695-4. - S. 211-214.

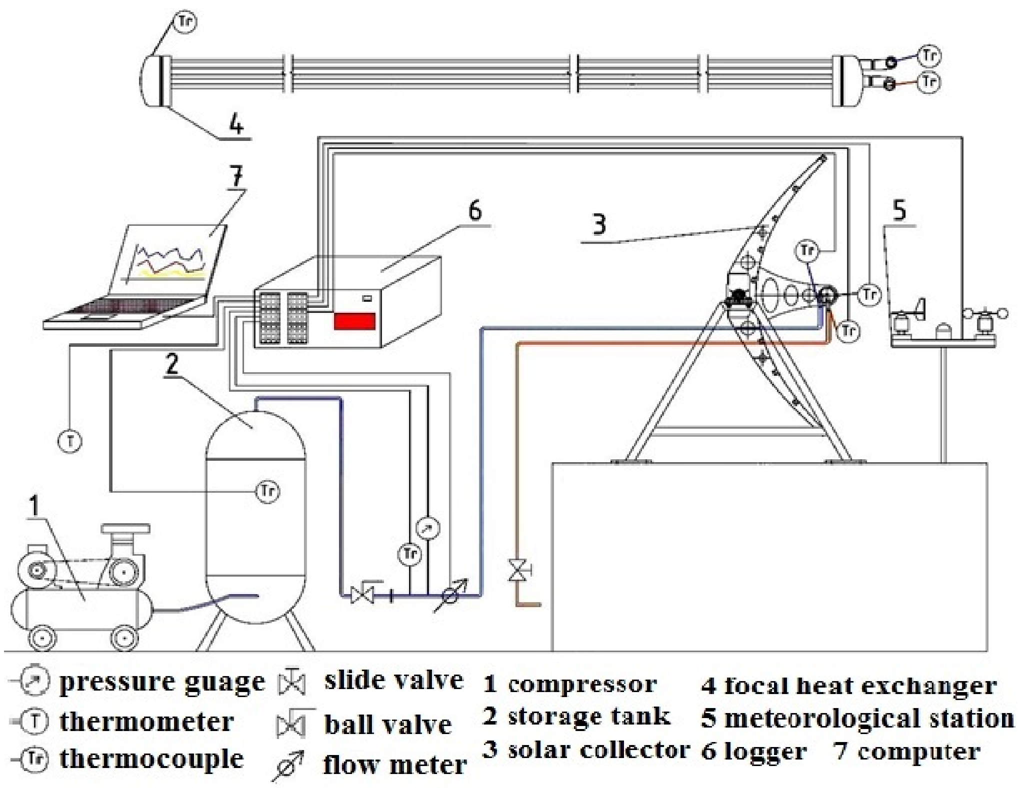

Fig. 5 Connection diagram of the components and sensors of experimental device for measuring performance parameters of heat exchanger in the focus of parabolic trough collector.

Numerical experiments on the performance of the RBF meshfree Galerkin Methods for solid mechanics

Abderrachid Hamrani, Eric Monteiro, Idir Belaidi, Philippe Lorong

Abstract—In this work the advances in meshfree methods, particularly the Radial Basis Function based meshfree Galerkin Methods, are presented with the purpose of analyzing the performance of their meshless approximations and integration techniques. The Radial Point Interpolation Method (RPIM) is studied based on the global Galerkin weak form performed using classical Gaussian integration and the stabilized conforming nodal integration scheme. The numerical performance of this category of methods is tested on their behavior on two elastic problems with regular node grids, and two other with distorted irregular grids. All RPIM methods perform very well in term of elastic computation, the Smoothed Radial Point Interpolation Method (SRPIM) shows a higher accuracy, especially in a situation of distorted node schemes. *Keywords*—adial Basis Function Radial Point Interpolation Method Galerkin weak form Nodal Integrationadial Basis Function Radial Point Interpolation Method Galerkin weak form Nodal IntegrationR

Keywords—Radial Basis Function, Galerkin weak form, Nodal Integration.

I. Introduction

One of the most important progress in the field of the numerical simulation was the development of the finite element method (FEM). In this method, a continuum solid defined by an infinity of material points is divided into finite elements which are connected between them by a kind of “grid”. The finite element method (FEM) proved to be effective and robust in several engineering fields because of its capacity to deal with complex geometries. However, it remains that this method suffers from some limitations related to the use of meshes, especially when severe element distortions take place under large deformation processes where the accuracy in FEM results are considerably lost [1]. To surmount these problems, numerical methods known usually as “meshless” or “meshfree” methods were proposed, in these methods the problem domain is represented by a set of scattered nodes, without the need of any, a priori, information on the relationship between them. The development of some of the meshless methods goes back to more than seventy years, with the appearance of collocation methods [3] [4] [5]. After that, the first well known meshless method: the Smoothed Particle Hydrodynamics (SPH) [6], was originally created for the simulation of astrophysical phenomena by Lucy [7], and from the early 1990s, numerous methods have been proposed; for instance the diffuse element method (DEM) [8], the reproducing kernel particle method (RKPM) [9] [10],the element free Galerkin (EFG) method [11], the point interpolation methods [12], the meshless local Petrov-Galerkin method (MLPG) [13]. These methods use “Meshless” shape functions to represent the field variables, since these shape functions are mathematically constructed by using only a set of nodes without requiring a mesh.

The Moving least square (MLS) interpolation was one of the first shape functions used by Belytschko et al. [14] for the development of the element free Galerkin (EFG) method, and because of the limitations which suffered this method, in particular, the complexity of the calculations of MLS shape functions and their partial derivatives, besides the difficulty to imposing boundary conditions [15], Liu and Gu [16], [17] proposed a new family of meshless shape functions, that they called ”Point Interpolation Methods”. Among these methods, the radial point interpolation method (RPIM) is preferred because the use of radial basis function avoids us falling in the singularity problem of the conventional PIM [18] [45], and shape functions resulting from RBF are stable and hence flexible for arbitrary and irregular nodal configurations. For the achievement of a numerical simulation for mechanics problems we need in combination with shape function a formulation procedure based on strong or weak-forms derived directly from the physical principles. In general, we use weak-form formulations to construct discretized system equations, and the most widely used approache is the Galerkin weak-forms.

For the requirement of a weaker consistency on the approximate function, weak forms need an integral operation performed numerically by the use of two major techniques, the classical Gauss integration and the stabilized conforming nodal integration (SCNI) proposed by Beissel and Belytschko [19] and after by Chen et al. [20] [21].

In the present work, our objectif is to study the RBF meshfree Galerkin Methods through their performances in term of : interpolations (RPIM shape function) and their numerical integration techniques (classical Gauss integration and the stabilized conforming nodal integration).

II. Construction of RPIM shape functions

The interpolation employed for the construction of the RPIM shape functions augmented with polynomials can be

A. Hamrani and I. Belaidi are with Equipe de recherche Mécanique et Ingénierie des Systèmes et Procédés, LEMI. University of M’Hamed Bougara de Boumerdes, 35000, Algérie. (e-mail : hamrani.abderrachid@gmail.com, idir.belaidi@umbb.dz)

E. Monteiro and P. Lorong are with PIMM, Arts et Métiers ParisTech, CNRS, 151 bd de l’Hôpital, 75013 Paris, France. (email : Eric.MONTEIRO@ensam.eu, Philippe.LORONG@ensam.eu)

written as [45]:

$$u(\mathbf{x}) = \sum_{i=1}^{n} r_i\left(\mathbf{x}\right)\, a_i + \sum_{j=1}^{m} p_j\left(\mathbf{x}\right)\, b_j = \mathbf{r}^T(\mathbf{x})\,\mathbf{a} + \mathbf{p}^T(\mathbf{x})\,\mathbf{b} \quad (1)$$

Where $r_i\left(\mathbf{x}\right)$ is a radial basis function (FRB), $p_j\left(\mathbf{x}\right)$ is a basis function of monomials $[x, y]$ (in 2D problems). Coefficients a_i and b_i are the corresponding constants yet to be determined, n is the number of RBFs, m is the number of polynomial basis functions.

To find out coefficients a_i et b_i, we have to satisfy equation (1) at the n nodes in the local support domain of the point of interest at $\mathbf{x}$, this leads to n linear equations, then the matrix form of these equations can be written as :

$$\mathbf{u} = \mathbf{R}_0\,\mathbf{a} + \mathbf{P}_m\,\mathbf{b} \quad (2)$$

where :

$$\mathbf{u} = \left\{ u_1 \quad u_2 \quad u_3 \quad \cdots \quad u_n \right\}^T \quad (3)$$

the FBR matrix :

$$\mathbf{R}_0 = \begin{bmatrix} r_1\left(d_1\right) & r_2\left(d_1\right) & \cdots & r_n\left(d_1\right) \\ r_1\left(d_2\right) & r_2\left(d_2\right) & \cdots & r_n\left(d_2\right) \\ \cdots & \cdots & \cdots & \cdots \\ r_1\left(d_n\right) & r_2\left(d_n\right) & \cdots & r_n\left(d_n\right) \end{bmatrix}_{(n\times n)} \quad (4)$$

Where d_i in $r_i(d_k)$ is defined as :

$$d_k = \sqrt{\left(x_k - x_i\right)^2 + \left(y_k - y_i\right)^2} \quad (5)$$

and the Polynomial basis functions matrix:

$$\mathbf{P}_m = \begin{bmatrix} 1 & x_1 & y_1 & \cdots & p_m\left(x_1\right) \\ 1 & x_2 & y_2 & \cdots & p_m\left(x_2\right) \\ \vdots & \vdots & \vdots & \ddots & \vdots \\ 1 & x_n & y_n & \cdots & p_m\left(x_n\right) \end{bmatrix} \quad (6)$$

in this case, there are $n+m$ variables in Eq.2, so an other m equations should be required. Golberg et al.[22] added the additional m equations by using the following constraint conditions :

$$\mathbf{P}_m^T\mathbf{a} = \sum_{i=1}^{n} p_j\left(\mathbf{x}_i\right) a_i = 0, \qquad j = 1,\ 2,\ \ldots,\ m \quad (7)$$

the vector that collect coefficients for RBFs is :

$$\mathbf{a}^T = \left\{ \ a_1 \quad a_2 \quad \cdots \quad a_n \ \right\} \quad (8)$$

the vector that collect coefficients for Polynomial basis functions is :

$$\mathbf{b}^T = \left\{ \ b_1 \quad b_2 \quad \cdots \quad b_m \ \right\} \quad (9)$$

the equation (2) can be written in the following form:

$$\tilde{\boldsymbol{u}} = \begin{bmatrix} \mathbf{u} \\ 0 \end{bmatrix} = \underbrace{\begin{bmatrix} \mathbf{R}_0 & \mathbf{P}_m \\ \mathbf{P}_m^T & 0 \end{bmatrix}}_{\mathbf{G}} \begin{Bmatrix} \mathbf{a} \\ \mathbf{b} \end{Bmatrix} = \mathbf{G}\,\mathbf{a}_0 \quad (10)$$

$$\mathbf{a}_0^T = \left\{ \ a_1 \quad a_2 \quad \cdots \quad a_n \quad b_1 \quad b_2 \quad \cdots \quad b_m \ \right\} \quad (11)$$

$$\tilde{\boldsymbol{u}} = \left\{ \ u_1 \quad u_2 \quad \cdots \quad u_n \quad 0 \quad 0 \quad \cdots \quad 0 \ \right\} \quad (12)$$

Since the matrix $\mathbf{R}_0$ is symmetric, the matrix $\mathbf{G}$ will also be symmetric, than by solving equation (10), we obtain :

$$\mathbf{a}_0 = \begin{Bmatrix} \mathbf{a} \\ \mathbf{b} \end{Bmatrix} = \mathbf{G}^{-1}\,\tilde{\boldsymbol{u}} \quad (13)$$

The RPIM shape function is finally expressed as

$$\mathbf{u}\left(\mathbf{x}\right) = \left\{ \ \mathbf{r}^T(\mathbf{x}) \quad \mathbf{p}^T(\mathbf{x}) \ \right\} \begin{Bmatrix} \mathbf{a} \\ \mathbf{b} \end{Bmatrix} \quad (14)$$

$$u\left(\mathbf{x}\right) = \left\{ \ \mathbf{r}^T(\mathbf{x}) \quad \mathbf{p}^T(\mathbf{x}) \ \right\} \mathbf{G}^{-1}\tilde{\boldsymbol{u}} = \tilde{\boldsymbol{\phi}}^T(\mathbf{x})\,\tilde{\boldsymbol{u}} \quad (15)$$

$$\tilde{\boldsymbol{\phi}}^T(\mathbf{x}) = \left\{ \ \mathbf{r}^T(\mathbf{x}) \quad \mathbf{p}^T(\mathbf{x}) \ \right\} \mathbf{G}^{-1} \quad (16)$$

$$\tilde{\boldsymbol{\phi}}^T(\mathbf{x}) = \left\{ \ \phi_1\left(\mathbf{x}\right) \quad \phi_2\left(\mathbf{x}\right) \quad \cdots \quad \phi_n\left(\mathbf{x}\right) \quad \phi_{n+m}\left(\mathbf{x}\right) \ \right\} \quad (17)$$

Where the RPIM shape functions corresponding to the nodal displacements are given by

$$\boldsymbol{\phi}^T(\mathbf{x}) = \left\{ \ \phi_1\left(\mathbf{x}\right) \quad \phi_2\left(\mathbf{x}\right) \quad \cdots \quad \phi_n\left(\mathbf{x}\right) \ \right\} \quad (18)$$

It can be seen that the resultant RPIM shape function has the delta Kronecker property and partition of unity, and due to the addition of polynomial basis, they also fulfill the reproducing properties. In this work, different radial basis functions augmented with the linear polynomial basis are used to construct the present RPIM shape function, the choice of the shape parameters in the RBFs are studied.

III. Galerkin weak form of 2-D solid mechanics

A 2-D problem of solid mechanics defined in the domain Ω bounded by Γ can be described by the following equilibrium equation :

$$\nabla \cdot \boldsymbol{\sigma} + \mathbf{F} = 0 \quad in\ \Omega \quad (19)$$

where $\boldsymbol{\sigma}$ is the Cauchy stress tensor and $\mathbf{F}$ the body forces vector. The boundary conditions for the equilibrium equations are :

$$\boldsymbol{\sigma}\,\mathbf{n} = \bar{\mathbf{t}} \quad on\ the\ natural\ boundary\ \Gamma_t \quad (20)$$

$$\mathbf{u} = \bar{\mathbf{u}} \quad on\ the\ essential\ boundary\ \Gamma_u \quad (21)$$

where $\bar{\mathbf{u}}$ is a prescribed displacement on boundary Γ_u, $\bar{\mathbf{t}}$ is a prescribed traction on the boundary Γ_t and $\mathbf{n}$ is the outward normal on the boundary.

The well-known Galerkin weak form is given by :

$$\int_{\Omega} \delta\left(\nabla \mathbf{u}^T\right) \cdot \boldsymbol{\sigma}\, d\Omega - \int_{\Omega} \delta \mathbf{u}^T \cdot \mathbf{F}\, d\Omega - \int_{\Gamma_t} \delta \mathbf{u}^T \cdot \bar{\boldsymbol{t}}\, d\Gamma = 0 \quad (22)$$

Discretization of Eq.(22) with interpolation function Eq.(15) yields

$$\mathbf{K}\,\mathbf{u} = \mathbf{f} \quad (23)$$

where

$$\begin{aligned}\mathbf{K}_{ij} &= \int_{\Omega} \mathbf{B}_i^T \, \mathbf{C} \mathbf{B}_j \, d\Omega, \; and \; \mathbf{f}_i \\ &= \int_{\Omega} \mathbf{\Phi}_i^T \, \boldsymbol{F} \, d\Omega + \int_{\Gamma_t} \mathbf{\Phi}_i^T \, \bar{\boldsymbol{t}} \, d\Gamma\end{aligned} \tag{24}$$

where $\mathbf{C}$ is the matrix of elastic constants and $\mathbf{B}_i$ is the strain matrix.

The integrals involved in Eq.(24) are usually evaluated numerically through the well known Gauss integration scheme as is commonly used in finite elements. In this study, a second scheme is also used : the stabilized conform-ingnodal integration scheme (SCNI). Both schemes are shortly explained below.

IV. Integration techniques

A. Gauss integration

In order to evaluate integrals over the global problem domain Ω and the global traction boundary Γ_t, the problem domain is discretized into a set of background cells. Hence, a global integration can be expressed as :

$$\int_{\Omega} \mathbf{G} \, d\Omega = \sum_{k=1}^{n_c} \int_{\Omega_k} \mathbf{G} \, d\Omega = \sum_{k=1}^{n_c} \sum_{i=1}^{n_g} \widehat{w}_i \, \mathbf{G}\left(\mathbf{x}_{Qi}\right) \, \left|\mathbf{J}_{ik}^D\right| \tag{25}$$

where n_c is the number of background cells, n_g is the number of Gauss points used in a background cell, $\mathbf{G}$ represents the integrand, Ω_k is the domain of the k^{th} background cell, $\widehat{w}_i$ is the Gauss weighting factor for the i^{th} Gauss point at $\mathbf{x}_{Qi}$, and $\mathbf{J}_{ik}^D$ is the Jacobian matrix for the area integration of the background cell k.

Similarly, we can obtain the formulation of the curve Gauss quadrature as

$$\int_{\Omega} \mathbf{G} \, d\Gamma_t = \sum_{l=1}^{n_{ct}} \int_{\Gamma_{tl}} \mathbf{G} \, d\Omega = \sum_{l=1}^{n_{ct}} \sum_{i=1}^{n_{gt}} \widehat{w}_i \, \mathbf{G}\left(\mathbf{x}_{Qi}\right) \, \left|\mathbf{J}_{il}^B\right| \tag{26}$$

n_{ct} is the number of the curve cells that are used to discretize boundary Γ_t, and n_{gt} is number of Gauss points used in a sub-curve, $\mathbf{J}_{il}^B$ is the Jacobian matrix for the curve integration of the sub-boundary l for the Gauss point at $\mathbf{x}_{Qi}$.

B. Nodal integration

In Gauss quadrature a global background cell structure has to be used, this fact made the method not truly meshless. To avoid the use of background cells Beissel and Belytschko [19] have proposed a nodal integration procedure based on a strain smoothing stabilization to eliminate spatial instability in nodal integration. This technique of integration is based on the substitution of the displacement gradient at a node $\mathbf{x}_k$ by averaging the displacement gradient over a cell accompanying that node [20] :

$$\nabla \mathbf{u}^h\left(\mathbf{x}\right) = \int_{\Omega_k} \nabla \mathbf{u}^h\left(\mathbf{x}\right) \, \tilde{W}\left(\mathbf{x}_k - \mathbf{x}\right) d\Omega \tag{27}$$

$\tilde{W}(\mathbf{x}_k - \mathbf{x})$ is a smoothing or weight function associated with $\mathbf{x}_k$, in general we use the following simplest form of the Heaviside-type smoothing function:

$$\tilde{W}\left(\mathbf{x}_k - \mathbf{x}\right) = \begin{cases} 1/A_k & \mathbf{x} \in \Omega_k \\ 0 & \mathbf{x} \notin \Omega_k \end{cases} \tag{28}$$

where A_k is the area of smoothing domain Ω_k. Equation 27 become :

$$\nabla \mathbf{u}^h\left(\mathbf{x}\right) = \frac{1}{A_k} \int_{\Omega_k} \nabla \mathbf{u}^h\left(\mathbf{x}\right) \, d\Omega \tag{29}$$

The surface (or volume) integral can be rewritten by means of the Gauss divergence theorem to a curve (surface) integral :

$$\begin{aligned}\tilde{\nabla} \mathbf{u}^h\left(\mathbf{x}\right) &= \int_{\Gamma_k} \mathbf{u}^h\left(\mathbf{x}\right) \, \mathbf{n}_k\left(\mathbf{x}\right) \, \tilde{W}\left(\mathbf{x}_k - \mathbf{x}\right) \, d\Gamma \\ &= \frac{1}{A_k} \int_{\Gamma_k} \mathbf{u}^h\left(\mathbf{x}\right) \, \mathbf{n}_k\left(\mathbf{x}\right) \, d\Gamma\end{aligned} \tag{30}$$

This nodal integration is based on strain/gradient smoothing technique, this technique is principaly used on the smoothed finite element methods (SFEM) [35] [36][37][38]. Numbers of SFEM models was developped, because of the types of smoothing domains used [43]. Different smoothing domains created based on cells (cell-based S-FEM (CS-FEM)) [40], nodes (node-based S-FEM (NS-FEM)) [42], edges (edge-based S-FEM (ES-FEM)) [41], and faces (face-based S-FEM (FS-FEM)) [40].

V. Error analysis for Radial Point Interpolation Method

Two sources of error are noticed in the case of RPIM: the Radial Basis Function interpolation error and the error in calculation of Galerkin weak form. The first error due to the interpolation can be evaluated by the error in fitting different curves and surfaces. The second error is evaluated through the study of convergence rate of RPIM in case of boundary-value problem.

A. RBF interpolation error

In this section, studies on the accuracy of the RPIM shape functions used for curve fitting are conducted . The fitting of functions is based on the nodal function value sets that are generated at regularly as well as at irregularly distributed nodes. The procedure carried out for curve fitting is : first we create a set of field nodes in the domain where the function is to be fitted, then for a given test node x (usually different from the set of field nodes) where the function is to be fitted, we choose n nodes in the influence domain of x, now we can construct RPIM shape functions, and finaly, using these shape functions we can calculate the function value at x and compare it with the real value.

The interpolation error of curve fitting at point i is measured by :

$$e_t = \frac{1}{n} \sum_{i=1}^{n} \left| \frac{\tilde{f}_i - f_i}{f_i} \right| \tag{31}$$

ISBN: 978-1-61804-288-0

Table I: Radial Basis Functions with global support used in this study.

RBF	Equation
MQ	$r_i(d_i) = \left(d_i{}^2 + (\alpha_c d_c)^2\right)^q$
Exp	$r_i(d_i) = \exp\left[-\alpha_c\,(\frac{d_i}{d_c})^2\right]$
TPS	$r_i(d_i) = d_i^\eta$

where f_i is the true function value at point i and $\tilde{f}_i$ is the fitted function value of the function f at point i in the influence domain.

To construct the RPIM shape function we have to compute the inverse of the matrix **G** (Eq.16), the numerical inversion of this matrix **G** affects the accuracy of interpolation [23], [24]. Therefore, we add a second indicator to the interpolation error wich is the condition number of matrix **G**.

1) Shape parameters analysis: In this section we will see how the shape parameters affect RPIM shape function. Because there is no rule governing the rational choice of the RBF parameters, this theme was and stay a problematic theme when the interpolation by the radial basis functions are used. Several works was made in this axis, we can find the paper of Franke [25] concerning the convergence study of the RBF interpolation, particularly the Multiquadrique (MQ), where he recommends to use an $\alpha_c = 1.25\, d_s/\sqrt{N}$. Hardy [26] recommends the value $\alpha_c = 0.815\, d_s$ where the average influence domain $d_s = (1/N)\sum_{i=1}^{N} d_i$ (d_i is the distance between the i^{th} node and his nearest natural neighbor). Rippa [27] proposes an optimization algorithm for the choice of the rational parameters, which will afterward be improved by Scheuerer [28]. We can also present some recent works including publications of Wang and Liu [29] [30] where they studied the optimal values of RBF-MQ and EXP shape parameters in 2D and 3D [31], they confirm that the condition number of matrix **G** directly affects the accuracy of RBF interpolation. R. Li et al [32] found a range of optimal values of the RBF-MQ shape parameters for the hybrid radial boundary node method.

For this analysis, RPIM shape functions are constructed in a domain of $(x, y) \in [-1,\, 1]\ [-1,\, 1]$ using three sets of $5\times5 = 25$ nodes patterns generated within this domain (Fig. 1).

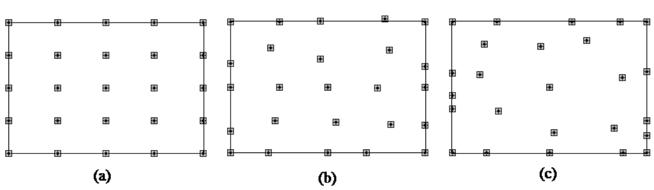

Figure 1: The three sets of nodes patterns.

A total of 100 points are defined as evaluation points. In this study we use three type of RBF with global support: Multiquadric (MQ), Gaussian (EXP), Thin Plate Spline (TPS) (Tab I), in addition of an RBF with compact support (Wu-C2) (Eq.32), with the use of polynomial terms (Eq. 1).

$$r_i(d_i) = \left(1 - \frac{d_i}{\delta_c}\right)^5 \left(8 + 40\frac{d_i}{\delta_c} + 48\frac{d_i{}^2}{\delta_c^2} + 25\frac{d_i{}^3}{\delta_c^3} + 5\frac{d_i{}^4}{\delta_c^4}\right) \tag{32}$$

The evaluation procedure can be prescribe as fellow : for a fixed number of nodes and sampling points, and for a range of RBF shape parameters, we calculate the interpolation error of curve fitting for function defined as :

$$f(x, y) = \sin\left(\sqrt{(x^2 + y^2)}\right) \tag{33}$$

For this exemple we choose a large influence domain that include all nodes of the problem, in order to study only the effect of the choice of the FBR parameters, and once good parameters are selected, we can pass to the choice of dimension of influence domain. All sets of nodes patterns (Fig. 1) are employed in order to evaluate the capacity of RPIM to deal with problems where nodes distribution are irregular.

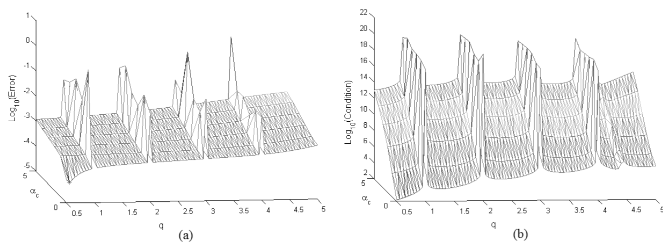

Figure 2: Effect of shape parameters q and α_c of RBF-MQ on (a) Interpolation error and (b) condition number of matrix **G**.

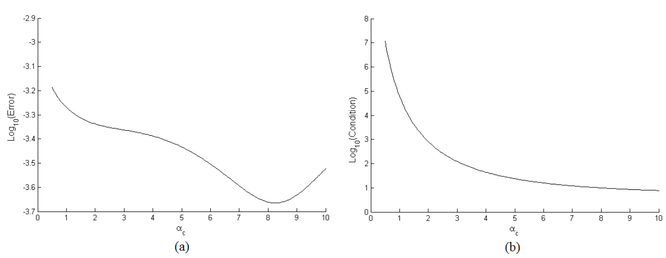

Figure 3: Effect of shape parameter α_c of RBF-EXP on (a) Interpolation error and (b) condition number of matrix **G**.

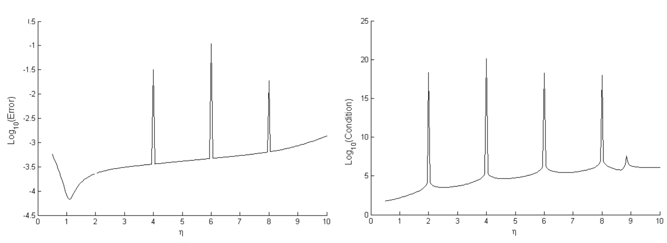

Figure 4: Effect of shape parameter η of RBF-TPS on (a) Interpolation error and (b) condition number of matrix **G**.

Through figures 2 to 9, conclusions can be summarized in the following points:

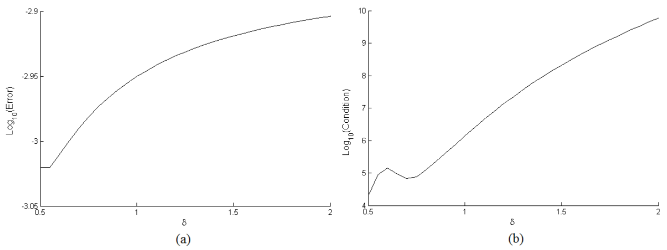

Figure 5: Effect of shape parameter δ of RBF-Wu-C2 on (a) Interpolation error and (b) condition number of matrix $\mathbf{G}$.

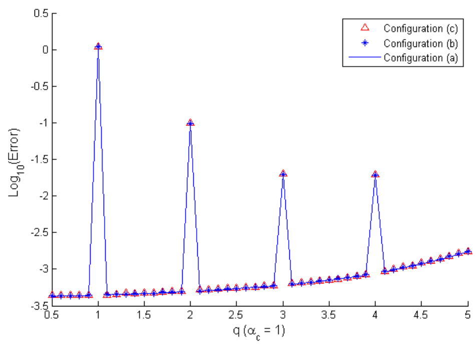

Figure 6: Effect of shape parameter q of RBF-MQ on Interpolation error with different sets of nodes patterns.

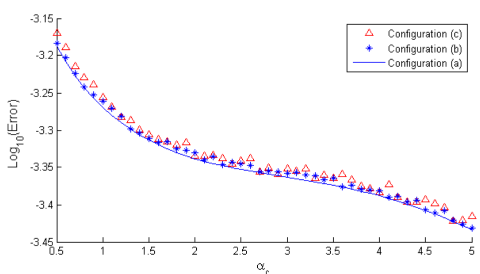

Figure 7: Effect of shape parameter α_c of RBF-EXP on Interpolation error with different sets of nodes patterns.

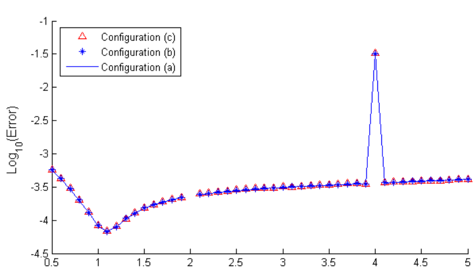

Figure 8: Effect of shape parameter η of RBF-TPS on Interpolation error with different sets of nodes patterns.

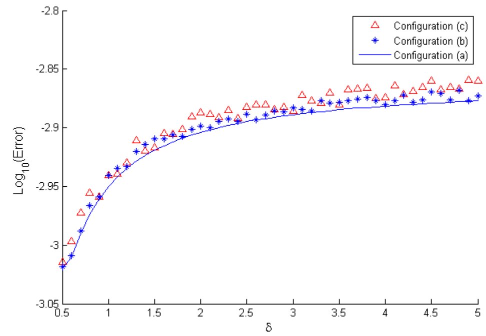

Figure 9: Effect of shape parameter δ of RBF-Wu-C2 on Interpolation error with different sets of nodes patterns.

1) In order to find the good parameters of the FBR, it would be necessary to find the just balance between the error of interpolation and the condition number of matrix $\mathbf{G}$.
2) Singular values found on the two basis MQ and TPS are resulting from the bad conditioning of the matrix $\mathbf{G}$ for these values.
3) Both Gaussian (EXP) and Wu-C2 basic functions present no singular behavior for all shape parameters values.
4) We can notice through figures 6 to 9, that the way nodes are distributed has no significant effect on the quality of RBF interpolation.

2) Dimensions of the influence domain: We suggest now to study the effect of the influence domain size (with circular shape) on the accuracy of RBF interpolation. For this, the domain of the problem is discrétised by 529 nodes distributed in an irrigular manner. By increasing gradually the size of the influence domain, the number of nodes inside thise domain wil increase, then we will proceed to the calculation of the interpolation error and the condition number of matrix $\mathbf{G}$.

The obtained results are illustrated in figures (10, 11) when we can draw the following conclusions :

1) The condition number of matrix $\mathbf{G}$ grows systematically with the increase of the dimensions of the influence domain, thus more the number of nodes inside this domain increases more the matrix $\mathbf{G}$ will be badly conditioned.
2) The interpolation error does not improve systematically by increasing the number of nodes inside the influence domain, in our opinion, this is due to two factors, the first one is that more the number of nodes implied in the interpolation is important more the number of computational arithmetic operations is important, this engenders numerical calculation errors, the second is that more the number of nodes is important more the condition number of the matrix $\mathbf{G}$ is larger this means that the matrix is ill-conditioned and its inversion will cause bigger error.
3) Larger influence domain means higher number of nodes included in the interpolation, and it implies the increase on the CPU operations (figure 12). we note that the meshless code is programmed in Matlab and the sim-

ulations are performed on a i5-2.5 GHz computer.

4) From this analysis we recommende that 6 to 25 nodes in the influence domain generate good result and a bigger or smaller number of nodes would lead to larger numerical error.
5) We can mention a technique used in [2] [33] [34], which is based on the concept of the natural neighbor for the construction of the influence domain, the interval recommended by the author for the number of nodes inside (first and second order natural neighbors) Joined what is previously mentioned.

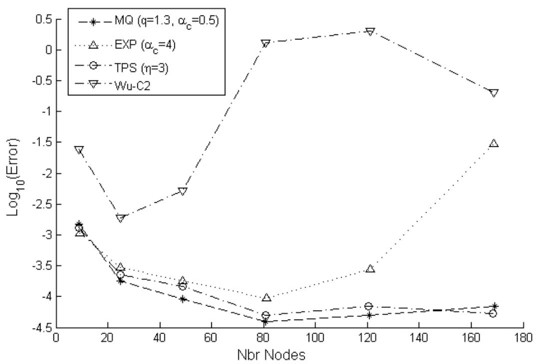

Figure 10: Effect of influence domain dimenssions on Interpolation error with different types of RBF.

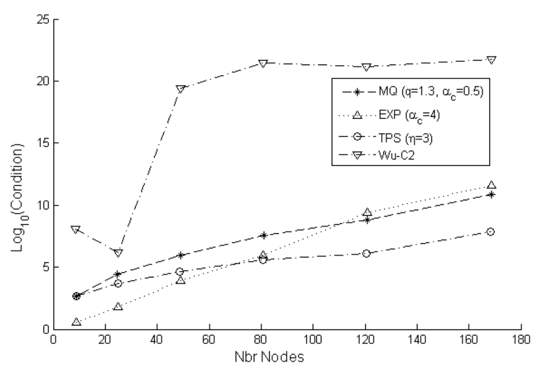

Figure 11: Effect of influence domain dimenssions on condition number of matrix **G** by different types of RBF.

B. Numerical experiments of 2-D solid mechanics problems

1) Error index: The error due to the calculation of Galerkin weak form should be different from that used to evaluate only RBF interpolation over scattered data.

A relative error of displacements is defined as follows :

$$e_{dep} = \frac{\left\| u - \widehat{u} \right\|_{L^2}}{\left\| u \right\|_{L^2}} = \frac{\left(\int\limits_{\Omega} \left(u - \widehat{u} \right)^T \left(u - \widehat{u} \right) d\Omega \right)^{1/2}}{\left(\int\limits_{\Omega} (u)^T \ (u) \ d\Omega \right)^{1/2}} \tag{34}$$

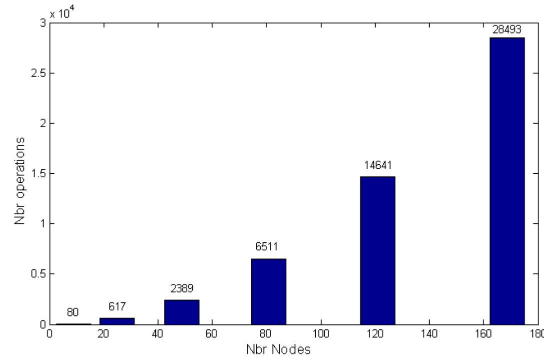

Figure 12: Effect of influence domain dimenssions on the number of computational arithmetic operations.

where $\widehat{u}$ and u are displacements computed by the RPIM and the exact analytical solution, respectively.

The error of energy is defined as follows :

$$e_{Edef} = \frac{\left(\int\limits_{\Omega} \frac{1}{2} \left(\varepsilon - \widehat{\varepsilon} \right)^T c \left(\varepsilon - \widehat{\varepsilon} \right) d\Omega \right)^{1/2}}{\left(\int\limits_{\Omega} \frac{1}{2} (\varepsilon)^T c \, (\varepsilon) \ d\Omega \right)^{1/2}} \tag{35}$$

Where $\widehat{\varepsilon}$ and ε are strain tensors obtained from the RPIM and the exact analytical closed-form solution, respectively.

In order to evaluate the convergence rates of RPIM methods, it is necessary to define a characteristic length "h". For a grid of triangular T3 background cells:

$$h = \sqrt{\frac{2 \, A_\Omega}{N_c}} \tag{36}$$

For a grid of quadrilateral Q4 background cells :

$$h = \sqrt{\frac{A_\Omega}{N_c}} \tag{37}$$

where A_Ω is the area of the problem domain and N_c the number of integration cells.

2) Cantilever beam problem: In this test the accuracy and convergence of combination of shape functions and integration schemes is examined on the problem of a cantilever beam. This problem is widely used to select the optimal parameters of RPIM [29], [30], [31], [32]. Almost all reported conclusions are obtained from this benchmarking numerical experiment.

Consider a cantilever beam shown in Fig.13. The beam is fixed at the left end and subjected to a parabolic traction force at the free end.

The analytical solution is defined as follows [44]:

$$u\,(x,\, y) = -\frac{Py}{6EI} \left[(6L - 3x)\, x + (2 + v) \left(y^2 - \frac{D^2}{4} \right) \right] \tag{38}$$

$$v\,(x,\, y) = \frac{P}{6EI} \left[3\, v\, y^2 \,(L - x) + (4 + 5\, v)\, \frac{D^2 x}{4} + (3L - x)\; x^2 \right] \tag{39}$$

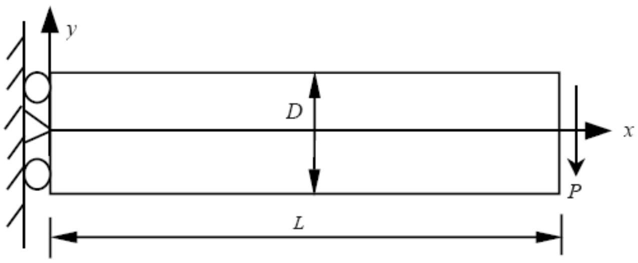

Figure 13: Cantilever beam problem.

where the moment of inertia I of the beam is given by $I = \frac{D^3}{12}$.

The corresponding stresses are :

$$\sigma_{xx}\left(x,\, y\right) = -\frac{P\left(L-x\right)y}{I} \tag{40}$$

$$\sigma_{yy} = 0 \tag{41}$$

$$\tau_{xy}\left(x,\, y\right) = \frac{P}{2I}\left[\frac{D^2}{4} - y^2\right] \tag{42}$$

The beam parameters are taken as $P = -1000N$, $E = 3\times10^{7}MPa$, $\upsilon = 0.3$, $D = 12mm$, $L = 48mm$.

3) Shape parameters analysis: For this test, two configurations of nodes will be used: 325 nodes distributed in a regular and irregular way respectively 14. Only two radial basis functions will be handled: the multiquadric (MQ) and the Gaussienne (EXP). Here circular influence domain circumvents 8 to16 nodes is used for each Gaussian point. Polynomial term is included for the rbf interpolation. For the gauss integration we use $4\times4 = 16$ gauss points for each cell of the set of 288 (24×12) background cells (figure 15). First, we study the effect of the Multiquadric shape parameters (MQ), results will be illustrated in figures 16, 17.

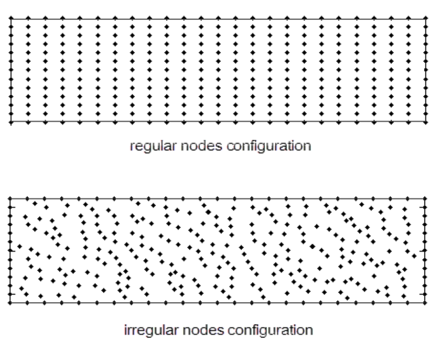

Figure 14: Nodes configurations of the cantilever beam problem.

1) For a uniform distribution of nodes, the optimal error values are registered for q between $1.5 - 2$ and all mentioned α_c ($\alpha_c = 0.5, 1, 1.5, 2$, we avoided the value of $q = 2$ because it is the particular value which makes the matrix $\mathbf{G}$ singular or strongly ill-conditioned.
2) For an irregular nodes distribution, the optimal value of q varies according to the value of α_c.

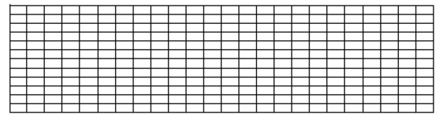

Figure 15: (24×12) background cells for numerical integration.

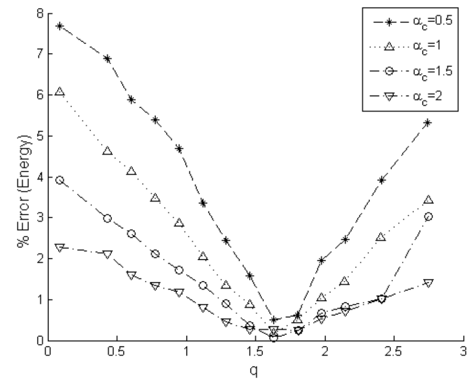

Figure 16: Effect of RBF-MQ shape parameters on energy error for regular nodes distribution.

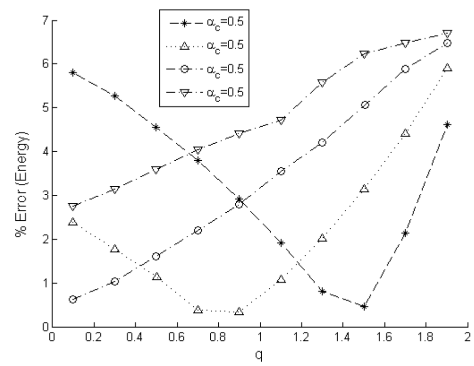

Figure 17: Effect of RBF-MQ shape parameters on energy error for irregular nodes distribution.

3) The recommended values for the Multiquadric (MQ) are: $\alpha_c = 0.5 \sim 2$ and $q = 0.4 \sim 2.2$ with the exception of the singular values (integers).

Secondly, we study the effect of the Gaussian shape parameters (EXP), results will be illustrated in figures 18.

1) For a uniform node disctribution, the values of the energy error remain relatively invariant for $\alpha_c > 0.03$.
2) For an irregular nodes distribution, the behavior of the error according to α_c is almost the same that for the uniform configuration.
3) The recommended values for Gaussian (EXP) are : $\alpha_c = 0.2 \sim 1$.

4) Dimensions of the influence domain: In this analysis, we adopt a configuration of 975 (39x25) nodes uniformly distributed, the same configuration is used for quadrilateral background cells (figure 19), four configurations of shape parameters for the FBR will be used : RBF-MQ with: $q = 1.3$

ISBN: 978-1-61804-288-0

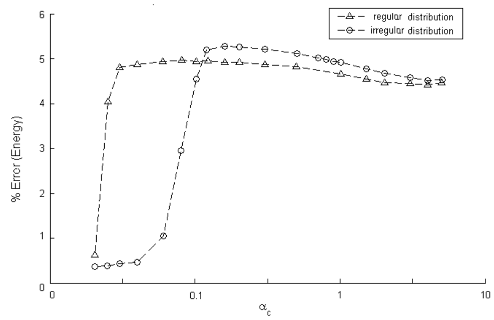

Figure 18: Effect of RBF-EXP shape parameters on energy error for regular/irregular nodes distribution.

and $\alpha_c = 0.5$ and $q = 1.9$ and $\alpha_c = 1.5$, RBF-EXP with: $\alpha_c = 0.2$ and $\alpha_c = 0.6$. The number of Gauss points is maintained to 16 points by cell.

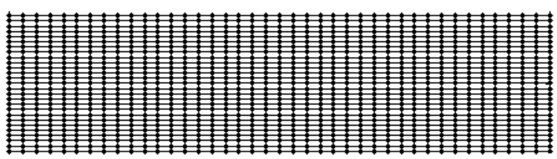

Figure 19: The two combined configurations of 975 (39x25) nodes and 1040 (40x26) background cells.

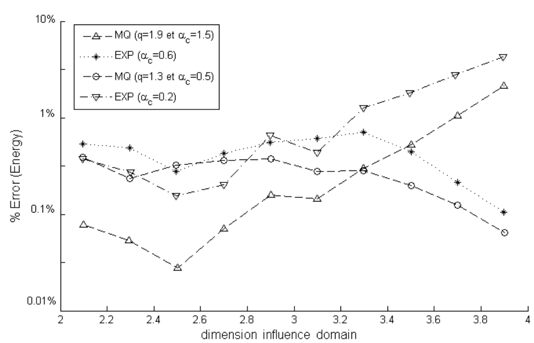

Figure 20: Effect of influence domain dimenssions on energy error.

1) Large size of influence domain does not imply systematically a good precision, quite the opposite, number of arithmetic operations required for the calculation increase, what would have consequence on increasing the CPU time (figure 21).
2) The number of nodes recommended to reach a good quality is of $9 \sim 30$ nodes inside the influence domain.

5) Number of Gauss points: To analyze how the number of Gauss points by cell used on the Gauss integration technique affect the accuracy of RPIM, we have to fix these parameters : for nodal discretization and background cells we use the previous uniform configurations Fig.14 and 15, two radial basis functions are considered : the RBF-MQ with $q = 1.9$ and $\alpha_c = 1.5$, the RBF-EXP with $\alpha_c = 0.2$, the influence domain being determined by 6-12 nodes inside.

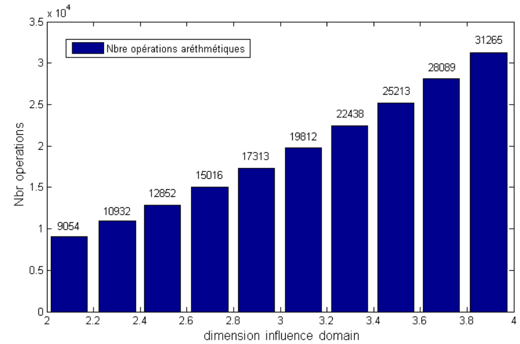

Figure 21: Effect of influence domain dimenssions on the number of computational arithmetic operations.

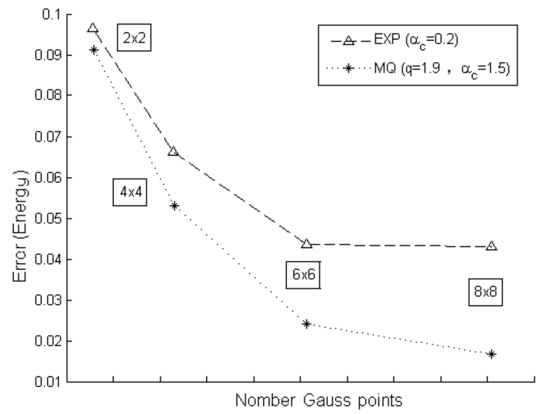

Figure 22: Energy error in function of the number of Gauss points.

Figure 22 shows the variation of the energy error according to the number of Gauss points of by cell, we notice that more the number of gauss points will be important, more the quality of RPIM results will be better until a relative stabilization for a number bigger than $64 = 8 \times 8$ quadrature points. On the other hand, it would be necessary to pay attention to the CPU time for numerical calculations which will tend to increase proportionally with the increase of Gauss points used. We can recommend to take a 4×4 up to 6×6 Gauss points for rectangular cells.

6) Effect of the integration technique: The objective of this section is the study of two numerical integration techniques : the classical Gauss integration and the Stabilized conforming nodal integration (SCNI).

In all what follows, the Radial basic function chosen is the Gaussian (EXP) with $\alpha_c = 0.2$, with addition of 1^{st} order polynomial terms, influence domain being determined with 8-16 nodes inside. A total of 6×6 Gauss points are used for the classic Gauss quadrature.

five set of regularely distributed nodes pattern and in the same time integration cells are used for this exemple : 1150, 798, 520, 360, 284.

ISBN: 978-1-61804-288-0

We notice, first, that the convergence rates of meshfree methods (RPIM, SRPIM) are better than those obtained by the FEM, this is due to the higher order of RBF interpolation comparing with the linear interpolation used in FEM triangular element, secondly, among RPIM meshfree methods the one who presents a better rate of convergence is SRPIM, who possesses the advantage of using a nodal stabilized integration with regard to the classic RPIM which use Gauss integration.

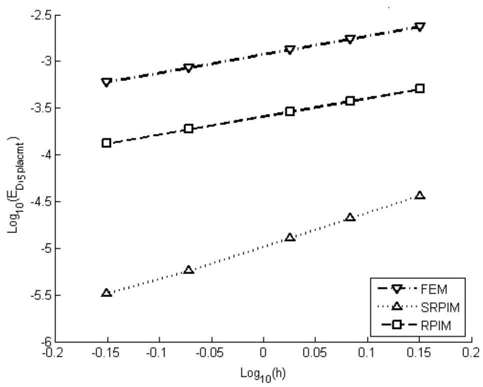

Figure 23: Relative error in displacement calculated for FEM, RPIM, SRPIM.

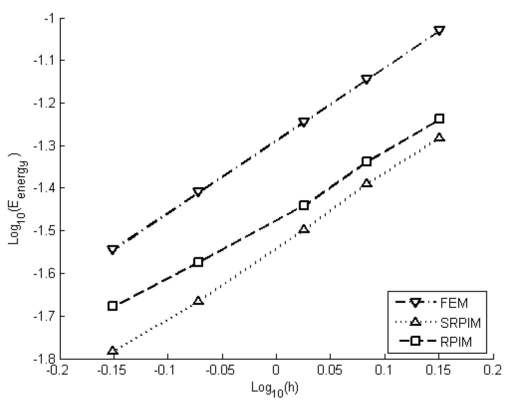

Figure 24: Relative energy error calculated for FEM, RPIM and SRPIM.

C. *Infinite plate with a circular hole*

We consider here a plate with a central circular hole with raduis $a = 1m$ subjected to a unidirectional tensile load of $F = 1N/m$ in the x-direction, due to symmetry, only the upper right quadrant of the plate is modelled as shown in Figure 25. Symmetry conditions are imposed on the left and bottom edges. The inner boundary is traction free. Plane strain conditions are assumed, and the problem constants are : $L = 5m, a = 1m, E = 10^3 N/m^2, \nu = 0,3, P = 1N/m$. analytical solution of these problem [44]:

$$u_1 = \frac{a}{8\mu}\left[\frac{r}{a}(\kappa+1)\cos\theta + 2\frac{a}{r}\left((1+\kappa)\cos\theta+\cos 3\theta\right) - 2\frac{a^3}{r^3}\cos 3\theta\right] \tag{43}$$

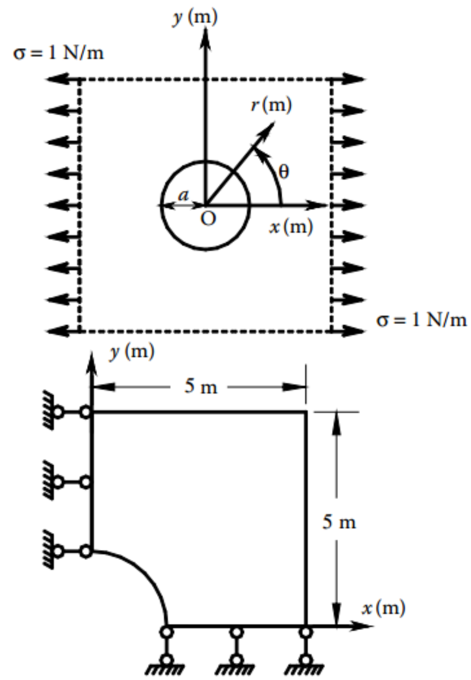

Figure 25: Geometry of the infinite plate with a hole problem.

$$u_2 = \frac{a}{8\mu}\left[\frac{r}{a}(\kappa-3)\sin\theta + 2\frac{a}{r}\left((1-\kappa)\sin\theta+\sin 3\theta\right) - 2\frac{a^3}{r^3}\sin 3\theta\right] \tag{44}$$

where (r, θ) are the polar coordinates with θ measured counter-clockwise from the positive x axis, $\mu = E/(2(1+\nu))$ et $\kappa = 3 - 4\nu$.

The analytical solution for the stresses of an infinite plate is :

$$\sigma_x(x, y) = 1 - \frac{a^2}{r^2}\left\{\frac{3}{2}\cos 2\theta + \cos 4\theta\right\} + \frac{3a^4}{2r^4}\cos 4\theta \tag{45}$$

$$\sigma_y(x, y) = -\frac{a^2}{r^2}\left\{\frac{1}{2}\cos 2\theta - \cos 4\theta\right\} - \frac{3a^4}{2r^4}\cos 4\theta \tag{46}$$

$$\sigma_{xy}(x, y) = -\frac{a^2}{r^2}\left\{\frac{1}{2}\sin 2\theta - \sin 4\theta\right\} + \frac{3a^4}{2r^4}\sin 4\theta \tag{47}$$

The displacement boundaryconditions are given by :

on the edge of $x = 0$: $u_x = 0$, on the edge of $y = 0$: $u_y = 0$.

As in the previous example, five nodes configurations will be used for this problem also, the total number of nodes used is: 169, 289, 625, on 1089 and 1681. Figures 26, 27, illustrate convergence rates of results obtained from RPIM, SRPIM and FEM. We notice as well in this problem that the convergence rates obtained from meshless methods, are better than those obtained by the FEM, and among the RPIM methods, SRPIM presents a better precision in term of displacement error and in energy error, what confirms the quality of the SCNI integration.

ISBN: 978-1-61804-288-0

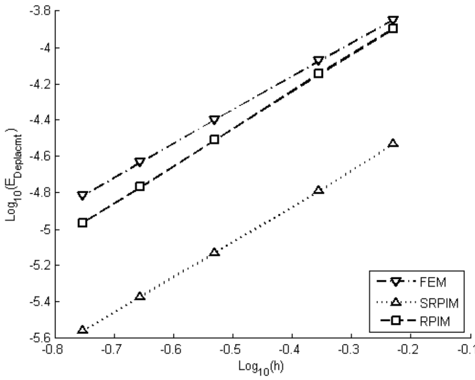

Figure 26: Relative error in displacement calculated for FEM, RPIM, SRPIM.

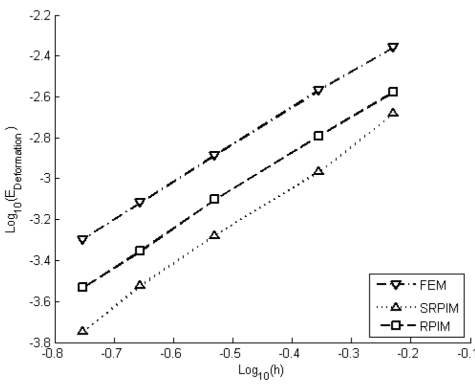

Figure 27: Relative energy error calculated for FEM, RPIM and SRPIM.

D. Distortion analysis

The example treated in this test is similar to the precedent test of cantilever beam (Figure 13), but with a different geometry and load (Figure 28), this geometry will be discretised by various nodes configurations (Figure 29).

The Radial basic function chosen is the Gaussian (EXP) with $\alpha_c = 0.2$, influence domain being determined with 8-16 nodes inside. A total of 6×6 Gauss points are used for the classic Gauss quadrature.

The exact solution calculated on the field of stress :

$$\sigma_{xx}(x) = \frac{3}{2}y, \quad \sigma_{yy}(x) = 0, \quad \sigma_{xy}(x) = 0 \tag{48}$$

The exact solution calculated on the field of strain :

$$\begin{aligned} \varepsilon_{xx}(x) &= \frac{3\,E\,(1-\upsilon)}{2\,(1-\upsilon)\,(1-2\upsilon)}\,y, \quad \varepsilon_{yy}(x) \\ &= \frac{3\,E\upsilon}{2\,(1-\upsilon)\,(1-2\upsilon)}\,y, \quad \varepsilon_{xy}(x) \\ &= 0 \end{aligned} \tag{49}$$

We notice in Figures 30 and 31 that for the first nodes configuration distributed in a regular way (configuration (1)), all RPIM methods gives satisfactory results and better than

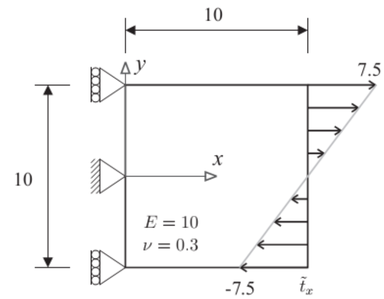

Figure 28: Model to examine distortional effects.

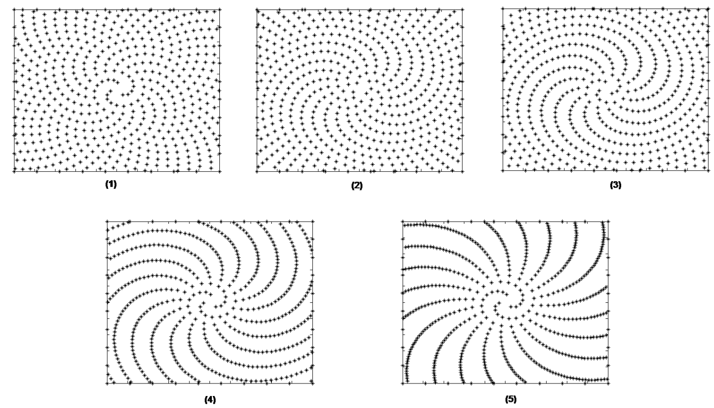

Figure 29: Grids used to examine the influence of distortion.

those obtained by finite element method (with linear triangular element mesh).

For the last nodes configuration, the most severe twisted configuration, and in spite of the fact that we use an influence domain guaranteeing a minimum number of nodes inside the latter, we notice that all RPIM methods diverges but by different degrees, the method which seems the least affected by this distortion is the S-RPIM (with SCNI technique). In summary, the more the distortion of the meshing of nodes is big, the more the error in displacement and in energy increases, however the methods using the SCNI integration technique are less affected by this degradation than those using the classical Gauss integration.

VI. Conclusion

In this paper a numerical analysis was performed on the RPIM meshless method with two integration schemes. The performance in the RBF shape function and in linear elasticity. It was shown that the Radial basis interpolation was important to the global accuracy of the RPIM. It was found that the condition number of the matrix **G** heavily affects the accuracy of interpolation. Shape parameters also had important effects on the condition number. A range of good shape parameters should balance the accuracy and the condition number. The folowing notes can be retained : Error was large when shape parameters takes singular values (q = integer values for RBF-MQ). Through numerical experiments, a range of shape parameters was found. Parameters from this range can give

ISBN: 978-1-61804-288-0

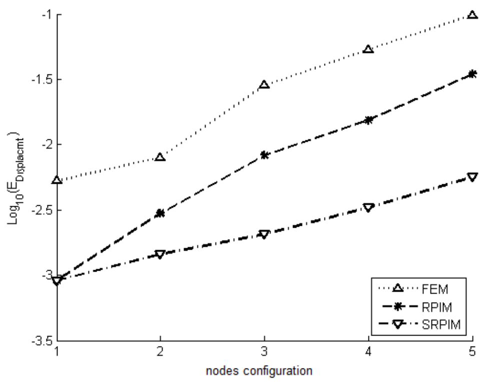

Figure 30: Relative error of displacement on results obtained by FEM, RPIM and SRPIM with several nodes configurations.

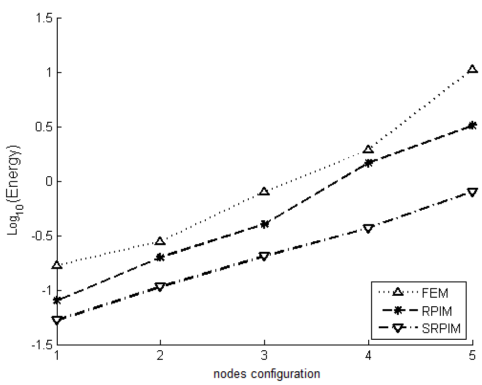

Figure 31: Energy error on results obtained by FEM, RPIM and SRPIM with several nodes configurations.

relatively good results. For regular nodal distribution, when the number of nodes inside the influence domain ranges from 6 to 25, the accuracy was high. With adding polynomial term and an appropriate influence domain size, shape parameters can be chosen from a larger range of values avoiding singular ones. Nodal distribution had little effect on the accuracy of RPIM interpolation. Further more it was observed that the SCNI integration scheme was less sensitive to distortion than the Gaussian integration scheme, and gives excellent results when compared to a Gaussian integration rule.

REFERENCES

[1] N. S. Lee, , K.J. Bathe , Effects of element distortions on the performance of isoparametric elements. Int. J. Numer. Meth. Engng., 36, 3553-3576 (1993).
[2] E. Cueto, N. Sukumar, B. Calvo, M. A. Martínez, J. Cegoñino, M. Doblaré, Overview and recent advances in natural neighbour galerkin methods, Archives of Computational Methods in Engineering, Volume 10, Issue 4, 307-384 (2003).
[3] J. Slater, Electronic energy bands in metals, Phys. Rev. 45, 794-801 (1934).
[4] R. Frazer, W. Jones, S. Skan, Approximations to functions and to the solutions of differential equations, Great Britain Aero Counc. London. Rep. and Memo. No.1799 1, 517-549 (1937).
[5] C. Lanczos, Trigonometric interpolation of empirical and analytical functions, J. Math. Phys 17, 123-199 (1938).
[6] M. B. Liu, G. R. Liu, Smoothed Particle Hydrodynamics (SPH): an Overview and Recent Developments, Archives of Computational Methods in Engineering, Volume 17, Issue 1, pp 25-76 (2010).
[7] L. Lucy, A numerical approach to testing the ssion hypothesis, Astron. J. 82, 1013-1024 (1977).
[8] B. Nayroles, G. Touzot, P. Villon, Generalizing the finite element method: diffuse approximation and diffuse elements, Computational Mechanics, 10 (5), 307-318 (1992).
[9] W. K. Liu, S. Jun, Y. F. Zhang, Reproducing kernel particle methods, Int. J. Numer. Methods Eng. 20 (8-9), 1081-1106 (1995).
[10] W. K. Liu, Y. Chen, S. Jun, J. S. Chen, T. Belytschko, C. Pan, R. A. Uras, C. T. Chang, Overview and applications of the reproducing Kernel Particle methods, Archives of Computational Methods in Engineering, Volume 3, Issue 1, pp 3-80 (1996).
[11] Y. Lu, T. Belytschko, L. Gu, A new implementation of the element free galerkin method, Computer Methods in Applied Mechanics and Engineering 113 (3-4), 397-414 (1994).
[12] J. G. Wang, G. R. Liu, Radial point interpolation method for elastoplastic problems, Proc. of the 1st Int. Conf. On Structural Stability and Dynamics, 703-708 (2000).
[13] S. N. Atluri, T. Zhu, A new meshless local petrov-galerkin (mlpg) approach in computational mechanics, Computational Mechanics 22 (2), 117-127 (1998).
[14] T. Belytschko, Y. Lu, L. Gu, Element-free galerkin methods, Int. J. Numer. Methods Eng. 37 (2), 229-256 (1994).
[15] J. Dolbow, T. Belytschko, An introduction to programming the meshless Element F reeGalerkin method, Archives of Computational Methods in Engineering, Volume 5, Issue 3, pp 207-241 (1998).
[16] G. Liu, Y. Gu, A point interpolation method, 4th Asia-Pacific Conference on Computational Mechanics Singapore, 1009-1014 (1999).
[17] G. R. Liu, Y. T. Gu, A point interpolation method for two-dimensional solids, Int. J. Num. Meth. Eng. 50, 937-951 (2001).
[18] G. Liu, Y. Gu, A matrix triangularization algorithm for the polynomial point interpolation method, Computer Methods in Applied Mechanics and Engineering 192 (19), 2269-2295 (2003).
[19] S. Beissel, T. Belytschko, Nodal integration of the element-free galerkin method, Computer Methods in Applied Mechanics and Engineer-ing 139, 49-74 (1996).
[20] J. Chen, C. Wu, S. Yoon, Y. You, A stabilized conform-ing nodal integration for galerkin mesh-free methods, Int. J. Num. Meth. Eng. 50, 435-466 (2001).
[21] . J. Chen, S. Yoon, C. Wu, Non-linear version of stabilized conforming nodal integration for galerkin mesh-free methods, Int. J. Num. Meth. Eng. 53, 2587-2615 (1993).
[22] M. Golberg, C. Chen, H. Bowman, Some recent results and proposals for the use of radial basis functions in the bem, Engineering Analysis with Boundary Elements 23, 285-296 (1999).
[23] J. Boyd, K. Gildersleeve, Numerical experiments on the condition number of the interpolation matrices for radial basis functions, Applied Numerical Mathematics 61 (4), 443-459 (2011).
[24] J. Chen, W. Hu, H. Hu, Localized radial basis function with partition of unity properties, Progress on Meshless Methods Computational Methods in Applied Sciences 11, 37-56 (2009).
[25] R. Franke, Scattered data interpolation: Tests of some methods, Mathematics of Computation 38(157), 200-292 (1982).
[26] R. Hardy, Multiquadric equations of topography and other irregular surfaces, Journal of Geophysical Research 176, 1905-1915 (1971).
[27] S. Rippa, An algorithm for selecting a good value for the parameter c in ra-dial basis function interpolation, Advances in Computational Mathematics 11, 193-210 (1999).
[28] M. Scheuerer, An alternative procedure for selecting a good value for the parameter c in rbf-interpolation, Advances in Computational Mathematics 34, 105-126 (2011).
[29] J. Wang, G. Liu, A point interpolation meshless method based on radial basis functions, International Journal for Numerical Methods in Engineering, 54 (11), 1623-1648 (2002).
[30] J. Wang, G. Liu, On the optimal shape parameters of radial basis func-tions used for 2d meshless methods, Computer Methods in Applied Mechanics and Engineering 191 (23/24), 2611-2630 (2002).
[31] G. Liu, G. Zhang, Y. GU, J. W. and, A meshfree radial point interpolation method (rpim) for three dimensional solids, Computational Mechanics, 36 (6), 421-430 (2005).
[32] L. Li, J. Zhu, S. Zhang, A hybrid radial boundary node method based on radial basis point interpolation, Engineering Analysis with Boundary Elements, 33 (11), 1273-1283 (2009).
[33] L. Dinis, R. N. Jorge, J. Belinha, Analysis of 3d solids using the natural neighbour radial point interpolation method, Computer Methods in Applied Mechanics and Engineering 196 (13-16), 2009-2028 (2007).

[34] L. Dinis, R.N. Jorge , J. Belinha, Analysis of plates and laminates using the natural neighbour radial point interpolation method, Engineering Analysis with Boundary Elements, Volume 32, Issue 3, Pages 267-279 (2008).

[35] G.R. Liu, K.Y. Dai, T.T. Nguyen, A smoothed finite element method for mechanics problems, Comput. Mech. 39, 859-877 (2007).

[36] K.Y. Dai, G.R. Liu, Free and forced vibration analysis using the smoothed finite element method (SFEM), J. Sound Vib. 301, 803-820 (2007).

[37] G.R. Liu, T.T. Nguyen, K.Y. Dai, K.Y. Lam, Theoretical aspects of the smoothed finite element method (SFEM), Int. J. Numer. Methods Eng.71 (8), 902-930, (2007).

[38] G.R.Liu, A generalized gradient smoothing technique and the smoothed bilinear form for Galerkin formulation of a wide class of computational methods, International Journal of Computational Methods, 5 (2), 199-236 (2008).

[39] G.R. Liu , Thoi. T. Nguyen, K.Y. Lam, An edge-based smoothed finite element method (ES-FEM) for static, free and forced vibration analysis.Journal of Sound and Vibration; 320: 1100-1130 (2009).

[40] Thoi. T. Nguyen, G.R. Liu , K.Y. Lam, G. Y. Zhang, A face-based smoothed finite element method (FS-FEM) for 3D linear and nonlinear solid mechanics problems using 4-node tetrahedral elements. International Journal for Numerical Methods in Engineering; 78: 324-353 (2009).

[41] Z. C. He , G.R. Liu , Z.H. Zhong , S.C. Wu , G.Y. Zhang , and A. G. Cheng, An edge-based smoothed finite element method (ES-FEM) for analyzing three-dimensional acoustic problems.Computer Methods in Applied Mechanics and Engineering; 199: 20-33 (2009).

[42] G.R. Liu, T. Nguyen-Thoi, H. Nguyen-Xuan, K.Y. Lam, A node-based smoothed finite element method (NS-FEM) for upper bound solutions to solid mechanics problems, Computers and Structures, 87 (1–2), 14-26 (2009).

[43] G. R. Liu, N. T. Trung, Smoothed Finite Element Method, Taylor and Francis, CRC Press (2010).

[44] S. Timoshenko, J. Goodier, Theory of Elasticity, McGraw-Hill, New York, (1970).

[45] G. Liu, Meshfree methods: moving beyond the finite element method, 2nd ed. Boca Raton: Taylor and Francis, CRC Press (2002).

Biocomposite Silicone: Synthesis, Mechanical Testing and Analysis

Siti Noor Azizzati Mohd Noor, Mohd Arif Fikri Khairuddin, and Jamaluddin Mahmud

***Abstract*—** Silicone elastomer is categorized under hyperlastic material. Its application is relatively limited due to the rather weak mechanical properties especially room temperature vulcanized silicone rubber (RTV) such as Ecoflex® Rubbers Supersoft 0030. This paper for the first time aims to produce reinforcing silicone rubber with kenaf powder fillers formed under synthesized process to increase the stiffness properties of the silicone rubber and to determine its mechanical properties in terms of material constants value by adapting hyperelastic constitutive models (i.e. neo-Hookean and Mooney-Rivlin). Initially, a pure silicone specimen was prepared. Meanwhile, Kenaf powder was selected to be used as silicone reinforcement or a filler material for synthesizing process and silicone reinforced with kenaf under 5 to 25 PHR units (part per hundred part of silicone rubber) was synthesized. This was followed by mechanical testing (uniaxial tensile test) and theoretical analysis which adapted hyperelastic constitutive models to determine the mechanical properties in terms of material constants value. Results indicate that addition of different percentage volumetric kenaf powders filler have improved the RTV weakness which allowed for exploration of wider applications for silicone rubber Results show that the silicone composites with kenaf fillers possess high stiffness compared to pure silicone. This resulted in variation of C_1 value, where it was found that greater value of C_1 indicates stiffer material behavior. Silicone reinforced with 25 phr kenaf powder possesses the highest value, 0.053 MPa (C_1) which means this specimen is the stiffest among the specimens. Meanwhile pure silicone possesses the lowest, 0.032 MPa (C_1) value which makes it the most elastic specimen. As for the Mooney-Rivin model, a similar scenario appeared where silicone reinforced with 25 phr kenaf powder possesses the highest 0.025 MPa and 0.111 MPa (C_1 and C_2) value and pure silicone possesses the lowest 0.020 MPa and 0.072 MPa (C_1 and C_2) value. Therefore, it can be concluded that the quantity of kenaf powder does influence the production of silicones reinforced with kenaf powder in terms of behaviour.

***Keywords*—** Silicone, kenaf, synthesis, hyperelastic constitutive model.

This work was supported in part by the Ministry of Education (MOE) Malaysia and Universiti Teknologi MARA (UiTM) under Grant No. 600-RMI/ERGS 5/3 (16/2012).

S.N.A.M. Noor is with Universiti Teknologi MARA, 40450 Shah Alam Selangor, Malaysia (e-mail: snazizzati@gmail.com).

M. A.F. Khairuddin is with Universiti Teknologi MARA, 40450 Shah Alam Selangor, Malaysia (e-mail: ichbin.ariffikri@gmail.com).

J. Mahmud is with the Faculty of Mechanical Engineering, Universiti Teknologi MARA, 40450 Shah Alam Selangor, Malaysia (corresponding author, phone: +603-5543-5133; fax: +603-5543-5160; e-mail: jm@salam.uitm.edu.my).

I. Introduction

The ability of silicone elastomer capable to stretch without experiencing in volume reduction generally depended on the bonded structure within the material [1]. This mechanical property relatively limits the applications of silicone rubber material [2]. The weaknesses can be overcome by reinforcing the silicone elastomer into biocomposite silicone material through synthesis process to improve the material stiffness [2]. This study has selected kenaf powder to be used as silicone reinforcement or a filler material. “Kenaf” or “*Hibiscus cannabinus*, L. family *Malvaceae*” is “ an herbaceous annual plant that can be grown under a wide range of weather conditions” [3]. From previous studies [3, 4], it was found that kenaf helps to improve the material strength of a composite construction with economical and availability advantages. In-depth study and knowledge on the synthesizing biocomposite silicone process is important to obtain a reliable result.

Tensile testing appeared to be one of the favourable methods to determine basic material properties of a material [5] and uniaxial tensile tests with regard to silicone elastomers have commonly been executed according to universal standards ASTM D412 [6-9] testing standards. Hence, the silicones reinforced with kenaf powder specimens were prepared according to ASTM D412 to observe the stress-stretch the behaviour of the material.

Silicone elastomers materials (rubber-like) are the most common examples of hyperelastic materials which possess hyperelasticity characteristics [8, 10-13]. Since mechanical testing is incapable of directly providing the mechanical properties of a material, hyperelastic constitutive models were adapted to theoretically quantify the material properties of the specimens (i.e. silicones reinforced with kenaf powder).

Two most popular hyperelastic constitutive models (i.e. neo-Hookean and Mooney-Rivlin) which were represented in strain energy density function (W) expressed in (1) and (2) respectively where C_1 and C_2 are the material constants, meanwhile $\bar{I}_1$ and $\bar{I}_2$ are the invariants [14, 15].

$$W = C_1(\bar{I}_1 - 3) \tag{1}$$

$$W = C_1(\bar{I}_1 - 3) + C_2(\bar{I}_2 - 3) \tag{2}$$

Hence this study focuses on synthesis a silicone rubber reinforced with kenaf powder and consequently followed by a mechanical testing (uniaxial tensile test) and theoretical analysis which adapted hyperelastic constitutive models (i.e. neo-Hookean and Mooney-Rivlin model) to determine their mechanical properties in terms of material constants value. This is novel as no similar syntheses related to reinforcement of silicone rubber with kenaf powder have been reported earlier.

II. Methodology

A total of three main stages (i.e. synthesis, experiment, and theoretical) are complied in this study. Figure 1 illustrates the process flow of the study which also includes the comparison between pure silicone and silicone reinforced with kenaf results.

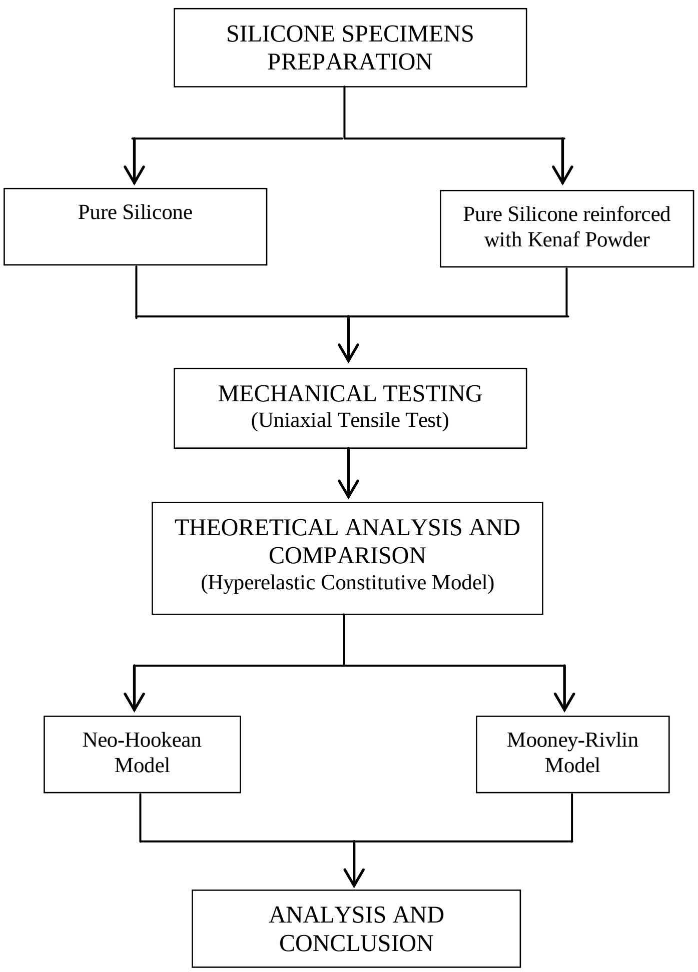

Fig. 1 Study Flow

A. *Synthesis of Biocomposite Silicone*

Initially, Pure Silicone specimens were prepared referring to ASTM D412 testing standard. Silicone matrix is quantified with parts per hundred (phr) units. To produce a single specimen of pure silicone, the ratio is 1:1 which is considered equal to 100 phr of silicone elastomer

Hence as shown in Figure 2 and 3, Pure Silicone (Ecoflex 0030) and its hardener were mixed at 50 percent of total volume for each. It is estimated that the total volume of a single dumbbell-shape ASTM D412 mold is 6cm ^{3} which gives 3cm^{3} in volume for Ecoflex 0030 and its hardener each. It is noted that every 1cm^{3} of silicone liquid is equal to 1g of its weight.

Once the mixture was ready, it was injected into ASTM D412 mould (Figure 4) properly before being placed in MCP vacuum machine for about 3 to 5 minutes. Lastly, the specimens underwent natural cure process for 72 hours at room temperature (28°C to 34°C) which completed the preparation of pure silicone specimens. One of the samples of pure silicone is shown in Figure 6(a).

Fig. 2 Silicone Ecoflex 0030 and hardener

Fig. 3 Mix Silicone Ecoflex with its harderner

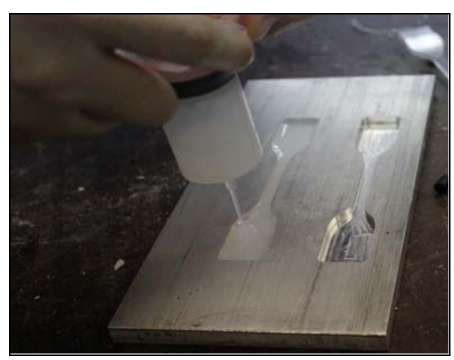

Fig. 4 Pour the mixture into ASTM D412 aluminium mould

The next process is to synthesize Kenaf Powder with Silicone. Kenaf powder (Figure 5) was extracted from bast fiber plant which was taken from the outer layer and core of the fiber (inner layer). Kenaf is widely used in many researches to determine material strength of a composite. Due to its ability to improve the tensile strength of composite, a synthesis process of kenaf powder compounded with silicone solution was done in this study.

Fig. 5 Kenaf Powder

Three main steps took place in synthesizing kenaf powder with silicone which are silicone preparation (Step 1), vacuum process (Step 2) and curing process (Step 3). During silicone preparation, it is important to measure the suitable volume or weight of filler material (kenaf powder) needed for synthesis process. Five different kenaf powders in grams (0.1, 0.2, 0.3, 0.5, and 0.6) which are equal to 5, 10, 15, 20, and 25 phr being premixed with silicone matrix during silicone preparation are tabulated in Table I.

Table I Composition of Kenaf Powder

phr	Mass (g)	Density (g/cm^3)	Volume (cm^3)
5	0.1	0.5702	0.2
10	0.2	0.5702	0.4
15	0.3	0.5702	0.6
20	0.5	0.5702	0.8
25	0.6	0.5702	1.0

Later the premixed kenaf - silicone matrix was poured (injected using a syringe) also into an aluminum dumbbell-shape mold as shown in Figure 4. Once the silicone was ready, Step 2 (vacuum process) took about 3 to 5 minutes which required MCP vacuum machine to reduce entrapped air bubbles from the specimen. After that, the natural curing process (Step 3) commenced by considering room temperature (28°C to 34°C) and curing of 72 hours, then only could the prepared specimen undergo a tension test. One of the silicones reinforced with kenaf powder specimen is shown in Figure 6(b).

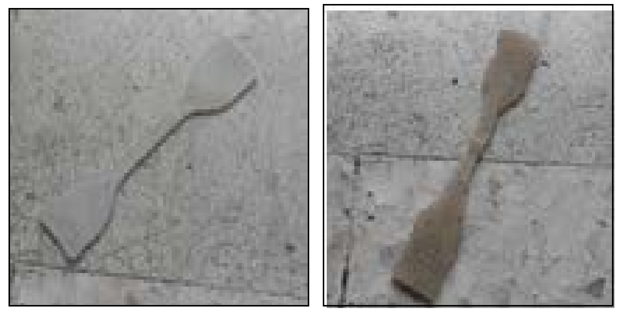

(a) (b)

Fig. 6 Specimen ready to be mechanically tested

B. Mechanical Testing

After all of the specimens had been prepared, uniaxial tensile test took place at Strength of Material Laboratory of Universiti Teknologi MARA, Malaysia. Using INSTRON 3382 Universal Testing Machine and referring to ASTM D412 testing standard, a total of five pure silicone specimens and twenty five silicones reinforced with kenaf powder specimens with different kenaf powder amount were tested till they reached their failure state. The speed was set to 500±50mm/min with the gauge width, 6mm, gauge thickness, 3mm and gauge length, 33mm. Figure 6(a) and 6(b) demonstrate the condition of the specimen while being tested and when it failed.

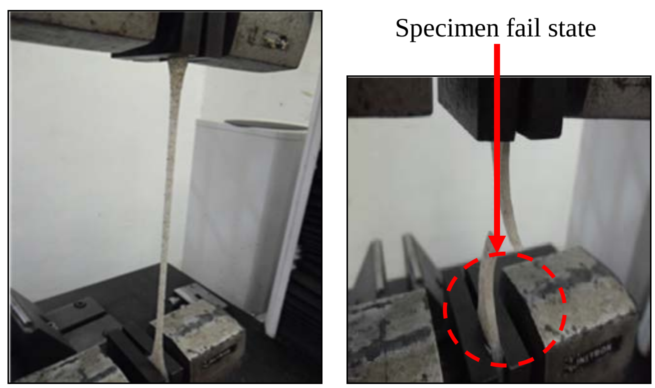

(a) (b)

Fig. 6 Specimen ready to be mechanically tested

C. Quantifying Material Constants

The material behaviour can be represented by the material constants ($C_1$and C_2) value which can be determined by adapting the theory of hyperelastic constitutive models (i.e. neo-Hookean and Mooney-Rivlin) in terms of stress-stretch relation formula. Referring to stress-stretch values obtained from the experiment, $C_1$and C_2 value can be determined using 3) and (4) for neo-Hookean and Mooney-Rivlin models respectively.

Stress-stretch curves were generated according to $C_1$and C_2 theoretical value determined and analysis was performed with the aid of Microsoft Excel 2010. Consequently parametric comparisons of different amounts of kenaf powder to pure silicone for all theoretical stress-stretch curves of neo-Hookean and Mooney-Rivlin were done.

ISBN: 978-1-61804-288-0

$$\sigma_E = (2C_1)\left(\lambda - \frac{1}{\lambda^2}\right) \tag{3}$$

$$\sigma_E = \frac{1}{\lambda}\left[\left(2C_1 + \frac{2C_2}{\lambda}\right)\left(\lambda^2 - \frac{1}{\lambda}\right)\right] \tag{4}$$

III. Results and Discussion

Uniaxial tensile test was conducted till specimen's failure stage on pure silicone and silicone reinforced with kenaf powder. Figure 7 illustrates the experimental results which are represented by the stress-stretch curves. X-axis represents stretch values while Y-axis represents stress values in MPa.

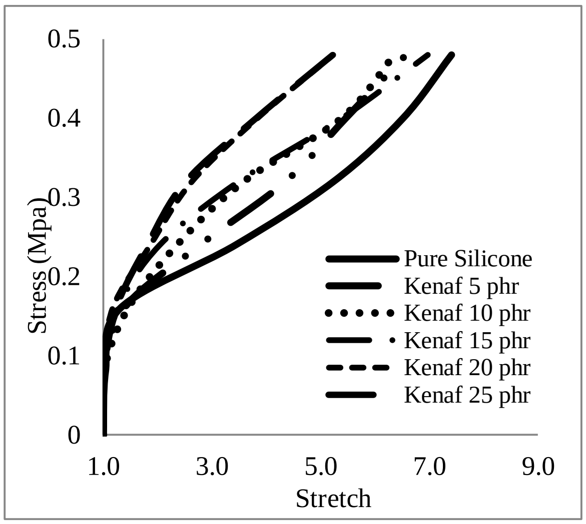

Fig. 7 Specimen ready to be mechanically tested

Each of the six curve plots shown in Figure 7 is the average of five (5) samples tested. This came from six different silicone mixtures which are pure silicone (0 phr kenaf powder), silicone reinforced with 5 phr kenaf powder, silicone reinforced with 10 phr kenaf powder, silicone reinforced with 15 phr kenaf powder, silicone reinforced with 20 phr kenaf powder and silicone reinforced with 25 phr kenaf powder.

From the results, it is noted that only silicone reinforced with 5 phr kenaf powder specimen behaves similarly to pure silicone while the remaining samples start to behave differently from pure silicone. It can be seen that amount of kenaf powder does influence the stiffness level of the specimen, where the specimen becomes stiffer along with the increment of kenaf powder amount.

Since experiment alone is incapable of quantifying the material properties, neo-Hookean and Mooney-Rivlin models were theoretically adapted to represent the properties in terms of material constants ($C_1$and C_2) value using experiment stress-stretch data previously obtained. Table II tabulates all of the material constants determined for pure silicone and each kenaf powder amount specimens.

From neo-Hookean's material constants (C_1) value was theoretically determined; Figure 8 demonstrates the differences between pure silicones with all 5 different silicone kenaf composite specimens for neo-Hookean model. This led to variation of C_1 value, where it was found that greater value of C_1 indicates stiffer material behavior. Silicone reinforced with 25 phr kenaf powder possesses the highest C_1 value which means this specimen is the stiffest among the specimens. Meanwhile pure silicone possesses the lowest C_1 value which makes it the stretchiest specimen. To summarize, the stiffness level of the specimen increases parallel to the amount of kenaf powder. Therefore the present kenaf powder in silicone matrix does influence silicone stiffness level.

As for the Mooney-Rivin model theoretical stress-stretch curve which is presented in Figure 9, a similar scenario appeared where silicone reinforced with 25 phr kenaf powder possesses the highest C_1 and C_2 values and pure silicone possesses the lowest C_1 and C_2 value. All specimens seem to be stiffer than pure silicone specimen.

Table II Material Constant theoretically determined for neo-Hookean and Mooney-Rivlin Model

	Hyperelastic Constitutive Model		
	Neo- Hookean	Mooney-Rivlin	
Kenaf Amount (phr)	C_1 (MPa)	C_1 (MPa)	C_2 (MPa)
0 (Pure Silicone)	0.032	0.020	0.072
5	0.038	0.025	0.068
10	0.040	0.025	0.075
15	0.039	0.019	0.106
20	0.052	0.024	0.111
25	0.053	0.025	0.111

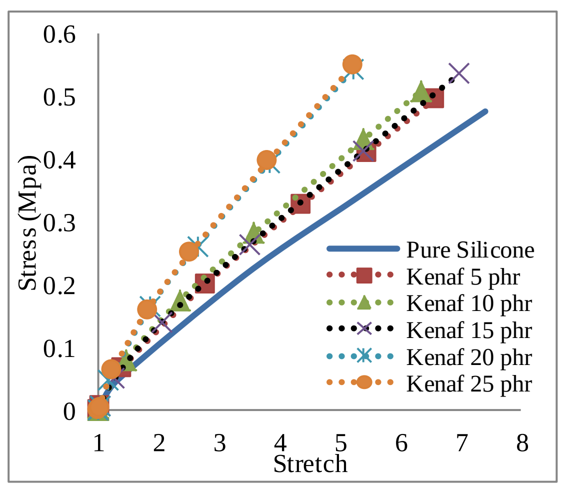

Fig. 8 Five different reinforced silicones kenaf powder with pure silicone using neo-Hookean Model

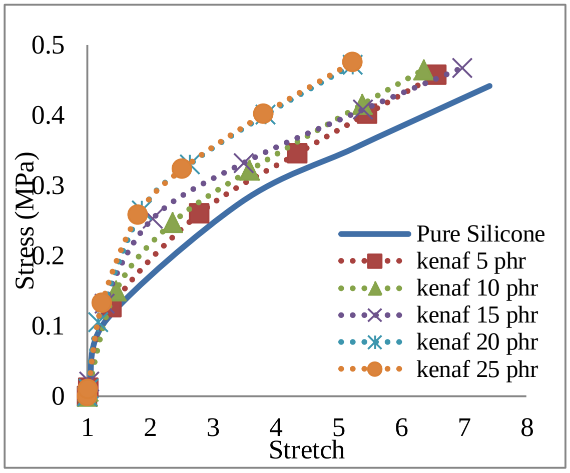

Fig. 9 Five different reinforced silicones kenaf powder with pure silicone using Mooney-Rivlin Model

IV. Conclusion

This paper has successfully presented a detailed procedure on synthesizing a biocomposite silicone mainly using a mixture of pure silicone and kenaf power. Based on experimental and theoretical results, it can be concluded that the greater value of material constant indicates high stiffness. This highlighted the influences of kenaf powder amount in the production of silicones reinforced with kenaf powder which also influence the behaviour. This study has also opened the gateway to further explore other hyperelastic constitutive models such as Ogden theory to determine material properties of hyperelastic material.

Acknowledgment

This work was supported in part by a grant from Ministry of Education (MOE) Malaysia and Universiti Teknologi MARA (UiTM) with a Grant No of 600-RMI/ERGS 5/3 (16/2012).

References

[1] W. Arayapranee, "Rubber abrasion resistance," *Abrasion Resistance of Materials, InTech, Rijeka*, pp. 147-166, 2012.

[2] P. Song, Z. Peng, Y. Yue, H. Zhang, Z. Zhang, and Y. Fan, "Mechanical properties of silicone composites reinforced with micron-and nano-sized magnetic particles," *Express Polymer Letters*, vol. 7, pp. 546-553, 2013.

[3] T. Nishino, K. Hirao, M. Kotera, K. Nakamae, and H. Inagaki, "Kenaf reinforced biodegradable composite," *Composites Science and Technology*, vol. 63, pp. 1281-1286, 7// 2003.

[4] N. Asilah and C. Aziz, "Mechanical performance of kenaf fibre reinforced thermoplastic composite," University Malaysia Pahang, 2011.

[5] X. Liu, "Understanding the effect of skin mechanical properties on the friction of human finger-pads," 2013.

[6] Q. Xu, M. Pang, L. Zhu, Y. Zhang, and S. Feng, "Mechanical properties of silicone rubber composed of diverse vinyl content silicone gums blending," *Materials & Design*, vol. 31, pp. 4083-4087, 2010.

[7] J.-H. Bae and S.-H. Chang, "A study on the mechanical behavior of silicone-organically modified montmorillonite composite under human body simulated environment," *Composites Science and Technology*, vol. 85, pp. 90-97, 2013.

[8] V. Vahapoglu, S. Karadeniz, and I. Yazici, "Uniaxial Tensile Testing of Rubber-Like Materials," *Experimental Techniques*, vol. 35, pp. 17-23, 2011.

[9] Y. J. Adeel, A. I. Muhammad, and A. Zeeshan, "Characterization of Hyperelastic (Rubber) Material Using Uniaxial and Biaxial Tension Tests," *Advanced Materials Research*, vol. 570, pp. 1-7, 2012.

[10] M. Noor, S. N. Azizzati, and J. Mahmud, "A Review on Synthetic Skin: Materials Investigation, Experimentation and Simulation," *Advanced Materials Research*, vol. 915, pp. 858-866, 2014.

[11] R. Jakel, "Analysis of Hyperelastic Materials with Mechanica-Theory and Application Examples," in *2nd Simulation Meeting SAXSIM (SAXon SImulation Meeting)*, T. U. Chemnitz, Ed., ed, 2010.

[12] J. de Sousa Crespoa, "Human Tissue Hyperelastic Analysis," Instituto Superior Tecnico, Universidade Tecnica de Lisboa, 2009.

[13] M. Sasso, G. Palmieri, G. Chiappini, and D. Amodio, "Characterization of hyperelastic rubber-like materials by biaxial and uniaxial stretching tests based on optical methods," *Polymer Testing*, vol. 27, pp. 995-1004, 2008.

[14] S. N. A. M. Noor and J. Mahmud, "Skin Prestretch Evaluation Adapting Mooney-Rivlin Model," *Journal of Medical and Bioengineering Vol*, vol. 4, 2015.

[15] M. Yusop, S. Hajar, A. Patar, M. N. Azmi, A. Majeed, P. Anwar, *et al.*, "A Parametric Investigation on the Neo-Hookean Material Constant," *Advanced Materials Research*, vol. 915, pp. 853-857, 2014.

Siti Noor Azizzati Mohd Noor has a Bachelor Engineering (Hons.) in Mechanical Engineering degree from Universiti Teknologi MARA (UiTM) Shah Alam and a Diploma in Mechanical Engineering from Universiti Teknologi MARA (UiTM) Pulau Pinang. Currently, she is pursuing her Masters study (Research mode) in Mechanical Engineering at Universiti Teknologi MARA (UiTM). Her areas of research interest include Biomechanics, Finite Element Simulation and Hyperelastic Materials, involving both experimental and numerical approaches.

Mohd Arif Fikri has a Bachelor Engineering (Hons.) in Mechanical Engineering degree from Universiti Teknologi MARA (UiTM) Shah Alam and a Diploma in Manufacturing Technology from Universiti Sultan Zainal Abidin (UniSZA) Terengganu, Malaysia. His areas of research interest include Biomechanics, Biocomposite Materials and Hyperelastic Materials, involving both experimental and numerical approaches.

Assoc Prof Dr J. Mahmud has a PhD degree in (Biomechanical) Engineering from Cardiff University UK, an MSc (Manufacturing) Engineering degree from International Islamic University, Malaysia (IIUM) and a B.Eng. (Hons.) Mechanical Engineering degree from Universiti Teknologi MARA (UiTM). He joined the Faculty of Mechanical Engineering UiTM as a lecturer in 2001. Currently he is an Associate Professor and a Deputy Dean. He has about three years of industrial experience, working as a service engineer at UMW Equipment Sdn. Bhd. Dr. J Mahmud has been lecturing on Biomechanics, Composite Materials, Finite Element Method, Manufacturing Processes and Product Design, which happens to be his areas of research interest and has published more than 90 technical papers in journals and conference proceedings locally and internationally. Due to his active exploration on the new application of motion capture system, a paper entitled '*Using motion capture and analysis to explore the mechanical properties of human skin in-vivo*' has been invited by IMechE, UK for presentation at the *IMechE Medicine and Health Division Meeting:* 15 October 2009.

Approach to solving the problem of vibration during the drilling phase $8^{1/2}$"in an oil southern Algerian fields.

A. MELLAK and K. BENYOUNES

Abstract— The present work is to conduct an analysis and study choices appropriate drilling tools to minimize vibration in the $8^{1/2"}$ hase in an oil field south of Algeria. In rotary drilling, vibrations of the drill string, whether lateral, torsional or axial, play an important role in the drilling of a well and influence its progression because these vibrations can be harmful and cause malfunctions during drilling operations. A vibration limits the forward speed of the tool and is increasing the price of drilled meter. Two optimization methods were used in this work to improve drilling performance by selecting the most appropriatetoolforthesection$8^{1/2"}$. The first method is based on two criteria, namely, first, the selection of the tool according to the drilled interval, ROP (advancement of the tool) and the meter price drilled and on the other hand, it will be based on the analysis of compressible strengths of the rock. The second method is based on the wear of the tool (dull grading) and performance of ROP. The price of fixed returns for a rock bit PDC (Polycrystalline Diamond Compact) is less than the price obtained by the tri-cone tool, but the problem is the appearance of vibrations that affect the advancement and thus cause wear of teeth the tool breakage**.**

Keywords— Drilling, rock bit. Oil field, vibrations.

I. INTRODUCTION

In rotary drilling, the drill stem vibrations are important and may cause drilling operations because malfunctions canlead to failure of the drill string, damage of the drilling tool and to the overall decline in drilling performance. Of the three types of vibrations of drill strings, lateral vibration and torsional vibration appear to play a major role, Depends on the axial vibration (Ledgerwood and Al, 2010).Many researchers have measured lateral vibration acceleration using measurement-while-drilling (MWD) tools.Many indicators confirm this trend. Indeed, while Dufeyte and Henneuse, (1991) felt that the most severe form of torsion vibration, stick-slip, occurred 50% of the effective drilling time, many technical developments drilling have only encourage the stick-slip since. Among the most important factors are: the significant increase in the market share of Polycrystalline Diamond Compact tools (PDC) (Rach, 2010); the return to the forefront of the art rotary drilling through the development of directional systems (Wade, 2007); the overall decrease in the rotational speeds applied to the drill stem to avoid entering into arrangements with lateral vibrations (Ledgerwood and Al, 2010). Dykstra et al. (1995) conclude that the weight on bit (WOB), rate of penetration, and mechanical properties of rock contribute to lateral drill string vibrations; the lateral vibration acceleration is normally more than 20 g and may be as high as 200 g(Zhu eu al., 2013).Many indicators confirm this trend. Indeed, while Whether Dufeyte and Henneuse (1991) felt that the most severe form of torsional vibration, stick-slip, occurred 50% of the effective drilling time, many technical developments drilling have only encourage the stick-slip since. Among the most important factors are: the significant increase in the share tools market Polycrystalline Diamond Compact (PDC) (Rach, 2010); the return to the forefront of the art rotary drilling through the development of steering systems; the overall decrease in the rotational speeds applied to the drill stem to avoid entering into arrangements with lateral vibrations (Ledgerwood et al., 2010); the general increase in friction between the pads and wells due to the complexity of current paths; increasing the depth of wells drilled and hardness associated rocks (Dykstra et al., 2010). Eliminate vibrations damaging these systems or reduce their performance is a major challenge.

A. Mellak, Prof. Doc, *is with the Laboratory Engineering Physics Hydrocarbons. Department of Mineral deposits and Oil. Boumerdès University- 35 000 – Algeria. (Mellakabder@yahoo.fr).*

K. Benyounes, Doc. is with the is with the Laboratory Engineering Physics Hydrocarbons. Department of Mineral deposits and Oil. Boumerdès University- 35 000 – Algeria.(Khaled_benyounes@yahoo.fr).

II. CASE STUDY

To optimize drilling performance in Section 8 ½,

To optimize drilling performance in Section 8 ½, two wells were chosen (which may be called RBK and EME), located in the same basin. According to the data of the daily reports of

ISBN: 978-1-61804-288-0

the two drilling the well, the drilling parameters such as weight on bit (WOB), the tool rotation (RPM) and the advancement of the tool (ROP) are presented in the following figures (1,2 and 3):

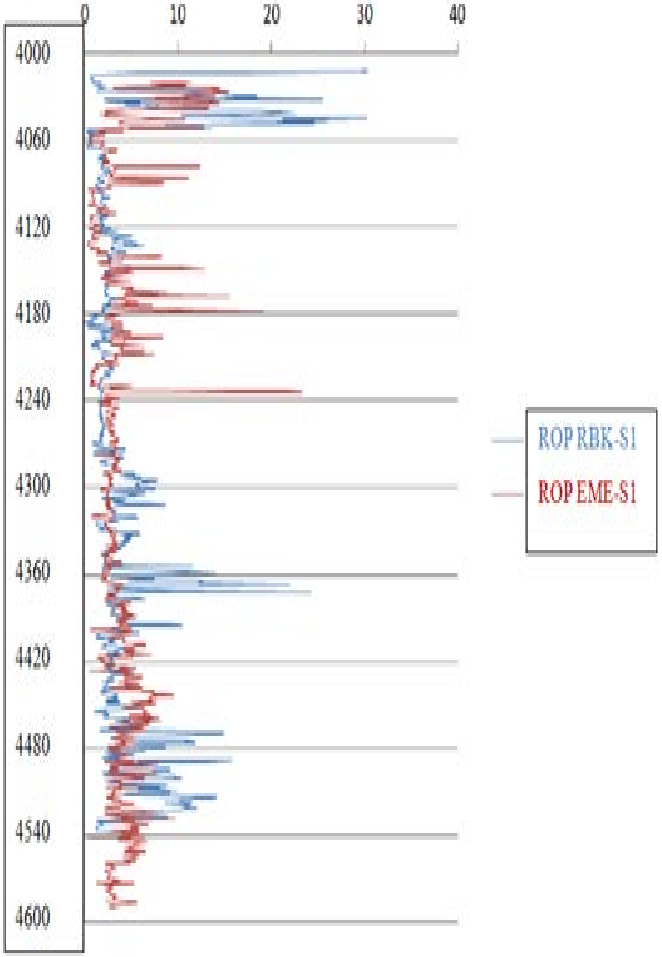

Fig.1: Penetration rate of two wells.

These figures show the rate of progress of each section of the selected well and also show the best drilled intervals. These graphs are essential and useful to select the best drilling parameters in the case of the same features of the training. When penetration is lower, it means that the drilling time will be slower and the cost of meter drilled will be higher.

There is in these graphs that the high status is obtained with a WOB and RPM low speed of 4000 m to 4060m for the two wells, and the low rate of progress with great WOB and RPM for well RBK to a depth of 4360 m where he reached another high penetration with low WOB.

For EME there is a low to high variation of the ROP with a low WOB in comparison with the RBK wells 4060 - 4240 m.

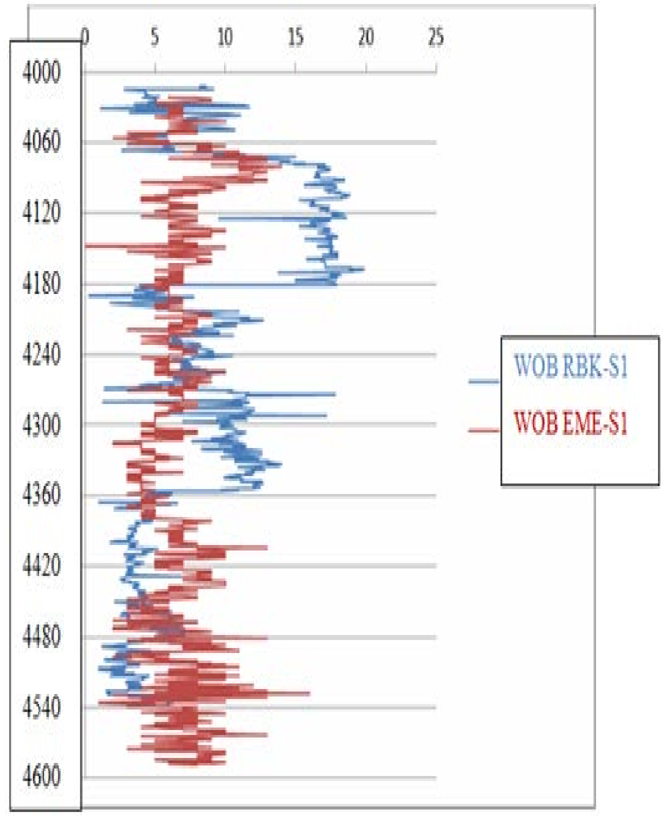

Fig.2: Weigh the tool for both wells.

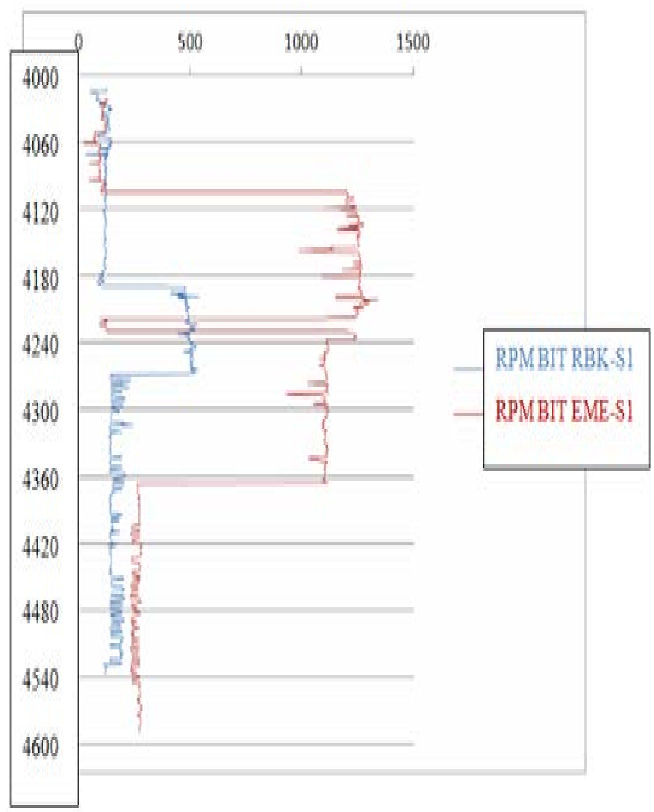

Fig.3: The rotation of the tool for selected wells (RPM (tr./min)).

This variation of high progress rates down is the result of the change in lithology with depth and type of tools used. The types of tools are different and are selected according to the hardness of the formation. The meters drilled for each tool varies depending on the hardness of the training and the efficiency of the bit. Table 1representstheperformanceof the tools used in the RBK wells.

Table 1: Performance of the RBK tool.

Bit type	IADC code	Meters drilling
PDC	M433	74
Insert	537	31
Impregnated	M841	25
Insert	537	10
Insert	637	22
Impregnated	M841	133
Insert	447	34
Impregnated	M841	333
PDC	460	460
PDC	19	19

Table2 shows the performance of the EME tool.

Table 2: Performance of the EME tool.

Bit type	IADC code	Meters drilling
Insert	447	07
PDC	M333	11
Insert	447	54
Impregnated	M844	17
Impregnated	M842	190
PDC	M843	18
Impregnated	M842	228
PDC	M432	421
PDC	M432	157

III. RESULTS AND DISCUSSION

The identification of the compressive strength and analysis was connected to training evaluation and prediction tool). This soft ware allows us to develop the most efficient drilling strategy based on the mechanical properties of the formation and incorporates the evaluation of training with a variety of performance measures to help define the selection of the most advantageous tool and drilling operating parameters for specific situations.

Figure 4 presents the analysis of Section 8½ " of well RBK. Data analysis of this well is based on data daily reports and logging of drilling muds. The Emsian layer is formed by clays and sandstones. It begins with a high level of hardness and abrasiveness with CCS (Confined Compressive Strength) ranging from 10to 40Kpsi. Great potential vibration and abrasion from 1 to100, which confirms the difficulties encountered in this lithology. Once the tool in clays, the hardness of the training down to its lowest level. The guide of the hardness of the rock (DSG) and the column of the tool Wear Guide (WG) shows the severity of dressing with yellow to red colors in these columns. The tool is in sandstone of Emsian. The Emsian is mainly formed by sandstones and clays with CCS (Confined Compressive Strength) of 20Kpsi to 35Kpsi and resistance to compression ranging from 10Kpsi confined to 20Kpsi. The top of the Emsian is formed by a strip of pyrite. We notice a sudden increase to 30 Kpsi- 60Kpsi in the CCS at 3950m. The index of vibration varies from 0.1 to 10 and the abrasive ranges from about 10. Once the tool reaches the stringers and sandstone bands, increasing the level of vibration is observed.

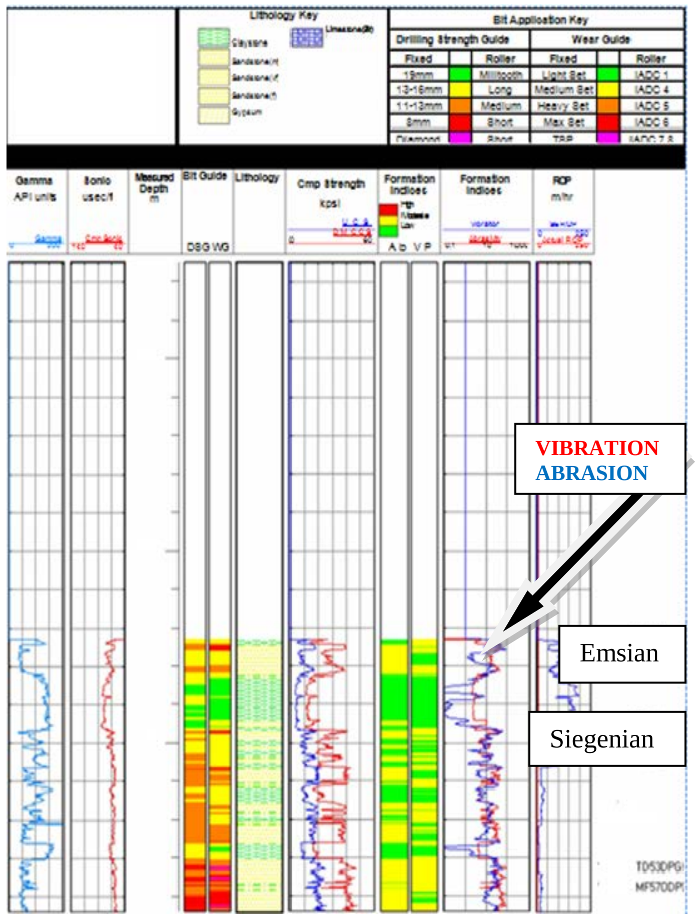

Fig.4: Analysis of the well RBK.

For a better selection than previous tools that were used in selected wells, two optimization methods can be applied namely; (i) Comparison of penetration (ii) The cost per meter drilled each tool. Concerning the primary optimization method for the selection of the tool, it is made according to the interval drilled, ROP and cost of meter drilled as well as the analysis of the rock of the strength of the drilled section. This method of primary optimization successful in identifying the causes of the short life of the tool and the determination of the characteristics of the tool to drill this section selected wells. According drilled interval, the POR and the cost per meter and after analysis, the choice of tools for drilling the section $8^{1/2}$" in tables 3 and 4.

Table 3: Performance of the RBK tool

Bit type	IADC code	Meters drilling	Cost $/m	Formation	ROP m/h	Dull grading
PDC	M433	74	1554	Couvinian Emsian Siegenien	3.00	13 WT N.XI.CT PR

Table 4: Performance EME well

Bit type	IADC code	Meters drilling	Cost $/m	Formation	ROP m/h	Dull grading
Inser t	447	34	4414	Couvinian	3.20	11 WT A E I NO.
Inser t	447	54	1210	Emsian	2.60	24 BT H EI WT

As regards the analysis performed on two wells (RBK and EME), the ROP performance obtained and the wear classification made for each tool, it could move the appropriate toolforthesection8halfof the basin in question, namely the PDC tool 11mm cut. It will be most suitable for drilling training between Couvinian and Sieginian. This tool provides the necessary resistance too vercome the abrasiveness and vibration due to the presence of band sofhards and stone, and abrasive compact.

IV. CONCLUSION

The aim of our work is to optimize drilling performance in $8^{1/2''}$ phase. To achieve this goal, two wells were selected in the same basin and the type of tool and its performances were taken from the mud logging reports. The identification of the compressive strength of the rock and the analysis for the $8^{1/2''}$ phase section has been achieved. Two optimization methods were used in this study to enhance the drilling performance by selecting the most appropriate tool for the section $8^{1/2''}$. The first method is based on two criteria, namely, first, the selection of the tool according to the drilled interval, ROP (advancement of the tool) and the meter price drilled and on the other hand, it will be based on the analysis of compressible strength of the rock. The second method is based on the wear of the tool (dull grading) and performance of ROP. After analyzing the results, the PDC cutting too l11mm seems most suitable to drill with a diameter of $8^{1/2''}$, training between the Couvinian and Sieginian and could overcome the abrasiveness and vibrations due in the presence of the formation, formed of strips of hard and stone, abrasive compact.

REFERENCES

[1] M. P. Dufeyte, and H. Henneuse. "Detection and monitoring of the slip-stick motion: Field experiments." *SPE/IADC drilling conference*.Society of Petroleum Engineers, 1991.

[2] V.A. Dunayevsky, F. Abbassian, and A. Judzis.. Dynamic Stability of DrillstringsUnder Fluctuating Weight on Bit. *SPE Drill & Compl* 8 (2):84-92. SPE-14329-PA.doi:10.2118/14329-PA.1993.

[3] M.W. Dykstra, ,D.C.K.Chen,, T.M. Warren, Drillstring component mass imbalance: a major source of down hole vibrations. In: Proceedings of the SPE/IADC 29350.1995

[4] M.W. Dykstra, B.V. Schneider &J. Mota. A systematic approach to performance drilling in hard rock environments. In SPE/IADC Drilling Conference and Exhibition. Society of Petroleum Engineers, 2011.

[5] L.W. Ledgerwood,, O.J.M.. Hoffmann,J.R. Jain,C. El Hakam, C.Herbig, & R. Spencer. Downhole Vibration Measurement Monitoring and Modeling Reveal Stick/Slip as a Primary Cause of PDC-Bit Damage in Today. In SPE Annual Technical Conference and Exhibition. Society of Petroleum Engineers 2010.

[6] M. Rastegar, A. Bashari, R. Nygaard & G. Hareland, G.. Optimization of multiple bit runs based on ROP models and cost equation: A new methodology applied for one of the Persian Gulf carbonate fields. In IADC/SPE Asia Pacific Drilling Technology Conference and Exhibition.Society of Petroleum Engineers SPE.M.2008.

[7] R. Sadi, N. Iraten, A. Mellak,, « Approche de la solution du problème dans la phase $8^{1/2''}$ (gédinien) dans le champ du sud Algérien. Mémoire de Master Forage. UMBB - 2014

[8] N. Rach. New Bits shine in the shales. E&P Mag, Hart Energy Publishing, LP,http://www.epmag.com/Magazine/2010/3/item53515.php. Aron Deen.2011,"Application of a Torsional Impact Hammer to Improve Drilling Effeciency". SPE 147193, 2010.

[9] S.F. Sowers, F.E. Dupriest,J.R. Bailey, &L. Wang. Use of Roller Reamers Improves Drilling Performance in Wells Limited by Bit and Bottomhole Assembly Vibrations. In SPE/IADC Drilling Conference and Exhibition. Society of Petroleum Engineers, 2009.

[10] Zhu, Xiaohua, and Weiji Liu. "The effects of drill string impacts on wellbore stability." Journal of Petroleum Science and Engineering 109, pp.217-229, 2013.

Numerical Study of Energy Separation in Counter-Axial Flows

Manimaran R.

Abstract— Energy separation is the redistribution of total energy in a flow without external heat or work, so that some portion of the fluid has higher total energy and other portion has lower total energy than the remaining fluid. In the present study, the mechanism of energy separation is numerically investigated in two opposite free jet flows. A commercial code is used to solve mass, momentum and total energy conservation equations. The physics of the flow is studied and found that vorticity plays an important cause for energy separation. Parametric studies are also carried out to understand the effect of energy separation on the Reynolds number and geometric length of free jets for two opposite axial flows.

Keywords—Energy separation, Computational Fluid Dynamics, Parametric studies, Shear flow, Turbulence.

INTRODUCTION

Energy separation presents the possibility to heat or cool fluid without using a conventional heating or cooling system. Further research to enlarge the temperature difference is still required. Not only this possiblilty, but also the understanding of the mechanism involved is important to predict the accurate temperature distribution in fluid flows where flows are used as heat transfer enhancement methods such as impinging jets. Recently few studies were performed to investigate the instantaneous mechanism experimentally and numerically. Experiments to measure instantaneous total temperature were performed in the wake of a circular cylinder [1], and a turbine blade [2]. Fox et. al [3] carried out a numerical analysis of the energy separation in a free jet with inviscid and non-conducting fluid assumption. Han and Goldstein [4] performed a numerical analysis of the same problem in a plan shear layer by solving the two – dimensional Navier-Stokes equations. However their analysis assumed a non-conducting fluid. Since Eckert and Weise [5] first found energy separation from the recovery temperature distribution on a circular cylinder, others have reported the existence of the phenomenon in various flows including boundary layers, jet flows and cross-flow across a circular cylinder and shear layers. Eckert [6] suggested two physical mechanisms of energy separation. One is the imbalance between the energy transport by viscous shear work and that by heat conduction. The other is due to pressure fluctuation within flow fields caused by moving vortices. Unlike the energy separation by the imbalance of shear force / energy due to heat conduction, energy separation from pressure fluctuation has time-dependent characteristics. He also pointed out that energy separation of a viscous flow is caused by both the mechanisms.

Understanding the motion of the coherent structure around a jet and its sensitive response to acoustic excitation has drawn significant researchers' attention. The experimental studies on free jets at Reynolds numbers 8000 and 120000 are carried out by Han and Goldstein [7]. For the low Reynolds number jet, spectral analysis of instantaneous velocity and flow visualization by a schlieren system are performed with/without acoustic excitation. The flow characteristics of the high Reynolds number jet are also investigated with spectral analysis, since energy separation is more prominent in high speed flows. The results provide useful information on the motion of the coherent structure and its response to acoustic excitation. This forms the basic building blocks of energy separation mechanism. The jet in cross flow or transverse jet has been studied extensively because of its relevance to a wide variety of flows in technological systems, including fuel or dilution air injection in gas turbine engines, thrust vector control for high speed air breathing and rocket vehicles, and exhaust plumes from power plants. These widespread applications have led over the past 50 years to experimental, theoretical, and numerical examinations of this fundamental flow field, with and without a combustion reaction, and with single or multi-phase flow. The complexities in this flow field, whether the jet is introduced flush with respect to the injection wall or from an elevated pipe or nozzle, present challenges are lying in accurately interrogating, analyzing, and simulating important jet features.

Numerical simulations of mean velocity and turbulent kinetic energy fields are presented by Ting and Li [8] for three-dimensional lateral jet in cross flow, at various injection angles with the RNG k-ε turbulence model, with the two-layer wall function method, is adopted to simulate the characteristics of this flow at the jet-to-cross flow velocity ratios, 1, 2 and 4. The results show that the injection angle and jet-to-crossflow velocity ratio can change the flow fields, and the range upstream affected by jet injected laterally and the curvature of jet trajectories varies along the flow direction.

Manimaran R. is with the Thermal and Automotive Research Group, School of Mechanical and Building Sciences, Vellore Institute of Technology, Chennai Campus, Vandalur-Kelambakkam road, Chennai – 600127, Tamilnadu, India phone: +91-44-3993-1426; fax: +91-44-3993-1555; (e-mail: manimaran.r@ vit.ac.in)

Furthermore, the separation events in the lee side of the jet exit and behind the jet bending-segment have been found, and the mechanisms of two vortex systems are analyzed. The radial velocities of the closely spaced opposed jets across various exit velocities, nozzle diameters and nozzle separations were studied experimentally by hot wire anemometry and analyzed theoretically on the basis of N-S equation. The criterion in determining the junctions of wake and jet flows lies in the velocity gradient equal to zero and determined by Chou et al [9]. In the wake region, the amplitude of the resonant instability appears to be much significant in both stream wise and transverse components. A succession of shedding vortices is then identified to dominate the wake flow dynamics. While in the jet region, both resonant and its sub-harmonic instabilities prevail in the same order of contributions to the development of the coherent structures. The vortex formation and merging processes now become dominant in the jet flow dynamics. As compared to the natural jet, the evolution of the coherent structures is greatly enhanced during the self-sustained oscillating flow field, which extends from the jet exit to the cylinder. The local maxima of fluctuation intensities, energy production and energy convection occur in the jet shear layer close to the jet–cylinder impingement region. The effect of unsteady vortical structures on the adiabatic wall temperature distribution in an impinging jet is explored by Fox et al [3]. A conceptual model is introduced for the separation of the total temperature, appealing to the dynamics of particle path lines and vortex rings in the jet. The presence of a region of higher total temperature on the inside of the jet and a region of lower total temperature toward the jet periphery, predicted by the model, exhibits good agreement with the theoretical and experimental data taken at high subsonic Mach number.

The vortex tube is a simple device used in industry for generation of cold and hot air streams from a single compressed air supply. This simple device is very efficient in separation of air streams of different temperatures and has been the focus of investigation since the tube's discovery. Different explanations for the phenomenon of the energy separation have been proposed, however there has not been a consensus in the hypothesis. Current explanations is based on

the working concept of a vortex tube. Hypotheses of pressure, viscosity, turbulence, temperature, secondary circulation and acoustic streaming towards the energy separation in vortex tube. The accurate numerical simulation of the flow in a vortex tube, resulting in an improved prediction capability of the kinematic and thermal properties of outgoing jets, could allow a correct estimation of the cooling performance of this device in jet impingement operation. The computations by Eiamsa [10] with selective source terms of the energy equation suppressed show that the diffusive transport of mean kinetic energy has a substantial influence on the maximum temperature separation occurring near the inlet region. In the downstream region far from the inlet, expansion effects and the stress generation with its gradient transport are also significant.

In the present study, a two dimensional co-annular jet has been considered for analysis of energy separation. Suitable turbulent models are selected and problem is solved by finite volume method. The importance of vorticity at different geometrical conditions are understood and turbulent intensities are calculated and compared among the various cases.

GEOMETRY OF THE MODEL

The geometry chosen for the investigation of energy separation between two co-annular jets is simple as shown in fig.1

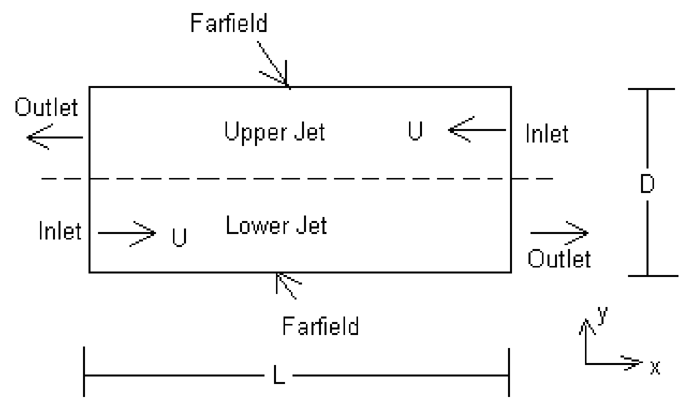

Fig. 1. Schematic diagram of model with boundary conditions

The length (L) and characteristic dimension (D) chosen by default are 0.1 m and 0.02 m respectively. However, parametric studies are performed by changing the length and characteristic dimensions. The geometry is meshed and shown in figure 2.

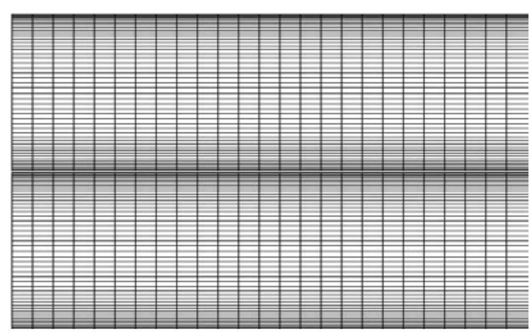

Fig. 2. Geometry mesh clustered at the centreline and near the farfield

NUMERICAL FORMULATION

Numerical simulation of flow between two co-annular opposite free jets is a very difficult and challenging task, as it deals with the prediction of compressible and turbulent flow. Moreover, strong temperature gradients exist between the two jets where energy separation is investigated. The temperature gradients arise in axial direction than in the radial direction. Hence the problem is strongly coupled with the flow and thermal characteristics. Due to its characteristics, mathematical modelling of the flow requires particular care in establishing the governing equations, in setting the solution techniques and in setting the turbulence closure models. As a consequence of the relevance of the thermal gradients (separation effect) and of the flow compressibility, the continuity and Navier-Stokes equations are completed using the energy equation and the gas equation of state. Thermo-physical properties of the air are assumed to be varying with the temperature as a third order polynomial function. The general form of the conservation equations to be solved by fluent can be represented in general form by

$$\frac{\partial}{\partial t}\left(\int_{CV}\rho\phi\, dV\right) + \int_{A}\mathbf{n}\cdot(\rho\phi\,\mathbf{u})\, dA = \int_{A}\mathbf{n}\cdot(\Gamma\, grad\,\phi)\, dA + \int_{CV} S_{\phi}\, dV \tag{1}$$

In the above equation, the left hand side represents the total derivative terms (local and convective terms) and the right hand side represents the diffusion and source terms for continuity () , momentum and energy. These equations are solved numerically by the built in coupled implicit solver of the commercial finite volume code FLUENT [11]. Boundary conditions are expressed by imposing pressure and temperature components values at the pressure inlet and outlet respectively.

Adiabatic conditions are set at the farfield conditions. The internal heat source has been neglected here as the energy separation between two jets are interested in the current problem under investigation. Newtonian fluid is assumed and turbulence closure model is varied and solutions are obtained after the convergence criterion ($1x10^{-6}$) are met for all the equations of continuity, momentum and energy. The modelling of some unclosed terms presents particular difficulties due to flow compressibility and their complete formulation is not yet achieved. Anyway, in this work, the RNG k–e model (Renormalization group k-e first order closure model) where k being the turbulent kinetic energy and e being the turbulent dissipation rate. The RNG k-e model is based on the Boussinesque’s hypothesis, and the RSM (Reynolds Stress Model second order differential closure model) have been used. A correction term is introduced in the k-e transport equation that is a function of the strain rate tensor and makes the RNG model more responsive to the effect of both rapid strain and streamline curvature with respect to the standard k-e model. Being the RNG k–e more suitable than the standard k-e model for the prediction of high speed jet flows, an intrinsic assumption is made by using a turbulent viscosity model. In fact, the components of the Reynolds stress tensor at each point and time are determined by the mean velocity gradient at the same point and time (local characteristic of the turbulence model). This assumption is verified only if the turbulence adjusts rapidly to the mean straining of the flow. This condition is true for simple turbulent flows (like round jet, mixing layer, boundary layer), in which the mean velocity gradient can represent the ‘‘history of mean distortion of the flow”, the non-local transport processes are small and the turbulence production almost balances dissipation. In these cases the local character of the Boussinesque’s hypothesis is acceptable and a turbulent viscosity model can be used. Moreover, in the first order closure models there is an explicit assumption related to the structure of Reynolds stress tensor. In fact, the Boussinesque’s relation imposes the isotropy of the normal components in the turbulent stress tensor. This assumption was found to be. The complete transport equations for Reynolds stresses are directly obtained from the momentum conservation equations, written following the RANS approach. Nevertheless, RANS and Reynolds stresses equations do not constitute a closed set system; hence, several terms require further modelling, like triple correlation, pressure–strain correlation, Reynolds stress dissipation, etc. In this work, these terms are modelled by means of linear relations between them and Reynolds stresses mean gradients. Anyway convection, production and molecular diffusion of Reynolds stresses are taken into account exactly by the transport equation. The discretization of convective terms in the mass, momentum and energy conservation equations relied on SOU (Second Order Upwind) scheme, whereas a QUICK (Quadratic Interpolation for Convective Kinematics) discretization scheme was used for the k, e and RSM equations. In fact, high values of Reynolds cell number advise against the use of centered schemes. Frictionless flux treatment was performed by means of a Roe Flux Difference Splitting scheme with the Courant number varying from 0.5 to 5. Lower under- relaxation factors ranging from 0.05 to 0.8 were chosen for momentum, pressure, swirl velocity and turbulent dissipation rate. Convergence criterion value for all the thermo-fluid dynamic variables was fixed to 10^{-6}. For convenience, the total temperature (To) difference between the inlet (suffix ‘i’) and exit (suffix ‘e’) of upper and lower jets are calculated and presented for the grid independent numerical studies.

Table 1. Grid Independency Studies

Sl. No	**No. of cells**	**To,i-To,e (k) for Upper Jet**	**To,i-To,e (k) for Lower Jet**
1	50,000	3	2
2	1,00,000	4	3
3	2,00,000	5	3
4	2,50,000	5	3

Results and Discussions

The geometry chosen for the investigation of energy separation between two co-annular jets is simple as shown in fig.1 The Reynolds number (Re) chosen is UD/ν, where ν is kinematic viscosity of air, D – characteristic length and U-free stream velocity prescribed at inlet. Re is found to be 80000 for the following simulations. The residuals for the convergence of three equations are shown in figure 3. From figure 3, it is seen that residuals reach to an order of 10^{-3} as the iterations progress in time towards a steady flow field. The residual in the continuity equation seems to oscillate due to dispersion and density field in the geometry gets affected by the two-jet shear mechanism.

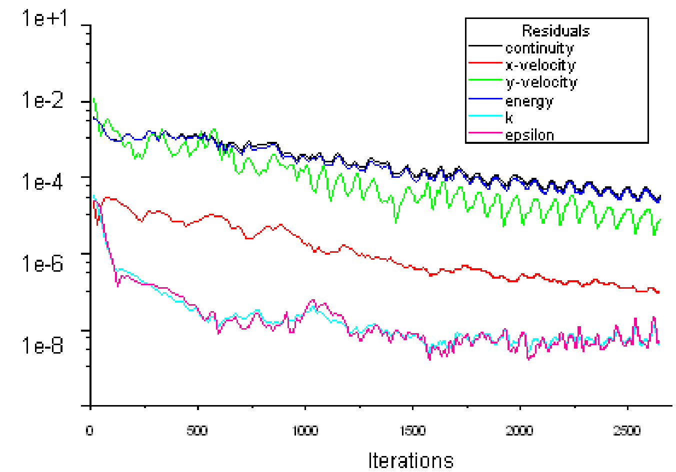

Fig. 3. Residual history of continuity, momentum and energy equations

A. *Physical Mechanism*

The total temperature plot is shown in figure 4, from which one can understand the energy redistribution in the geometry. There are patches of total temperature regions seen in figure 4, the coherent structure of vortices can attribute to the separation of energy in the flow. The jets exchange momentum and hence energy due to shear work and heat transfer by conduction and convection are involved.

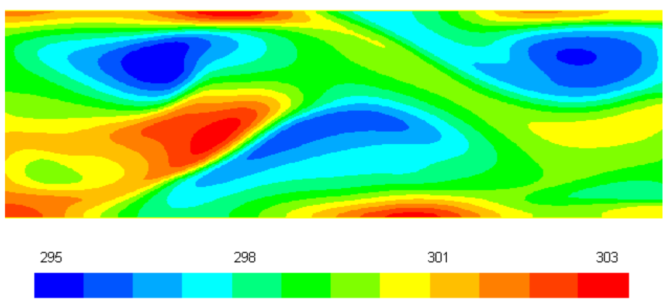

Fig. 4. Total temperature (K) contours in the flow field

The static temperature field in shown in figure 5. It is clearly understood there is heat transfer by conduction from a lower jet to an upper jet as there is a difference in static temperature in the 'y' direction. Moreover there is a mean static temperature at the centre-line in the geometry where the flow is at inlet temperature. Jet shear is caused by some other mechanism although heat transfer by conduction is one among them. Hence shear work must be investigated to identify the cause for total energy separation. In shear work, viscosity gets affected due to turbulent kind of flow. The velocity gradients provide a more useful information in the understanding of energy separation between two opposite jets.

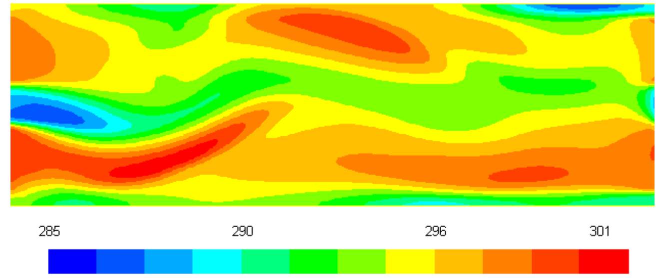

Fig. 5. Static temperature (K) contours in the flow field

As there is a change in total temperature, so does the total energy and hence energy in the upper jet is depleted due to lower jet and hence energy patches are formed as shown in figure 6. The shear layer is well observed in figure 6 between the upper and lower jets.

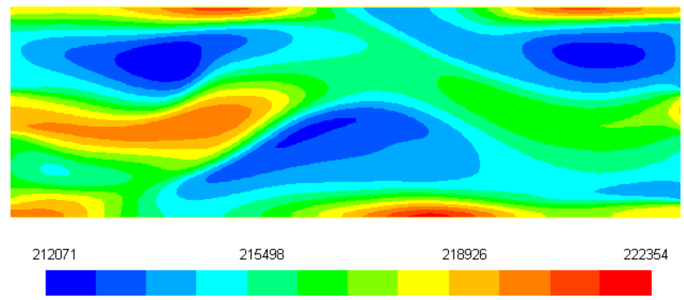

Fig. 6. Total energy contours (J/kg)

The internal energy contours shown in Figure 7 present a meaning among the energy transfer due to molecular activities in turbulent flow. The internal energy produce a change in temperature field by molecular thermal exchange and viscosity tries to dampen the flow or the speed of molecules.

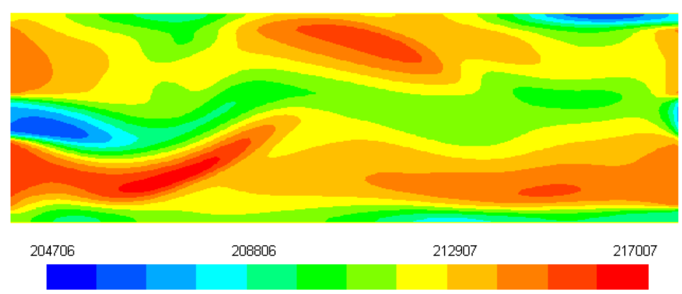

Fig. 7. Contours of internal energy (J/kg) in the flow field

Hence the energy redistribution in the two opposite free jets are acknowledged and the flow details have to be identified and cause for the energy separation should be investigated. Details into the turbulence features in the flow field can give insight into the energy separation and is discussed next.

ISBN: 978-1-61804-288-0

B. Turbulence phenomena

The flow in the jets generally have many small structures or grains in the turbulent regime. Hence those grains can be seen in the turbulent kinetic energy and intensities and vorticity contours. The kinetic energy resulting from a turbulent flow is shown in figure 8 and many features can be identified in it. The production of kinetic energy happens at the shear layer between two jets and proceeds along the jet direction. Turbulent kinetic energy is reducing its magnitude at the middle of the flow field while it again picks up at the opposite end of the jet, i.e. near the outlet.

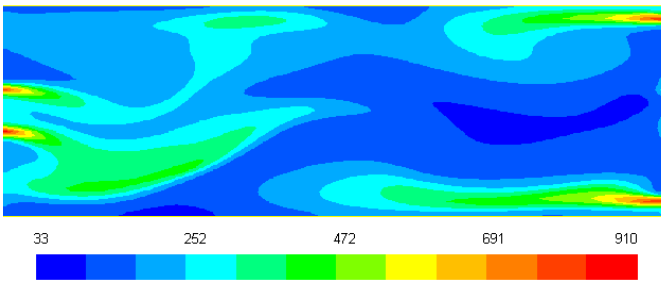

Fig. 8. Turbulent kinetic energy (m^2/s^2) contours in the flow field

The turbulent intensity is found to be maximum near the inlets and exits as shown in figure 9. The intensity of turbulence is enormous that the flow field is fully turbulent and the fluctuating velocities are significantly higher. It is also understood from preliminary studies that energy redistribution is nearly absent in laminar flow.

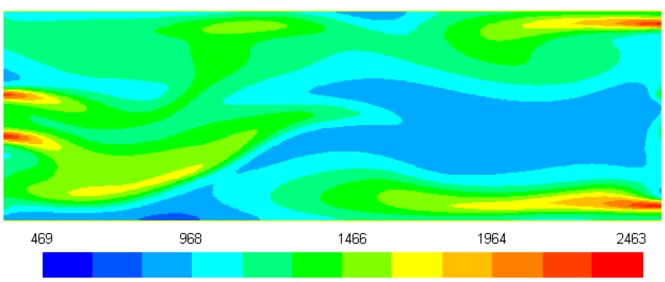

Fig. 9. Turbulent intensity contours in the flow field

The generation of vorticity at the source, and its convection and diffusion into only a narrow portion of the total space available, gives a jet its defining experience. The onset of instability and the resulting amplification of fluctuating vorticity, especially when the disturbances cause further confinement of vorticity. For the plane jet issuing from the line source of momentum, the equations reduce to simply a balance between the convection of vorticity downstream and viscous diffusion of vorticity into the surrounding stream. It is well known that high Reynolds number laminar jets develop into fully turbulent flows. Vorticity can be generated locally by stretching and turning. The viscous diffusion of vorticity, acting primarily at the smallest scales of motion where the gradients are largest, acts to propagate vorticity into the region where vorticity magnitude is least. However, the production small scale vorticity is largely controlled by the straining provided by much larger scales of motion. Thus, the entrainment rate is controlled by the speed at which the interface contortions with the largest scales move into the surrounding fluid. These controlling large scale vortices tend to be coherent and easily recognizable features. Here the correlation between total energy and vorticity can be compared between figures 6 and 10.

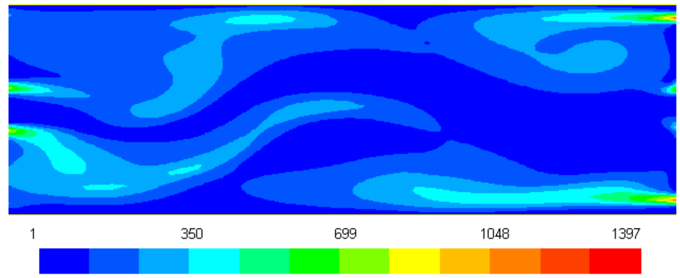

Fig. 10. Vorticity (1/s) contours in the flow field

The self similar structure of velocity is understood in the single turbulent jets, but twin jets are not much explored and hence open for research studies. The energy changes happening in the flow field manifests the flow to happen and the vice-versa.

C. Parametric studies

The jet studies provide knowledge about the energy redistribution, shear layers, transition from laminar to turbulent regime and many more. However, the parametric studies form other side whether the length or characteristic dimension can be changed and its effects are studied. Figure 11 shows the schematic where 3 stations are identified for evaluation of temperature or vorticity magnitude for analysis. For convenience, station 1 is at 0.025 m from the extreme left and station 2 and 3 are 0.05 m and 0.075 respectively. x = 0 m and x = 0.1 m represent the edges where the inlet and outlet conditions are specified.

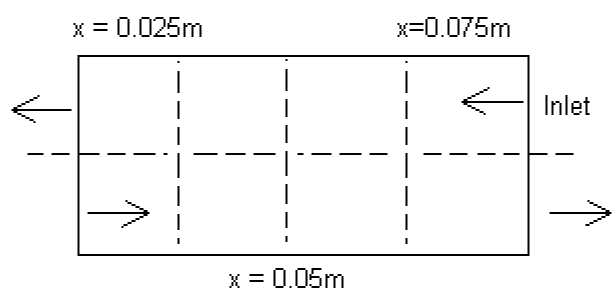

Fig. 11. Schematic Illustration of 3 stations in the flowfield

The total temperature at three stations are plotted from y = -0.01 to y= +0.01for Re = 80000 in the figure 12.. It can be understood that the jets produce asymmetries in the flow field and thereby the total temperature distribution also.

ISBN: 978-1-61804-288-0

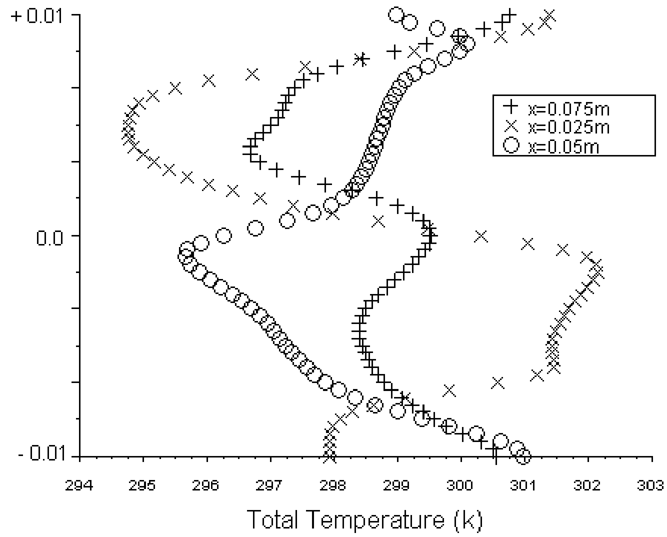

Fig. 12. Total temperature (K) at 3 stations in the flow field

The vorticity plots are shown for the same in figure 13 where again asymmetry is present.the vorticity magnitude is maximum near y=0.0 and is evident from the plot. The shear layer is at the centreline and hence vorticity can be expected to be maximum at the centreline. There is a positive correlation between total temperature and vorticity. The effects of increasing the length L and dimension D are mentioned next.

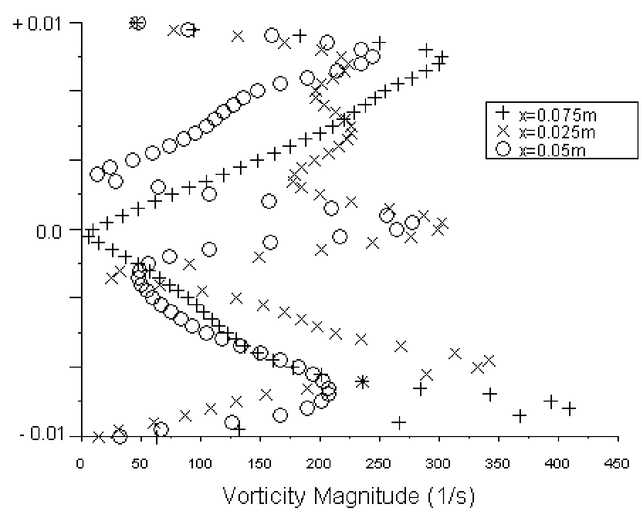

Fig. 13. Vorticity in 1/s at 3 stations in the flow field

When the length L is doubled the shear layer interaction becomes ineffective and hence the energy distribution is less affected. The total temperature is less affected in this case and the flowfield is responsible for energy separation effect. The same effect can be compared to the situation in a vortex tube where the effect of length to diameter ratio has significant effect until 40, after which the energy separation decreases. The magnitude of total temperature decreases as L is increased by comparing the figures 12 and 14.

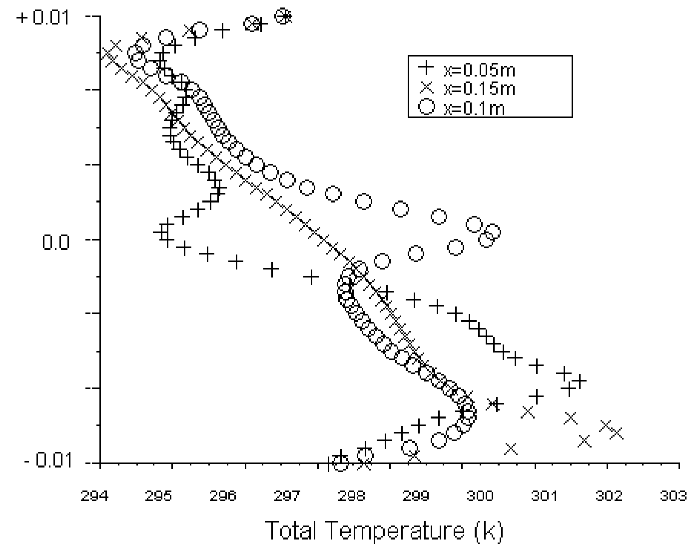

Fig. 14. Total temperature (K) for twice the length, L

The dimension D also has a significant effect on the energy separation as it is doubled where D=0.2m and compared with the schematic shown figure 1. The Reynolds number is calculated based on the characteristic dimension D and hence Reynolds number is also doubled in this case.

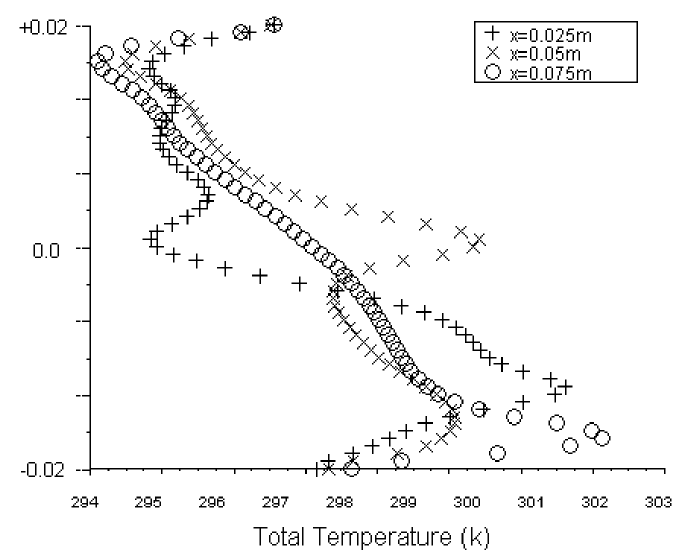

Fig. 15. Total temperature (K) for twice the diameter

The total temperature is less effective at x =0.075 m and this may be due to presence of larger turbulence structures. The flow field has big turbulence scales and hence turbulent fluctuation terms are quite low in this case and this seems to predict a lower energy separation. The final case is shown in figure 16 where the velocity inlet U is increased such that Reynolds number is increased by a factor of 5. The plot shows an intensive change in total temperature at three stations. As the inlet velocity (U) is increased, the shear layer increases in

ISBN: 978-1-61804-288-0

thickness and hence higher chance for energy redistribution in the flow field. Hence higher Reynolds number increases the energy distribution.

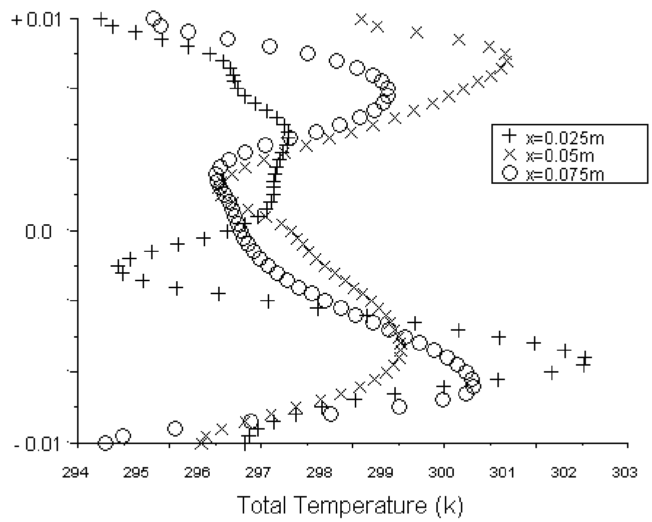

Fig. 16. Total temperature (K) as Reynolds number is increased by 5 times

CONCLUSIONS

A numerical study examines the steady flow simulations of the two co-annular jets where the mechanism of energy separation is investigated. Two dimensional Navier-Stokes equations with the k-e turbulence model constitutive equations are solved until the convergence conditions are attained. From the two jets, a strong correlation between vorticity and total energy can be seen from the contours and it is found that transport of vortices in the large coherent structure is responsible for energy separation. As Reynolds number increases, the energy separation is intensified due to more rapid development of vortices. The energy separation gets affected if there is an increase in length L and dimension D as discussed in parametric studies.

REFERENCES

[1] W.F. Ng, W.M. Chakroun, M.Kurosaka, Time resolved measurements of total temperature and pressure in the vortex street behind a cylinder. Phys, Fluids A 2 (1990) 971-978.

[2] W. E. Carscallen, T. Cuurrie, S.I. Hogg, J.P. Gostelow, Measurement and computation of energy separation in the vortical wake flow of a turbine nozzle cascade, Technical Report, ASME 98-GT-477, 1998.

[3] M.D. Fox, M.Kurosaka, L.Hedges, K. Hirano, The influence of vertical structure on the thermal fields of jets, J. Fluid Mech. 255 (1993) 447-472.

[4] B. Han, R.J. Goldstein, Instantaneous energy separation in shear layer, in : Proceedings of the seventeenth symposium on energy engineering science, Argonne National Laboratory, Argonne, IL, 1999, pp. 63-73.

[5] E. Eckert, W. Weise, Messungen der temperaturverteilumg auf der overflache schnell angestrometer unberheizter korper, Jahrb deutschen Luftfahrtforsch II (1940) 25-31.

[6] E.R.G. Eckert, Cross transport ofenergy in fluid streams, Warme-und Stoffubertranung 21 (1987) 73-81.

[7] B. Han R. J. Goldstein. (2003) Instantaneous energy separation in a free jet. Part 1. Flow measurement and visualization, Int’l J. Heat and Mass Transfer (46) pp 3975-3981.

[8] G. T. Ting and S. H. Li (2006) Numerical simulation of turbulent jets with lateral injection into a crossflow, J of Hydrodynamics 18 (3) pp 319- 32.

[9] Y. W Chou, F.B. Hsiao , C. C. Hsu, J. M. Huang (2002) Experimental thermal and fluid science (26) pp 445-454.

[10] S. Eiamsa-ard and P. Promvonge (2007) Numerical investigation of the thermal separation in a Ranque-Hilsch vortex tube, Int’l J Heat and Mass Transfer (50) pp 821-832.

[11] Fluent user’s Guide, release 6.3.26, Ansys Inc. USA, 2006.

Manimaran R., Ph.D. is an invited speaker to INASE conference 2015, He is also a member of international association of engineers and senior member in universal association of mechanical and aeronautical engineers. His interests are in the fields of computational fluid dynamics, heat transfer, combustion and fluid flow. He has 10 yrs of academic and research experience in his record. He holds awards, fellowships and meritorious candidature during the masters programme. He has organized workshops and training programmes related to CFD. He published papers in SAE, ASME and Begell House journals and presented conference papers worldwide.

Dynamic Modeling and Parametric Analysis on Nonlinear Vertical Cutting Process with Variable Stiffness

Mahmood Reza Mehran, Mehdi Mehran

***Abstract*—**In this investigation a nonlinear dynamic analysis was conducted on metal cutting process to evaluate system stability regarding to changing in the metal stiffness. For this propose a model with the forces due to coulomb friction and variable stiffness was solved. The manner is based on multiple time scales perturbation method that presents acceptable solution for non-resonance condition and stiffness with time variable. The important role of feed, depth and length of cutting and also effect of physical constants in system stability was carried out.

***Keywords*—**Metal cutting process, Perturbation methods, Multiple Time Scales, Time variable stiffness

I. INTRODUCTION

TODAYS, there is no piecework in industry that no machining process was done on it. In some strategic industries such as power plants, airspace and so on, non-suitable operation even one part causes operations stop in massive projects. One of the important reasons of this can refer to the manner of production and machining accuracy. Products with complicate shapes need to high quality and this makes the role of machining be more colored than past. The promotion of machines and developments of mathematic models in these lately years states that there are good validations and harmony between output machining and result of math modeling for controlling of machine process specially in metal cutting.

The early dynamic models of the cutting process were more focused on the physical effect of interaction between machine mechanics and cutting process by solving of numerical equations of self-exited vibration models [1], [2]. Self-exited vibrations during cutting process are limitation factors in machining accuracy and lead to failure and break down the device quickly. Hence, this is undesired phenomena and many researches were dedicated to it [3]-[8]. Later another phenomenon in the form of stick-slip effects in chisel movement on work piece was entered in researches [9]-[10]. In more attempts researchers found chaos and turbulent in the machine response when chattering of machining tool were occurred [11]-[12]. Also, the effects of the tools and chisel arranging and their position on work piece with different dynamic variables were studied by them and found out that intermittency joint and disjoint that is chattering machine tool lead to instability behavior. With depth vision, there are many applied data for systems that causes instability and chaos. This means that control of metal cutting process is hard and the stability of cutting can't obligatory guaranty for all systems and also shows reduction efficiency in metal changing process. In practice, effects of stick-slip, chattering and intermittency may be due to work piece deviations and also chips replete due to change of chip thickness causes non-smoothness surface on work piece.

One of the important issue about the parts and work pieces is that should not only have sufficient strength but also hove logical justification for economic production that is the weight of parts could be reduced without strength decreasing which lead to stiffness reduction. Naturally the work piece with high softness and low stiffness can cause significant problems. Some outstanding researchers who studied on these problems are Warminski et al. [13] that conducted on the dynamic effects of the vertical metal cutting and dynamic chaos and they also worked on the dynamic analysis of chaos in a 2D model with constant coefficient. Vibration behavior of a cutting system based on random distribution was carried out by Lipski and the others [14].

The presence investigation has dedicated to cutting analysis of work piece with variable stiffness when chisel is perpendicular on work piece. In lately years, analytically approximation solutions were presented for modeling of nonlinear dynamic behavior of vertical cutting process and also studies on analysis of nonlinear dynamic cutting forces and their effects on cutting system using multiple time scales were presented by Hwang [15] and Nayfeh et al. [16]. In presence research also effects of cutting depth, cutting length and particular physical constants on stability were considered. For this propose, dynamic models were presented by Wiercigroch [17] and Rusinek [18] which refer to variable stiffness an coulomb friction is regarded.

Wiercigroch [17] propose the revision model that first time had been presented by Grabec [19], [20]. These Grabec [19] works has done base on Juilian [21] and point to existence inherent discontinuity in cutting process and also imply on a

F. A. Department of Mechanical Engineering, East Tehran Branch, Islamic Azad University, Tehran, IRAN, (e-mail: mahmood_mehran@yahoo.com).

S. B. Manager of R&D in NIDC, Ahvaz, IRAN, (e-mail: m_mehran57@yahoo.com).

ISBN: 978-1-61804-288-0

feedback between chisel and real cutting process.

The revision model of Wiercigroch [17] was based on adding friction term regarding to Hasting et al. [22]. The result of their work states that there is a mathematic relation between cutting forces and they show this relation formed form effects of discontinuity friction. So, based on above works and also regarding to variable stiffness that presented by Rusinek [18], a developed model as a logical indicator of cutting process was considered as in Fig. 1.

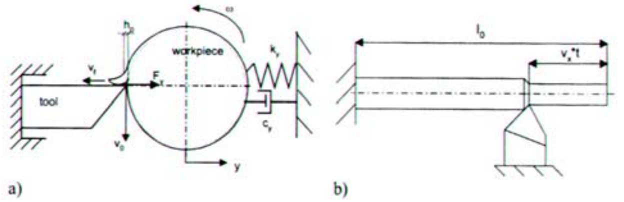

Fig. 1 physical model of vertical cutting process [18]

II. Metal Cutting System Equations

First the stiffness parameter introduced and discussed and then related dynamic equations regarding to variable stiffness is presented:

A. Evaluation of Stiffness Parameter

Based on test and laboratory results, the amount of experimental stiffness in the cutting process is less than the theoretical one [18].

$$k = \frac{3EI}{l_0^{\ 3}} \tag{1}$$

It is clear that the equation (1) should correct with an extra coefficient called (α) which depends on work piece length (l_0) and real cutting length (l).

$$k_y = \frac{3EI\alpha}{l_0^{\ 3}} \tag{2}$$

$$\alpha = \alpha_1 \frac{l}{l_0} \tag{3}$$

Therefore (α_1) is regarded as a particular coefficient for work piece which is hold by vice versa jaws.

Fig. 2 shows both theoretical and experimental stiffness curves. To fitting perfectly of these two curves on each other and convergence of the answers, correction of theoretical stiffness equation was done by adding (α) coefficient.

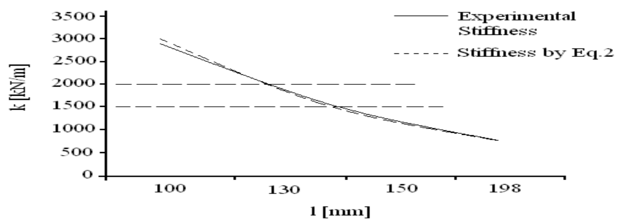

Fig. 2 theoretical and experimental stiffness of cutting process [18]

B. Dynamic Equations of Metal Cutting System

As mentioned before the model of cutting process based on developed model of Wiercigroch [17] and Rusinek [18] has been shown in Fig. 1. This model is one degree of freedom in Y direction. (f_y) is the force component related to friction force which heavy side and sign functions were appeared in it. These parameters are needed to show discontinuity of joint between chisel and work piece. The related velocity parameter (v_f) that shows feed rate of chisel in Y direction also should be presented. The developed dynamic equations of mentioned model based on Warminski [23] are:

$$m\ddot{y} + k_y(t)y + c_y\dot{y} = f_y \tag{4}$$

Introducing the ($k_z(t)$) as a monotonic time function and substitution in related equation, so:

$$k_z(t) = \frac{3EI\alpha_1}{l_0(l_0 - v_x t)^2} = \frac{3EI\alpha_1}{l_0^{\ 3}(\frac{l_0 - v_x t}{l_0})^2} \tag{5}$$

$$if \qquad \beta = \frac{\alpha_1}{(\frac{l_0 - v_x t}{l_0})^2} \quad , \quad a = \alpha_1 \tag{6}$$

$$\begin{aligned} &\ddot{y} + 2\xi_y\sqrt{\beta}\dot{y} + \beta y = [C_2(\left|v_f\right| - 1)^2 + 1][C_3(h-1)^2 \\ &+ 1]H(f)\operatorname{sgn}(v_f)q_0 h[C_1(\left|v_0\right| - 1)^2 + 1] \\ &H(h)\left(H(v_0)\frac{1}{1+\mu_0} + \operatorname{sgn}(v_0)\frac{\mu_0}{1+\mu_0}\right) = f_y \end{aligned} \tag{7}$$

Where (c_y, k_y, f_y) are stiffness, damping and force of cutting respectively. (q_0) is magnitude of cutting force, (h_0) is initially cutting depth, (h) is real cutting depth, (μ_0) is static friction coefficient and (v_f) is related velocity of chisel in Y direction. Also, (C_{1-4}, v_0, R, R_0) are constants of process, absolute velocity of work piece, coefficient of cutting plastic deformation and the constant of cutting plastic deformation respectively, that define as follow:

$$v_f = v_0 - R\dot{y} \quad , \qquad h = h_0 - y \tag{8}$$

$$\begin{aligned}&\ddot{y} + 2\xi_y\sqrt{\beta}\dot{y} + \beta y = Q_3(h_0 - y)[C_1\sigma_2 + 1][C_2\delta_1^2 \\ &- 2C_2\delta_1\delta_4\dot{y} + C_2\delta_4^2\dot{y}^2 + 1] * \\ &\qquad [C_3\sigma_1 + C_3y^2 + 2C_3y - 2C_3h_0y + 1]\end{aligned} \tag{9}$$

where

$$\begin{aligned}&Q_3 = H(f)\operatorname{sgn}(v_f)Q_1, \\ &\sigma_1 = h_0^2 - 2h_0 + 1, \\ &\sigma_2 = v_0^2 - 2v_0 + 1, \\ &\delta_1 = v_0 - 1, \\ &\delta_2 = R_0C_4, \quad \delta_3 = 2R_0C_4(v_0 - 1), \\ &\delta_4 = R_0(C_4v_0^2 - 2C_4v_0 + C_4 + 1), \\ &Q_1 = q_0\left[H(v_0)\frac{1}{1+\mu_0} + \operatorname{sgn}(v_0)\frac{\mu_0}{1+\mu_0}\right]H(h)\end{aligned} \tag{10}$$

$$C_1 = \varepsilon\overline{C_1} \quad , \quad C_2 = \varepsilon\overline{C_2} \quad , \quad C_3 = \varepsilon\overline{C_3} \quad , \quad \xi_y = \varepsilon v_y \tag{11}$$

$$\begin{aligned}&P_1 = \varepsilon\overline{P_1} = [-2Q_3C_3h_0(1-h_0) + Q_3C_1\sigma_2 + \\ &Q_3C_3\sigma_1 + Q_3C_2v_0^2 - 2Q_3C_2v_0 + Q_3C_2], \\ &P_2 = \varepsilon\overline{P_2} = [Q_3C_1h_0\sigma_2 + Q_3C_3h_0\sigma_1 + \\ &Q_3C_2h_0v_0^2 - 2Q_3C_2h_0v_0 + Q_3C_2h_0]\end{aligned} \tag{12}$$

$$\begin{aligned}&\overline{\lambda_1} = 2\overline{C_2}Q_3h_0R_0(1-v_0), \quad \overline{\lambda_2} = \overline{C_2}Q_3h_0R_0^2, \\ &\overline{\lambda_3} = \overline{C_3}Q_3, \quad \overline{\lambda_4} = 2\overline{C_2}Q_3R_0(1-v_0), \\ &\overline{\lambda_5} = \overline{C_2}Q_3R_0^2, \\ &\overline{\lambda_6} = \overline{C_3}Q_3(3h_0 - 2), \quad \overline{\lambda_7} = Q_3h_0\end{aligned} \tag{13}$$

$$\begin{aligned}&\ddot{y} + (\beta + Q_3)y = \varepsilon[-2v_y\sqrt{\beta} + \overline{\lambda_1}]\dot{y} - \\ &\varepsilon\overline{P_1}y + \varepsilon\overline{\lambda_2}\dot{y}^2 - \varepsilon\overline{\lambda_3}y^3 - \varepsilon\overline{\lambda_4}y\dot{y} - \\ &\varepsilon\overline{\lambda_5}y\dot{y}^2 + \varepsilon\overline{\lambda_6}y^2 + \varepsilon\overline{P_2} + \varepsilon^0\overline{\lambda_7}\end{aligned} \tag{14}$$

C. *Perturbation Analysis*

For solving the nonlinear equation the multiple time scales was applied. The principle of this manner is that dependent variables have been expanded in the form of infinitive series by two or more terms of independent variables which called as scales. The first term of these expansions is a linear term and gradually order of these terms would be increased. Also, time derivations of dependent variables define similarity. The independent variable of multiple time (T_j) in terms of real time (t) is defined as $T_j = \varepsilon^j t,\ j = 0,1,2,...$

So, time derivations are defined as:

$$\begin{aligned}&\frac{d}{dt} = D_0 + \varepsilon D_1 + ... \\ &\frac{d^2}{dt^2} = D_0{}^2 + 2\varepsilon D_0D_1 + ...\end{aligned} \tag{15}$$

Where ($D_j = \dfrac{\partial}{\partial T_J}$) and one can assume the solution form of y as:

$$y = y_0 + \varepsilon y_1 \tag{16}$$

Ordering and separation the terms lead to perturbation equation of system for y, lead to:

$$O(\varepsilon^0): \qquad D_0{}^2y_0 + (\beta + q)y_0 = \overline{\lambda_7} \tag{17}$$

$$\begin{aligned}&O(\varepsilon^1): \qquad D_0{}^2y_1 + (\beta + q)y_1 = -2D_0D_1y_0 + \\ &[-2v_y\sqrt{\beta} + \overline{\lambda_1}]D_0y_0 - \overline{P_1}y_0 + \overline{\lambda_2}(D_0y_0)^2 - \overline{\lambda_3}y_0{}^3 - \\ &\overline{\lambda_4}(D_0y_0)y_0 - \overline{\lambda_5}(D_0y_0)^2y_0 + \overline{\lambda_6}y_0{}^2 + \overline{P_2}\end{aligned} \tag{18}$$

III. Evaluation of Effective Parameters in Stability of Cutting Process with Variable Stiffness

Based on the solution of perturbation method used before, effect of parameters such as depth, length and velocity of cutting and also particular physical coefficient on stability of system with variable stiffness was considered. Numeric data used in all curves include: l=1m, h_0=0.5, Q_3=1, C_1=.3, C_2=0.7, C_3=1.5, C_4=1.2, $R_0 = 2.2, \mu_0 = 0.1, \xi_x = \xi_y = 0.1$ with boundary conditions of $y(0) = 0, \dot{y}(0) = 0$. Note that it was attempted to magnify significant parts of each figures below itself.

In Fig. 3, the (a) parameter is defined as one of particular physical coefficient. As seen in the start cutting tool movement the group of the curves is all the same that shows this parameter has no effect on start of movement. As time is passing, and increasing this parameter the system becomes stable. It is notable that when the (a) parameter approaches to zero the nonlinear equation convert to linear one.

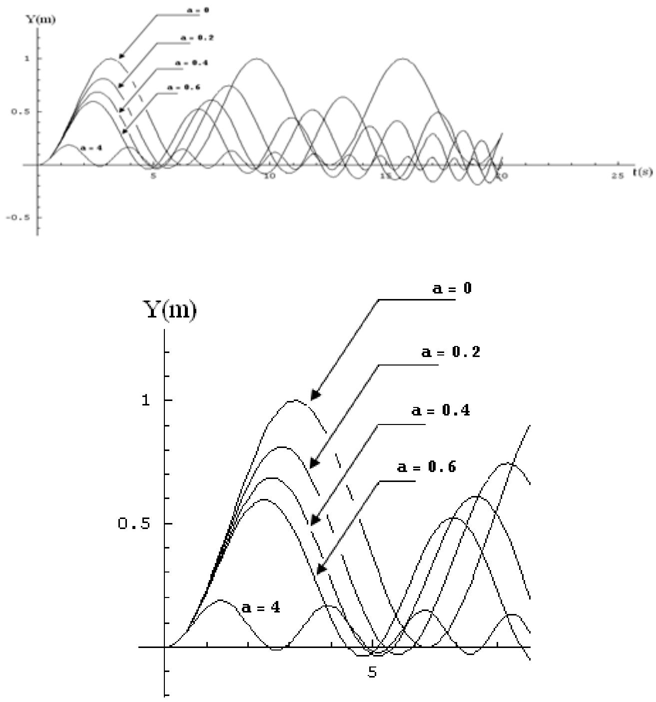

Fig. 3 time response due to particular physical coefficient changes of (a) on vibration amplitude

The effect of cutting depth on the stability was shown in Fig. 4. There are no phases difference with different cutting depths and equality of frequencies for all cutting depths in every semi cycle are visible.

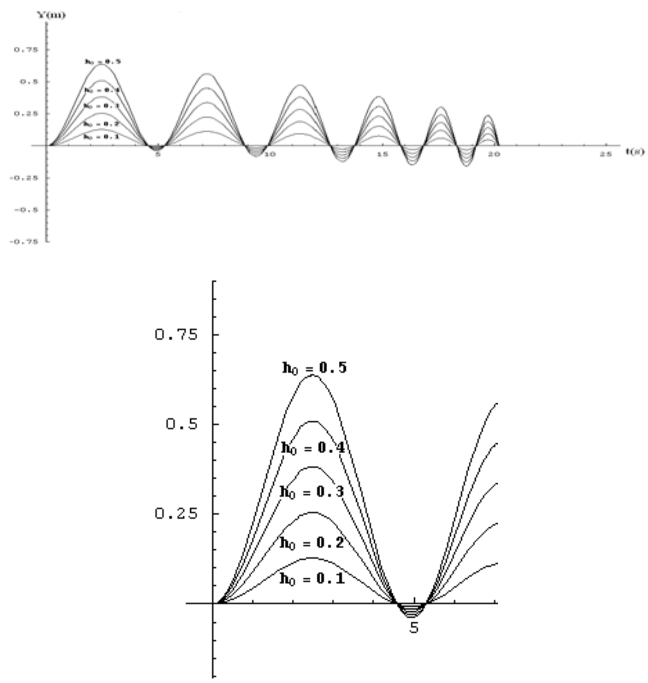

Fig. 4 time response due to cutting depth (h_0) on vibration amplitude

Q_3 is also another particular physical coefficient and effect of this parameter on system stability with great amount of it, is observed in Fig. 5.

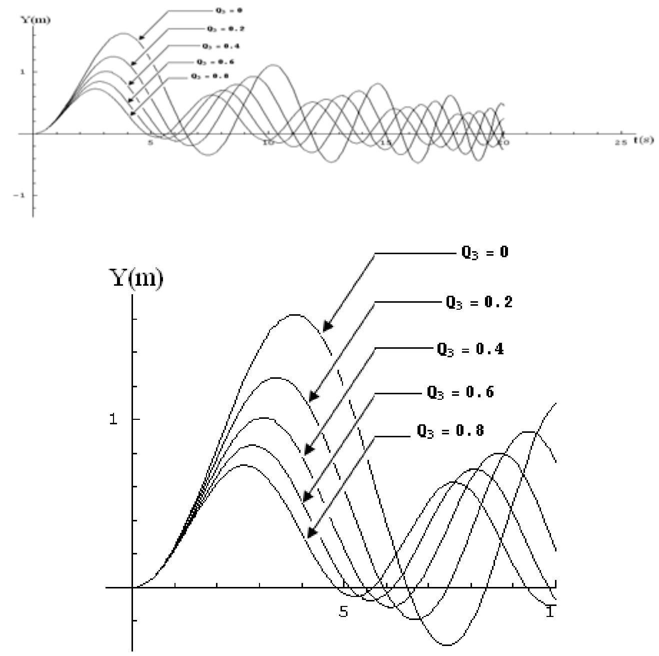

Fig. 5 time response due to particular physical coefficient changes of (Q_3) on vibration amplitude

FIG. 6, shows when the length is changing several amplitudes and frequencies are appeared which due to inherent properties of a continuous system.

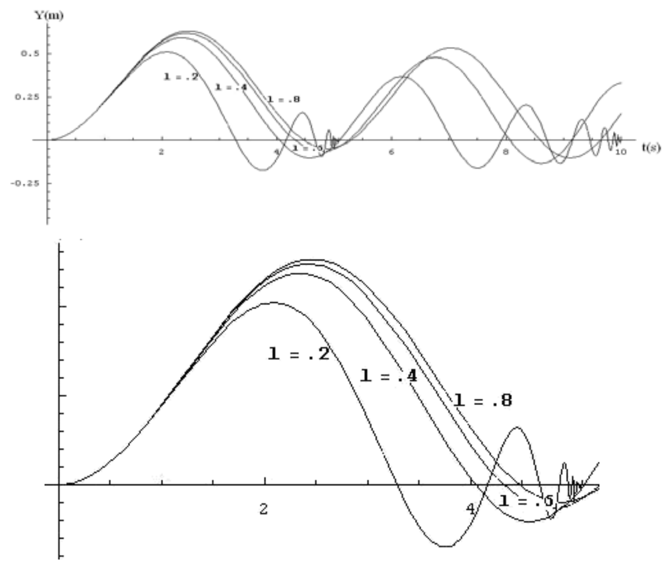

Fig. 6 time response due to cutting tool (chisel) along the work piece and its effect on vibration amplitude

Finally, velocity changes causes changes in vibration rate which shown in Fig. 7. It is also shows that chattering in low

ISBN: 978-1-61804-288-0

feed rate causes instability even with presence of friction and in high speed lead to stability in system.

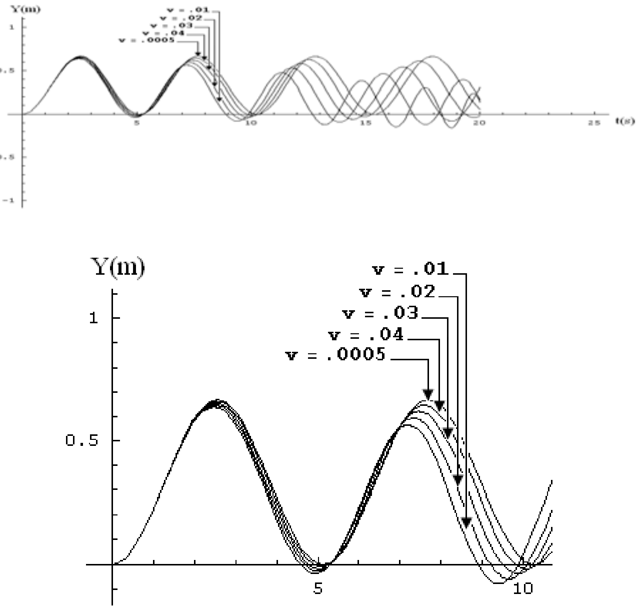

Fig. 7 time response due to cutting velocity changes (V) on vibration amplitude

IV. CONCLUSION

In this research a numeric solution for vertical cutting process with self-exited vibration with time variable stiffness due to chattering was presented and solved by multiple time scales perturbation method. The following conclusions are made:

1) During the cutting process, generate the sets of frequencies that due to inherent properties of continuous system and also as chisel approach to vice jaws the amplitude of vibrations was reduced.
2) It is observed chattering and vibration of chisel even with presence of friction causes instability in low speed rates.
3) This research shows that results have harmony with expectations and outputs provide suitable and logical responses.

REFERENCES

[1] Opitz H., Bernardi F., *"Investigation and calculation of the chatter behavior of lathes and milling machines "*, Annuals of the CIRP 18, 1970, pp.335-343.

[2] Tlusty J., *"Dynamics of high speed milling "*, ASME, J. Engineering for industry 108, 1986, pp. 59-67.

[3] Tlusty J., Ismail F., *"Basic nonlinearity in machining chatter "*, Annuals of the CIRP 30, 1981, pp.299.

[4] Shi H.M., and Tobias S.A., *"Theory of finite amplitude machine tool instability "*, Int. J. Machine and Tool Design Research, 24, 1984, pp.45.

[5] Lin J.S., Weng C.I., *"A nonlinear dynamic model of cutting "*, Int. J. Machine Tool Manufacture, 30, 1990, pp.53-64.

[6] Lin J.S., Weng C.I., *"Nonlinear dynamic of the cutting process "*, Int. J. Mechanical Sciences, Vol. 33, 1991, pp.645-657.

[7] Gradisk J., Govekar E., Grabec I., *"A chaotic cutting process and determining optimal cutting parameter using neural networks "*, Int. J. Machine Tool manufacture, 36, 1996, pp. 1161-1172.

[8] Nosyreva E.P. and Molinari A., *"Analysis of Nonlinear Vibrations in Metal Cutting "*, Int. J. Mechanical Sciences, Vol. 40, No.8, 1998, pp. 735-748.

[9] Bell R., Burdekin M., *"A study of stick-slip motion of machine tool drives "*, Proceeding of Institution of Mechanical Engineering, 184, 1970, pp. 543-557.

[10] Wiercigroch M., "Modeling of dynamic interaction between machine tool and cutting process (in polish), Ph.D. Thesis, Silesian technical university, Gliwice, Poland, 1989.

[11] Kalmar-Nagy T., Pratt J.R., *"Experimental and analytical investigation of the subcritical instability in metal cutting "*, Proceeding of *DETC* 1997, 17th biennial Conf. on Mechanical Vibrations and Noise, Las Vegas, USA, DETC99/VIB-8060.

[12] Wiercigroch M., Cheng A.H.D., *"Chaotic and stochastic dynamics of orthogonal metal cutting"*, Chaos, Solutions and fractals 8, 1997, pp.715-726.

[13] Warminski J., Litak G., Lipski J., Wiercigroch M., Cartmell M.P., *"Chaotic Vibrations in Regenerative Cutting Process.*", IUTAM / IFTOMM Symposium on Synthesis of Nonlinear Dynamical Systems. Kluwer Academic Publishers 2000.

[14] Lipski J., Litak G., Rusinek R., Szabelski K., Teter A., J.Warmiński J., K.Zaleski K., *"Modeling of nonlinear vibrations in a cutting process considering surface quality of work material"*, 3rd International Symposium "Investigation of Nonlinear Dynamics Effects in Production Systems" Cottbus 2000.

[15] Hwang C.C., Fung R.F., Lin J.S., *"Strong nonlinear dynamics of cutting process "*, J. Sound and Vibration, Vol.203, 1997, pp.363-372.

[16] Nayfeh A.H., Chin C.M., Pratt J., *"Perturbation methods in nonlinear dynamics applications to machining dynamics "*, J. Manufacturing Science and Engineering, Vol.195, 1997, pp.485-493.

[17] Wiercigroch M., *"Chaotic vibrations of a simple model of machine tool-cutting process system "*, Transaction of the ASME, Journal of Vibration and Acoustics, Vol. 119, 1997, pp. 468-475.

[18] Rusinek R., Warmiński J., Szabelski K., Teter A., Litak G., Lipski J., *" Dynamical model of cutting process with stiffness changeable in time. "*,W: Insperger S.G. (ed.) Proceedings of 2-nd Workshop on Dynamics and Control of Mechanical Processing, Budapest, 15.VI.2001. Publishing Company of Technical University of Budapest, Budapest, 2001, p. 47-51.

[19] Grabec I., *"Chaotic generated by the cutting process "*, Physics Letters A 117, 1986, pp. 384-386.

[20] Grabec I., *"Chaotic generated by the cutting process "*, International Journal of Machine Tool Manufacture V28, 1988, pp. 19-31.

[21] Juilian F., Zhejun Y. and Yingxue Y., *"A unified system model of cutting chatter and its transformation function "*, International Journal of Machine Tool Manufacture V29, 1989, pp. 601-609.

[22] Hasting W.F., Mathew P. and Oxley P.L.B., *"A machining theory for predicting chip geometry, cutting forces, etc. from material properties and cutting conditions "*, Proceedings of Royal Society of London, A 371, 1980, pp.343-354.

[23] Warminski J., Litak G., Cartmell M.P., Khanin R. and Wiercigroch M., *"Approximate analytical solutions for primary chatter in the nonlinear metal cutting model "*, J. Sound and Vibration, Vol. 259, No.4, 2003, pp. 917-933.

CFD simulation of Free Convection Heat Transfer in a Vertical Conical Partially Annular Space

B. Ould said, N. Retiel, and E.H. BOUGUERRA

Abstract— The present paper is dedicated to present the numerical simulation of thermal convection in a two dimensional vertical conical partially annular space. The constant properties and the Boussinesq approximation for density variation is used to solve the governing equations of mass, momentum and energy using the CFD FLUENT 12.0. The results of streamlines and the isotherms of the fluid are discussed for different annuli with various boundary conditions and Rayleigh numbers. Emphasis is placed on the height influences of the inner vertical cone on the flow and the temperature distribution. In more, the effects on the heat transfer are treated for different values of physical parameters of the fluid in the annulus geometry. The heat transfer on the hot walls of the annulus is also computed in order to make comparisons the cylinder annulus for boundary conditions and several Rayleigh numbers. The results obtained of Nusselt number has been found between the present previsions and available data from the published literature data.

Keywords—Annular space, CFD Fluent, Conical partially, Free convection; CFD simulation

I. Introduction

The heat transfer analysis by natural convection in an enclosure is an large research topic owing to its wide variety of engineering applications involving energy conversion, storage and transmission systems. Instances of using annulus geometry solar energy collection and nuclear reactor design [1]. A comprehensive review of natural convection in various cavity shapes has been documented in the open literature. Among the very first investigations, [2] has been analyzed numerically the heat transfer problem by natural convection in rectangular enclosure is filled by micropolar fluid, to studied the influence of the conductive vertical divider. The case of square and cubic cavities was reported by [3] and [4]. Other investigations [5] have been studied by cfd simulation the effect of the physical and geometrical parameters in two-dimensional vertical enclosure by heat transfer with correlations generalized. The complex shapes such that inclined cavities with wavy walls by [6], and trapezoidal cavities by [7]. Natural convection and fluid flow was studied for triangular enclosures mostly with boundary conditions, see [8] and [9]. [10] Have carried investigations of heat transfer by protruding isothermal heater within an triangular enclosure. The study numerically of this phenomenon of natural convection flow in vertical concentric annular with isothermal inner and outer vertical walls. Several problems that have been extensively studied due to its several practical applications have received much attention. The studies conducted by [11] in a vertical cylindrical cavity, A parametric study numerically of the thermal convection in vertical annulus by the heat generation rod variation centrally vertically by [12]. The effect study of tilted angle and diameter ratio on natural convection heat transfer in the case of horizontal cylindrical annulus by [13]. Investigation the transition effect and turbulence flows on natural convection along a horizontal annular cavity with local and mean Nusselt number were presented by [14] and recently by [15]. Few research works have been reported for the case of conical, have numerically solved the heat transfer by natural convection and radiation problem in a conical annular cylinder porous fixed is presented by [16].These studies were restricted to conduction heat transfer only. The present paper covers the laminar natural convection in a vertical conical cylinder partially annular space. On the other hand, the direct numerical simulation necessary for well resolved the study of heat transfer, (DNS) approach which requires computational resources well beyond actual capacities for the majority of real industrial problems. We will be concerned with the effect of the Rayleigh number and annulus radius ratio as well as the cavity geometry on the heat transfer.

II. Physical and Mathematical Formulation

A. Physical Domain

In this present problem the geometry is schematized for studied the flow produced by natural convection in a vertical conical partial annulus; where the annulus is filled with air. The analysis domain is delimited by two concentric, conics with isothermal walls of the inner and outer axial height h, H respectively. The top and bottom walls of the outer cone are considered adiabatic, as shown in Fig. 1. The bottom radius of inner and outer conics are r_i and r_o and the inner and outer wall temperature are T_i and T_o, respectively. The horizontal walls of the outer cone are insulated. The buoyancy induced flow is

B. O. Author is with the Laboratory of Numerical and Experimental Modeling of Mechanical phenomena, Department of Mechanical, University of Mostaganem Abdelhamid Ibn Badis, UMAB, BP300, Route Belhacel, Mostaganem (27000), Algeria; e-mail: kazemou@ yahoo.fr).

N. R. Author, was with Laboratory of Numerical and Experimental Modeling of Mechanical phenomena, Department of Mechanical, University of Mostaganem Abdelhamid Ibn Badis, UMAB, BP300, Route Belhacel, Mostaganem (27000), Algeria; e-mail: retieln@ yahoo.fr).

E. H. B. Author is with Mechanical Engineering Department, Saad Dahlab University, Blida, Algeria. (e-mail: ehbouguerra@yahoo.fr)

assumed to be laminar, and the fluid studied is incompressible with constant fluid properties except the density variation. The Boussinesq approximation is used for calculated the density variation with the temperature. Then, the mathematical model used is based on the hypothesis of a two-dimensional (axisymmetric) flow.

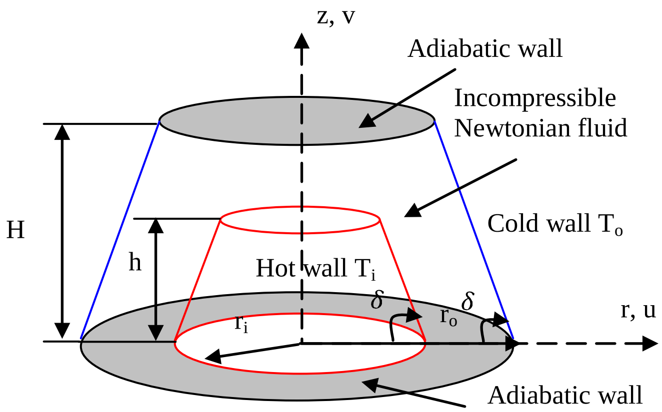

Fig. 1Physical Model

B. *Governing Equations*

The problem description and the assumptions application on the fluid properties, the governing differential equations in vector form can be written as:

Continuity,

$$\vec{\nabla}.\vec{V} = 0 \quad (1)$$

Momentum,

$$\rho(\vec{V}.\vec{\nabla})\vec{V} = \mu\nabla^2\vec{V} - \vec{\nabla}p - \rho\vec{g} \quad (2)$$

Energy,

$$\rho c_p(\vec{V}.\vec{\nabla})T = \lambda(\vec{\nabla}.\vec{\nabla})T \quad (3)$$

In present study can be written as the governing dimensionless equations in cylindrical coordinates in the following forms.

Continuity,

$$\frac{1}{R}\frac{\partial}{\partial R}(RU) + \frac{\partial V}{\partial Z} = 0 \quad (4)$$

R momentum,

$$U\frac{\partial U}{\partial R} + V\frac{\partial U}{\partial Z} = -\frac{\partial P}{\partial R} + Pr\left[\frac{\partial}{\partial R}\left(\frac{1}{R}\frac{\partial}{\partial R}(RU)\right) + \frac{\partial^2 U}{\partial Z^2}\right] \quad (5)$$

Z momentum with the Boussinesq approximation for the buoy-ancy term,

$$U\frac{\partial V}{\partial R} + V\frac{\partial V}{\partial Z} = -\frac{\partial P}{\partial Z} + Pr\left[\frac{1}{R}\frac{\partial}{\partial R}\left(R\frac{\partial V}{\partial R}\right) + \frac{\partial^2 V}{\partial Z^2}\right] + PrRa(T^* - 0.5) \quad (6)$$

Energy

$$U\frac{\partial T^*}{\partial R} + V\frac{\partial T^*}{\partial Z} = \frac{1}{R}\frac{\partial}{\partial R}\left(R\frac{\partial T^*}{\partial R}\right) + \frac{\partial^2 T^*}{\partial Z^2} \quad (7)$$

Where the dimensionless variables and numbers are defined as follows:

$$U = \frac{uL}{\alpha}; V = \frac{vL}{\alpha}; R = \frac{r}{L}; Z = \frac{z}{L}; Ar = \frac{H}{L}; X = \frac{h}{L} \quad (8)$$

$$T^* = \frac{T - T_o}{T_i - T_o}; P = \frac{pL^2}{\rho\alpha^2}; Pr = \frac{\nu}{\alpha}; Ra = \frac{\beta g \Delta T L^3}{\alpha\nu} \quad (9)$$

C. *Boundary Conditions*

The corresponding dimensionless boundary conditions for the radial and vertical velocity are equals to zero at all walls. The temperature boundary conditions are as follows.

At $0 \le Z \le \le \frac{H}{L}$ and $R_o \le R \le R_o - \frac{H}{L}$ cotgδ: U= V= 0 and T^*=0 for the isothermal Cold tilted wall

-At $0 \le Z \le \frac{h}{L}$ and R =R$_i$: U= V= 0 and T^*=1 for the isothermal hot vertical wall

-At $Z = \frac{h}{L}$ and $0 \le R \le R_i$: U= V= 0 and T^*=1 for the isothermal hot horizontal wall

-At $Z = \frac{H}{L}$ and Z =0: U= V= 0 and $\frac{\partial T^*}{\partial Z}$=0 for the adiabatic walls

III. NUMERICAL METHOD

To solve the governing equations using the finite volume method was used The FLUENT 12.0, CFD code, with first order formulation was solved the segregated implicit. The conservation governing equations was solved independently, by the segregated solver. The first order upwind differencing scheme is used the equations of momentum and energy. The discretization scheme used for pressure was body force weighted to take the density variations in consideration. The pressure–velocity coupling is ensured using the SIMPLE algorithm. The Gambit used for created and meshed the geometrical model with a simple quadrilateral cell. If necessary for correctly resolving the steep gradients in the thin buoyancy-driven boundary layer. A very fine spacing near the walls in conical partially annular grid. All the variables were calculated right up to the walls without using any wall function. On the wall boundary conditions, the radial and vertical velocity values were to zero. The dimensionless temperature of the active walls is set to 0 and 1 respectively. While meshing the domain, it is taken care that the mesh size does not influence the solution.

The residuals of continuity, momentum and energy equations are required to be lower 10^{-7} in order to achieved totally converging solution. The relaxation parameters have been adapted for every simulation in order to speed up convergence.

IV. NUMERICAL SOLUTIONS

A. *Nusselt Number*

The energy transmitted by the inner cylinder of the annulus are expressed in values to obtain the local and mean Nusselt numbers. The local Nusselt number for the annulus inner cylinder is obtained from temperature gradients by the following relationships:

$$Nu_1 = \left.\frac{\partial T^*}{\partial n}\right|_{l=\frac{X}{\sin\delta}} \text{ and } Nu_2 = \left.\frac{\partial T^*}{\partial Z}\right|_{Z=X} \quad (10)$$

ISBN: 978-1-61804-288-0

The mean Nusselt number is defined by

$$\overline{Nu} = \frac{\int_0^{2\pi}\int_0^{\frac{X}{\sin\delta}}\left(\frac{\partial T^*}{\partial R}\sin\delta + \frac{\partial T^*}{\partial Z}\cos\delta\right)Rd\phi dl}{\frac{\pi}{\cos\delta}[R_i^2-(R_i-X\cot\delta)^2]+\pi(R_i-X\cot\delta)^2} + \frac{\int_0^{2\pi}\int_0^{R_i-X\cot\delta}\frac{\partial T^*}{\partial Z}Rd\phi dR}{\frac{\pi}{\cos\delta}[R_i^2-(R_i-X\cot\delta)^2]+\pi(R_i-X\cot\delta)^2}$$

$$\overline{Nu} = \frac{2\pi\left[\int_0^X \frac{\partial T^*}{\partial R}(R_i-\tan\delta\, Z)dZ - \int_{R_i}^{R_i-X\cot\delta}\frac{\partial T^*}{\partial Z}RdR\right]}{\frac{\pi}{\cos\delta}[R_i^2-(R_i-X\cot\delta)^2]+\pi(R_i-X\cot\delta)^2} + \frac{\int_0^{R_i-X\cot\delta}\frac{dT^*}{dZ}2\pi RdR}{\frac{\pi}{\cos\delta}[R_i^2-(R_i-X\cot\delta)^2]+\pi(R_i-X\cot\delta)^2} \quad (11)$$

B. Validation

Before continuing, it's required to ensure the dependability and the precision of the present numerical model and the FLUENT 12.0 CFD code. The heat transfer data computed for differentially heated of the conical annular, with different parameters which correspond to the cone angle δ = 90°, aspect ratio Ar = H / L, radius ratio K = r_o / r_i, height ratio h = X / L & Rayleigh number $10^4 \le Ra \le 10^5$. The present problem is to numerically investigate the natural convection flow in a vertical cylinder annular space and the average Nusselt number variation is compared with those of reference from the literature data. Table 1 demonstrated the comparison between the current results and those of [17] and [18]. It is clearly demonstrated in Table 1 that, for several values of Rayleigh number. Was checked and ensured with the present results and those obtained by these authors. There is a satisfactory agreement.

Table 1
Values of the overall Nusselt number at the Isothermal Walls for Annulus Aspect ratio Ar=10 and K=2, δ=90°

Rayleigh number	[17]	[18]	Present
10^4	2.355	2.33	2.343
510^4	3.718	3.758	3.755
10^5	4.558	4.568	4.564

V. Results and Discussion

A. Effects of Rayleigh number Number

In this study the results obtained with respect to different parameters being Ar=1, K=2, X=0.5 and δ=45°. Fig.2 shows for Rayleigh number $10^3 \le Ra \le 10^4$ that there is a logarithmic temperature distribution in the all-region of the annulus illustrates that heat from the left wall toward the right wall is transferred by conduction regime for Rayleigh number Ra=5×10^4. The temperature gradient become slightly flatter at the core of the annulus which indicates that the conduction dominance is slashed in reason to a small quantity of convection established in the central part. The flow models show where convection promotes the transfer of heat. Fig. 2 shows the Rayleigh number Ra = 10^5 A vertical steep temperature gradient formed near the active wall. This confirms the increased in heat transfer rate due the existence of the cells models formed at interior annulus. This regime transition, wherein the boundary layer formed at the left and right active wall attain the central part of the annulus and merges all. Therefore, ago a rotational movement of the fluid, provoking mixing and ameliorate in heat transfer evaluation. However, for Rayleigh number Ra = 10^6, the nucleus was considered almost isothermal with the temperature gradient just about equal to zero. This indicates that the heat transfer in the annulus is mainly drawn by the moving boundary layers close by the walls and the fluid flow is in the regime of the laminar boundary layer. The heat transferred through the nucleus is negligible.

Vertical velocity profiles are presented in Fig. 3 for different Rayleigh numbers ranging from Ra = 10^3 to Ra =10^6. The profiles are plotted along the horizontal direction. Other geometric parameters were selected as Ar =1, K = 2, X = 0.5and δ=45°. As expected, the velocity is very low across wherever in the annulus at Ra ≤10^4. The fluid move is not effectual confirmed that the conductive regime is predominant effective under this condition. This means that the fluid is virtually stagnant in the annulus at 0 ≤ R ≤ 0.5 and 0.9 ≤ R ≤1.1. But, when the Rayleigh number is in the range of 5 × 10^4 ≤ Ra ≤ 10^5, the fluid entrained by the buoyancy-driven force in annulus is begins to accelerate from the base and forms the primary flow in the vertical direction to up. The velocity increases when the Rayleigh number is large enough Ra= 10^6, and the fluid flow is now confined adjacent at a time in the hot wall (0.37 ≤ R ≤ 0.67) and the cold wall (1, 09 ≤ R ≤ 1.33).

The Rayleigh number effects on streamlines (left) and isotherms (right) Fig. 4 (a) - (d) Present Ar = 1, K = 2, X = 0.5 and δ=45° visualizations are given from Ra = 10^3 to Ra = 10^6. The single cell is formed, shown from these figures, of all values of the Rayleigh numbers considered, which is in the direction of rotation clockwise. At lower Rayleigh number Ra ≤ 10^4 such that Fig. 4 a-b the isotherms are almost vertical at the active wall for most of the annulus, illustrating the mechanism of heat transfer flow by conduction dominated. For higher values of the Rayleigh number (i.e.10^5 ≤ Ra ≤ 10^6) as shown in Fig. 4 c-d, due to the increase of the mode of convection heat transfer, two thin boundary layers were formed vicinity of the hot and cold walls for 1 ≤ R ≤ 2. The isotherms are deformed and crowded adjacent the bottom left and upper right of the annulus and are stratified horizontally. The flow majority moves to upwardly right and top of the annulus in reason to the presence of the wall partly cooled and heated. Because of adiabatic boundaries at the upper and the bottom of the annulus the Flow becomes motionless. However, the increased convection mode of heat transfer provoked by increasing the Rayleigh number and the virtually parallel distribution to the horizontal walls. It can also be seen from streamlines, the fluid velocity increases and the fluid direction and revolved towards the top right and bottom left of the annulus when the increase of the Rayleigh number.

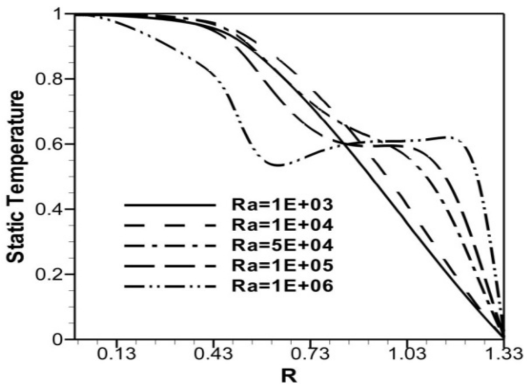

Fig.2 Temperature profiles variation with horizontal distance for annulus Aspect ratio Ar=1, K=2, X=0.5 and δ=45° at Z=0.75.

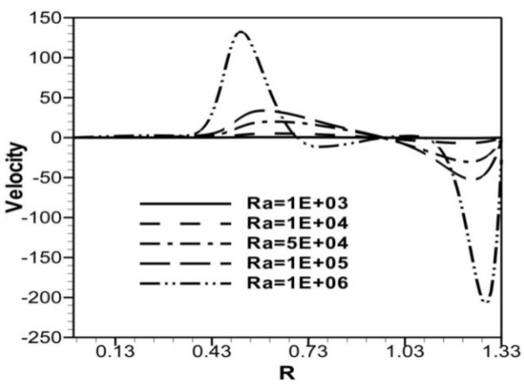

Fig. 3 Axial velocity profiles variation with horizontal distance for annulus Aspect ratio Ar=1, K=2, X=0.5 and δ=45° at Z=0.75.

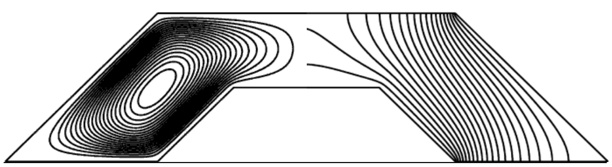

a) Ra=10^3

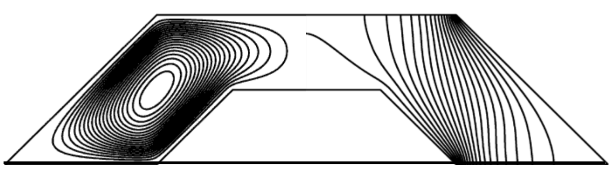

b) Ra=10^4

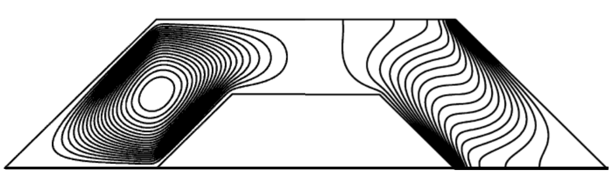

c) Ra=10^5

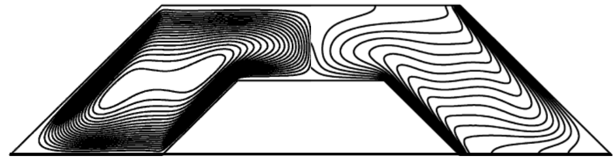

d) Ra=10^6

Fig.4 Streamlines and isotherms for annulus Aspect ratio Ar=1, K=2, X=0.5 and δ=45°.

B. Effects of Aspect ratio

The isotherms (on the right) and streamlines (on the left) are depicted variations for aspect ratio Ar As can be seen from Fig. 5. The figure obtained for different aspect ratio values i.e. Ar=1, 1.5 & 2 and three different values of title angles δ=45°, 56.31°& 63.44°corresponding to K =2, X=0.5, 0.75 &1 and Ra = 10^5. The form of the isotherms show that increasing the aspect ratio provoked to the isotherms crowding at the bottom left and top right of the annulus. The temperature gradient in the hot wall, there is continuous variations low aspect ratio Fig. 5a indicates that the heat transfer rate continuously varies along the vertical height of the hot wall, which is not the case at higher aspect ratio Fig. 5c. The fluid flow center increased when aspect ratio increases.

The increase in the Nusselt number for different aspect ratio Ar = 1, 1.5 and 2, and height ratio X = 0.5, 0.75 and 1, and its linear variation with the Rayleigh number on a logarithmic scale are presented in Fig. 6. The other parameters are K = 2 and δ=45°, 56.31°& 63.44°. For the hot wall, the average heat transfer rate increases as the Rayleigh number is increased by the growing contribution of natural convection. And the heat transfer rate increases with increase in the annulus aspect ratio.

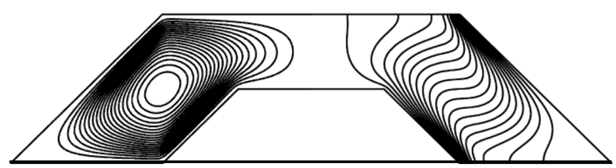

a) Ar=1, δ=45°

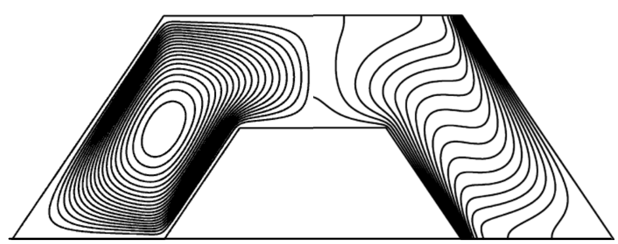

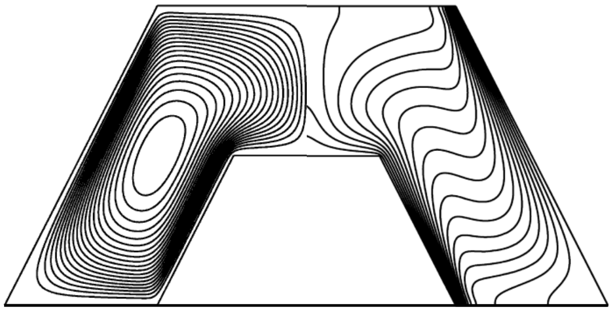

c) Ar=2, δ=63.44°

Fig. 5 Streamlines and isotherms for different Annulus Aspect ratio at Ra=10^5 and K=2.

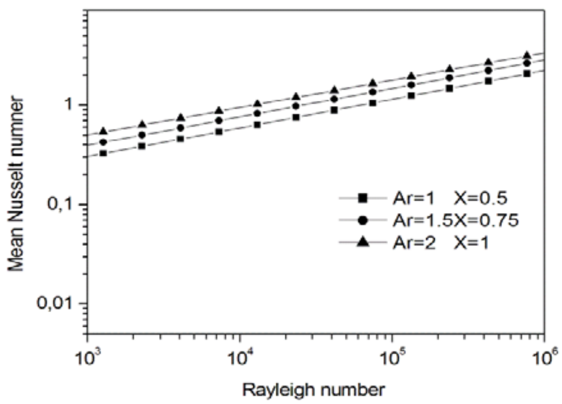

Fig. 6 Nusselt number variation with Rayleigh number and annulus Aspect ratio, Height ratio at K=2 and δ=45°,56.31°&63.44°.

C. *Effects of Height ratio*

The isotherms (on the right) and streamlines (on the left) with different annulus height ratio X as demonstrated in Fig. 7. This figure corresponds to the several values Ra = 10^5, Ar=1, K = 2 and δ =45°. It's clearly noted from this figure that the isotherms move to the hot wall with a ratio of height increasing. This informs that increasing of the annulus height ratio provoked increasing the heat transfer from the hot wall of annulus. The temperature gradient hot wall can also be seen from the isothermal continuous decrease as the decrease in the ratio of the height. (The fluid flow is clearly visualized in the streamlines, The fluid flow is clearly visible in the streamlines). The complete cycle formed through the fluid circulation directed upward toward the hot wall falls then to the cold wall of the annulus. Showing that the fluid flow concentrates of the circular cell at the entire annular space of small height ratio, but it moves half of the annular space (1 ≤ R ≤ 2), the height ratio increases. When the ratio of the height increases the orientation of the cell becomes parallel to the vertical inner cone.

The Nusselt number variation with aspect ratio X for several Rayleigh number. The figure corresponds to Ar = 1, K = 2 and δ=45° are plotted in Fig. 8. As expected, the heat transfer rate is greater at the Rayleigh number is greater. It can be inferred from the figure that the growth rate effect is higher than the line for Ra ≤10^5 is stronger at higher Rayleigh number values and the line corresponding to Ra = 10^6. The height ratio does not influence the heat transfer rate when Ra ≤ 10^5, because the fluid move is very slow, and therefore the conductive regime prevails over convection regime, which explains the almost constant value the Nusselt number.

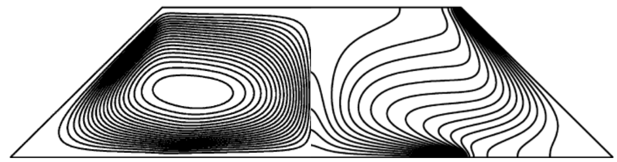

a) X=0

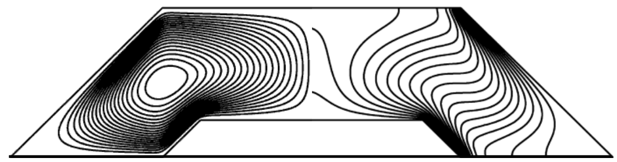

b) X=0.25

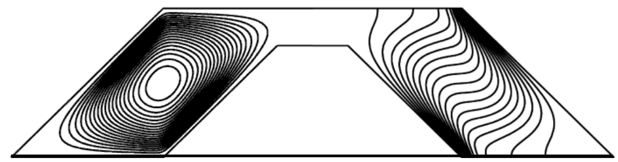

d) X=0.75

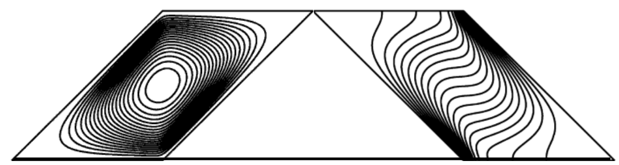

e) X=1

Fig. 7 Streamlines and isotherms for different annulus Height ratio at Ra=10^5, Ar=1 ,K=2 and δ=45°.

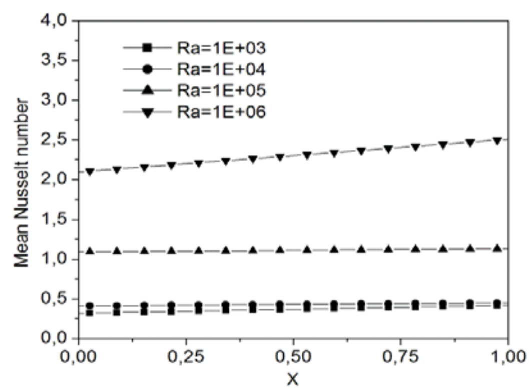

Fig.8 Nusselt number Variation with annulus Height ratio and Rayleigh number at Ar=1 and K=2, δ=45°.

VI. Conclusion

In this paper, the numerical study of natural convection in a Two-Dimensional vertical conical partially annular space for steady-state regime with differentially heated walls has been analyzed. The effect of main parameters as Rayleigh number, Aspect ratio and Height ratio of annulus. Concise summaries of the major results are reported in the following:

1) The heat transfer rate increases with increasing Rayleigh number. The heat transfer rate increasing is a function of the annulus Aspect ratio.

2) For lower Rayleigh number values we observed a dominance of conduction heat transfer. At higher values of Rayleigh number was observed that heat transfer rate increased and dominated by convection mode.

3) The natural convection regime has been bounded by Rayleigh number. When the Rayleigh number is weak, the fluid is practically stagnant. But for higher values of Rayleigh number the fluid entrained and begins to accelerate by the buoyancy-driven force in annulus from the base and forms the primary flow in the vertical direction to up.

4) It's finds that the annulus height ratio is one of the more important parameters on flow and temperature fields and heat transfer. The Nusselt number increase is a function of the annulus height ratio.

5) For high value of the annulus height ratio the cell orientation becomes parallel to the vertical inner cone i.e. the fluid motion is accelerated fully in the $1<R\leq 2$ and they is almost zero in the other side $0\leq R\leq 1$ at above the inner cone. But when height ratio decreases the fluid motion is accelerated increasingly in the zone $0\leq R\leq 1$ (the circular cell of the fluid motion is concentrated at the all in this zone).

References

[1] A. Sridhar and K.S. Reddy, "Transient analysis of modified cuboid solar integrated-collector-storage system, " *Applied Thermal Engineering*, vol. 27, pp.330-346, 2007.

[2] S.G. Wang and T.Y. Li and P.T. Hsu and Kaohsiung and Taiwan, "Natural convection of micropolar fluid in a partially divided enclosure," *Acta Mechanica*, vol. 136, pp. 41 – 53, 1999.

[3] Y.L. He and W.W. Yang and W.Q. Tao, "Three-Dimensional Numerical Study of Natural Convective Heat Transfer of Liquid in a Cubic Enclosure," *Numerical Heat Transfer Part A Applications*, vol. 47, pp.917-934, 2005.

[4] HN. Dixit and V. Babu, " Simulation of high Rayleigh number natural convection in a square cavity using the lattice Boltzmann method," *International Journal of Heat and Mass Transfer*, vol. 49, pp. 727–739, 2006.

[5] A.A. Ganguli and A.B. Pandit and J.B. Joshi, " CFD simulation of heat transfer in a two-dimensional vertical enclosure," *Chemical Engineering Research and Design*, vol. 87, pp. 711–727, 2009.

[6] M. Aounallah and Y. Addad and S. Benhamadouche and O. Imine and L. Adjlout and D. Laurence, "Numerical investigation of turbulent natural convection in an inclined square cavity with a hot wavy wall," *International Journal of Heat and Mass Transfer,* vol. 50, pp. 1683–1693, 2007.

[7] Y. Varol and H.F. Oztop and I. Pop, "Natural convection in right-angle porous trapezoidal enclosure partially cooled from inclined wall," *International Communications in Heat and Mass Transfer*, , vol. 36, pp.6–15, 2009.

[8] E. Fuad Kent and E. Asmaz and S. Ozerbay, "Laminar natural convection in right triangular enclosures", *Heat and Mass Transfer*, 2007, Vol. 44, pp. 187–200.

[9] I. Hajri and A. Omri and S. Ben Nasrallah, "A numerical model for the simulation of double-diffusive natural convection in a triangular cavity using equal order and control volume based on the finite element method," *Desalination*, vol. 206, pp. 579–588, 2007.

[10] Y. Varol and H.F. Oztop and T. Yilmaz, " Natural convection in triangular enclosures with protruding isothermal heater,"*International Journal of Heat and Mass Transfer*, vol. 50, pp. 2451–2462, 2007.

[11] A. Hadjadj and S. Maamir and B. Zeghmati, "A new study of laminar natural convection in two concentric vertical cylinders," *Heat and Mass Transfer*, vol. 35, pp. 113-121, 1999.

[12] P. Venkata Reddy and G. S.V.L. Narasimhamn, "Natural convection in a vertical annulus driven by a central heat generating rod," *International Journal of Heat and Mass Transfer*, vol. 51, pp.5024–5032, 2008.

[13] F A. Hamad and M K. Khan, "Natural convection heat transfer in horizontal and inclined annuli of different diameter ratios", Energy Conversion and Management, 1998, Vol. 39, pp. 797-807.

[14] E.L.M. Padilla and A. Silveira-Neto, "Large-eddy simulation of transition to turbulence in natural convection in a horizontal annular cavity," *International Journal of Heat and Mass Transfer*, vol. 51, pp. 3656-3668, 2008.

[15] M. Habibi Matin and I. Pop, " Natural convection flow and heat transfer in an eccentric annulus filled by Copper nanofluid," *International Journal of Heat and Mass Transfer*, vol. 61,pp. 353–364, 2013.

[16] N.J.A. Salman and A.B. Irfan and Z.A. Zainal and H.M.T. Khaleed and K. Jeevan, " Heat transfer in a conical cylinder with porous medium," *International Journal of Heat and Mass Transfer*, vol. 52, pp. 3070–3078, 2009.

[17] G. de Vahl Davis and R.W.Thomas, " Natural Convection Between Concentric Vertical Cylinders High Speed Computing in Fluid Dynamics," *Physics of Fluids*, vol. 2, pp. 198–207, 1969.

[18] R. Kumar and M.A. Kalam, "Laminar Thermal Convection between Vertical Coaxial Isothermal Cylinders," *International Journal of Heat and Mass Transfer*, vol. 34, pp. 513-524, 1991.

First A. Author (M'76–SM'81–F'87) and the other authors may include biographies at the end of regular papers. Biographies are often not included in conference-related papers. This author became a Member (M) of **EUROPMENT** in 1976, a Senior Member (SM) in 1981, and a Fellow (F) in 1987. The first paragraph may contain a place and/or date of birth (list place, then date). Next, the author's educational background is listed. The degrees should be listed with type of degree in what field, which institution, city, state or country, and year degree was earned. The author's major field of study should be lower-cased.

The second paragraph uses the pronoun of the person (he or she) and not the author's last name. It lists military and work experience, including summer and fellowship jobs. Job titles are capitalized. The current job must have a location; previous positions may be listed without one. Information concerning previous publications may be included. Try not to list more than three books or published articles. The format for listing publishers of a book within the biography is: title of book (city, state: publisher name, year) similar to a reference. Current and previous research interests ends the paragraph.

The third paragraph begins with the author's title and last name (e.g., Dr. Smith, Prof. Jones, Mr. Kajor, Ms. Hunter). List any memberships in professional societies other than the **EUROPMENT**. Finally, list any awards and work for **EUROPMENT** committees and publications. If a photograph is provided, the biography will be indented around it. The photograph is placed at the top left of the biography. Personal hobbies will be deleted from the biography.

Finite Element Analysis of Debonding Propagation in FM73 Joint under Static Loading

Reza Hedayati, Meysam Jahanbakhshi

Abstract--In this work, Fracture Mechanics is used to predict crack propagation in the adhesive jointing aluminum and composite plates. Three types of loadings and two types of glass-epoxy composite sequences: $[0/90]_{2s}$ and $[0/45/\text{-}45/90]_s$ are considered for the composite plate. Therefore 2*3=6 cases are considered and their results are compared. The debonding initiation load, complete debonding load, crack face profile and load-displacement diagram have been compared for the six cases.

Keywords—Adhesive joint, APDL, Debonding, Fracture, LEFM.

I. Introduction

WITH the increase in the number of bonded composite aircraft components and in the number of bonded repairs made to cracked metallic structures, knowledge of adhesive bonding is becoming crucial to aircraft design and life extension. Design and analysis of adhesively bonded joints has traditionally been performed using a variety of stress-based approaches [1]. The use of fracture mechanics has become increasingly popular for the analysis of metallic components but has seen limited use in bonded structure joints. Durability and damage tolerance guidelines, already in existence for metallic aircraft structures, need to be developed for bonded structures, and fracture mechanics provides one method for doing so [1].

In this work, Fracture Mechanics is used to predict crack propagation in the joint between aluminum and composite plates. The setup considered in this work is shown in Fig. 1. Three types of loadings: $\lambda = 0$, $\lambda = 0.5$ and $\lambda = 1$ are considered while two types of glass-epoxy composite sequences: $[0/90]_{2s}$ and $[0/45/\text{-}45/90]_s$ have being considered for the composite plate. Therefore 2*3=6 cases are considered in this study, and their results are compared. Afterwards the sequence $[0/90]_{2s}$ is called Sequence 1, and $[0/45/\text{-}45/90]_s$ is called Sequence 2. Half of a typical crack face shape is shown in Fig. 2 for the symmetrical problem considered in this work. The main parameter in analyzing crack propagation is called the stress intensity factor which is shown by K_I, K_{II} and K_{III} for opening, shearing, and out of plane shearing fracture modes. The stress intensity factor is the representative of stress intensity around a crack or crack tip or face.

R. Hedayati is with the Young Researchers and Elite Club, Najaf Abad Branch, Islamic Azad University, Najaf Abad, Isfahan, Iran (corresponding author; e-mail: rezahedayati@gmail.com).

M. Jahanbakhshi is with the Young Researchers and Elite Club, Najaf Abad Branch, Islamic Azad University, Najaf Abad, Isfahan, Iran (e-mail: jahanbakhshimeysam@gmail.com).

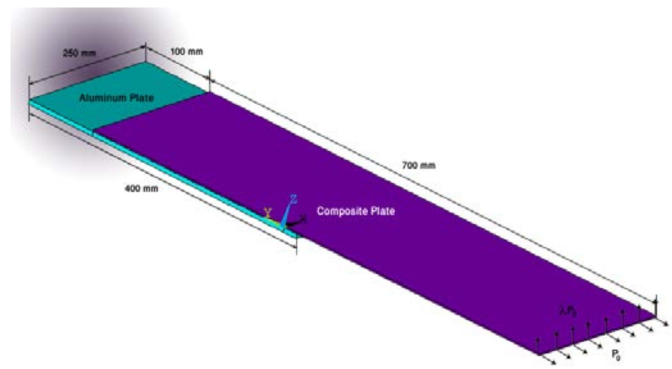

Fig. 1 The composite/Aluminum Joint Studied

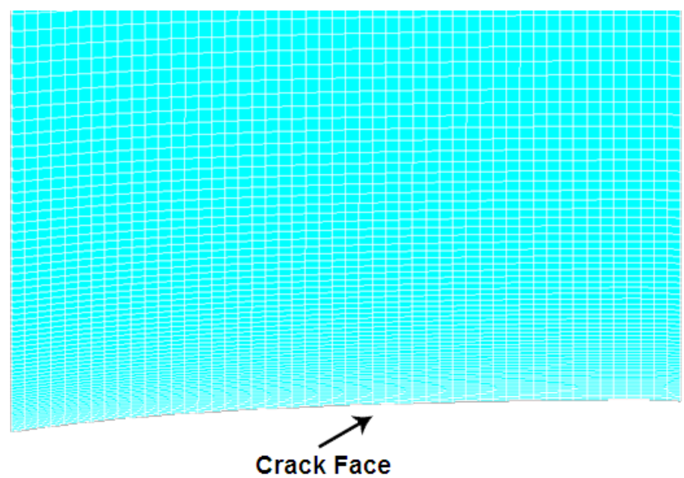

Fig. 2 A typical crack face shape

In this project, crack propagation in the adhesive joining composite and aluminum plates is studied. For investigating crack propagation in static loading, two criteria are needed: initiation criteria and propagation criteria. The crack propagates through the middle of the adhesive layer, relatively distant from either adhesive-adherent interface, leaving an adhesive layer on both adherents[1].

In order to find the shape and size of initial crack, a simple method is used. After applying the load, initial debonding is made at the locations in which the YZ shear stress is higher than the adhesive shear yield stress. The crack initiation load is the load which (after creating the initial debonding) satisfies

ISBN: 978-1-61804-288-0

the propagation criteria on the nodes located on the crack front to a small extent.

The crack propagation criteria used in this study is [2]:

$$\frac{G_I}{G_{Ic}} + \frac{G_{II}}{G_{IIc}} + \frac{G_{III}}{G_{IIIc}} = 1 \quad (1)$$

Using $G = \frac{K^2}{E}$ and by considering only the first and the second modes of fracture:

$$\left(\frac{K_I}{K_{Ic}}\right)^2 + \left(\frac{K_{II}}{K_{IIc}}\right)^2 = 1 \quad (2)$$

In order to calculate $K_I$and K_{II}, the following substitutions were made to (4) and (8):

$$\begin{aligned} \sigma_{22} &= \sigma_{zz} \\ \sigma_{12} &= \sigma_{yz} \end{aligned} \quad (3)$$

X, Y and Z directions are shown in Fig. 1. In this study, the adherent chosen for bonding aluminum and composite plates is FM 73. The material properties of the FM73 adhesive are listed in Table I [1].

TABLE I
MATERIAL PROPERTIES OF THE FM300 ADHESIVE AND ALUMINIUM 2024 [3]

Property	FM300	Aluminium 2024
Elasticity Modulus	2.73 GPa	72 GPa
Yield Stress	50 MPa	280 MPa
Poisson's ratio	0.33	0.27
d (Paris constant)	4.5	-
b (Paris constant)	$1.5*10^{-15}$	-

II. FINITE ELEMENT MODELING

In this project, a macro program is developed using ANSYS Parametric Design Language(APDL) to model debonding growth. At each step, the debonding face propagation, which is non-uniform, is calculated. Then the elements are completely cleared and a new model which consists of the updated crack face is created and then meshed. This mesh deletion and creation is done at each propagation step in order to keep the accuracy of calculations well. The major steps of the developed Macro program are as follows:

(1) Define material properties of the model.
(2) Define crack initiation load
(3) Generate the geometry and mesh of the composite and aluminum plates and the adhesive.
(4) Define the loading and constraints.
(5) Perform the linear elastic solution.
(6) Predict the initial debonding area using the crack initiation criterion.
(7) Move all the nodes located on crack front 0.2 mm in positive Y direction
(8) Perform the linear elastic solution.
(9) Calculate the stress intensity factors (K_I and K_{II}) at each node located on the crack face.
(10) Move back the nodes which have not satisfied the propagation criterion to their previous location (move them back 0.2 mm in the negative Y direction)
(11) If none of the nodes located on the crack front satisfy the propagation criterion, increase the applied load
(12) If the crack has reached its end (it has moved 300 mm) stop the solution
(13) Return to step (8)

The finite element model of the problem is shown in Fig. 3, and is zoomed in at the adhesive interface in Fig. 4. For the composite plate 6000 8-noded SOLID46 elements, for the aluminum plate 22000 8-noded SOLID45 elements, and for the adhesive 8000 SOLID45 elements have been used. For the composite plate, the aluminum plate and the adhesive, one, four and two elements through the thickness have been used. The elements at the two interfaces are glued. In other words, the composite and the adhesive share the same nodes at their interface. The same is true about the aluminum and the adhesive interface. This can be better seen in Fig. 4. Since the structure is symmetrical with respect to a plane perpendicular to X direction, only half of the model is created. The nodes located at the symmetry plane position are not allowed to move in X direction. For discretizing the entire model, mapped meshing has been used.

Using a Core2Due 2.26 GHz CPU, each crack propagation step took about 2 min. For each load step, about 400 propagation steps was needed. It must be noted that the crack initially moved quickly, but near the end of crack propagation at each load step, a long time is taken to move forward and backward most of the nodes on the crack face. Considering 4 to 6 load steps, solving each problem (the 6 cases in this project) takes about 40 hours.A more complete information on the materials and method can be found in [4] and [5].

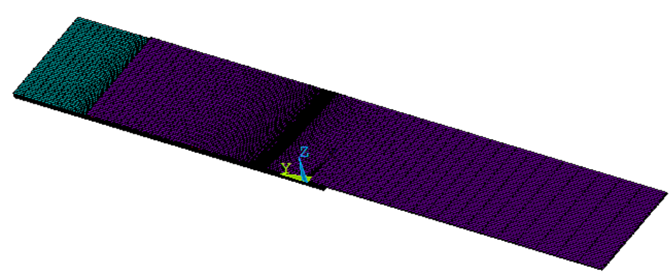

Fig. 3 Finite Element model of the Aluminum/Composite Joint

III. RESULTS AND DISCUSSION

A. Crack Initiation Load

The load versus crack propagation for λ=0 and for two composite sequences is shown in Fig. 5. As it can be seen, the crack initiation load for the first and the second sequences are 232 kN/m and 224 kN/m, respectively. It also can be seen that he complete debonding load for the first and the second sequences are 656 kN/m and 496 kN/m, respectively. Therefore it can be concluded that the crack initiation load is

ISBN: 978-1-61804-288-0

close for the two sequences, but as the crack propagates, the load necessary for crack propagation is lower in sequence 2 than that in sequence 1.

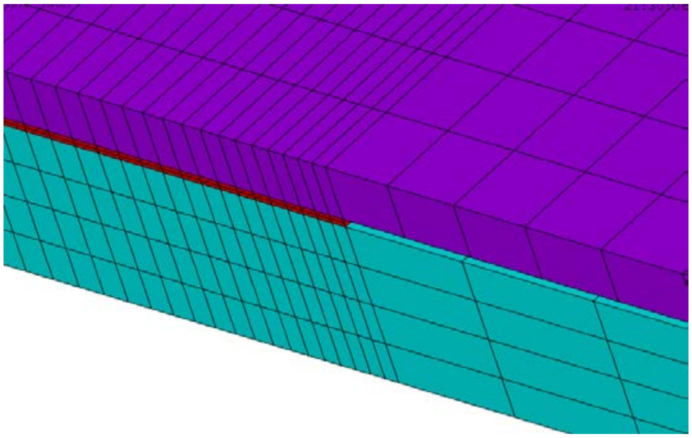

Fig. 4 FE model of the Aluminum/Composite Joint (Zoomed in)

The load versus crack propagation for λ=0.5 and λ=1, and for two composite sequences are shown in Fig. 6. The initiation and the complete debonding load for the two composite sequences and for three values of λ are listed in Tables II and III. The following conclusion can be made:

- When λ=0.5 or 1, by increasing the load slightly over the crack initiation load, the crack propagates immediately about 150 mm (Fig. 6). But on the other hand it can be seen from Fig. 5 that when λ=0, by increasing the load slightly over the crack initiation load, the crack propagates immediately only about 50 mm which is much lower than 150 mm.
- In all values of λ, the initiation and the complete debonding load is lower in the cases with composite sequence of 2.
- In both the composite sequences, the initiation and the complete debonding load is higher in λ=0.5 than that in λ=1.

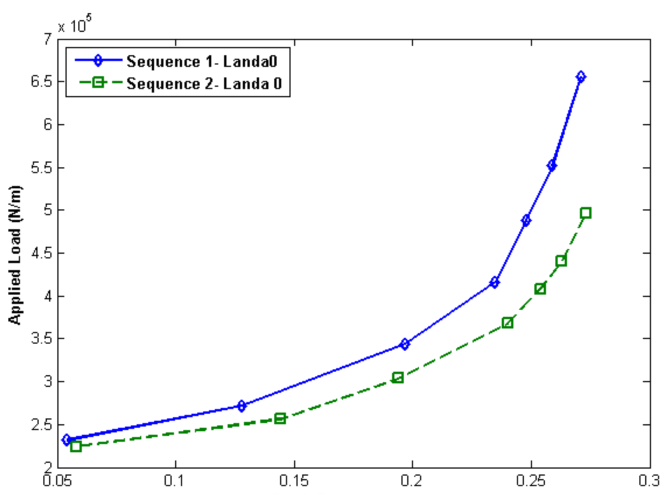

Fig. 5 Load vs. crack propagation for two composite sequences (λ=0)

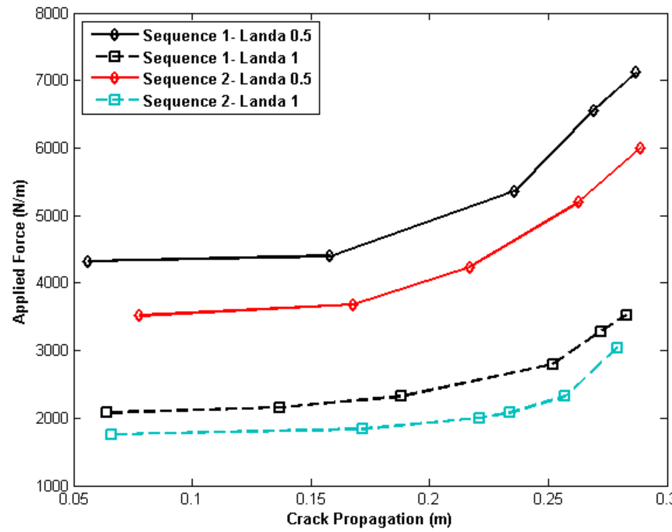

Fig. 6 Load versus crack propagation for four composite sequences (λ=0.5 and λ=1)

TABLE II
CRACK INITIATION LOAD FOR THE SIX CASES CONSIDERED

	λ = 1	λ = 0.5	λ = 0
Sequence 1	2.08 kN/m	4.32 kN/m	232 kN/m
Sequence 2	1.76 kN/m	3.52 kN/m	224 kN/m

TABLE III
COMPLETE DEBONDING LOAD FOR THE SIX CASES CONSIDERED

	λ = 1	λ = 0.5	λ = 0
Sequence 1	3.52 kN/m	7.12 kN/m	656 kN/m
Sequence 2	3.04 kN/m	6 kN/m	496 kN/m

B. Crack Face Profile

The crack face profile in different crack propagations can be seen in Fig. 7(a-d) for the two sequences and λ=0 and 1. The difference between the debonding propagations of the ends and the middle of the debonding front is listed for the six cases in Table IV. The oscillations visible in the profiles are because of two reasons:

- First, for better visibility of crack face profiles indifferent crack propagations, the crack dimension in Y direction (parallel to the direction the crack moves) is scaled about10 times in Fig. 7 (a)-(d). Therefore the real oscillations in crack profile are exaggerated in plots,
- Second, since each node is allowed to move forward and backward only by 0.2 mm, therefore, the crack face profile cannot be completely smooth. By decreasing the movement value to smaller values, a smoother crack face profile can be obtained.

It can be seen from Fig. 7 (a)-(d). and Table IV that:

- For both the sequence types, in cases with λ=0 the ends of the crack face propagates forward more than its middle part, while in cases with λ=0.5 or λ=1 the middle part of the crack face moves forward more than its ends.
- For all values of λ, the difference between the debonding propagations of the ends and the middle of the crack face

ISBN: 978-1-61804-288-0

of cases with composite sequence of 2 is higher than that of sequence 1. This can be more recognized when λ=0.

- For both the sequence types, the difference between the debonding propagations of the ends and the middle of the crack face of the case with λ=0 is higher than that in the corresponding case with λ=0.5 or λ=1.
- Regardless of the sequence type, when λ=0 the debonding face profile can be divided in three regions: (a) at the beginning of debonding propagation, the difference between the debonding propagations of the ends and the middle of the crack face is small, (b) when the maximum propagation of the crack face is higher than 50 mm, the difference between the debonding propagations of the ends and the middle of the crack face gets larger and remains almost constant until near the end of propagation, and, (c) when the crack face has reached near the end of adhesive film, the difference between the debonding propagations of the ends and the middle of the crack face gets small again.
- Regardless of the sequence type, when λ=0.5 or λ=1, the difference between the debonding propagations of the ends and the middle of the crack face gets larger consistently. In other words, the difference between the debonding propagations of the ends and the middle of the crack face is small at the beginning, then for a large range of debonding propagation remains almost constant, and finally at the end of propagation gets large.
- For any value of λ, the difference between the debonding propagations of the ends and the middle of the crack face is very close in cases λ=0.5 and λ=1.

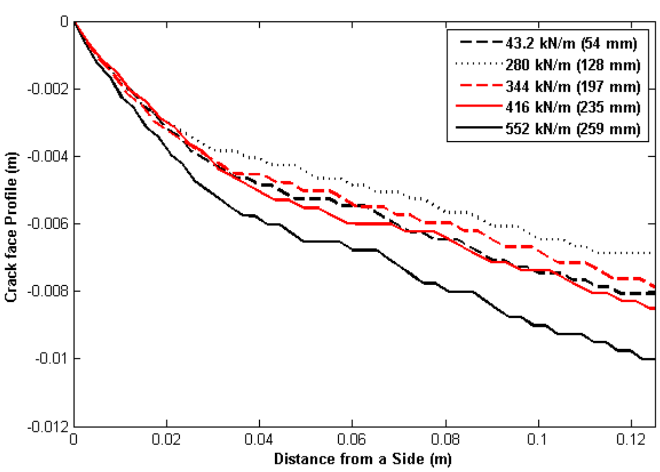

(a)

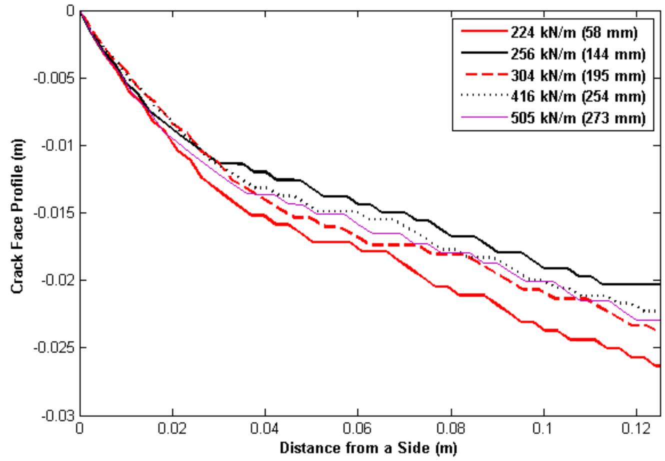

(b)

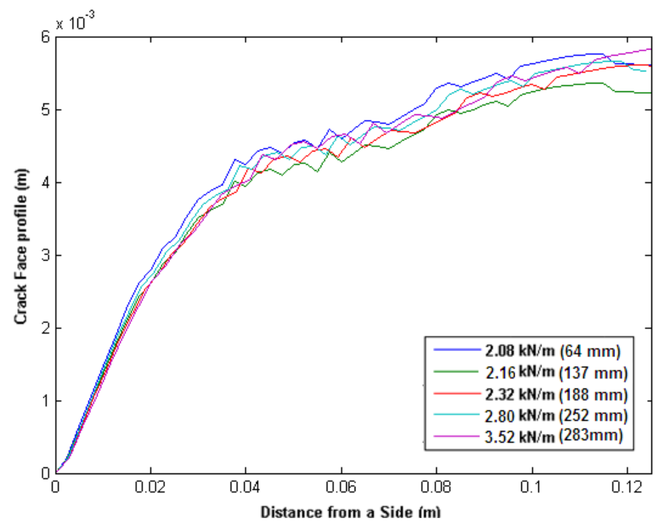

(c)

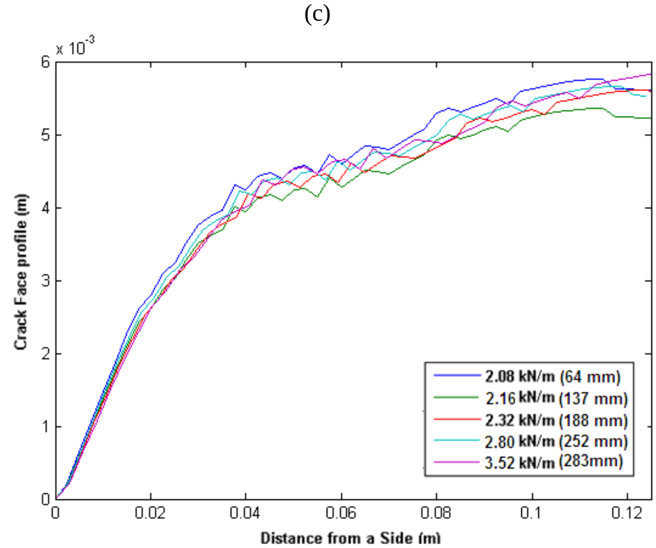

(d)

Fig. 7 Comparison of crack face profile for different crack propagations: (a) Sequence 1 and λ=0, (b) Sequence 2 and λ=0, (c) Sequence 2 and λ=0, (d) Sequence 2 and λ=1

TABLE IV
DIFFERENCE BETWEEN THE CRACK PROPAGATION BETWEEN THE ENDS AND THE MIDDLE PARTS OF THE CRACK FACE

	$\lambda = 0$	$\lambda = 0.5$	$\lambda = 1$
Sequence 1	10 mm	7.2 mm	5.9 mm
Sequence 2	26 mm	15 mm	17 mm

C. Load-Displacement Diagrams

For plotting the load-displacement diagram, the displacement at the end of composite plate is measured. In λ=0, the horizontal displacement and in λ=0.5 and 1, the vertical displacement is measured. This is also true for λ=0.5, because the horizontal displacement of the composite end is negligible compared to its vertical displacement. The following conclusions can be made:

- Change in load-displacement slope from the initial debonding until the completed bonding in cases with λ=0.5 and 1 is more than that incases with λ=0.
- Regardless of the composite sequence if λ=0, the complete debonding happens when the displacement at the end of the composite plate reaches 1 cm.
- Regardless of the composite sequence if λ=0.5 and 1, the complete debonding happens when the displacement at the end of the composite plate reaches 16 cm.

The load-displacement diagrams at the complete debonding is compared for the two sequences and λ=0.5 and 1 in Fig. 8. It is interesting to see that the sequence type does not affect the load-displacement slope very much. On the other hand, the value of λ has a significant effect on the slope of load-displacement diagram.

IV. CONCLUSIONS

In this work, Fracture Mechanics is used to predict crack propagation in the adhesive jointing aluminum and composite plates. Three types of loadings:$\lambda = 0$,$\lambda = 0.5$ and $\lambda = 1$ are considered while two types of glass-epoxy composite sequences: $[0/90]_{2s}$ and $[0/45/-45/90]_s$ have being considered for the composite plate. Therefore, 2*3=6 cases are considered in this study, and their results are compared. It was seen that the crack initiation load is close for the two sequences, but as the crack propagates, the load necessary for crack propagation is lower in sequence $[0/45/-45/90]_s$ than that in sequence $[0/90]_{2s}$. About the debonding front profile, it was seen that for both the sequence types, in cases with λ=0 the ends of the debonding front propagates forward more than its middle, while in cases with λ=0.5 or λ=1 the middle part of the debonding front moves forward more than its ends. It was also seen that regardless of λ, the difference between the debonding propagations of the ends and the middle of the debonding front is very close in cases λ=0.5 and λ=1. For the load-displacement diagram, it was seen that the sequence type does not affect the load-displacement slope very much. On the other hand, the value of λ has a significant effect on the slope of load-displacement diagram.

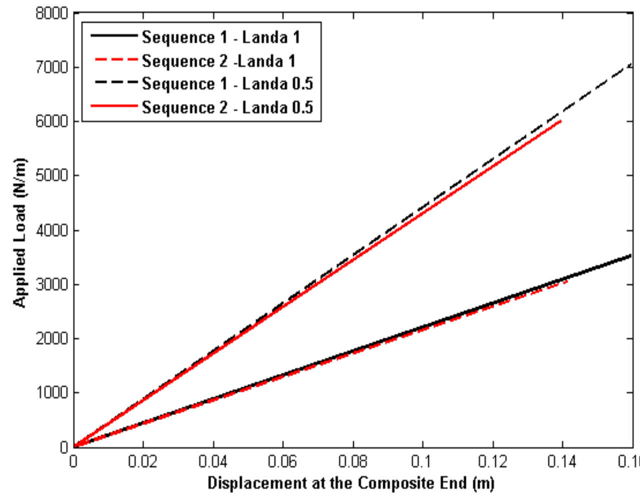

Fig.8 Comparison of load-displacement diagrams near the complete debonding for the two sequences and λ=0.5 and 1.

REFERENCES

[1] J. Tomblin, W. Seneviratne, P. Escobar, Y. Yoon-Khian,“Applications of Fracture Mechanics to the Durability of Bonded Composite Joints”. DOT/FAA/AR-97/56.

[2] H. Hosseini-Toudeshky, B. Mohammadi, B. Hamidi, H.R., Ovesy. “Analysis of composite skin/stiffener debounding and failure under uniaxial loading”. *Composite Structures*, vol. 75, pp. 428–436, 2006.

[3] R. Hedayati,, S. Ziaei-Rad. "Foam-core effect on the integrity of tailplane leading edge during bird-strike event." *Journal of Aircraft*, vol. 48, no. 6 pp. 2080-2089, 2011.

[4] R. Hedayati, S. GhorbaniKhouzani, and MeysamJahanbakhshi. "Investigation of debonding propagation in aluminum/composite joints under fatigue loading." *Journal of Adhesion Science and Technology*ahead-of-print,pp. 1-15, 2014.

[5] R. Hedayati, M. Jahanbakhshi, S. GhorbaniKhouzani. "Prediction of static crack propagation in adhesive joints." *Journal of Theoretical and Applied Mechanics*, vol. 52, no. 4, pp. 937-946, 2014.

Determination of elastic modulus of cortical bone using small punch testing and inverse finite element method

N. K. Sharma, M. K. Yadav, D. K. Sehgal, and R. K. Pandey

***Abstract*—**Detailed characterization of mechanical properties of cortical bone is important form engineering as well as medical point of view. This requires determination of mechanical properties for different anatomic locations of cortical bone using very small size of specimens. However, it is a challenging task to perform conventional tests on small size specimens of bone material due to various constraints. Small punch testing can be used in this direction to overcome these constraints. This technique has been employed in the present study along with the inverse finite element (FE) method to evaluate the elastic modulus of cortical bone at different anatomic locations. This way the load-displacement curves obtained from small punch testing were matched with the corresponding FE simulated curves to determine the elastic modulus of cortical bone at a particular anatomic location. This study shows that the predicted values of elastic modulus for different anatomic locations of the mid diaphysis of bovine tibiae cortical bone range from 20.4 GPa to 26.3 GPa. These results are almost similar to those obtained in previous investigations performed on bone material by using conventional tensile testing. Based on the results of the present study, it has been suggested that the same technique can be used to evaluate the anatomic variation in other mechanical and fracture properties of cortical bone.

***Keywords*—**Cortical bone, Elastic modulus, Inverse finite element method, Small punch testing.

I. INTRODUCTION

BONE is a highly heterogeneous and anisotropic material [1]-[11]. The heterogeneity of bone material is responsible for variation in its mechanical properties from one anatomic location to another. The investigations on the anatomic distribution of mechanical properties of bone would not only be helpful for the clinical scientists but also for the engineers working on bio-inspired materials. Most importantly, the evaluation of key mechanical properties of bone such as its elastic modulus at different anatomic locations is required for the design and development of prosthetic bone implants and whole bone finite element models.

The anatomic variation in elastic modulus of cortical bone can be analyzed by conducting experiments on small optimum size specimens. The optimum dimensions of the small size specimen should be maintained by keeping continuity of the hierarchical level of bone in to consideration. However, it is a challenging task to evaluate the value of strain during experimental deformation of small size specimens. Further the irregularity in specimen shapes, incorporation of defects during sample preparation and difficulty of comparison of results are the other constraints [12]-[17]. These constraints may be overcome by incorporating small punch technique in bone material testing. Previously, many researchers have applied this technique to determine the mechanical and fracture behavior of various engineering materials. Recently, this technique has been employed by Sharma *et al.* [18]-[19] to investigate the deformational behavior of bone material.

The present study is focused on the application of small punch testing technique to evaluate the anatomic variation in load-displacement behavior of cortical bone. An inverse finite element technique is further applied to compute the values of elastic modulus from the experimental load-displacement curves obtained for different anatomic locations. This has been achieved by matching the initial slope of the load – displacement curve obtained from experimental setup with the corresponding finite element simulated load-displacement curve.

II. MATERIALS AND METHOD

The present study has been conducted in tibiae bone obtained from young bovine of age between 24 to 36 months. The bones were obtained under institutional permission from the farm raised just after animal's natural death. In all, twenty small specimens were prepared from different anatomic locations (Anterior, Medial, Posterior and Lateral) of the middle diaphysis. These specimens were prepared with square dimension (10 mm x 10 mm) having 1.5 mm thickness as shown in Fig. 1. All these specimens were preserved in a solution of 50% ethanol and 50% saline at all time until testing.

The small punch test was conducted on MTS 858 Table Top Machine with very small strain rate of 0.5 mm/min. The small bone specimen fixed inside the specimen die is shown in Fig. 2

N.K. Sharma is with the School of Technology, The Glocal University, Mirzapur Pole, Saharanpur 247001, India (phone: +91-7409755378; e-mail: nitin@theglocaluniversity.in, enksharma@yahoo.com).

M. K. Yadav is with the Indian Institute of Technology Delhi, Hauz Khas, New Delhi 110016, India (e-mail: mukeshmech2011@gmail.com).

D. K. Sehgal is with the Indian Institute of Technology Delhi , Hauz Khas, New Delhi 110016, India (e-mail: profsehgal@yahoo.com).

R. K. Pandey is with the Indian Institute of Technology Delhi , Hauz Khas, New Delhi 110016, India (e-mail: rkpiitd@yahoo.com).

(a), whereas, complete fixture for small punch testing is shown in Fig. 2 (b). The installation of small punch test fixture on MTS machine is shown in Fig. 3. The displacement during small punch testing was measured with the help of clip gauge and the loading was applied using hemispherical headed punch of tip diameter 2.309 mm.

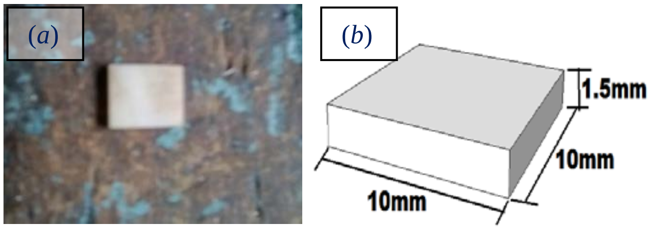

Fig. 1 (*a*) Small specimen prepared from cortical bone and (b) dimensions of the square cross-section small specimen

A three dimensional finite element (FE) model is used for simulating small punch testing with a square shape small (fixed plate) specimen under quasi-static loading applied by a hemispherical headed rigid punch.

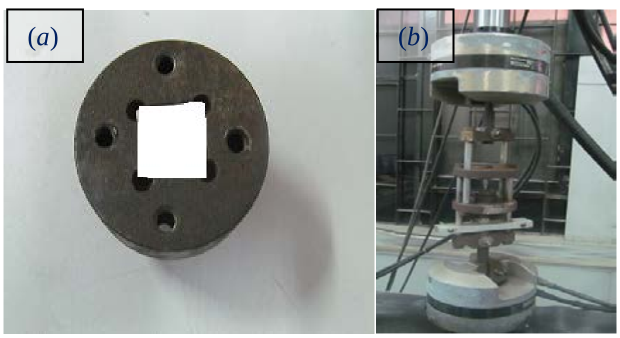

Fig. 2 (a) Small bone specimen fixed inside the specimen die and (b) complete fixture for small punch testing

Fig. 3 Installation of small punch test fixture on MTS Table Top machine

The dimensions of the small specimen are decided on the basis of the inner borehole cross-section of the specimen holder. The FE model is discretized with 8 nodded hexahedral elements (C3D8R) as shown in Fig. 4. The hemispherical headed punch of tip diameter 2.309 mm is modeled as analytically rigid.

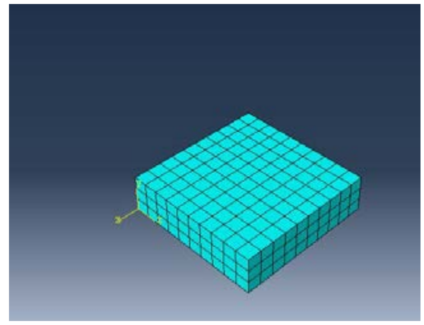

Fig. 4 Discretized (C3D8R) FE model of small specimen

All the nodes along the four edges of the small square shape specimen are fixed by boundary condition option ENCASTER (rigidly constrained). The top surface of square specimen is defined as SLAVE surface, whereas, hemispherical headed tip of rigid punch is defined as MASTER surface. A closed surface interaction of SLAVE and MASTER surface is developed by contact algorithm of ABAQUS. A tie interface is used to account for the contact between the punch head and specimen. The quasi-static loading is applied using amplitude option and small incremental steps are used at the reference node of hemispherical headed punch. The three dimensional FE model of small punch test is shown in Fig. 5.

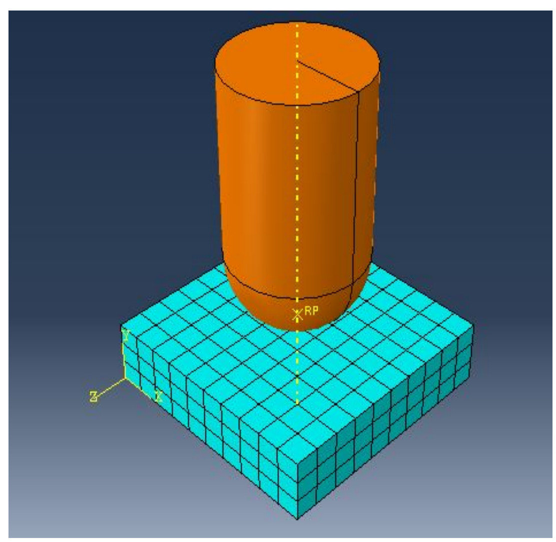

Fig. 5 Three dimensional FE model of small punch test

The FE analysis is carried out using inverse finite element process which is an iterative process. During this process the time history of output variable is defined and using this the time history of corresponding input variable is determined. As

ISBN: 978-1-61804-288-0

per our previous study, the load-displacement curve obtained from FE model was found to be closer to the experimental curve while considering bone as an isotropic material [19]. Therefore, in this study bone material is considered as an isotropic material.

The initial slope of the experimental load-displacement curve obtained from the small punch testing is matched with the slope of corresponding FE simulated load-displacement curve to obtain the elastic modulus of cortical bone at different anatomic locations. The FE load-displacement curve is generated in iterative manner by increasing or decreasing the value of elastic modulus such that curve matches with the corresponding experimental load-displacement curve. After final iteration when both the curve matches, prescribed input value of the elastic modulus should be equal to the elastic modulus of the bone material for the corresponding anatomic location. During this analysis the values of Poisson's ratio are defined from our previous study [8].

III. Results and Discussion

The values of maximum load (P_{max}) and displacement corresponding to the maximum load (δ) are determined from various load-displacement curves. These values are listed in Table 1 for different anatomic locations of the cortical bone. The small cortical bone specimens after conducting small punch testing are shown in Fig. 6. The experimental load-displacement curves for different anatomic locations of cortical bone are shown in Fig. 7. The values of elastic moduli obtained for different anatomic locations of cortical bone using inverse FE method are reported in Table 2 and the variation in elastic moduli across the cross-section of the cortical bone is shown in Fig. 8.

Table 1
Experimental values of maximum load and corresponding displacements for different anatomic locations of cortical bone

Anatomic location	Maximum load, P_{max} (N) $n = 5$	Corresponding displacement, δ (mm) $n = 5$
Anterior	582.7 ± 42.4	0.42 ± 0.052
Medial	551.6 ± 18.1	0.34 ± 0.056
Posterior	662.7 ± 24.0	0.37 ± 0.057
Lateral	639.6 ± 25.2	0.39 ± 0.062
ANNOVA	$p < 0.05$	$p > 0.05$

The values listed are the average of five values. Standard deviation is also given.

Table 2
Computed values of elastic modulus for different anatomic locations of cortical bone

Anatomic location	Computed elastic modulus E (GPa)
Anterior	21.4
Medial	26.3
Posterior	20.4
Lateral	24.3

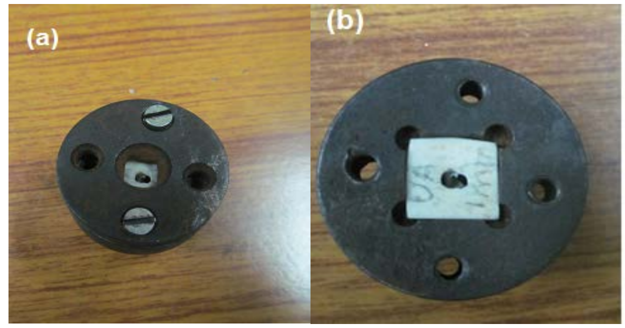

Fig. 6 (a) Small punch specimen placed inside the fixture just after testing (b) deformed specimen when upper die is removed

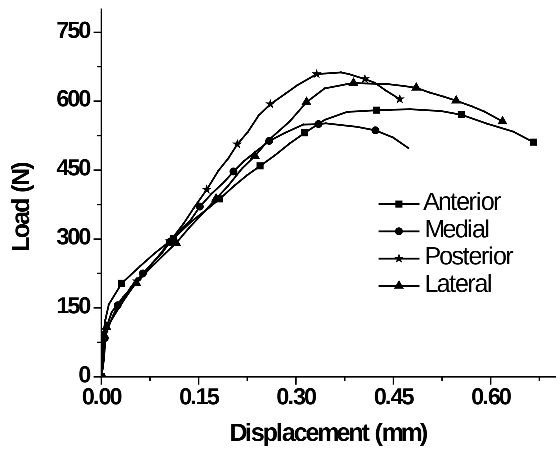

Fig. 7 Load-displacement curves for different anatomic locations of cortical bone

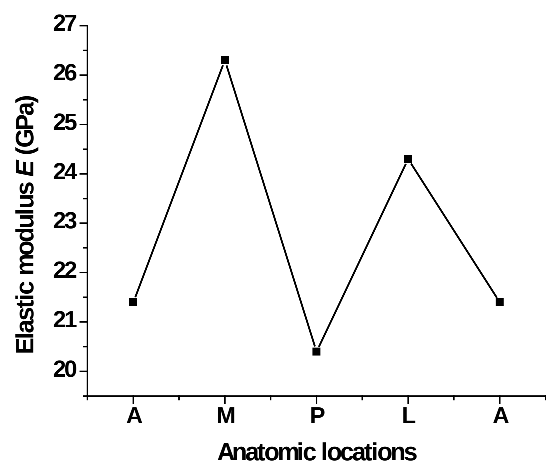

Fig. 8 Anatomic variation in elastic moduli along the cross-section of the cortical bone (A = Anterior, M = Medial, P = Posterior and L = Lateral)

The values of maximum load obtained for different anatomic locations of bone diaphysis indicate that one or more means of these values are statistically different. The experimental results reported in Table 1 show that the value maximum load at posterior location is highest as compared to the other locations, whereas, displacement corresponding to the maximum load is highest at anterior location. As per the *t*-test analysis, the values of maximum load for posterior and lateral locations are not found to be significantly different, similarly, the later values for anterior and medial locations are not found to be statistically different. However, maximum load for posterior location is found to be significantly greater ($p < 0.005$) than that for anterior and medial locations. The ANNOVA result shows that the mean values of displacement corresponding to the maximum load are not statistically different along the cross-section of the bone diaphysis.

The values of elastic modulus determined using inverse FE analysis are reported in Table 2. As per these results, the elastic modulus is found to be highest for the medial and lowest for the posterior location. These predicted values of elastic moduli range from 20.4 GPa to 26.3 GPa. It is interesting to note that almost similar range of elastic moduli have been reported for the bovine cortical bone in earlier investigations [6], [8], [20], [21]. This shows that the realistic values of elastic modulus can be predicted for different locations of bone diaphysis using small punch testing and inverse FE approach. The same approach can be further applied to evaluate the locational variation in other mechanical and fracture properties such as yield strength, shear modulus and fracture toughness.

IV. Conclusion

The values of elastic modulus were evaluated for different anatomic locations of the cortical bone using small punch testing and inverse FE approach. The small punch testing was conducted on square cross-section small specimens of cortical bone having 1.5 mm thickness. These specimens were obtained from four different anatomic locations of the middle diaphysis. The results of small punch testing were obtained in terms of load-displacement curves for different anatomic locations. The values of maximum load were found to be significantly greater for posterior and lateral anatomic locations as compared to the anterior and medial locations. An inverse FE technique has been further applied to determine the values of elastic modulus for different corresponding anatomic locations. The values of elastic modulus so obtained were found to be consistent with the corresponding values obtained in other previous reports. Based on the predicted results for elastic modulus, this study suggest that small punch testing and inverse FE technique can be applied together to predict the locational variation in other important mechanical and fracture properties of cortical bone.

Acknowledgment

We thank Mr. Anil Kumar (Lab Technician, IIT Delhi) and Mr. Mohd. Ashqueen (UG student, Glocal University) for helping in conduction of experimental test and manuscript preparation.

References

[1] C. J. Hernandez, G. S. Beaupre, T. S. Keller, and D. R. Carter, “The influence of bone volume fraction and ash fraction on bone strength and modulus,” *Bone. J.*, vol. 29, pp. 74–78, 2001.

[2] T. S. Keller, Z. Mao, and D. M. Spengler, “Young’s modulus, bending strength, and tissue physical properties of human compact bone,” *Orthop. Res. J.*, vol. 8, pp. 592–603, 1990.

[3] R. B. Ashman, S. C. Cowin, W. C. Van Buskirk and J. C. Rice, “A continuous wave technique for the measurement of the elastic properties of cortical bone,” *Biomech. J.*, vol. 17, pp. 349–361, 1984.

[4] X. N. Dong, and X. E. Guo, “The dependence of transversely isotropic elasticity of human femoral cortical bone on porosity,” *Biomech. J.*, vol. 37, pp. 1281–1287, 2004.

[5] N. Sasaki, N. Matsushina, T. Ikawa, H. Yamamura, and A. Fukuda, “Orientation of bone minerals and its role in the anisotropic mechanical properties of bone transverse isotropy,” *Biomech. J.*, vol. 22, pp. 157–164, 1989.

[6] N. K. Sharma, D. K. Sehgal, and R. K. Pandey, “Effect of orientation on elastic-plastic fracture toughness of cortical bone,” in *2011 Proc. WCE Conf.*, pp. 2298–2302.

[7] R. B. Martin, and D. L. Boardman, “The effect of collagen fiber orientation, porosity, density and mineralization of bovine cortical bone bending properties,” *Biomech. J.*, vol. 26, pp. 1047–1054, 1993.

[8] N. K. Sharma, Ruchita Pal, D. K. Sehgal, and R. K. Pandey, “Application of elastic-plastic fracture mechanics to determine the locational variation in fracture properties of cortical bone,” *Materials Performance and Characterization J.*, vol. 3, pp. 429–447, 2014.

[9] A. Ascenzi, P. Baschieri, and A. Benvenuti, “The torsional properties of single selected osteons,” *Biomech. J.*, vol. 27, pp. 875–884, 1994.

[10] K. Choi, J. L. Kuhn, M. J. Ciarelli, and S. A. Goldstein, “The elastic moduli of human subchondral, trabecular and cortical bone tissue and the size-dependency of cortical bone modulus,” *Biomech. J.*, vol. 23, pp. 1103–1113, 1990.

[11] J. D. Currey, “Biocomposites: Micromechanics of biological hard tissues,” *Current Opinion on Solid State Material Science*, vol. 1, pp. 440–445, 1996.

[12] M. P. Manahan, A. E. Browning, A. S. Argon, and O. K. Harling, “Miniaturized disk bend test technique development and application, the use of small-scale specimen for testing irradiated material,” *STP 888.*, ASTM, Philadelphia, pp. 17–49, 1986.

[13] G. E. Lucas, “Review of small specimen test technique for irradiation testing,” *Metallurgical Transaction A J.*, vol. 21A, pp. 1105–1119, 1990.

[14] S. H. Song, R. G. Foulkner, P. E. J. Flewitt, R. F. Smith, P. Marmy, and M. Victoria, “Irradiation-induced embrittlement of 2.25 Cr Mo Steel,” *Nuclear Materials J.*, vol. 280, pp. 162–168, 2000.

[15] J. R. Foulds, P. J. Woytowitz, T. K. Parnell, and C. W. Jewell, “Fracture toughness by small punch testing,” *Testing and Evaluation, JTEVA, J.*, vol. 23, pp. 3–10, 1995.

[16] X. Mao, H. Takahashi, and T. Kodaira, “Estimation of mechanical properties of irradiated nuclear pressure vessel steel by use of sub-sized CT specimen and small punch specimen,” *Scripta Metallurgical J.*, vol. 25, pp. 2487–2490, 1991.

[17] F. Dobes, and K. Milicka, “On the monkman-grant relation for small punch test data,” *Materials Science and Engineering A J.*, vol. 336, pp. 245–248, 2002.

[18] N. K. Sharma, Swati Sharma, Daya K. sehgal and Rama Kant Pandey “Detailed analysis of deformation behavior of plexiform bone using small specimen testing and finite element simulation,” in *Transactions on Engineering Technologies*, H. K. Kim, S. L. Ao, and M. A. Amouzegar Ed. New York: Springer, 2014, pp. 661–673.

[19] N. K. Sharma, S. Sharma, D. K. Sehgal and R. K. Pandey, “Studies on deformational behavior of cortical bone using small punch testing and finite element simulation,” in *2013 Proc. WCECS Conf.*, pp. 920–924.

[20] S. P. Kotha, and N. Guzelsu, “Tensile damage and its effects on cortical bone,” *Biomech. J.*, vol. 36, pp. 1683–1689, 2003.

[21] U. Stefan, B. Michael and S. Werner, “Effects of three different preservation methods on the mechanical properties of human and bovine cortical bone,” *Bone J.*, vol. 47, pp. 1048–1053, 2010.

EFFECT OF FLOW CHARACTERISTICS ON THE HEAT TRANSFER PERFORMANCE ACROSS LOW-FINNED FIN BANKS

Seif A. Ahmed
*Department of Mechanical Engineering, College of Engineering
University of Beni-Suef, dr.sife2011@yahoo.com

Abstract- Air is a cheap and safe fluid, widely used in electronic, aerospace and air conditioning applications. Because of its poor heat transfer properties, it always flows through extended surfaces, such as finned surfaces, to enhance the convective heat transfer. In this paper, experimental results are reviewed and numerical studies during air forced convection through extended surfaces are presented. The thermal and hydraulic behaviors of a reference trapezoidal finned surface, experimentally evaluated by present authors in an open-circuit wind tunnel, has been compared with numerical simulations

Keywords - Heat Exchanger, Fins, Radiation, Free and Forced convection.

I INTRODUCTION

Heat exchangers are commonly used in many fields of industry, which are composed of finned surfaces for dissipation of heat by convection and radiation. The calculation of heat transfer of a cooling fin in heat exchanger system is the good practical application of heat transfer. Such fins are used to increase the cooling area of system available for heat transfer between metal walls and conducting fluid such as gases and liquids. In a chemical process, the reactor at hot temperature is cooled using cooling fins. The coolant is the surrounding air. Heat transfer in heat exchanger is dominated by convection from the surfaces, although the conduction within the fin may also influence on the performance. A convenient method to treat convection cooling is to use heat transfer coefficients, **h**. The present work is aimed to identify by an experimental study of the effect of inlet flow angle, and free-stream turbulence level on heat transfer rate to a row of fins arranged horizontally

Q. Zhang1, L. et al. [1] indicated that the inlet boundary layer thickness has little impact on the heat transfer over the tip surface as well as the pressure side near-tip surface. However, noticeable changes in heat transfer are observed for the suction side near-tip surface. Similar to the inlet turbulence effect, such changes can be attributed to the interaction between the passage vortex and the OTL flow.

H. P. Hodson [2] concluded that the aerodynamic efficiency of an axial-flow turbine is significantly less than that predicted by measurements made on equivalent cascades which operate with steady inflow. The turbine rotor midspan profile loss was approximately 50 percent higher than that of the rectilinear cascade. The 50 percent increase in loss is due to the time-dependent transitional nature of the boundary layers.

G. J. Walker [3] decided that the computed performance values show an almost unique relation between the blade losses and the suction surface diffusion ratio. However the correlation of losses with the equivalent diffusion ratio is found to break down at high values of the latter parameter.

Sunita Kruger and Leon Pretorius [4] indicated that the presence of baffles influenced the heat transfer from the hot wall considerably, and it was concluded that a partitioned enclosure containing conducting partitions can be used to represent an enclosed greenhouse containing raised benches with single/multiple racks.

Syeda Humaira Tmasni et al. [5] demonstrated that the attached horizontal obstruction adds some thermal insulation effect. This finding is important in double wall space filled with fiberglass insulation in contemporary buildings, where the side wall is reinforced on the inside with structural members.

Gongnan Xie et al. [7] decided that a double-layer micro channel cannot only reduce the pressure drop effectively but also exhibits better

ISBN: 978-1-61804-288-0

thermal characteristics. Due to the negative heat flux effect, the parallel-flow layout is found to be better for heat dissipation when the flow rate is limited to a low value while the counter-flow layout is better when a high flow rate can be provided.

A J Neely1 et al. [8] investigated that the correct selection of fin geometry can result in a significant increase in overall convective cooling performance.

Parinya Pongsoi et al. [9] showed that the convective heat transfer coefficient (h_o) for a fin pitch of 2.4 mm is relatively low compared with that of other fin pitches with the same air frontal velocity. Using larger fin pitches (i.e., 4.2, 6.2, and 6.5 mm) resulted in negligible differences in the pressure drop.

Parinya Pongsoi et al. [10] decided that no significant effect for either number of tube rows or fin materials on the heat transfer performance is found at high Reynolds number.

V. Dharma Rao et al. [11] demonstrated that the highest heat transfer rates are obtained from a fin array when the base is vertical and the fins attached to it are vertical width-wise.

II Experimental Apparatus and Procedure

A system is catalytic reactor with heat exchanging fins (Fig.1), which has a square base (30 Cm×30 Cm). This base contains fourteen square fins. Each fin (30 ×2.2×0.6) Cm^3 (length ×height ×width) respectively. The space between each two fins is 1.0 Cm. A natural air of a different velocities (0, 0.35, 0.7, 1.2, 2.0, and 3.0 m/s) passes across and a longitudinal the fins. Also, the air passes at an angles 0˚, 45˚, and 90˚. The temperature of inlet end rises rapidly, and then gradually decreases. During operation, the temperature inside the fin is maintained. The heat is conducted within the fins and then transferred to the surrounding air. There is a thermal load system as a galvanized tank with a dimensions of (0.3 ×0.3×0.2) m^3 (length ×width ×height) respectively as shown in Fig.2. There is a thermal resistance located inside the tank. The thermal resistance has an electric power 400 watt. The tank is filled with water before experiments through a hole located at a distance 0.15 m from the beginning near the upper tank surface. The water temperature was maintained at temperature 40˚C. As the air is heated, buoyancy effects cause heat to transport upward by heated air which rises (free convection) or heat sweep to right by forced stream of air (forced convection).

III Measuring Technique

There are a five thermocouple joints a longitudinal the fin at a distance (5, 10, 15, 20, 25 Cm) from the fin end. These joints supplied with a thermocouple of type **k**. The thermocouple terminals connected with a data logger which calculate the five local temperature values immediately, Fig.2. The total measured points each experiment are seventy local points. In this paper we study the centerline measured temperature value (at 15 cm).

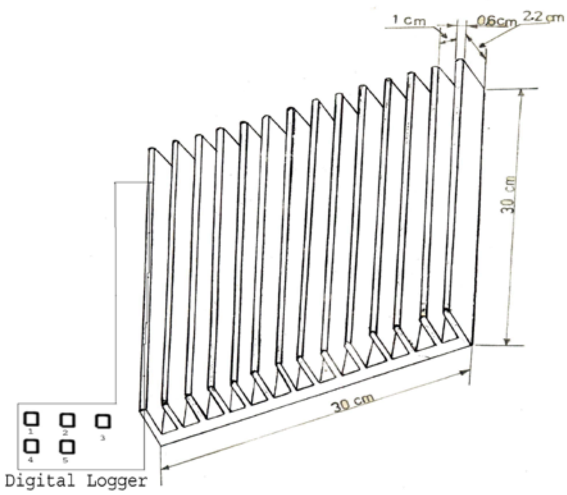

Fig. 1 Types of Used Fins

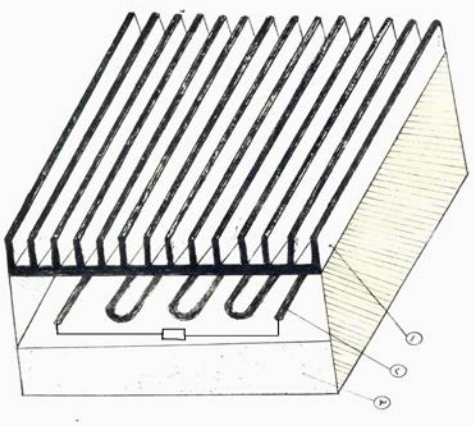

1. Fin. 2. Electic resistance (400 w)

3. Heating load.
Fin arrays
Fig. 2

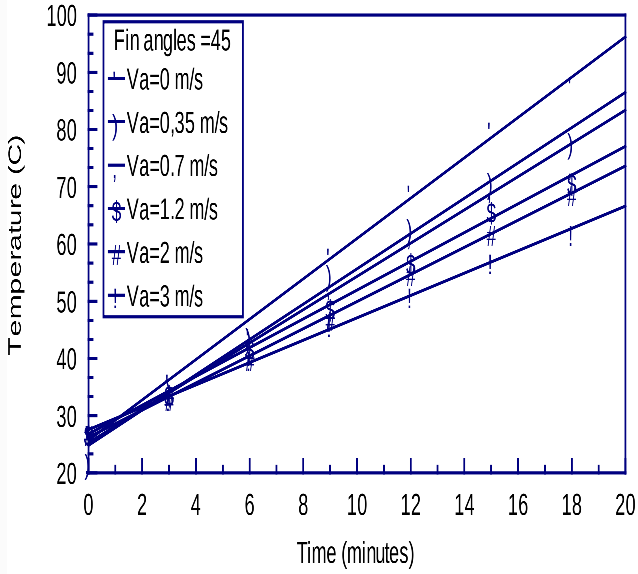

Fig. (3)

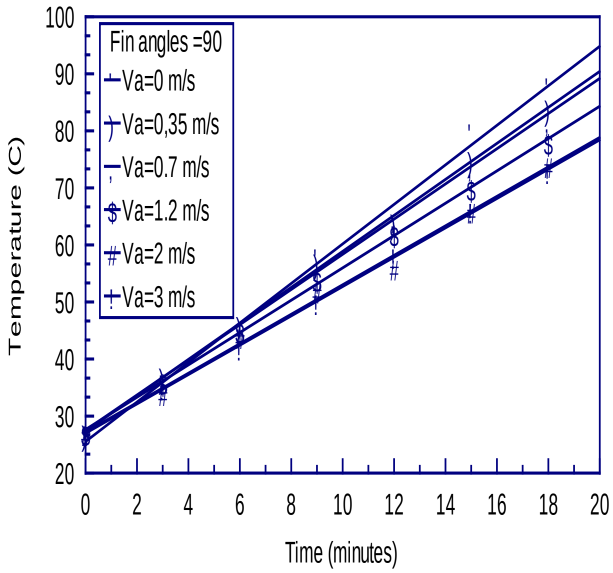

Fig. (4)

IV Results and Discussion

IV. 1 Effect of Fin angle on Heat Transfer Rate:

Fig. (3) shows the relation between the temperature C˚ and the time at variable air velocities (at the range of (0 to 3m/s) at the flow air angle = 45˚. It is obvious from Figures (3), (4) and (5) that the flow angle affect on the fan heat transfer. It is noted from Fig. 3 that for flow angle = 45˚, the temperature range from (68 C˚ to 95 C˚) nearly. It is decided also that as the air velocity increased, as the fins temperature decreased. This as a result of, as the air velocity increased, the heat transfer rate increased, so, the fin temperature decreased.

Also, it is noted from Fig. 4 that for flow angle =90˚, the fins temperature at the range of (75 C˚ to 93 C˚) is slightly high as compared with flow angle = 45˚. It is noted also from Fig. 5, that for flow angle =0˚, the fins temperature at the range of (52 C˚ to 90 C˚) is slightly low as compared with flow angle = 45˚. This decided that as the flow angle increased, as the fin temperatures range decreased.

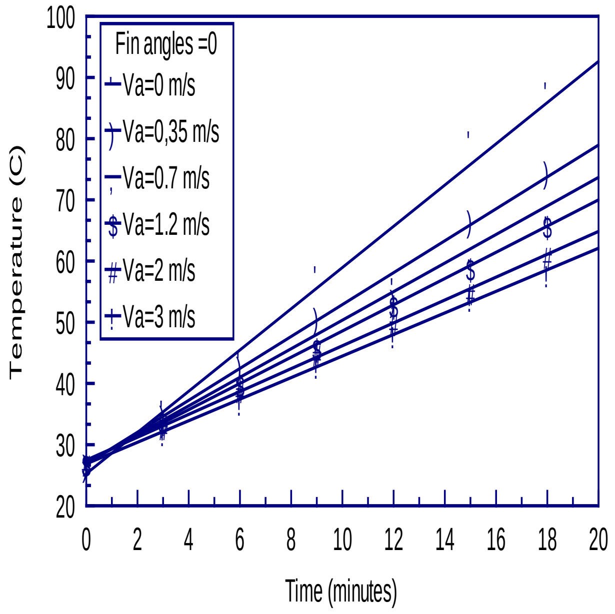

Fig. (5)

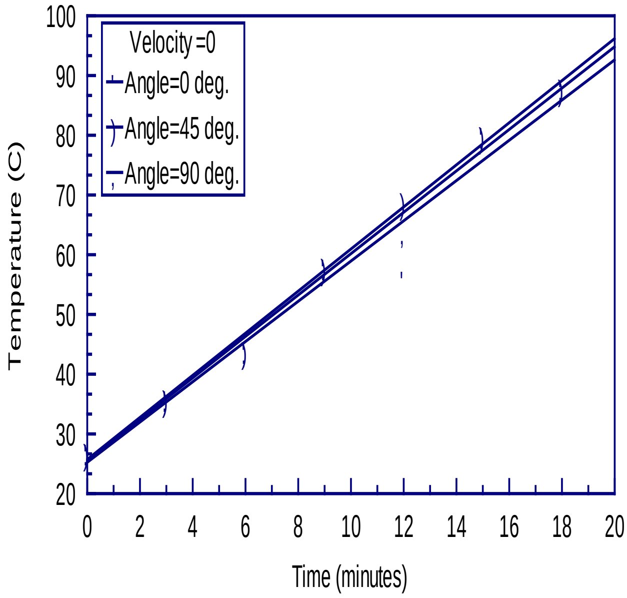

Fig. (6)

Also, notified from Figures (3), (4) and (5) that as flow velocity increased, as fin temperature decreased. This is as a result of increasing heat transfer rate.

IV. 2 Effect of Air Velocities on Heat Transfer Rate:

From Figures (6) to (11). It is noted from Fig. 6 that the temperature range from (90 ˚C to 95 ˚C), but from Fig. (7), the temperature range from (75 ˚C to 90 ˚C). Also, it is evident from Fig. 8 that the temperature range from (70 ˚C to 92 ˚C). This decided that as the air velocity increased, as the fins temperature decreased. This is because the heat transfer rate increased. Also, noted that as the flow angle increased, as the fin temperature decreased.

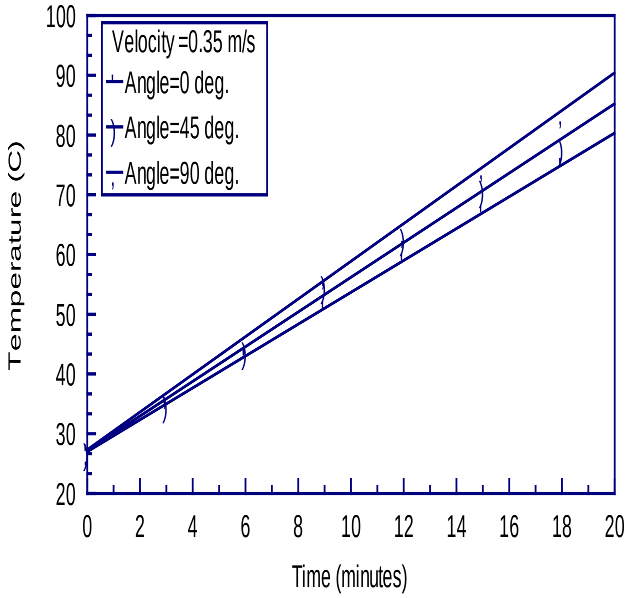

Fig. (7)

ISBN: 978-1-61804-288-0

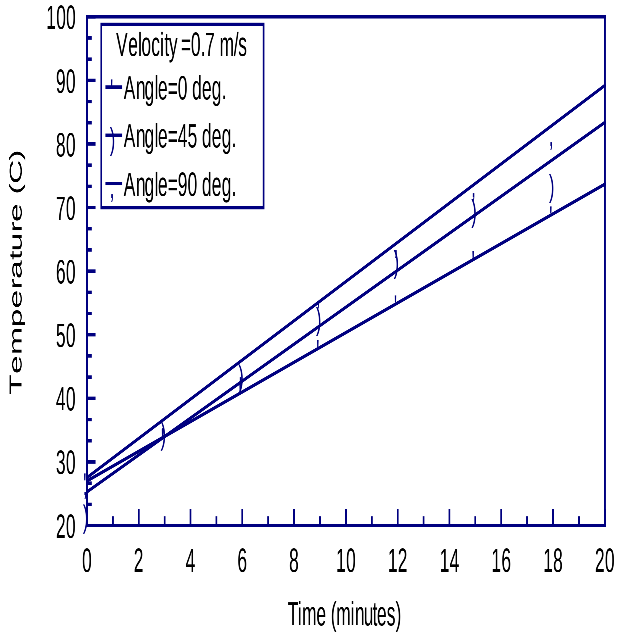

Fig. (8)

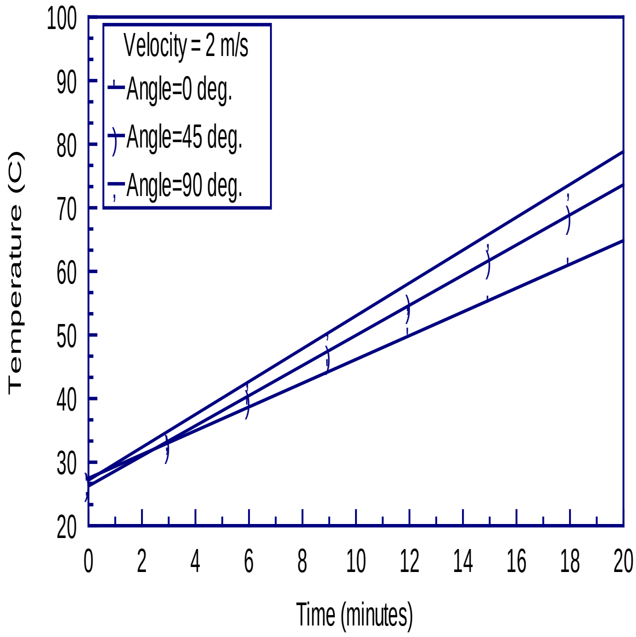

Fig. (10)

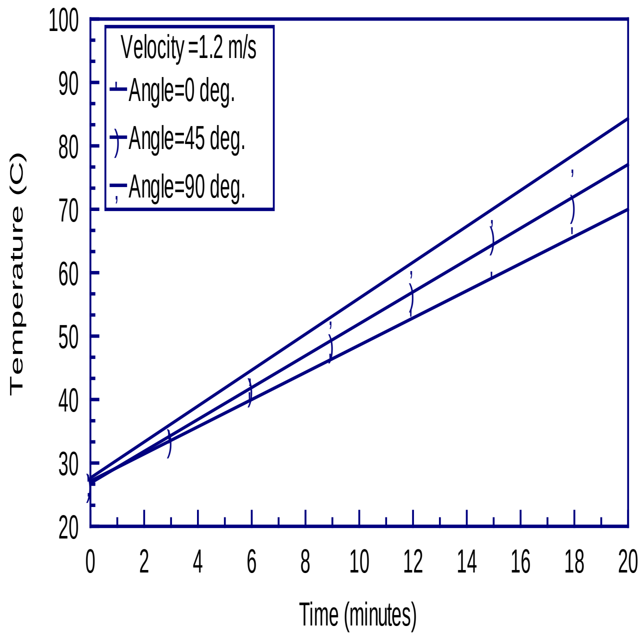

Fig. (9)

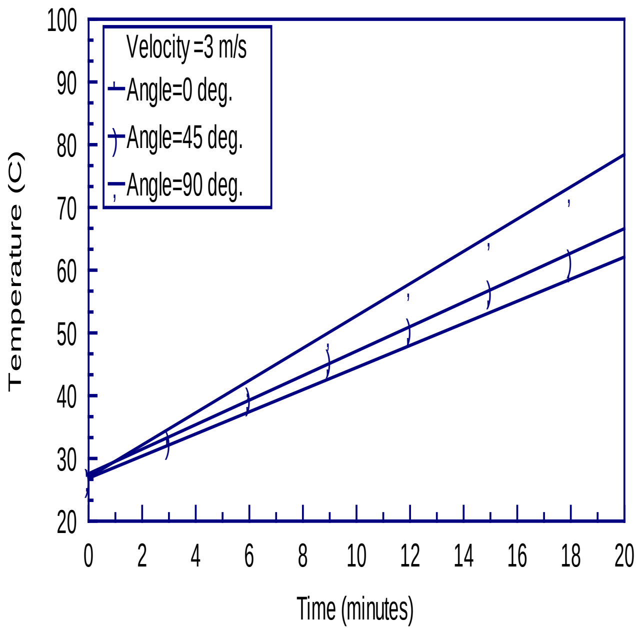

Fig. (11)

It is evident from Fig. (9) that the temperature range nearly (67˚C to 85 ˚C), but from Fig. (10), the temperature range from (63 ˚C to 75 ˚C). Also, it is evident from Fig. (11) that the temperature range from (57 ˚C to 78 ˚C). This decided that as the air velocity increased, as the fins temperature decreased. This is because the heat transfer rate increased. Also, noted that as the flow angle increased, as the fin temperature decreased.

IV.3 Effect of Air Velocities on Heat Transfer Rate:

It is decided from Figures (12) to (14) that both the flow angle and flow speed affect strongly on fins heat transfer rate. Also, noted that both the flow angle = 45˚ , and flow velocity = 3 m/s are the best. Because they reduced the fin temperature approximately 30%.

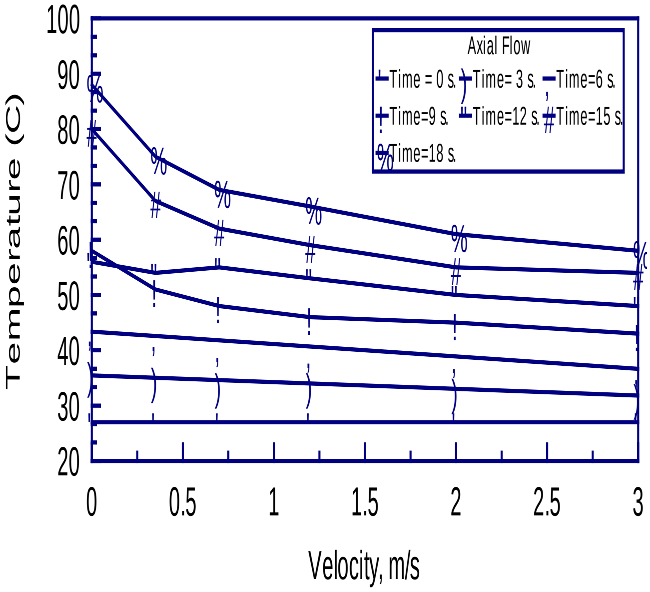

Fig. (12)

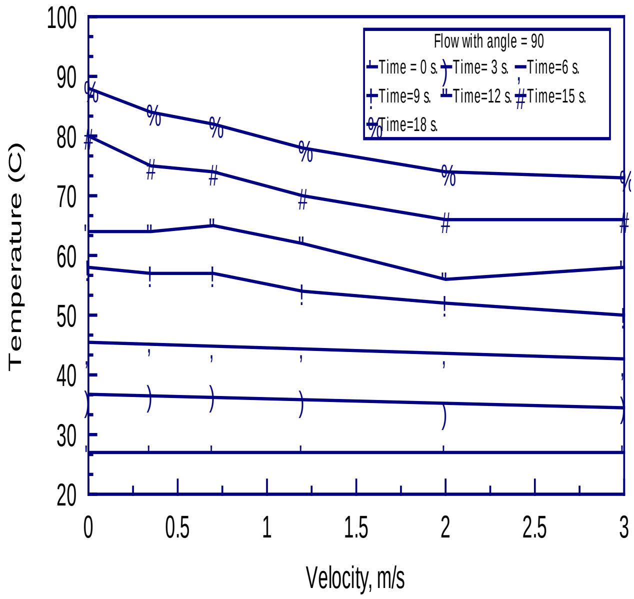

Fig. (14)

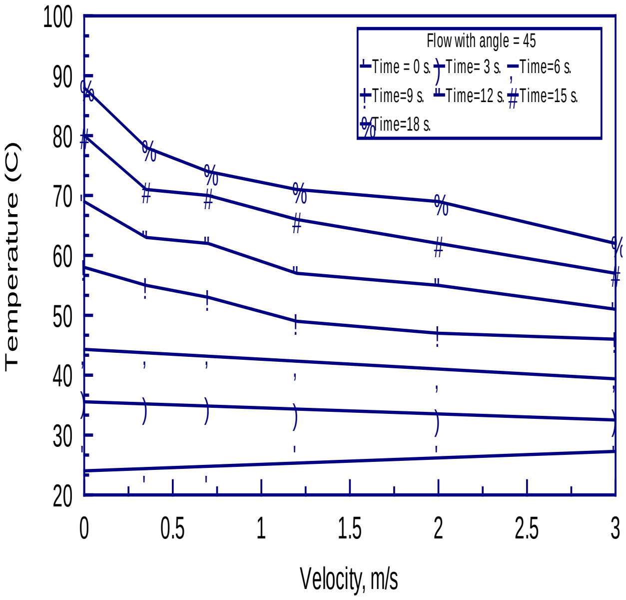

Fig. (13)

IIV. CONCLUSION

1-The radiation heat transfer in forced convection cooled finned surfaces is usually disregarded for two reasons. First, forced convection heat transfer is usually much larger than that due to radiation, and the consideration of radiation causes no significant change in the results. Second, the heat exchanger fin convection cooled systems are mounted so close to each other that a component is almost entirely surrounded by other components at about the same high temperature. As air velocity increased, as the fins temperature decreased. This is because the heat transfer rate increased. Also, noted that as the flow angle increased, as the fin temperature decreased.

2- The radiation effect is most significant when free convection cooled finned surfaces due to convection heat transfer coefficient is small (thus free convection cooling is limited). Also, as the flow angle increased, as the fin temperatures range increased also.

3. The flow angle and flow speed affect strongly on heat transfer fin rate.

4. Both the flow angle = 45° , and flow velocity = 3 m/s are the best. Because they reduced the fin temperature approximately 30%.

ISBN: 978-1-61804-288-0

REFERENCES

[1] Q. Zhang1, L. He and A. Rawlinson " Effects of Inlet Turbulence and End-Wall Boundary Layer on Aerothermal Performance of a Transonic Turbine Blade Tip", Journal of Engineering for Gas Turbines and Power | Volume 136 | Issue 5 | research-article , January 01, 2013.

[2] H. P. Hodson " Boundary Layer and Loss Measurements on the Rotor of an Axial-Flow Turbine" J. Eng. Gas Turbines Power, Vol. 106(2), pp. 391-399 (Apr 01, 1984).

[3] G. J. Walker " A Family of Surface Velocity Distributions for Axial Compressor Blading and Their Theoretical Performance", J. Eng. Power Vol. 98(2), pp. 229-238 (Apr 01, 1976).

[4] Sunita Kruger and Leon Pretorius " The Effect of Vertical and Horizontal Partitions on Natural Convection in a Heated Enclosure", 7th International Conference on Energy Sustainability, ASME , Minneapolis, Minnesota, USA, Jul 14y–19, 2013.

[5] Syeda Humaira Tmasni et all [5]" Energy Streamlines Analyses on Natural Convection Within Porous Square Enclosure With Internal Obstructions", Journal of Thermal Science and Engineering Applications | Volume 5 | Issue 3 | research-article, January 28, 2013.

[6] E. Farsad, S. P. Abbasi and M. S. Zabihi, " Fluid Flow and Heat Transfer in a Novel Microchannel Heat Sink Partially Filled With Metal Foam Medium", Journal of Thermal Science and Engineering Applications, September 05, 2013.

[7] Gongnan Xie et al." Computational Study and Optimization of Laminar Heat Transfer and Pressure Loss of Double-Layer Microchannels for Chip Liquid Cooling", Journal of Thermal Science and Engineering Applications | Volume 5 |, Feb 22, 2013.

[8] A J Neely1 et al. " Extended surface convective cooling studies of engine components using the transient liquid crystal technique", 4] Journal of Engineering for Gas Turbines and Power | Volume 106 | Issue 2 .

[9] Parinya Pongsoi et al., "Effect of fin pitches on the optimum heat transfer performance of crimped spiral fin-and-tube heat exchangers", International Journal of Heat and Mass Transfer, Volume 55, Issues 23–24, November 2012, Pages 6555–6566.

[10] Parinya Pongsoi et al. " Effect of number of tube rows on the air-side performance of crimped spiral fin-and-tube heat exchanger with a multipass parallel and counter cross-flow configuration", International Journal of Heat and Mass Transfer, Volume 55, Issue 4, 31 January 2012, Pages 1403–1411

[11] V. Dharma Rao et al. " Effect of Orientation of Fin Array on Heat Transfer: An Experimental Study", The IUP Journal of Mechanical Engineering, Vol. IV, No. 1, pp. 36-48, February 2011.

Authors Index